Canadian
Journal of Physics

ON THE STABILITY OF DISPLACEMENT FRONTS
IN POROUS MEDIA:
A DISCUSSION OF THE MUSKAT–ARONOFSKY MODEL[1]

A. E. Scheidegger

ABSTRACT

It is well known that, during the displacement of a fluid contained in a porous medium by another less viscous one, the displacement front may become unstable: Fingers occur which proceed rapidly through the system.

The Muskat–Aronofsky model of displacement in porous media, in which it is assumed that a sharp front exists with maximum saturation by the respective fluid being present on either side of the front, is analyzed in the light of the phenomenon of fingering. It is shown that the Muskat–Aronofsky model, in fact, demands that fingering occurs for mobility ratios (displaced/displacing fluid) smaller than *one*. This model should, therefore, *not* be used for the calculation of the *steady* progress of a front for such mobility ratios. The Muskat–Aronofsky model also yields some conditions regarding the geometry of fingers; the latter are deduced. It does not, however, describe the fingering process completely. In this connection, one would have to take recourse to the statistical geometry of porous media. This will be done in a separate paper.

I. INTRODUCTION

Displacement processes in porous media occur in nature during the intrusion of salt water into the fresh water lens beneath oceanic islands. They have been put to commercial use in connection with the recovery of oil from petroleum reservoirs. In the latter case, the displacing fluid is water or gas, whereas the displaced fluid is crude oil. An understanding of these displacement processes is therefore of utmost importance.

An attempt along these lines has been made by Muskat (1934), who considered a simple theoretical model of the displacement process. Aronofsky (1952) used Muskat's model to calculate the shapes of displacement fronts in various types of flooding patterns (five-spot, etc.) of a porous medium for a number of mobility ratios. In particular, he investigated the behavior of the displacement fronts for various cases where the displaced fluid is less mobile than the displacing fluid. This case is particularly important to the oil industry as the displacing fluid (water or gas) is usually more mobile than the displaced oil. It was generally found that the smaller the mobility ratio (of oil/displacing fluid), the poorer is the recovery of oil, a fact which is well-known from experimental investigations.

[1]Manuscript received August 6, 1959.

Although the qualitative predictions of the Muskat–Aronofsky model thus seem to be in agreement with experimental evidence, it will be shown that this model, in fact, lacks self-consistency for mobility ratios smaller than *one*. The very assumptions inherent in the model make it unavoidable that the displacement front becomes unstable ("fingers" out) for such mobility ratios, but stability of the front is a necessary assumption in Aronofsky's calculations.

The present investigation, thus, shows that the fact that "fingering" occurs in a displacement process is the outcome of the presence of a discontinuity in the derivative of the flow potential in the two types of fluids; it has nothing to do with the properties of the porous medium. The Muskat–Aronofsky model even imposes certain conditions upon the geometry of fingers, but it does not, in fact, give the complete description of the fingering process. In this connection, the statistical properties of the porous medium *are* of importance. For a further analysis of the fingering problem, the statistical geometry of porous media has to be known. This will be done in a separate paper (Scheidegger 1960).

II. THE MUSKAT-ARONOFSKY MODEL

If a fluid is being displaced by another in a porous medium, the region in which the saturation changes rapidly from a high value for one fluid to a high value for the other is referred to as "displacement front". It is convenient to treat this front as a surface of discontinuity although this is, in fact, strictly correct only in the case of *immiscible* displacement. In the case of miscible displacement, the front becomes always diffuse due to the mixing that occurs at the interface.

A common way of treating displacement problems is by assuming that, on one side of the front, there is a maximum saturation with one fluid, on the other side a maximum saturation with the second fluid. The displacement is thus assumed as complete, except for an irreducible restsaturation. On both sides of the displacement front, Darcy's law is assumed to be valid with a transmissibility characteristic for the fluid. The solution of a particular displacement problem, then, is effected by a successive approximation: For an initial position of the front, the velocities in the displaced fluid are calculated for a first time step from Darcy's law, which amounts to solving a Laplace equation. It is then assumed that the front moves during the first time step with the calculated velocity which enables one to determine the position of the front at the end of that time step. This procedure is then repeated.

The treatment of the displacement process outlined above has been suggested for the first time by Muskat (1934). It has then been applied by Aronofsky (1952) to an investigation of the influence of the mobility ratio on the sweep efficiency during water encroachment in various types of flood patterns. Aronofsky obtained very interesting results.

From the above remarks, it is quite obvious that the Muskat–Aronofsky treatment of the displacement process is very simplified. First of all, no immiscible displacement process is "complete", i.e. the discontinuity of the saturation is not from 0 to 1 at the front, but something less. This has been

taken into account in investigations of Buckley and Leverett (1942). However, the Buckley–Leverett solution of the displacement process has been obtained only in the case of a linear displacement as the analytical procedures become too involved to permit one to calculate anything but the simplest cases.

Second, a very stringent assumption in the Muskat–Aronofsky treatment is that the front displaces itself in a regular manner during each time step. This assumption would appear by no means assured. It is, in fact, well known (see, for example, Van Meurs 1957) that, instead of a regular displacement of the whole front, protuberances can occur in the latter which may shoot through the porous medium at relatively great speed. This effect is commonly referred to as "fingering". It represents the case where the regular displacement of the front is no longer stable, but other modes of displacement take place with greater preference.

Needless to say, the occurrence of fingering is a severe limitation of many commercial displacement processes, particularly in the oil industry, since a displacing fluid is by-passing large quantities of fluid in the porous medium which one would like to have displaced. An understanding of the whole question of stability of a displacement front is therefore of utmost importance.

III. THE CONDITIONS FOR INSTABILITY

Let us now investigate the stability of a displacement front in the light of the model of fluid displacements in sands which was considered by Muskat and by Aronofsky. Accordingly, we assume the front as sharp, the displacement as complete, and Darcy's law as valid on both sides of the front. The Aronofsky procedure is to assume an initial front, and then to calculate the progress of that front numerically. This is a method which is obviously insufficient for the setting-up of general criteria for the stability of the front. What one would like to do is to assume an Aronofsky-type solution, then to introduce a perturbation into the latter, and, finally to determine a criterion as to whether the perturbation will decay or grow in the course of time. Unfortunately, this is, in general terms, a very difficult problem, as it contains a floating boundary condition which is not easy to treat analytically.

It is therefore suggested to make certain simplifications, which, however, will still preserve the basic physical features of the Muskat–Aronofsky model. Thus, let us assume that a linear displacement experiment is being made (see Fig. 1) where the pore velocity of fluid injection is v. If the displacement
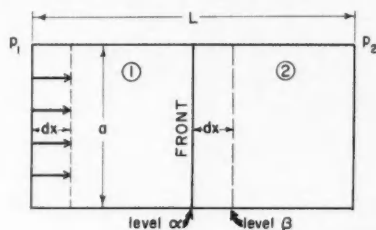
FIG. 1.

process is total and stable, then the displacement front also will move with the velocity v. During the time dt, the displacement of the front will, therefore, be

$$(3.1) \qquad\qquad dx = vdt.$$

The quantity of fluid injected is then $Padx$, a being the cross-sectional area.

In order to have the front moving with the velocity v, there must be a pressure gradient present in the fluids. Denoting the displacing fluid by 1, the displaced fluid by 2, this yields for the pressure gradient in fluid 1

$$(3.2a) \qquad\qquad \mathrm{grad}\ p_1 = \frac{\mu_1 P}{k_1} v$$

and for the pressure gradient in fluid 2

$$(3.2b) \qquad\qquad \mathrm{grad}\ p_2 = \frac{\mu_2 P}{k_2} v.$$

The case represented in Fig. 1 corresponds to stable displacement. We shall refer to it as "case A".

We shall now consider instead of the above case of a stable displacement, the case where a "finger" might develop ("case B"). This possibility is shown in Fig. 2. During the time dt the same quantity adx as before is being injected,
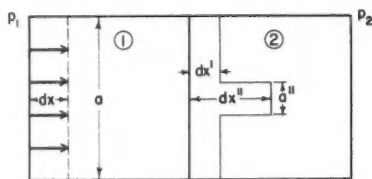
FIG. 2.

and the problem is to determine whether the stable (case A) or the fingered (case B) displacement is more likely to occur under given external circumstances.

The possibility of the existence of a finger, as compared with the stable displacement process, depends on various conditions.

(i) *Volumetric Condition*

The volume of the fluid contained in the finger and the small displacement of the front must be equal to the total fluid injected.
Hence

$$(3.3) \qquad\qquad Padx = P(a'\ dx' + a''\ dx'')$$

where
$$a'' = a - a''.$$

(ii) *Equilibrium Condition*

A finger can be maintained only if there is no tendency for it either to spread out or else to get pinched to nothing. This entails that the pressure gradient in

the finger must be the same as that in the surrounding fluid. Since the mobility of the fluid contained within the finger is different from that contained in the surrounding part of the porous medium, this requires a different velocity in the finger and in the surrounding fluid. Equating (3.2a) and (3.2b) yields

$$P\frac{\mu_1}{k_1}v_1 = P\frac{\mu_2}{k_2}v_2.$$

And, since $v = dx/dt$ (with $m_i = k_i/\mu_i$), $m_1dx' = m_2dx''$

or

(3.4) $$\frac{dx''}{dx'} = \frac{m_1}{m_2}.$$

(*iii*) *Energy Condition*

A finger will develop only if, by its formation, it consumes less energy than the corresponding stable displacement of the whole front.

Let us, therefore, calculate the energy that is required for obtaining the corresponding displacements during the time dt in the two cases (A and B) that are under consideration.

Case A

In this case, the displacement front is shifted steadily by the amount dx during the time dt.

On the side containing fluid 1, the pressure drop is grad p_1. Hence the work W_1^A required to move a slug of fluid 1 into the space between level α and level β (see Fig. 1) is

(3.5) $$W_1^A = a \text{ grad } p_1\, dx^2.$$

Similarly, the work W_2^A required to move a slug of fluid *out* of the space between level α and level β is

(3.6) $$W_2^A = a \text{ grad } p_2\, dx^2.$$

However, one can now express the pressure gradients in terms of the mobility. One has

(3.7) $$\text{grad } p_i = \frac{\mu_i}{k_i}P\frac{dx}{dt}$$

where k_i is the permeability and P the porosity of the medium. Thus, the total work required to move the quantity of fluid under consideration is, in *case A*,

(3.8) $$W^A = Pa\, dx^2\left(\frac{\mu_1}{k_1}+\frac{\mu_2}{k_2}\right)\frac{dx}{dt}.$$

Case B

We shall now consider case B, i.e. the case where there is a finger.

On the side where there is the fluid 1 the work required is

(3.9) $$W_1^B = a' \text{ grad } p_1\, (dx')^2 + a'' \text{ grad } p_2\, (dx'')^2$$

where use has been made of the fact that the pressure gradient in the finger must be the same as that in the surrounding *displaced* fluid (condition (*ii*)).

Similarly, the work required to move the corresponding slug of displaced fluid is

(3.10) $$W_2^B = a' \operatorname{grad} p_2 \, (dx')^2 + a'' \operatorname{grad} p_2 \, (dx'')^2.$$

Again, it is possible to express the pressure gradients in terms of the mobilities. One has

(3.11) $$\operatorname{grad} p_i = \frac{P}{k_i} \mu_i \frac{dx'}{dt}.$$

Hence

(3.12) $$W^B = \frac{dx'}{dt} P \left[\frac{\mu_1}{k_1} a'(dx')^2 + 2 \frac{\mu_2}{k_2} a''(dx'')^2 + \frac{\mu_2}{k_2} a'(dx')^2 \right].$$

The energy condition, as stated earlier, is

(3.13) $$W^B \leqslant W^A;$$

hence

(3.14) $$dx' \left[\frac{\mu_1}{k_1} a'(dx')^2 + 2 \frac{\mu_2}{k_2} a''(dx'')^2 + \frac{\mu_2}{k_2} a'(dx')^2 \right] \leqslant a \, dx^3 \left(\frac{\mu_1}{k_1} + \frac{\mu_2}{k_2} \right).$$

IV. THE CRITICAL CONDITION FOR THE MOBILITY RATIO

It is now possible to combine the three conditions (i, ii, iii, i.e. eqs. 3.3, 3.4, and 3.14) to yield a condition for the critical mobility ratio at which fingering must develop.

For the sake of abbreviation, we write

(4.1) $$a'/a = \alpha'; \qquad a''/a = \alpha''$$

(4.2) $$dx'/dx = \xi'; \qquad dx''/dx = \xi''$$

(4.3) $$k_1 \mu_2 / (k_2 \mu_1) \equiv m_1 / m_2 = \eta.$$

Then the three relevant conditions can be simplified to read

(4.4) $$(i) \qquad 1 = \alpha' \xi' + \alpha'' \xi'',$$

(4.5) $$\alpha' = 1 - \alpha'';$$

(4.6) $$(ii) \quad \xi'' = \eta \xi';$$

(4.7) $$(iii) \quad \xi'(\alpha' \xi'^2 + 2\eta \alpha'' \xi''^2 + \eta \alpha' \xi'^2) \leqslant 1 + \eta.$$

The three conditions can be treated so as to yield a critical condition for the (inverse) mobility ratio η, which can be achieved by a procedure of elimination of the other variables from the system of equations.

From the two equations (i) one has

(4.8) $$\alpha' = \frac{\xi'' - 1}{\xi'' - \xi'},$$

(4.9) $$\alpha'' = \frac{1 - \xi'}{\xi'' - \xi'}.$$

If this be inserted into the third condition, one obtains

$$(4.10) \qquad \xi' \left(\frac{\xi''-1}{\xi''-\xi'} \xi'^2 + 2\eta \frac{1-\xi'}{\xi''-\xi'} \xi''^2 + \eta \frac{\xi''-1}{\xi''-\xi'} \xi'^2 \right) \leqslant 1+\eta$$

and, using condition (ii) for the elimination of ξ',

$$(4.11) \qquad \frac{1}{\eta} \left[\frac{\xi''-1}{1-(1/\eta)} \frac{1}{\eta^2} \xi''^2 + 2\eta \frac{1-(1/\eta)\xi''}{1-(1/\eta)} \xi''^2 + \eta \frac{\xi''-1}{1-(1/\eta)} \frac{1}{\eta^2} \xi''^2 \right] \leqslant 1+\eta,$$

$$(4.12) \qquad \frac{1}{\eta-1} \xi''^2 \left[\frac{1}{\eta^2} (\xi''-1) + 2(\eta-\xi'') + \frac{1}{\eta} (\xi''-1) \right] \leqslant 1+\eta,$$

$$(4.13) \qquad \xi''^2 \left(\frac{\xi''}{\eta} - \frac{1}{\eta^2} + 2\eta - 2\xi'' + \frac{1}{\eta} \xi'' - \frac{1}{\eta} \right) \leqslant \eta^2-1,$$

$$(4.14) \qquad \xi''^2 \left(\frac{\xi''}{\eta^2} - \frac{1}{\eta^2} + 2\eta - 2\xi'' + \frac{1}{\eta} \xi'' - \frac{1}{\eta} \right) \leqslant \eta^2-1.$$

A finger exists only if $\xi'' < 1$, as this is, indeed, the very definition of a finger. Looking at the limiting case $\xi'' = 1$, one obtains a condition for η:

$$(4.15) \qquad 1 - 2\eta^2 + \eta - 1 + 2\eta^3 - \eta - \eta^4 + \eta^2 \leqslant 0$$

or

$$(4.16) \qquad \eta^2 - 2\eta + 1 > 0$$

which is always satisfied.

However, condition (ii) (i.e. 4.6) implies that *geometrically*, a finger can exist only if

$$(4.17) \qquad \eta > 1$$

since the very definition of a finger implies

$$(4.18) \qquad \xi'' > \xi'.$$

The last result shows that the Muskat–Aronofsky model automatically implies that fingering should and will occur as soon as the mobility ratio of displacing vs. displaced fluid exceeds 1. In this instance, it becomes obvious that this model should not be used to calculate sweep efficiencies, etc., for such mobility ratios greater than 1, since the fronts thus calculated cannot possibly remain stable.

V. GEOMETRY OF FINGERS

Finally, one can investigate what predictions the Muskat–Aronofsky model makes about the *geometry* of fingers.

First of all, we know now that the model postulates that fingering should *always* occur if the (inverse) mobility ratio is $\eta > 1$. Since an even (not-fingered) displacement front represents an unstable steady state, it must be assumed that the particular size of a disturbance in the front that will start a finger going will be determined by the statistical properties of the porous medium.

However, once a disturbance has been started, the conditions for instability impose certain limitations as to how the finger may grow.

First of all, the energy condition requires that the left-hand side of (4.14) is always smaller than zero. Denoting the latter by y, this condition can be expressed as follows:

$$(5.1) \qquad y = \xi''^3(1-2\eta^2+\eta)+\xi''^2(-1+2\eta^3-\eta)-\eta^2(\eta^2-1) \leqslant 0.$$

This is a cubic equation in ξ''. One can convince oneself that y is always zero or less for $\xi'' = 1$, $\eta>1$. For, setting $\xi = 1$ yields the following fourth-order expression in η:

$$(5.2) \qquad y_{\xi=1} = -\eta^4+2\eta^3-\eta^2.$$

This is zero for $\eta = 1$; there is, in fact, a double root for $\eta = 1$. There is a further double root at $\eta = 0$, and, since the expression is negative for large $\pm\eta$, it must have the general form shown in Fig. 3. This confirms that for $\eta>1$, there is always a range of values of ξ'' for which the energy condition (5.1) is satisfied.
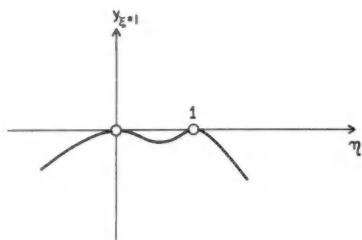
FIG. 3.

This range of possible values for ξ'', however, may not necessarily be the whole domain $\xi''>1$. It is obvious that, for large ξ'', the expression for y becomes negative. However, it may be positive between $\xi'' = 1$ and $\xi''\to\infty$. This can be demonstrated as follows. The maximal positive value that y can attain must be an extremal value. The extremal values of y are obtained by differentiating y with regard to ξ'' and setting the result equal to zero,

$$(5.3) \qquad 0 = \frac{\partial y}{\partial \xi''} = 3\xi''^2(1-2\eta^2+\eta)+2\xi''(-1+2\eta^3-\eta),$$

which yields

$$(5.4) \qquad (a) \ \xi'' = 0,$$

$$(5.5) \qquad (b) \ \xi'' = -\frac{2}{3}\frac{(-1+2\eta^3-\eta)}{1-2\eta^2+\eta}.$$

For large (inverse) mobility ratios η, the last expression becomes

$$(5.6) \qquad \xi''_{max}\sim\frac{2}{3}\eta.$$

Hence, $y(\xi''_{max})$ becomes (for large η, i.e. keeping only the largest powers of η)

$$(5.7) \qquad y \sim \frac{8}{27}\eta.$$

For large η, the function $y(\xi'')$ has, therefore, the shape as shown in Fig. 4.

An inspection of Fig. 4 shows that the energy function y is positive (for large η) for a certain range of ξ''. This implies that there is a forbidden range for the speed of a finger.
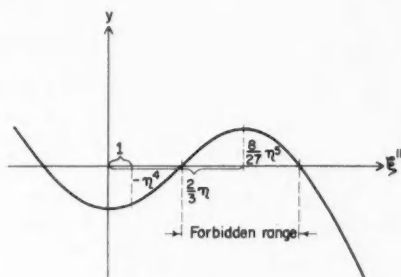
FIG. 4.

A further geometrical condition for fingers can be obtained from a combination of eqs. (4.4), (4.5), and (4.6). For, inserting (4.6) into (4.9) (the latter is already a combination of (4.4) and (4.5)) yields

$$(5.8) \qquad \alpha'' = \frac{1}{\xi''} \frac{\eta - \xi''}{\eta - 1}.$$

This shows that the Muskat–Aronofsky model does not allow fingers to be of arbitrary size. In other words, if a certain fraction of the cross section of a porous material during a linear displacement experiment is fingering out, then eq. (5.8) gives the speed (ξ'') at which these fingers progress into the medium.

VI. CONCLUSION

The discussion of the Muskat–Aronofsky model of displacements in porous media has yielded the result that a displacement front always should become unstable as soon as the mobility ratio (of displacing fluid vs. displaced fluid) exceeds *one*. Furthermore, some conditions have been obtained regarding the geometry of fingers. The Muskat–Aronofsky model is entirely based upon a consideration of the flow potentials in the two fluids, and does not depend at all on the properties of the porous medium. In other words, the fact that fingering *does* occur for certain mobility ratios is the outcome of a discontinuity in the derivative of the flow potential at the interface and not, for instance, an outcome of the statistical properties of the porous medium. Even some of the geometrical properties of the fingers are conditioned by the nature of that discontinuity.

On the other hand, *where* a finger starts and *what* its geometrical characteristics are, within those that are allowed by the framework of the Muskat–Aronofsky model, must need be conditioned by the heterogeneities present in the porous medium. A further investigation of the fingering problem cannot, therefore, be achieved unless the statistical properties of the porous medium in question are examined (see Scheidegger 1960).

From experimental investigations, it is well known that fingering *does* occur. However, specific determinations of the various factors that are involved in causing fingering (such as viscosity ratio, heterogeneities) do not seem to have been undertaken. There have been many "floods" performed (see, for example, Scheidegger 1957) on petroleum well cores to determine the "recovery" of oil by the use of various flooding agents, but, in general, only the total result has been reported which makes it impossible to evaluate these experiments in terms of the displacement mechanism that is taking place. It would appear, though, that fingering does not always occur at $\eta = 1$ as would be a consequence of the Muskat–Aronofsky model. It seems, therefore, that this model neglects an effect which is basic in the mechanism of fingering. It would be the opinion of the writer that this effect is again due to the statistical properties of the porous medium in question: On the one hand, heterogeneities are instrumental in starting fingers by introducing small perturbations into a basically unstable process; the latter then grow to form the fingers. On the other hand, heterogeneities also oppose the formation of fingers by providing for dispersion and remixing of small protuberances. The relative influence of these two effects, and therewith the conditions relevant for finger formation over and above those resulting from the Muskat–Aronofsky model, cannot be estimated unless the statistical–geometrical properties of porous media are known. This will be attempted in a separate paper (Scheidegger 1960).

REFERENCES

ARONOFSKY, J. S. 1952. Trans. AIME, **195**, 15.
BUCKLEY, S. E. and LEVERETT, M. C. 1942. Trans. AIME, **146**, 107.
MUSKAT, M. 1934. Physics, **5**, 250.
SCHEIDEGGER, A. E. 1957. The physics of flow through porous media (University of Toronto Press, Toronto, Ont.).
——— 1960. Phys. of Fluids, **3**, No. 1. In Press.
VAN MEURS, P. 1957. Trans. AIME, **210**, 295.

THE K–LL AUGER SPECTRUM OF $_{62}Sm^{152}$ [1]

G. T. EWAN, R. L. GRAHAM, AND L. GRODZINS[2]

ABSTRACT

The $K–LL$ Auger spectrum of $_{62}Sm^{152}$ has been studied in the Chalk River high-resolution β-ray spectrometer with a proportional counter detector. Seven lines were observed in the Auger spectrum with the following energies and relative intensities:

Energy (kev)	31.20 ±.02	31.62 ±.02	32.01 ±.02	32.19 ±.02	32.25 ±.02	32.61 ±.02	33.22 ±.02
Relative intensity	1.0 ±.05	1.39 ±.06	0.26 ±.06	1.18 ±.06	0.29 ±.09	3.14 ±.13	1.39 ±.06

These measurements are compared with the theoretical predictions of Asaad and Burhop. The measured energies are ~50–60 ev higher than their predictions. Discrepancies exist in the relative intensities but these are smaller than were observed at $Z = 94$.

INTRODUCTION

In a previous paper (Ewan *et al.* 1959a) we reported results of a high-resolution study of the $K–LL$ Auger spectrum of $_{94}Pu^{239}$. The results of these experiments were compared with the predictions of the recent theoretical treatment of Asaad and Burhop (1958). The energies of the lines were in satisfactory agreement with their theoretical predictions, but there were large discrepancies between experiment and theory in the relative intensities of the lines. As the treatment of Asaad and Burhop was non-relativistic it is of interest to test the theory at a lower value of Z where relativistic effects would be expected to be of less importance than at $Z = 94$.

In their theoretical treatment Asaad and Burhop assume that the coupling between the electron shell vacancies is intermediate between $L–S$ and $j–j$, approaching $j–j$ at high Z. They predict the existence of nine $K–LL$ Auger lines instead of the six that would be predicted by pure $j–j$ coupling. The three additional lines at high Z are expected to be weak and to be close satellites of three of the six lines predicted by pure $j–j$ coupling. In our results for $_{94}Pu^{239}$ we observed one of these satellite lines. The other two lines were not resolved in these experiments. The observation of one or more of these satellite lines at another value of Z would support their theoretical approach.

The present paper reports measurements of the relative intensities and energies of the $K–LL$ Auger lines of $_{62}Sm^{152}$. These were observed in a high-resolution study of the low-energy conversion electron spectrum of the 9-hour isomer of Eu^{152}. The measurements were made using the Chalk River $\pi\sqrt{2}$ spectrometer operated at 0.05% resolution in momentum. The energies have been measured with an accuracy of ±0.02 kev and the relative intensities of the more intense lines have an estimated accuracy of ±5%.

EXPERIMENTAL PROCEDURE AND RESULTS

Sources of Eu^{152} were prepared by irradiating enriched Eu^{151} (99%) in the NRX reactor for 12 hours at a flux of 6×10^{13} n/sq. cm/sec. The irradiated material was dissolved in nitric acid. The europium nitrate was sublimed from a boat-shaped tantalum filament at 2000° C through a slot 0.015 in. wide by 0.5 in. long onto a backing of Al foil 800 $\mu g/cm^2$ thick. Two different sources were used, having estimated thicknesses 10 $\mu g/cm^2$ and 25 $\mu g/cm^2$.

The Auger spectrum was studied in the high-resolution spectrometer described in our previous paper. The instrumental resolution was set at 0.05% in momentum. The observed line width was considerably greater due to the natural width of the K and L shell vacancies involved. The spectrometer was operated automatically; the current was cycled through a series of equally spaced increments, and the counts accumulated at each current setting were recorded on an electric typewriter. To get good statistics and to check on reproducibility of the results, repeated scans were made over the Auger region, using the thinner source. The focussed electrons were detected in a continuous flow proportional counter with a 900 $\mu g/cm^2$ mylar window coated on its inner surface with a conducting film of colloidal graphite (Aquadag) of 100 $\mu g/cm^2$ to prevent charging.

The K–LL Auger spectrum of $_{62}Sm^{152}$ obtained with the thinner source is shown in Fig. 1, plotted on a linear scale. The data were also plotted on a semi-log scale after the background and β-ray continuum contributions had been subtracted. The contributions of the low-energy tails to neighboring lines
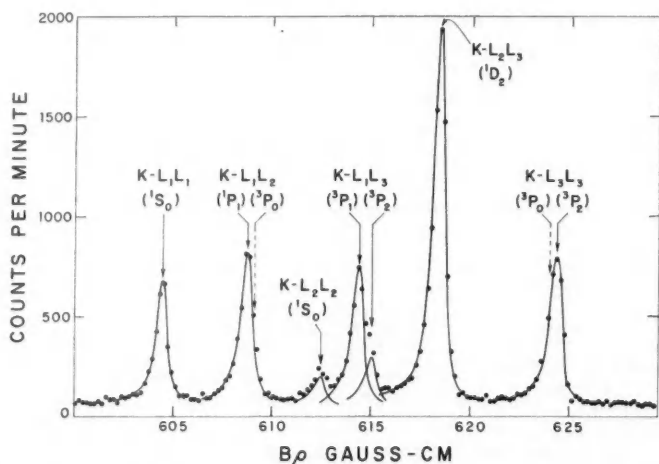
FIG. 1.   The K–LL Auger spectrum of $_{62}Sm^{152}$. Seven lines were observed as indicated by solid lines. The positions of the additional two satellite lines predicted by Asaad and Burhop but not resolved in these experiments are indicated by dashed lines.

were estimated from the semilog plot where it is easier to compare line shapes, as discussed by Ewan *et al.* (1959b). The spectrum obtained from the thicker source was similar, although all lines had much more prominent low-energy tails due to energy degradation in the source material.

The measured energies and relative intensities of the Auger lines are listed in Table I. The errors in the energies allow for the apparent fluctuation

TABLE I

Comparison of experimental and theoretical energies and relative intensities of K–LL Auger lines in $_{62}$Sm^{152}

	Energy, kev		Theoretical, $Z = 62$		Experimental	
Transition	Exptl.	Theor.	(a)	(b)	$_{62}$Sm^{152}	$_{64}$Gd^{156}(c)
$L_1L_1(^1S_0)$	$31.20\pm.02$	31.14	1.0	.70	1.0 ± 0.05	1.0 ± 0.07
$L_1L_2(^1P_1)$	$31.62\pm.02$	31.57	1.34	.94	$\begin{cases}1.39\pm0.06\end{cases}$	1.40 ± 0.10
$L_1L_2(^3P_0)$		31.60	0.047	.033		
$L_2L_2(^1S_0)$	$32.01\pm.02$	31.95	0.18	.13	0.26 ± 0.06	0.27 ± 0.07
$L_1L_3(^3P_1)$	$32.19\pm.02$	32.14	1.82	1.28	1.18 ± 0.06	1.11 ± 0.09
$L_1L_3(^3P_2)$	$32.25\pm.02$	32.20	0.24	.17	0.29 ± 0.09	0.19 ± 0.09
$L_2L_3(^1D_2)$	$32.61\pm.02$	32.55	4.47	3.14	3.14 ± 0.13	3.08 ± 0.18
$L_3L_3(^3P_0)$		33.13	0.25	.18	$\begin{cases}1.39\pm0.06\end{cases}$	1.28 ± 0.09
$L_3L_3(^3P_2)$	$33.22\pm.02$	33.16	1.98	1.39		

NOTE: (a) Normalized to the experimental value for the $L_1L_1(^1S_0)$ line.
(b) Normalized to the experimental value for the $L_3L_3(^3P_2)$ line.
(c) Ewan and Merritt (1960).

(counting statistics and earth's field variations) in the position of the peaks in successive runs of 5 parts in 10^5, uncertainty in calibration due to source positioning (1 part in 10^4) and a possible error in the absolute cancellation of the earth's magnetic field of $\sim5\times10^{-4}$ gauss which would result in a shift of the zero of the momentum scale vs. coil current. These effects give a standard deviation in the absolute energy measurements of ±20 ev.

The relative intensities of the lines were obtained by measuring the areas of the lines after subtraction of the contribution of neighboring lines. The shape of the K–L_1L_1 line was used in estimating these contributions. The measurements were corrected for the variation in transmission of the counter window which increases from 62% at the K–L_1L_1 line to 65% at the K–L_3L_3 line (Geiger *et al.* 1960). Although the absolute value of this correction may be in error by several per cent, the relative correction in this region is only 5%, and is believed to be accurate to $\sim1\%$. The errors quoted for the intensities of the five intense lines are standard deviations deduced from counting statistics only. For the two weak lines an additional error is included to take account of the uncertainty in the subtraction of contributions from neighboring lines. The intensity values listed in Table I are those obtained with the thinner source. The results from the thicker source were similar except for an increased error due to the increased uncertainty in the subtraction of the low-energy tails of neighboring lines.

DISCUSSION OF RESULTS

(a) Energies of Lines

The measured energies are compared with the values predicted by Asaad and Burhop for $Z = 62$. Recent measurements of the $K\alpha_2$ and $K\alpha_1$ X-ray binding energies by Bergvall (1959) have shown that the $K-L_2$ and $K-L_3$ energy differences are 39.523 and 40.118 kev respectively. In computing the theoretical values these differences have been used together with the L_1-L_3 energy difference and the absolute value of the L_3 binding energy listed by Wapstra *et al.* (1959). The measured energies are all ~ 50–60 ev higher than those predicted by Asaad and Burhop, although the relative spacings of the lines are in good agreement within the experimental accuracy. A similar discrepancy of ~ 50–60 ev is also observed for the $K-LL$ Auger lines in Gd^{156} (Ewan and Merritt 1960). These discrepancies in the absolute energies are significantly larger than the error in measurement and may indicate the effect of approximations implicit in Asaad and Burhop's formulation or an uncertainty in the absolute values of the binding energies.

(b) Relative Intensities

The relative intensity values could be affected by the presence of weak conversion lines coinciding with the $K-LL$ Auger lines. However it is very unlikely that such lines, corresponding to unreported γ-transitions, would occur at the same position in the Auger spectrum for two neighboring nuclides. In Table I our present results are compared with the relative intensities of the $K-LL$ Auger lines in Gd^{156} observed in a study of the β-decay of Eu^{156} (Ewan and Merritt 1960). The agreement between the two sets of results indicates that neither set is being seriously affected by unreported conversion lines.

The results are also compared in Table I with the theoretical relative intensities for $Z = 62$ calculated by Asaad and Burhop (1958). The agreement with the theoretical values for $Z = 62$ is considerably better than for the case of $Z = 94$. This is presumably due to the fact that Asaad and Burhop's calculations are non-relativistic and the relativistic effects are less important at the lower Z. However, the disagreement with the calculated intensities is still well outside the experimental error. It is of interest to note that if the measurements are normalized to the experimental value for the $L_1L_1(^1S_0)$ line as in column (a) in Table I the intensities of lines involving the L_3 shell are in disagreement with the theory. However the relative intensities of members of this group are in agreement as indicated in column (b) where the results are normalized to the experimental value for the $L_3L_3(^3P_2)$ line. The present disagreement with theory probably indicates that relativistic effects are still important or that more rigorous wave functions have to be used in the calculations.

It is of interest to note that the $K-L_1L_3$ satellite line predicted by Asaad and Burhop was again observed at $Z = 62$ as well as at $Z = 94$. The other two satellite lines, $K-L_1L_2(^3P_0)$ and $K-L_3L_3(^3P_0)$, expected theoretically were not observed as would be expected from the low-predicted intensity and close

proximity to intense lines, as indicated in Fig. 1. The observation again, at $Z = 62$, of a clearly distinguishable satellite line is clear evidence that the Auger effect cannot be correctly described in terms of pure j–j coupling.

REFERENCES

ASAAD, W. N. and BURHOP, E. H. S. 1958. Proc. Phys. Soc. **71**, 369.
BERGVALL, P. 1959. Arkiv Fysik, **16**, 57.
EWAN, G. T., GEIGER, J. S., GRAHAM, R. L., and MACKENZIE, D. R. 1959a. Can. J. Phys. **37**, 174.
———— 1959b. Phys. Rev. **116** (4).
EWAN, G. T. and MERRITT, J. S. 1960. Can. J. Phys. This issue.
GEIGER, J. S., GRAHAM, R. L., and EWAN, G. T. 1960. Nuclear Phys. To be published.
WAPSTRA, A. H., NIJGH, G. J., and VAN LIESHOUT, R. 1959. Nuclear spectroscopy tables (North-Holland Pub. Co.).

DIFFRACTION BY A UNIDIRECTIONALLY CONDUCTING HALF-PLANE[1]

R. A. HURD

ABSTRACT

The problem of the diffraction of a plane electromagnetic wave by a uni-directionally conducting half-plane is solved by transform techniques. A comparison is made with the results previously obtained by Karp.

INTRODUCTION

A unidirectionally conducting surface has been defined by Toraldo di Francia (1956) as a surface which is perfectly conducting in one direction, and perfectly insulating in the orthogonal direction. Such a surface is an idealization of an array of narrow, closely spaced conducting strips.

The problem of the diffraction of a plane electromagnetic wave by a unidirectionally conducting half-plane was solved recently by Karp (1957). A short time ago, the present author became interested in this problem, and not knowing of Karp's work, obtained a solution by transform techniques. Since the transform approach seems somewhat simpler than Karp's method, and since the answer obtained is readily reduced to known integrals, it was thought worth while to publish the work.

In order to simplify comparison of the two results, the present paper adheres closely to Karp's notation. A discussion of the results is given, and a comparison with Karp's solution is made.

DESCRIPTION OF THE PROBLEM

A unidirectionally conducting half-plane occupies the region $z = 0$, $x > 0$ of the (x,y,z) space. A second rectangular co-ordinate system (ξ,η,z) is set up which is related to the (x,y,z) co-ordinates by

$$(1) \quad \begin{aligned} x &= \xi \cos \alpha - \eta \sin \alpha, \\ y &= \xi \sin \alpha + \eta \cos \alpha, \\ z &= z, \end{aligned}$$

where α is the angle between the positive x and the positive ξ directions, $-\pi/2 \leqslant \alpha \leqslant \pi/2$.

It is assumed that the conductivity is infinite in the ξ direction. In the η direction the conductivity is taken to be zero.

Upon the screen there is incident a plane electromagnetic wave, whose electric components are given by

(2)
$$\mathbf{E}^{(1)} = \mathbf{A}e^{i(\mathbf{k}\cdot\mathbf{r}-\omega t)},$$

where

$$\mathbf{k} = \{k_1,k_2,k_3\},$$
$$\mathbf{r} = \{x,y,z,\}.$$

The total fields are denoted by $\mathbf{E}$, $\mathbf{H}$, and the scattered fields by $\mathbf{E}^{(s)}$, $\mathbf{H}^{(s)}$.

It is required to find the fields, $\mathbf{E}$, $\mathbf{H}$, which satisfy the following boundary conditions:

(3) $E_\xi = 0$ on the screen,

(4) E_η continuous across the screen,

(5) H_ξ continuous across the screen.

In addition, it is necessary to postulate that the various field components have singularities of order less than or equal to $\rho^{-\frac{1}{2}}$ where ρ is the distance to the edge of the screen.

SOLUTION OF THE PROBLEM

Since the current flow on the screen is in the ξ direction, one expects that the scattered fields can be derived from an electric Hertz vector $\mathbf{\Pi}^{(s)}$ with a single component $\Pi_\xi^{(s)}$. This choice gives $H_\xi^{(s)} = 0$, and hence satisfies eq. (5).

Furthermore, since the unidirectionally conducting screen can be regarded as a limiting case of a planar array of closely spaced conducting strips, the symmetry relations

(6)
$$H_{x,y}^{(s)}(z) = -H_{x,y}^{(s)}(-z),$$

(7)
$$E_{x,y}^{(s)}(z) = E_{x,y}^{(s)}(-z),$$

must hold. Note that eq. (4) is satisfied in virtue of eq. (7).

A Hertz vector of appropriate form is

$$\mathbf{\Pi}^{(s)} = \{\Pi_\xi^{(s)},0,0\}$$

with

(8)
$$\Pi_\xi^{(s)} = \int_{-\infty}^{\infty} f(w)e^{i(wx+k_2y\pm\beta z)}dw,$$

where

$$\beta^2 = \kappa^2 - w^2,$$
$$\kappa^2 = k^2 - k_2^2,$$
$$k = \text{free space propagation constant.}$$

The $(+)$ and $(-)$ signs refer to the regions $z > 0$ and $z < 0$ respectively.

Making use of eq. (1) and of the relations

$$\mathbf{E}^{(s)} = \nabla \times \nabla \times \mathbf{\Pi}^{(s)},$$

$$\mathbf{H}^{(s)} = -ikc\epsilon_0 \; (\nabla \times \mathbf{\Pi}^{(s)}),$$

c being the velocity of light in vacuum, one finds that

(9) $$E_\xi^{(s)} = \int_{-\infty}^{\infty} P(w)f(w)e^{i(wx+k_2 y \pm \beta z)}dw,$$

(10) $$H_\eta^{(s)} = \pm kc\epsilon_0 \int_{-\infty}^{\infty} \beta f(w)e^{i(wx+k_2 y \pm \beta z)}dw,$$

where

(11) $$P(w) = \beta^2 + (k_2 \cos \alpha - w \sin \alpha)^2.$$

The boundary condition $E_\xi = 0$, together with eqs. (2) and (9), implies that

(12) $$\int_{-\infty}^{\infty} P(w)f(w)e^{iwx}dw + A_\xi \, e^{ik_1 x} = 0, \qquad \text{for } x > 0.$$

Equation (12) will be satisfied if $P(w)f(w)$ has a simple pole with the proper residue at $w = k_1$;* and if $P(w)f(w)$ is regular elsewhere in the half-plane

$$\text{Im}(w) > -\delta, \; \delta > 0.$$

Therefore

(13) $$P(w)f(w) = \frac{R^+(w)}{w - k_1},$$

(14) $$R^+(k_1) = iA_\xi/2\pi,$$

where $R^+(w)$ is regular for $\text{Im}(w) > -\delta$.

Continuity of $H_{\text{tan}}^{(s)}$ (i.e. $H_\eta^{(s)}$) for $x < 0$, $z = 0$ leads to

(15) $$\int_{-\infty}^{\infty} \beta f(w)e^{iwx}dw = 0, \qquad \text{for } x < 0.$$

Hence

(16) $$\beta f(w) = R^-(w),$$

where $R^-(w)$ is a regular function of w for $\text{Im}(w) < \delta$.

It follows that if $f(w)$ is eliminated from eqs. (13) and (16), then

(17) $$\frac{P(w)R^-(w)}{\beta} = \frac{R^+(w)}{w - k_1}, \qquad \text{for } \delta \geqslant \text{Im}(w) \geqslant -\delta.$$

*It is assumed that $\text{Im}(k) > 0$, and that $\text{Im}(\kappa) > 0$. The pole at $w = k_1$ will lie either above or below the real axis depending upon the angle of incidence. The analysis is here carried out for $\text{Im}(k_1) > 0$; the contrary assumption leads by a similar analysis to the same form for $f(w)$.

Now, from eq. (11), $P(w)$ is a quadratic function of w, and can be written

$$P(w) = -(w-c^+)(w-c^-)\cos^2\alpha,$$

where
$$c^+ = k\sec\alpha - k_2\tan\alpha,$$

$$c^- = -k\sec\alpha - k_2\tan\alpha.$$

For $-\pi/2 \leqslant \alpha \leqslant \pi/2$ it may be shown that

$$\text{Im}(c^+) \geqslant \text{Im}(\kappa) \quad \text{and} \quad \text{Im}(c^-) \leqslant \text{Im}(-\kappa).$$

Hence eq. (17) may be written as

$$(18) \quad \frac{-(w-c^+)R^-(w)\cos^2\alpha}{\sqrt{(\kappa-w)}} - \frac{R^+(k_1)\sqrt{(\kappa+k_1)}}{(w-k_1)(k_1-c^-)}$$
$$= \frac{1}{w-k_1}\left\{\frac{R^+(w)\sqrt{(\kappa+w)}}{w-c^-} - \frac{R^+(k_1)\sqrt{(\kappa+k_1)}}{k_1-c^-}\right\}.$$

The left-hand side of eq. (18) is regular in $\text{Im}(w) < \delta$, the right-hand side is regular in $\text{Im}(w) > -\delta$. Therefore each side is equal to a function $R(w)$ regular in the entire w plane. Furthermore, by using the radiation and edge conditions it may be readily shown that $R^-(w)$ is bounded as $|w|\to\infty$, for w in the lower half-plane, and that $w^{-1}R^+(w)$ is bounded as $|w|\to\infty$ for w in the upper half-plane (see Baker and Copson 1950, pp. 173–174).

This being the case, one finds that $R(w) = 0(w^{\frac{1}{2}})$ for w in the lower half-plane, and $R(w) = 0(w^{-\frac{1}{2}})$ for w in the upper half-plane. Thus by the extension of Liouville's theorem, $R(w) = 0$.

It follows that

$$(19) \quad R^-(w) = \frac{-R^+(k_1)\sqrt{(\kappa+k_1)}\sqrt{(\kappa-w)}\sec^2\alpha}{(w-k_1)(w-c^+)(k_1-c^-)}.$$

Hence using eqs. (8), (14), (16), and (19), the solution of the problem is found to be

$$(20) \quad \Pi_\xi^{(s)} = \frac{iA_\xi(k_1-c^+)\sqrt{(\kappa+k_1)}}{2\pi P(k_1)} \int_{-\infty}^{\infty} \frac{e^{i(wx+k_2y+\beta z)}dw}{(w-k_1)(w-c^+)\sqrt{(\kappa+w)}}.$$

REDUCTION OF THE SOLUTION

On using partial fractions, eq. (20) may be written as the sum of two integrals

$$(21) \quad \Pi_\xi^{(s)} = C\int_{-\infty}^{\infty} \frac{e^{i(wx+k_2y\pm\beta z)}}{\sqrt{(\kappa+w)}}\left\{\frac{1}{w-k_1} - \frac{1}{w-c^+}\right\}dw,$$

$$= C(I_1 - I_2),$$

where
$$C = \frac{iA_\xi}{2\pi}\frac{\sqrt{(\kappa+k_1)}}{P(k_1)}.$$

I_1 is recognized as an integral encountered in the ordinary half-plane problem, and as shown by Copson (1949) and Baker and Copson (1950, pp. 139–140), can be reduced to Fresnel integrals. Putting $x = \rho \cos \phi$, $z = \rho \sin \phi$ one finds

$$(22) \quad I_1 = 2\sqrt{\frac{\pi}{\kappa + k_1}} \, e^{i(k_2 y + \pi/4)} \{ e^{i\kappa\rho \cos (\phi+\theta)} F[-\sqrt{2\kappa\rho} \sin \tfrac{1}{2}(\phi+\theta)]$$
$$+ e^{i\kappa\rho \cos (\phi-\theta)} F[-\sqrt{2\kappa\rho} \sin \tfrac{1}{2}(\phi-\theta)]\},$$

where
$$F(a) = \int_{-\infty}^{a} e^{i\lambda^2} d\lambda,$$

and
$$\theta = \cos^{-1}(k_1/\kappa), \qquad\qquad 0 \leqslant \theta \leqslant \pi.$$

I_2 has the same form as I_1 and may be reduced in a similar manner.

$$(23) \quad I_2 = 2\sqrt{\frac{\pi}{\kappa + c^+}} \, e^{i(k_2 y + \pi/4)} \{ e^{i\kappa\rho \cos (\phi+i\psi)} F[-\sqrt{2\kappa\rho} \sin \tfrac{1}{2}(\phi+i\psi)]$$
$$+ e^{i\kappa\rho \cos (\phi-i\psi)} F[-\sqrt{2\kappa\rho} \sin \tfrac{1}{2}(\phi-i\psi)]\}^*$$

where
$$\psi = \cosh^{-1}(c^+/\kappa).$$

The complete solution is then

$$(24) \quad \Pi_\xi^{(s)} = \frac{-A_\xi}{P(k_1)} \frac{e^{i(k_2 y - \pi/4)}}{\sqrt{\pi}} \left\{ e^{i\kappa\rho \cos (\phi+\theta)} F[-\sqrt{2\kappa\rho} \sin \tfrac{1}{2}(\phi+\theta)] \right.$$
$$+ e^{i\kappa\rho \cos (\phi-\theta)} F[-\sqrt{2\kappa\rho} \sin \tfrac{1}{2}(\phi-\theta)]$$
$$- \sqrt{\frac{\kappa + k_1}{\kappa + c^+}} \left[e^{i\kappa\rho \cos (\phi+i\psi)} F[-\sqrt{2\kappa\rho} \sin \tfrac{1}{2}(\phi+i\psi)] \right.$$
$$\left. \left. + e^{i\kappa\rho \cos (\phi-i\psi)} F[-\sqrt{2\kappa\rho} \sin \tfrac{1}{2}(\phi-i\psi)] \right] \right\}.$$

LIMITING BEHAVIOR OF THE SOLUTION

For large values of its argument, the Fresnel integral may be approximated by

$$(25) \quad F(a+ib) \simeq \sqrt{\pi} \, e^{i\pi/4} - \frac{ie^{i(a+ib)^2}}{2(a+ib)}, \qquad\qquad \text{if } a \gg 1;$$

$$(26) \quad F(a+ib) \simeq \frac{-ie^{i(a+ib)^2}}{2(a+ib)}, \qquad\qquad \text{if } a \ll -1.$$

When the real part of the argument is small

$$(27) \quad F(a+ib) \simeq \sqrt{\pi} \, e^{i\pi/4} + 0(a) + 0(b^{-1}), \qquad \text{if } |a| \ll 1, b \gg 1;$$

*Fresnel integrals of complex argument have been tabulated by Clemmow and Munford (1952).

(28) $$F(a+ib) \simeq 0(a)+0(b^{-1}), \qquad\qquad \text{if } |a| \ll 1,\, b \ll -1;$$

providing that $|ab| \ll 1$.

The asymptotic behavior of I_1 for large ρ is found from eqs. (25) and (26) with $b = 0$. There are three regions of different behavior:

(i) $$I_1 \simeq \frac{2\pi i}{\sqrt{(\kappa+k_1)}} e^{i[k_2 y + \kappa\rho \cos(\phi-\theta)]} + I_1', \qquad 0 \leqslant \phi < \theta;$$

(ii) $$I_1 \simeq I_1', \qquad\qquad\qquad \theta < \phi < 2\pi-\theta;$$

(iii) $$I_1 \simeq \frac{2\pi i}{\sqrt{(\kappa+k_1)}} e^{i[k_2 y + \kappa\rho \cos(\phi+\theta)]} + I_1', \qquad 2\pi-\theta < \phi \leqslant 2\pi;$$

where

$$I_1' = 2\sqrt{\frac{\pi}{\rho}} \frac{\sin\phi/2}{\kappa\cos\phi-k_1} e^{i(k_2 y-\pi/4+\kappa\rho)}.$$

Region (i) is the geometrical shadow in which the dominant part of I_1 produces an $E_\xi^{(s)}$ which cancels $E_\xi^{(i)}$. In region (ii) there is no component of scattered field of the same magnitude as the incident field. This is the region of uniform illumination. Region (iii) is the reflection zone in which I_1 produces the ordinary reflected wave.

Next consider I_2. For $\rho \to \infty$, the real part of $-\sqrt{2\kappa\rho}\,\sin\frac{1}{2}(\phi\pm i\psi)$ is large and negative, except in the vicinity of $\phi = 0$ or $\phi = 2\pi$.

If these regions are excluded, application of eq. (26) gives

(29) $$I_2 \simeq 2\sqrt{\frac{\pi}{\rho}} \frac{\sin\frac{1}{2}\phi}{\kappa\cos\phi-c^+} e^{i(k_2 y+\kappa\rho-\pi/4)}, \qquad 2\pi-\epsilon \geqslant \phi \geqslant \epsilon.$$

On the other hand, when ϕ is so near zero or 2π that $\kappa\rho \sin\phi \ll 1$ when $\rho \gg 1$, then providing ψ is not too small, eqs. (27) and (28) are applicable. It is found that

(30) $$I_2 \simeq \frac{2\pi i}{\sqrt{(\kappa+c^+)}} e^{i[k_2 y+\kappa\rho \cos(\phi-i\psi)]} + 0(\rho^{-\frac{1}{2}}) + 0(\phi), \qquad \phi < \epsilon;$$

(31) $$I_2 \simeq \frac{2\pi i}{\sqrt{(\kappa+c^+)}} e^{i[k_2 y+\kappa\rho \cos(\phi+i\psi)]} + 0(\rho^{-\frac{1}{2}}) + 0(2\pi-\phi), \qquad \phi > 2\pi-\epsilon.$$

This surface wave has the following characteristics:

(i) it is exponentially decreasing with increasing $|z|$,

(ii) it proceeds in a direction given by $\gamma = \tan^{-1}(k_2/c^+)$, γ being measured from the positive x axis.

(iii) it is a slow wave whose propagation velocity is $v = kc(k_2^2+c^{+2})^{-\frac{1}{2}}$,

(iv) it has both $E_\xi = 0$ and $H_\xi = 0$.

COMPARISON WITH KARP'S SOLUTION

In the notation of the present paper, Karp's solution may be written

(32) $$\Pi_\xi^{(s)} = \frac{A_\xi}{P(k_1)} \sqrt{\frac{\kappa+k_1}{\pi}} e^{i(k_2 y-\pi/4)} (J_1-J_2),$$

where

$$(33) \qquad J_1 = e^{ik_1 z} \int_{-\infty}^{z} e^{i(\kappa \rho_0 - k_1 x_0)} \, \sin \, (\tfrac{1}{2} \tan^{-1} z/x_0) \frac{dx_0}{\sqrt{\rho_0}},$$

$$(34) \qquad J_2 = e^{ic^+ z} \int_{-\infty}^{z} e^{i(\kappa \rho_0 - c^+ z_0)} \, \sin \, (\tfrac{1}{2} \tan^{-1} z/x_0) \frac{dx_0}{\sqrt{\rho_0}},$$

in which

$$\rho_0^2 = x_0^2 + z^2.$$

The two solutions will be identical if it can be shown that

$$J_1 = \frac{iI_1}{2\sqrt{\pi}} e^{-i(k_2 y - \pi/4)},$$

$$J_2 = \frac{iI_2}{2\sqrt{\pi}} e^{-i(k_2 y - \pi/4)}.$$

Actually, it will be shown that the J's are the negative of the above quantities involving the I's. The difference of sign is attributed to an error in Karp's work. (Karp's eq. (15) follows from his eq. (14) only by changing the sign of $E_\xi^{(1)}$.)

In J_1 the change of variable $x_0 = z \sinh t$ is made.

$$(35) \qquad J_1 = \sqrt{\frac{z}{2}} \, e^{ik_1 z} \int_{-\infty}^{\sinh^{-1}(x/z)} e^{-iz(k_1 \sinh t - \kappa \cosh t)} \, (\cosh \tfrac{1}{2} t - \sinh \tfrac{1}{2} t) dt.$$

Now putting

$$k_1 = k_3 \sinh \tau, \text{ and } \kappa = k_3 \cosh \tau,$$

and making the change of variable $t - \tau = s$, one finds

$$(36) \qquad J_1 = \sqrt{\frac{z}{2}} \, (\cosh \tfrac{1}{2}\tau - \sinh \tfrac{1}{2}\tau) e^{ik_1 z} \int_{-\infty}^{a} e^{ik_3 z \, \cosh \, s}(\cosh \tfrac{1}{2}s - \sinh \tfrac{1}{2}s) ds,$$

with

$$a = \sinh^{-1}(x/z) - \sinh^{-1}(k_1/k_3).$$

In eq. (36) put $v = \sqrt{2k_3 z} \sinh \tfrac{1}{2}s$ in the first term, and put $v = \sqrt{2k_3 z} \cosh \tfrac{1}{2}s$ in the second term, giving

$$(37) \qquad J_1 = \frac{1}{\sqrt{k_3}}(\cosh \tfrac{1}{2}\tau - \sinh \tfrac{1}{2}\tau) e^{ik_1 z} \left\{ e^{ik_3 z} \int_{-\infty}^{\sqrt{2k_3 z} \, \sinh \, \frac{1}{2}a} e^{iv^2} dv \right.$$
$$\left. + e^{-ik_3 z} \int_{-\infty}^{-\sqrt{2k_3 z} \, \cosh \, \frac{1}{2}a} e^{iv^2} dv \right\}.$$

It can be shown without difficulty that

$$\sqrt{2k_3 z} \, \sinh \tfrac{1}{2}a = -\sqrt{2\kappa\rho} \, \sin \tfrac{1}{2}(\phi - \theta),$$

$$\sqrt{2k_3 z} \, \cosh \tfrac{1}{2}a = \sqrt{2\kappa\rho} \, \sin \tfrac{1}{2}(\phi + \theta),$$

and

$$\cosh \tfrac{1}{2}\tau - \sinh \tfrac{1}{2}\tau = \sqrt{\frac{k_2}{\kappa + k_1}}\,.$$

Therefore,

$$(38) \quad J_1 = \frac{1}{\sqrt{\kappa + k_1}}\Big\{ e^{i\kappa\rho \,\cos\,(\phi+\theta)} F[-\sqrt{2\kappa\rho}\,\sin \tfrac{1}{2}(\phi+\theta)]$$

$$+ e^{i\kappa\rho \,\cos\,(\phi-\theta)} F[-\sqrt{2\kappa\rho}\,\sin \tfrac{1}{2}(\phi-\theta)]\Big\}.$$

Comparing this result with the expression for I_1 (eq. (22)) gives

$$(39) \qquad\qquad J_1 = \frac{-iI_1}{2\sqrt{\pi}}\, e^{-i(k_2 y - \pi/4)},$$

which is the result desired. The reduction of J_2 proceeds along similar lines, and there is no necessity to carry it out here.

REFERENCES

BAKER, B. B. and COPSON, E. T. 1950. The mathematical theory of Huyghens' principle (Oxford University Press).
CLEMMOW, P. C. and MUNFORD, C. M. 1952. Phil. Trans. Roy. Soc. A, **245**, 189.
COPSON, E. T. 1946. Quart. J. Math. **17**, 19.
KARP, S. N. 1957. New York University Institute of Mathematical Sciences, Report EM-108.
TORALDO DI FRANCIA, G. 1956. Nuovo cimento, **3**, 1276.

THE INFRARED FUNDAMENTAL BAND OF LIQUID AND SOLID HYDROGEN[1]

H. P. Gush,[2] W. F. J. Hare,[3] E. J. Allin, AND H. L. Welsh

ABSTRACT

The infrared fundamental band of liquid and solid hydrogen was investigated over a range of para-concentrations from 25% to 100% with a prism spectrometer and, in part, with a grating spectrometer at a resolution of ~ 0.2 cm^{-1}. The spectrum of the solid shows (a) comparatively sharp Q, $S(0)$, and $S(1)$ lines due to quadrupolar interaction, (b) broad bands interpreted as combination tones of the molecular frequencies with the lattice frequencies (phonon spectra), and (c) weak double transitions of the type $S_1(0) + S_0(0)$. At high resolution the quadrupolar $S(0)$ and $S(1)$ groups show weak single transitions, $S_1(0)$ and $S_1(1)$, and much stronger double transitions of the type $Q_1(J) + S_0(J)$, $J = 0, 1$. In solid parahydrogen the lines become very sharp and the double transition, $Q_1(0) + S_0(0)$, shows a complex structure; the observations are in good agreement with the theory of the rotational and vibrational levels of solid parahydrogen by Van Kranendonk. The quadrupolar Q branch shows a structure which is interpreted as double transitions of the type $Q \pm \delta_i$, where the δ_i are the small changes in energy due to the orientational transitions of two ortho-molecules. The phonon spectra show a maximum at the Debye temperature of the solid, and, at higher resolution, a structure indicative of the various branches of the lattice frequencies. A long extension of the phonon spectrum towards high frequencies is probably due to multiple phonon creation. Double transitions, for which the cancellation principle in induced absorption does not apply, account for at least 98% of the intensity of the spectrum of the solid.

INTRODUCTION

The changes which take place in the fundamental band of the pressure-induced infrared absorption spectrum of gaseous hydrogen on passing to the condensed phases and the general features of the spectra of the liquid and solid have been described in a series of short communications (Allin *et al*. 1955; Hare *et al*. 1955; Gush *et al*. 1957; Allin *et al*. 1958). In the present paper a detailed description of the band in the condensed phases, based on more recent work at higher spectral resolution, will be given. The Raman spectrum of solid hydrogen has been very important in unravelling the more complex structure of the infrared spectrum. The original Raman study of the solid by Allin *et al*. (1956) has now been supplemented by a high dispersion investigation by Bhatnagar *et al*. (1960). Many features of the infrared and Raman spectra have been rendered intelligible by the recent theoretical study of the rotational and vibrational energy bands of solid parahydrogen by Van Kranendonk (1959, 1960).

EXPERIMENTAL

The experimental arrangement for observing the fundamental band of liquid and solid hydrogen is essentially quite simple, since the band lies in the region 2.0–2.5 μ and absorption path lengths of only a few millimeters are

required. Two cryostats of somewhat different designs using liquid helium as the coolant have been employed; these are illustrated in Fig. 1.

The cryostat shown in Fig. 1(a) was employed for temperatures in the range 22–10° K. Liquid helium, C, was contained in a glass vacuum flask, A,
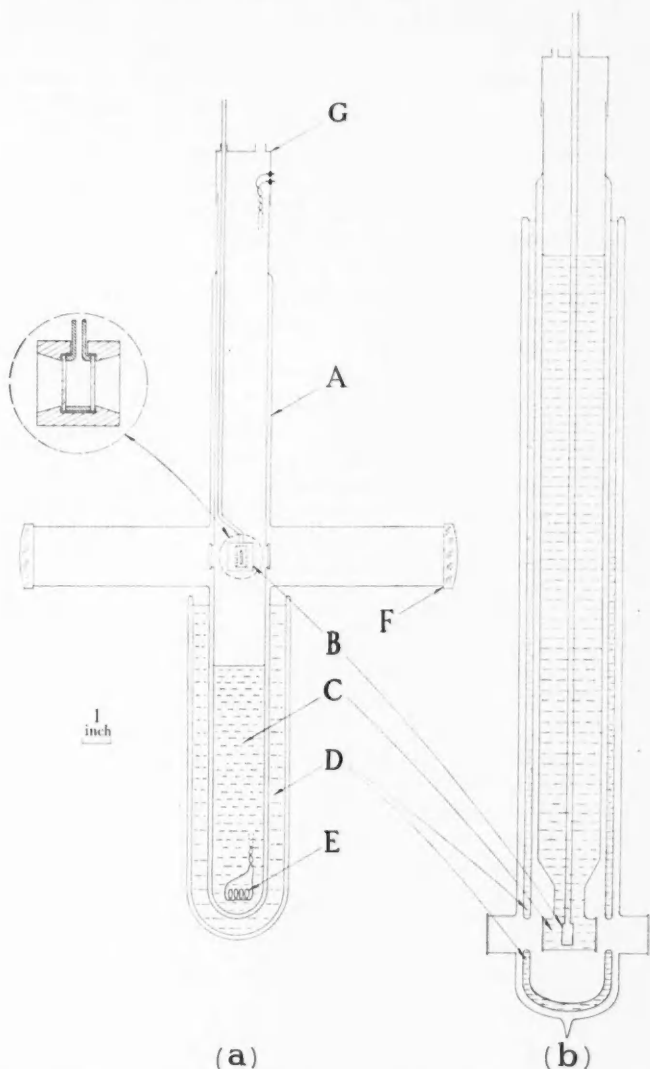
FIG. 1.   Two cryostats for infrared studies at low temperatures: (a) for temperatures above 4.2° K, (b) for temperatures below 2.2° K.

and surrounded by the liquid air flask, D. Two parallel plane windows were cemented with Araldite on the inner wall of A in diametrically opposite positions. The outer wall of A was extended to form a crossarm in line with the windows, and closed by a second set of windows or by rock salt lenses, F. The purpose of the crossarm was to prevent condensation of atmospheric moisture on the outer windows. The absorption cell, B, was suspended in line with the windows and cooled by cold helium gas evaporating from the liquid. The rate of evaporation of the liquid helium, and hence the rate of cooling of the cell, could be controlled by the electric heater, E. Unless precautions were taken this method of cooling produced a vertical temperature gradient in the absorption cell, which, although it facilitated the growth of a clear solid, made the temperature of the specimen rather indefinite. The absorption cell was therefore enclosed in a heavy copper block with slots to permit the passage of radiation. In addition, the windows of the cell were made of synthetic sapphire, which has a relatively high thermal conductivity at low temperatures (Berman 1951), and were attached to the pyrex spacer by Araldite cement. Commercial electrolytic hydrogen, purified by slow distillation in a separate cryostat, was admitted to the cell by an inlet tube extending through the top of the cryostat. By controlling the rate of boiling of the liquid helium, the hydrogen could be kept as a liquid or cooled to form a clear solid. The temperature of the hydrogen in the absorption cell was inferred from its vapor pressure, using the data of Woolley, Scott, and Brickwedde (1948). In forming the solid it was noted that the temperature of the surface of the liquid, as determined from the vapor pressure, was about $0.5°$ K higher than the fusion temperature when solidification began to take place, usually at the windows of the cell. The error in the measured temperatures is therefore of the order of $0.5°$ K in the range $22-10°$ K; below $10°$ K the vapor pressure of the solid is too low to be used for temperature measurement.

In the second cryostat, shown in Fig. 1(b), the absorption cell was immersed in liquid helium. This was used for observations on solid hydrogen at temperatures below $2.2°$ K, the transition temperature from liquid helium I to liquid helium II; above $2.2°$ K the formation of bubbles in helium I precluded any absorption measurements. The liquid helium and the liquid air reservoirs were combined in a single four-walled vacuum flask; plane windows were sealed in the walls near the bottom, in such a way that light could pass through the liquid helium chamber without passing through the liquid air in the outer chamber. The absorption cell, B, a short cylinder of pyrex glass with plane ends, was first raised above the surface of the liquid helium and filled with liquid hydrogen; the hydrogen was then solidified and the cell lowered into position between the windows. The temperature of the hydrogen in the cell was assumed to be the same as that of the helium bath which could be measured from the helium vapor pressure.

Observations were made on the absorption of normal hydrogen, pure parahydrogen, and mixtures containing known proportions of ortho- and parahydrogen. The latter were prepared by adding known volumes of parahydrogen to known volumes of normal hydrogen at room temperature and pressures

somewhat below atmospheric. Pure parahydrogen was prepared by liquefying hydrogen in a vessel containing a chrome–alumina catalyst (Grilly 1953) and allowing the liquid hydrogen to remain in contact with the catalyst for some hours.

The absorption was first studied with a Perkin–Elmer Model 12C spectrometer using a LiF prism and a PbS detector. Emission lines in the spectrum of the mercury arc, Edser–Butler fringes, and bands due to absorption by atmospheric water vapor were used to determine the frequency calibration of the recorded spectra. In later experiments details in the contours of the sharp components were resolved with a grating instrument, the Perkin–Elmer Model 98G, having as dispersing element a 62.5×62.5 mm, 600 line/mm plane grating; the detector was a cooled PbS cell. A prism monochromator limited the radiation incident on the absorption cell to a narrow wavelength range in the desired region of the spectrum. The frequency standards used here were visible and infrared lines from a neon discharge. The instrumental line width was 0.2 cm^{-1}.

With both spectrometers the source of radiation was a commercial 750-watt, 115-volt projection lamp operated at a current of 5.5 amperes from a stabilized a-c. power supply. The light was focussed on the absorption cell and an image of the cell formed on the slit of the spectrometer; this was in general accomplished by a system of mirrors. In some experiments using the cryostat in Fig. 1(a), the outer windows were replaced by rock salt lenses; the first of these focussed the light on the cell while the second formed the image of the cell on the spectrometer slit.

THE SPECTRA AT LOW RESOLUTION

The absorption profiles in Fig. 2 show the gross changes in the shape of the fundamental band of normal hydrogen as the temperature is lowered from room temperature to 11° K. The two profiles for the gas, at 298° and 70° K, show that the various components of the band become sharper as the temperature is lowered; this effect is a consequence of the longer duration of molecular collisions at lower temperatures. Further sharpening of the components is evident in the spectra of the liquid and solid, and new resolved features appear, particularly in the spectrum of the solid.

The Q branch, which corresponds to $\Delta J = 0$, where J is the rotational quantum number, has three components in the spectrum of the gas. The central component, Q_Q, which can barely be distinguished* in the cases shown in Fig. 2(a), becomes a sharp line in the spectrum of the liquid and the solid, its frequency remaining close to that of the band origin, ν_0. The components, Q_R and Q_P, in the spectrum of the gas have been interpreted by Chisholm and Welsh (1954) as summation and difference tones, $\nu_0 \pm \nu_k$, where ν_0 denotes the vibrational frequency of the hydrogen molecule and $h\nu_k$ is the continuum of kinetic energies of the relative motion of the absorbing molecule and its

---

*The Q_Q component is evident only at high gas pressures where the broad Q_P and Q_R components are more widely separated, and is most clearly resolved for heavy perturbing molecules such as N$_2$ or A (Hare and Welsh 1957).
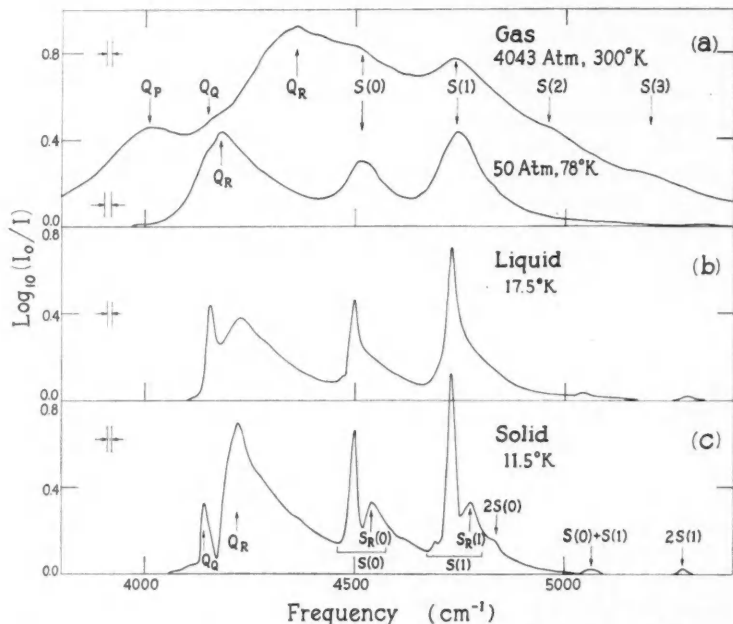
FIG. 2. The fundamental band of normal hydrogen at low resolution in (a) the compressed gas, (b) the liquid, and (c) the solid.

nearest neighbors. The difference tone, Q_P, decreases rapidly in intensity as the temperature is lowered and is no longer apparent in the spectra of the liquid and solid. Q_R, on the other hand, persists in the condensed phases as a broad continuum, which, in the case of the solid, must be construed as a spectrum of summation tones of ν_0 with the vibrational frequencies of the crystal lattice. The Q_R component thus constitutes a "phonon" spectrum of the solid.

Only two of the rotational transitions, $S(J)$, persist at very low temperatures; these are $S(0)$, the $J = 0 \rightarrow J = 2$ transition in parahydrogen, and $S(1)$, the $J = 1 \rightarrow J = 3$ transition in orthohydrogen. The presence of these transitions in infrared absorption and in the Raman effect (McLennan and McLeod 1929; Allin, Feldman, and Welsh 1956) shows that molecular rotation is more or less unhindered in the liquid and solid. The $S(0)$ and $S(1)$ transitions appear in the spectrum of the liquid and the solid as *groups* of lines, in each of which one component, designated S_R in Fig. 2, is broad and similar in shape to the Q_R component. It is clear that the $S_R(0)$ and $S_R(1)$ features can be associated with summation tones of the type, $\nu_0 + \nu(J) + \nu_k$, where $\nu(J)$ indicates the frequency associated with a rotational transition.

In addition to the $S(0)$ and $S(1)$ groups three weak absorption maxima, designated $2S(0)$, $S(0)+S(1)$, and $2S(1)$ in Fig. 2, appear in the spectra of the

liquid and solid. These can be assigned to double transitions in which one molecule executes a rotation–vibrational transition and a second molecule a purely rotational transition in the ground vibrational state. The $2S(0)$ transition is most clearly apparent in the spectrum of pure parahydrogen (Allin *et al.* 1955).

It is well-known that the infrared spectrum of hydrogen, which is forbidden for reasons of symmetry in the free molecule, appears in the compressed gas as a result of distortions of the electron distribution during molecular collisions. The theory of pressure-induced absorption in gaseous hydrogen (Van Kranendonk 1958) shows that quadrupolar interaction is responsible for most of the intensity of the S lines and a small part of the intensity of the Q branch; the greater part of the intensity of the Q branch, on the other hand, is due to overlap interaction of the colliding molecules. From experimental evidence (Chisholm and Welsh 1957; Hare and Welsh 1957) it appears that the Q_Q component should be associated with quadrupolar interaction, and the Q_R and Q_P components with overlap interaction. It is therefore reasonable to assume that Q_Q and the other sharp lines in the spectrum of solid hydrogen are due to quadrupolar interaction; this view is borne out by the detailed theory of the rotational energy bands in solid parahydrogen by Van Kranendonk (1960).

Solid hydrogen thus presents a very particular case of induced absorption. For the explanation of the quadrupolar lines, the solid can be considered in the first approximation as a set of freely rotating molecular quadrupole moments with a regular spatial distribution of their centers of mass on an hexagonal close-packed lattice. There is, however, a small dependence of the intermolecular forces in solid hydrogen on the molecular orientations, and this anisotropic part of the molecular interaction prevents the molecular rotation from being entirely free. The fine structure of the quadrupolar lines, discussed in the next section, is a consequence of the anisotropy of the intermolecular potential. An explanation of the broad components of the spectrum of the solid would involve, on the other hand, a detailed theory of the interaction of the molecular vibration and rotation with the translational motions of the molecules, that is, the lattice vibrations of the solid.

THE SPECTRA AT HIGH RESOLUTION

The frequencies of the quadrupolar lines of the solid could be determined in most cases to within ± 0.1 cm^{-1}, and form the basis of the interpretation of the spectrum. If the molecular rotation in the solid were entirely free, the rotational structure of the Raman and infrared spectra could presumably be analyzed with the familiar rotational energy scheme for a free diatomic molecule. This procedure cannot, however, be carried out in detail because of the complexity introduced into the rotational states of the crystal by the anisotropic part of the molecular interaction. The perturbation and splitting of the energy states in the solid have also the effect that the infrared and Raman frequencies do not coincide exactly since the selection rules are not the same for the two types of spectra. The Raman spectrum, which is of course allowed even in the free molecule, is in general the simpler of the two. As a basis for the

analysis of the infrared spectrum we have therefore chosen the Raman fre-
quencies $Q_1(0) = 4149.8$ cm^{-1} and $S_1(0) = 4485.8$ cm^{-1} of solid parahydrogen
and $Q_1(0) = 4151.8$ cm^{-1} and $Q_1(1) = 4143.4$ cm^{-1} of solid normal hydrogen,
as observed at high resolution by Bhatnagar et al. (1960); these frequencies
are indicated by the solid triangles on the abscissa axis in Figs. 3 to 6 below.
Additional frequencies occurring in the rotational analysis were calculated by
using the values of B_v and D_v derived by Stoicheff (1957) from the Raman
spectrum of the low pressure gas; these are indicated by open triangles on the
abscissa axis of the diagrams. An additional complication in the frequency
analysis is the fact that the frequencies observed in both the Raman and the
infrared spectrum are somewhat dependent on the ortho–para ratio of the
sample. This is particularly true of the vibrational frequency; for example, the
Raman $Q_1(0)$ frequency has the value 4149.8 cm^{-1} in solid parahydrogen and
4151.8 cm^{-1} in solid normal hydrogen.

The $S(0)$ Quadrupolar Lines

It is convenient to begin the discussion of the quadrupolar lines with the
$S(0)$ transition. Figure 3 shows absorption profiles in the neighborhood of
4500 cm^{-1} for a series of para-concentrations (C_p) from 0.25 to 1; the absorption
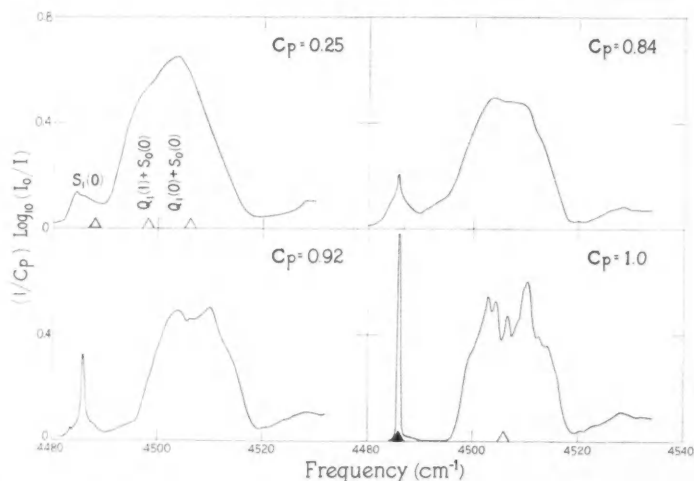
FIG. 3.   The quadrupolar $S(0)$ lines of hydrogen at high resolution for a series of ortho–para
ratios (C_p = fractional para-concentration) with a path length of 1.0 mm at 1.9° K.

intensity, $(1/C_p)\log_{10}(I_0/I)$, is normalized to unit para-concentration. For
normal hydrogen ($C_p = 0.25$) the absorption consists of a weak component
near the calculated frequency of the $S(0)$ Raman line of solid normal hydrogen
and a much stronger band at higher frequencies with two overlapping compo-
nents. The two components of the latter band have been interpreted as double
transitions in which one molecule makes the vibrational transition and a

second molecule makes the rotational transition in the ground vibrational state (Gush *et al.* 1957). The vibrational transition can take place in either a para- or an ortho-molecule, so that the double transitions can be designated $Q_1(0)+S_0(0)$ and $Q_1(1)+S_0(0)$.* The double transitions are separated in frequency from one another and from the single transition, $S_1(0)$, because of the rotation–vibration interaction. Frequencies of the double transitions calculated from the approximate constants and indicated by the open triangles in Fig. 3 show a satisfactory agreement with the partially resolved components for normal hydrogen. As C_p increases, the component $Q_1(0)+S_0(0)$ gains intensity at the expense of $Q_1(1)+S_0(0)$, and the band shifts slightly to higher frequencies.

The high intensity of the double transitions as compared with the single transition can be explained qualitatively as follows. Since solid hydrogen has an hexagonal close-packed lattice structure, any given molecule is almost, but not quite, an inversion center of the crystal. If the given molecule were exactly an inversion center the dipoles induced by it in its neighbors would cancel, and the molecule could not perform a transition. However, the cancellation does not occur if the rotational part of the transition takes place in a second molecule. The situation will be clarified by a consideration of the simple case of three molecules shown in Fig. 4, in which the central molecule is an inversion center
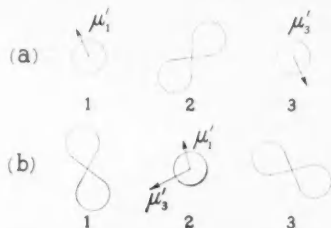
Fig. 4. Illustrating the cancellation principle in induced absorption. The principle is operative for a single transition (*a*), but inoperative for a double transition (*b*).

of the configuration. In (*a*) the quadrupole moment of molecule 2 induces equal and opposite dipoles in molecules 1 and 3. The vibrational transition dipoles are of the form, $\mu_1' \propto Q_2'\alpha_1$ and $\mu_3' \propto Q_2'\alpha_3$, where Q_2' is the rate of change of the quadrupole moment of molecule 2 with respect to its vibrational co-ordinate and α_1 and α_3 are the polarizabilities of molecules 1 and 3. As molecule 2 rotates μ_1' and μ_3' remain equal and oppositely directed so that their resultant is always zero. In (*b*) the transition dipoles induced in molecule 2 by Q_1 and Q_3 are of the form, $\mu_1' \propto Q_1\alpha_2'$ and $\mu_3' \propto Q_3\alpha_2'$; if there is no phase relationship between the rotations of 1 and 3, μ_1' and μ_3' are independent and there is no cancellation effect. The double transitions (1,2) or (2,3) are therefore possible, the central molecule performing of course the vibrational transition. The low intensity of the single transition, $S_1(0)$, in solid hydrogen is thus a direct

*To designate double transitions the usual spectroscopic nomenclature is modified by adding a suffix to the transition symbol to indicate Δv, the change in the vibrational quantum number involved.

consequence of the hexagonal close-packed structure; if the lattice were cubic close-packed the single transition would be absent. The double transition, on the other hand, has appreciable intensity, since it depends on the strength of the interaction but not directly on the symmetry of the lattice. The absence of a cancellation effect for double transitions has been proved quite generally by Van Kranendonk (1957, 1959); it will be shown that the principle is very important for all aspects of the spectrum of solid hydrogen.

If the interpretation of the strong component of the $S(0)$ group in terms of the double transitions, $Q_1(1)+S_0(0)$ and $Q_1(0)+S_0(0)$, is correct, one might expect the integrated intensity of the component to obey the relation,

$$\int \alpha d\nu = aC_pC_o+bC_p^2,$$

where $\alpha \equiv \alpha(\nu)$ is the absorption coefficient and C_o and C_p are the fractional concentrations of ortho- and para-molecules, respectively. The observed intensities do in fact obey this relation very closely; the constants a and b, which are proportional to the transition probabilities, have values in the ratio 3:1.

The profiles in Fig. 3 show a remarkable sharpening of the components of the $S(0)$ group as the para-concentration increases to 100%. In pure parahydrogen the single transition, $S_1(0)$, has a half-width which is substantially equal to the spectral slit-width, 0.2 cm^{-1}; its intrinsic half-width must therefore be less than this. The double transition, $Q_1(0)+S_0(0)$, for pure parahydrogen retains its rather large over-all width but shows a structure in which some eight components are resolved.

According to Van Kranendonk's theory (1959, 1960) of the rotational energy levels of solid parahydrogen the structure of the double transition arises from the fact that the rotational excitation is not localized on any one of the neighbors of the molecule which is vibrationally excited, but must be described by travelling rotational excitations. The theory gives an over-all width for the double transition band between 20 and 22.4 cm^{-1}, in good agreement with the experimental value of ~ 22 cm^{-1} (Fig. 3). The excitation of the upper state of the single transition, $S_1(0)$, is localized on one molecule so that the cancellation effect applies; the calculation shows that the intensity of the line is reduced to 1/46 of the value which it would have if the cancellation were not taken into account. The ratio of the intensities of the $S_1(0)$ and $Q_1(0)+S_0(0)$ transitions is equal to $(5S_1^2/8S_2)$ $(Q'^2\alpha^2/Q^2\alpha'^2)$, where S_1 and S_2 are lattice sums which can be evaluated. The polarizability constants α and α' are known from experiment, and Q and Q' have been calculated theoretically by James and Coolidge (1938). This theoretical value of Q, 0.45 ea_0^2, is probably fairly accurate since it is close to that obtained by Harrick and Ramsey (1952) from molecular beam experiments and by Kiss, Gush, and Welsh (1959) from the intensity of the pressure-induced rotational spectrum of hydrogen. However, the theoretical value of Q', 0.30 ea_0, is much lower than the value, 0.54 ea_0, obtained recently by Hunt (1959) from an analysis of the pressure-induced fundamental band of hydrogen gas. The ratio of the intensities of the

single and double transitions is $1:46$ using James and Coolidge's value of Q' and $1:14$ using Hunt's value. The measured value of the intensity ratio from the present high dispersion study is $1:15$; the experimental value of Q' given by Hunt is thus confirmed.

With the addition of even a small concentration of ortho-molecules the structure in the double transition becomes diffuse and the width of the single transition increases. The energy levels of the solid are thus clearly dependent on the ortho–para ratio, as is also evident in the Raman spectrum (Bhatnagar *et al.* 1960). This dependence is shown in a striking way when the detail of the absorption in the neighborhood of the single transition, $S_1(0)$, is studied in thicker crystals. Figure 5 shows the absorption in this region with a path
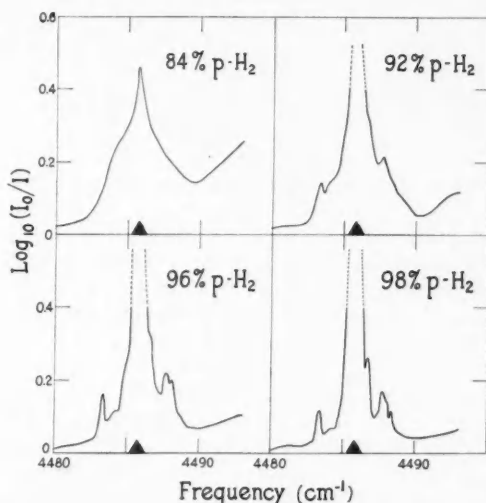
FIG. 5.   The single transition, $S_1(0)$, at high resolution for a series of high para-concentrations with an absorption path length of 3.9 mm at 1.9° K.

length of 3.9 mm instead of 1 mm as used for the profiles in Fig. 3. With an ortho-concentration of only 2% a whole series of weak components is observed; these are shifted from $S_1(0)$ to higher and lower frequencies by amounts up to 3 cm^{-1}. These satellites must arise from the perturbation of the $v = 1$, $J = 2$ state of a para-molecule which has one or more ortho-molecules in its shell of nearest neighbors. As the ortho-concentration increases, the "pure" para-component, arising from absorption in a para-molecule surrounded by para-molecules, decreases in intensity and the pattern of the single transition as a whole becomes diffuse.

The S(1) Quadrupolar Lines

In Fig. 6 the variation of the $S(1)$ group with ortho–para ratio is shown. The group consists of the single transition, $S_1(1)$, and two double transitions,

$Q_1(1) + S_0(1)$ and $Q_1(0) + S_0(1)$, with frequencies close to those calculated from the Raman data. The frequency separation of the single and double transitions is greater for the $S(1)$ than for the $S(0)$ transition, so that even in normal hydrogen the single transition $S_1(1)$ is easily distinguishable. As the ortho–para
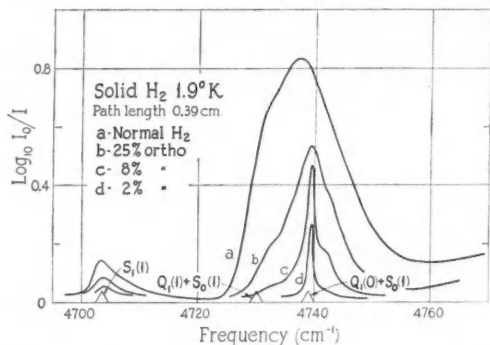
Fig. 6.   The quadrupolar $S(1)$ lines at high resolution for a series of ortho-concentrations.

ratio decreases the $Q_1(1) + S_0(1)$ transition decreases rapidly in intensity. With only 2% orthohydrogen present the $Q_1(0) + S_0(1)$ transition alone is observed; the line has a half-width of ~ 1 cm^{-1}, and its frequency must be characteristic of an ortho-molecule surrounded by para-molecules. The intensity of the double transition obeys the relation,

$$\int \alpha d\nu = a'C_o^2 + b'C_oC_p,$$

where the constants a' and b' are approximately in the ratio $1:2.5$.

The Q Quadrupolar Lines

The variation of the Q quadrupolar lines with ortho–para ratio in solid hydrogen is shown in Fig. 7. In normal hydrogen two rather broad maxima are present; although it seems probable that these should be associated with $Q_1(0)$ and $Q_1(1)$ transitions, their frequencies are higher than the corresponding Raman frequencies by 1.2 and 3.1 cm^{-1}, respectively. As the ortho-concentration decreases the maxima become sharper, and at very low ortho-concentrations three sharp components emerge. Finally, in pure parahydrogen no quadrupolar Q lines are present; this is understandable since in both the initial and the final state all the molecules are in the $J = 0$ rotational state and no quadrupolar interaction is possible.

From the shift in frequency from the Raman values and the appearance of at least three components at low ortho-concentrations, it seems unlikely that the Q transitions observed are single transitions. Moreover, the Q branch as a whole at high ortho-concentrations has an intensity comparable with the $S(0)$ and $S(1)$ double transitions and much greater than the $S(0)$ and $S(1)$
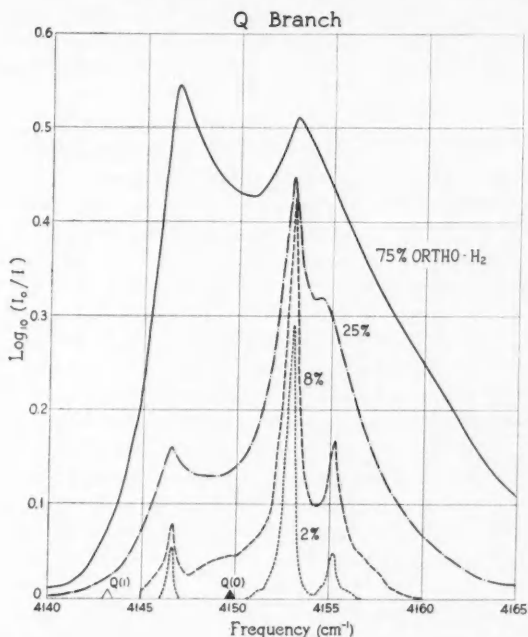
FIG. 7.   The Q quadrupolar lines at high resolution for a series of ortho–para ratios with an absorption path length of 3.9 mm at 1.9° K.

single transitions. The conclusion that the Q branch owes most of its intensity to double transitions is confirmed by the fact that the integrated intensity obeys the relation,

$$\int \alpha d\nu = a''C_o^2 + b''C_oC_p,$$

where a'' and b'' have values approximately in the ratio 3:2.

The only general type of double transition which can be associated with the Q branch is that in which a purely vibrational transition in one molecule is accompanied by an orientational transition in one (or more) of its nearest neighbors. Since the para-molecules are in the $J = 0$ state, orientational transitions can occur only for ortho-molecules; this agrees with the expression given above for the integrated intensity, which contains no term in C_p^2.

The three lines observed in low ortho-concentrations (Fig. 7) at 4146.6, 4153.0, and 4155.2 cm^{-1} might be assigned tentatively to the double transitions $Q_1(0) - \delta_a$, $Q_1(0) + \delta_a$, and $Q_1(0) + \delta_b$, where $\delta_a = 3.2$, $\delta_b = 5.4$, and $Q_1(0) = 4149.8$ cm^{-1}. This value of $Q_1(0)$ is the same as the Raman value for solid parahydrogen, but this coincidence is not necessarily significant. The difference tone, $Q_1(0) - \delta_a$, should have an intensity less than that of the sum-

mation tone, $Q_1(0)+\delta_a$, by the factor $\exp(-\delta_a hc/kT)$, which has the value 0.10 at 2° K; the observed relative intensities are in approximate agreement with this value. The transition, $Q_1(0)-\delta_b$, would, on the other hand, be too weak to be observed.

At first sight the transitions, δ_a and δ_b, inferred from the experimental data might seem to be associated with two different orientational transitions of a single ortho-molecule. However, a simple calculation shows that, because of the hexagonal symmetry of the crystal, an orientational transition of a single ortho-molecule surrounded by para-molecules involves a change in energy only of the order of 0.1 cm^{-1}. On the other hand, a pair of neighboring ortho-molecules can perform orientational transitions with changes in energy of the order of δ_a and δ_b; for these the quadrupole–quadrupole interaction becomes operative and removes the ninefold rotational degeneracy of the pair. It therefore seems probable that the lines observed should be associated with transitions of this type. If two ortho-molecules are indeed involved in the orientational transition, the intensities of the lines should show a characteristic variation with C_o in the region of low ortho-concentrations. Unfortunately, the data obtained up to the present are too meager to confirm the hypothesis. It is also evident that the intensity of a transition of the type, $Q_1(0)-\delta$, should show a strong temperature dependence, but the present high dispersion results, which all refer to 1.9° K, cannot be used to check this point. It should be noted that, if the orientational transitions involve two ortho-molecules, the magnitude of the intensities observed at low ortho-concentrations would probably require some clustering of ortho-molecules rather than a random distribution; such an effect would not be inconsistent with the anomalies observed in the specific heat of solid hydrogen.

At higher ortho-concentrations it is clear that different types of orientational transitions would be possible and the spectrum would become increasingly complex; thus, in Fig. 7, a considerable change in the shape of the profile is evident even with an ortho-concentration of 8%. Except at very low ortho-concentrations purely ortho-transitions of the type, $Q_1(1)+\delta$, should also be present. The net result of the superposition of many different types of double transitions could then give in the case of normal hydrogen the observed broad intensity distribution with two maxima, the frequencies of which are somewhat higher than the $Q_1(0)$ and $Q_1(1)$ Raman frequencies of normal hydrogen.

Further experiments are now in progress to check these more or less tentative conclusions on the origin of the structure of the Q branch in solid hydrogen.

SUMMARY OF THE OBSERVED FREQUENCIES AND THEIR ASSIGNMENTS

The frequencies of the maxima observed in the fundamental band of solid normal hydrogen are summarized in Table I, and those of solid 98% and 100% parahydrogen in Table II, along with the assignments deduced from the preceding discussion. The sharp lines in the spectra at high resolution could be measured with an error of about ± 0.1 cm^{-1}. The broad maxima have for the most part a possible error of ± 1 cm^{-1}, but the double rotational transitions ($2S(0)$, etc.), which were measured only at low dispersion, have a somewhat greater error. The Raman frequencies for solid normal hydrogen (Table I) and

TABLE I

Frequencies and assignments for the fundamental band of solid n-H_2

| Transition | Observed frequencies, cm^{-1} | | Assignment |
	Infrared	Raman*	
Q	4146.5	4143.4	$Q_1(1)$
	4153.0	4151.8	$Q_1(0)$
	4223	—	Q_R
$S(0)$	4484.5	(4488)	$S_1(0)$
	4497	(4498)	$Q_1(1)+S_0(0)$
	4503.5	(4506)	$Q_1(0)+S_0(0)$
	4547	—	$S_R(0)$
$S(1)$	4703.3	(4703)	$S_1(1)$
	4732	(4730)	$Q_1(1)+S_0(1)$
	4738	(4739)	$Q_1(0)+S_0(1)$
	4770	—	$S_R(1)$
$2S(0)$	4835	(4843)	$S_1(0)+S_0(0)$
$S(0)+S(1)$	5060	(5058)	$S_1(1)+S_0(0)$
	5072	(5075)	$S_1(0)+S_0(1)$
$2S(1)$	5295	(5290)	$S_1(1)+S_0(1)$

*Measured by Bhatnagar *et al.* (1960).

TABLE II

Frequencies and assignments for the fundamental band of solid p-H_2

| Transition | Observed frequencies, cm^{-1} | | | Assignment |
| | Infrared | | Raman* | |
	100% p-H_2	98% p-H_2		
Q	—	4146.6	—	$Q_1(0)-\delta_a$
	—	—	4149.8	$Q_1(0)$
	—	4153.0	—	$Q_1(0)+\delta_a$
	—	4155.0	—	$Q_1(0)+\delta_b$
	4227	n.o.†	—	Q_R
$S(0)$		4483.4		
		4484.2		
		4485.0		
	4486.0	4485.9	4485.8	$S_1(0)$
		4486.8		
		4487.8		
		4488.2		
	4503	4503		
	4504.3			
	4506.6	4506.5	(4506)	$Q_1(0)+S_0(0)$
	4509.7	4510		
	4510.6			
	4514	4513		
	4550	n.o.	—	$S_R(0)$
$S(1)$	—	4703.8‡	(4703)	$S_1(1)$
	—	4739.7	(4739)	$Q_1(0)+S_0(1)$
$2S(0)$	4841	n.o.	(4843)	$S_1(0)+S_0(0)$

*Measured by Bhatnagar *et al.* (1960).
†No observations.
‡Observed in 75% p-H_2.

solid parahydrogen (Table II) are taken from the measurements of Bhatnagar *et al.* (1960); the frequencies which are not in parentheses are observed values and the frequencies in parentheses are calculated using the observed Q branch frequencies of the solid and the rotational constants determined by Stoicheff (1957) for the low pressure gas. It should be stressed that a difference between the infrared and Raman frequencies for a given transition does not represent experimental error, but rather a basic difference in the physical processes involved, i.e. absorption and scattering of light. The theory of the precise nature of these differences for the case of solid parahydrogen has been discussed by Van Kranendonk (1960).

THE PHONON SPECTRUM OF SOLID HYDROGEN

The identification of the sharp lines in the spectrum of the solid allows some further insight into the nature of the broad components, Q_R, $S_R(0)$, and $S_R(1)$. As pointed out above, these features of the spectrum must be assigned to combination tones of the molecular rotation–vibrational frequencies with the vibrational frequencies of the crystal lattice. Phonon spectra do not appear in Raman scattering since the translational motions of the molecules in the lattice do not lead to a change in the polarizability of the crystal.

We shall assume for the moment that the molecular frequencies involved in the combination tones which constitute the phonon spectra are the frequencies of *single* transitions. In Table III the frequency shifts, ν_R^{max}, of the maxima of

TABLE III

Frequency shifts, ν_R^{max}, of the maxima of the phonon spectra

	ν_R^{max}, cm^{-1}			
	$Q_R - Q_1(0)$	$S_R(0) - S_1(0)$	$S_R(1) - S_1(1)$	Debye ν_{max}, cm^{-1}
n-H$_2$	71	63	67	73
p-H$_2$	77	64	—	63

the Q_R, $S_R(0)$, and $S_R(1)$ components from the positions of the corresponding single infrared or Raman transitions are summarized. The shifts are all of the same order of magnitude, with an average value of ~ 68 cm^{-1}. From the known values of the Debye temperature for solid normal hydrogen (Woolley *et al.* 1948) and parahydrogen (Mendelsohn, Ruhemann, and Simon 1931), 105° K and 91° K, respectively, one can calculate the values, 73 cm^{-1} and 63 cm^{-1}, for the maximum frequency, ν_{max}, of the Debye frequency distribution. It thus appears that the maximum of the phonon spectrum can be associated with the Debye ν_{max}. The part of the phonon spectrum between its low frequency limit (at the corresponding molecular single transition) and the maximum is therefore a spectrum of the lattice frequencies of solid hydrogen.

A notable feature of the phonon spectrum is the great extension of the profile beyond the maximum towards higher frequencies; Fig. 2(c) shows that there is detectable intensity at least 400 cm^{-1} beyond the maximum. The probable explanation of this higher frequency part of the spectrum is that

multiple phonons can be created by the absorption of light. One would then expect secondary maxima to occur at frequency shifts of $2\nu_{max}$, $3\nu_{max}$, etc. These are not very evident in the spectrum of normal hydrogen, but at least the first, at $2\nu_{max}$, is readily recognizable in the Q_R component of parahydrogen (Hare et al. 1955).

The Debye frequency distribution of an actual three-dimensional crystal has, not one, but $3n$ branches, where n is the number of atoms per unit cell. The phonon spectra were therefore re-examined at high resolution in an attempt to detect structure which might have been missed in the low dispersion work; the profiles obtained for the $S_R(0)$ component in 25%, 75%, and 100% parahydrogen are shown in Fig. 8. In 100% parahydrogen three maxima
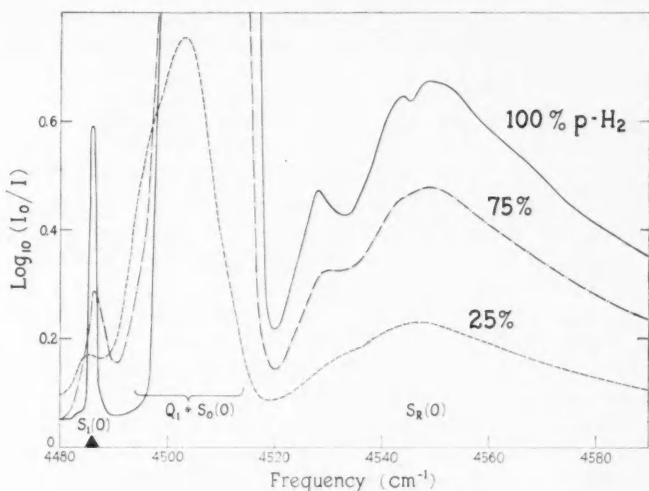
Fig. 8.   The phonon spectrum, $S_R(0)$, at high resolution for a series of para-concentrations with a path length of 3.9 mm at 12° K.

are well resolved; these have frequency shifts from $S_1(0)$ equal to 42, 58, and 64 cm^{-1}. The structure becomes less pronounced as the para-concentration is reduced and is not at all marked in normal hydrogen. A similar but less well-defined structure was also observed in the Q_R component of pure parahydrogen.

In principle the intensity of the phonon spectrum up to ν_{max} could be represented by a function of the lattice frequencies, ν_L, of the form

$$I(\nu_L) = [M(\nu_L)]^2 \times \rho(\nu_L)$$

where $M(\nu_L)$ is the matrix element of the combination transition involved and $\rho(\nu_L)$ is the distribution function of the lattice vibrations. Since the higher values of ν_L belong to the lattice modes with higher wave numbers and shorter wave lengths in the crystal, for these the relative displacement of adjacent molecules, and hence the change in dipole moment from induction effects, is

greatest. One would therefore expect $M(\nu_L)$ to be a smoothly rising function of ν_L, so that the maxima in Fig. 8 can be related with some certainty to maxima in the distribution function, $\rho(\nu_L)$.

The three phonon spectra, Q_R, $S_R(0)$, and $S_R(1)$, observed in the fundamental band are of course double transitions for which the cancellation effect is not operative. Thus, for example, $S_R(0) \equiv S_1(0) + \nu_L$ has a relatively high intensity although the single transition $S_1(0)$ is very weak. There seems to be no a priori reason why phonon spectra should not be associated also with the double quadrupole transitions. Thus, one would expect to observe in the curves of Fig. 8 a second maximum in the phonon spectrum, shifted from the first towards higher frequencies by ~ 20 cm^{-1}, the separation of the single and double $S(0)$ transitions. The weak maximum centered at ~ 4570 cm^{-1} can perhaps be identified with such transitions, the diffuseness of the phonon spectrum resulting from the width of the quadrupolar double transition band.

Although the main effort in the present work was concentrated on the quadrupolar lines of solid hydrogen, it is evident that the phonon spectra are of great interest and merit a detailed experimental and theoretical investigation.

COMPARISON OF THE SPECTRA OF THE LIQUID AND SOLID

In the first experiments on the fundamental band of liquid and solid hydrogen it was believed that the spectrum characteristic of the solid persisted in the liquid state at least 1° K above the melting point (Allin *et al.* 1955). However, when the experiments were repeated with precautions to insure only a small temperature gradient in the absorption cell, it became apparent that there was an abrupt change in the spectrum at the melting point. The components $S_R(0)$ and $S_R(1)$ are not resolved from the corresponding sharp S lines in the liquid spectrum (Fig. 2). Although the Q_R component is resolved in the liquid, the overlapping of Q_R and Q_Q is much greater in the liquid than in the solid. The single transitions, $S_1(0)$ and $S_1(1)$, are not observed in the spectrum of the liquid; this conclusion has been checked by high dispersion spectrograms. In spite of these differences the spectra of the liquid and solid show a remarkable similarity. The fact that the Q_R component has a similar shape in the two cases shows that the intervention of the translational motion of the molecules in the absorption process in the liquid must be very similar to the intervention of the lattice vibrations in the solid.

A comparison of the absorption profiles (*b*) and (*c*) in Fig. 2 shows that the total absorption intensity is nearly the same for the liquid and the solid. However, since the profile consists of sharp lines as well as broad bands an accurate value of the integrated absorption intensity cannot be obtained from low resolution recordings of the spectrum. On the other hand, the determination of the total intensity at high resolution would require measurements with several different cell thicknesses, since the absorption coefficient for the true profile varies over a great range. For this reason accurate intensity measurements are so far available only for those isolated features of the band which have been examined at high resolution. The most interesting of these is perhaps the $S(0)$ group of quadrupole transitions in solid parahydrogen, containing the

single transition $S_1(0)$, and the double transition $Q_1(0)+S_0(0)$ (Fig. 3, $C_p = 1.0$). The measured integrated absorption coefficient for this portion of the spectrum is 0.45×10^{-13} sec^{-1} cm^3, where the coefficient is defined as

$$\bar{\alpha} = \frac{C}{Nl} \int \frac{1}{\nu} \left(\log_e \frac{I_0}{I} \right) d\nu$$

in which N is the number of molecules per cm^3 and ν is given in sec^{-1}. The corresponding theoretical intensity calculated by Van Kranendonk (1960) is 0.48×10^{-13} sec^{-1} cm^3.

Perhaps the most interesting general result of the foregoing analysis of the fundamental band of hydrogen in the condensed phases is the great prominence of double transitions of various types, which include of course the phonon spectra. Thus, it is estimated from the experimental data for solid para-hydrogen that double transitions account for at least 98% of the total intensity.

REFERENCES

ALLIN, E. J., FELDMAN, T., and WELSH, H. L.   1956.   J. Chem. Phys. **24**, 1116.
ALLIN, E. J., GUSH, H. P., HARE, W. F. J., and WELSH, H. L.   1958. Nuovo cimento, Suppl. **9**, 77.
ALLIN, E. J., HARE, W. F. J., and MacDONALD, R. E.   1955.   Phys. Rev. **98**, 554.
BERMAN, R.   1951.   Proc. Roy. Soc. (London), A, **208**, 90.
BHATNAGAR, S. S., ALLIN, E. J., and WELSH, H. L.   1960.   To be published.
CHISHOLM, D. A. and WELSH, H. L.   1954.   Can. J. Phys. **32**, 291.
GRILLY, E. R.   1953.   Rev. Sci. Instr. **24**, 899.
GUSH, H. P., HARE, W. F. J., ALLIN, E. J., and WELSH, H. L.   1957.   Phys. Rev. **106**, 1101.
HARE, W. F. J., ALLIN, E. J., and WELSH, H. L.   1955.   Phys. Rev. **99**, 1887.
HARE, W. F. J. and WELSH, H. L.   1957.   Can. J. Phys. **36**, 88.
HARRICK, N. J. and RAMSEY, J. F.   1952.   Phys. Rev. **88**, 228.
HUNT, J. L.   1959.   Ph.D. Thesis, University of Toronto, Toronto, Ontario.
JAMES, H. M. and COOLIDGE, A. S.   1938.   Astrophys. J. **87**, 438.
KISS, Z. J., GUSH, H. P., and WELSH, H. L.   1959.   Can. J. Phys. **37**, 362.
McLENNAN, J. C. and McLEOD, J. H.   1929.   Trans. Roy. Soc. Can. **23** (III), 19; Nature, **123**, 160.
MENDELSOHN, K., RUHEMANN, M., and SIMON, F.   1931.   Z. physik. Chem. **15**, 121.
STOICHEFF, B.   1957.   Can. J. Phys. **35**, 730.
VAN KRANENDONK, J.   1957.   Physica **23**, 825.
———   1958.   Physica **24**, 347.
———   1959.   Physica. To be published.
———   1960.   Can. J. Phys. **38**, 240.
WOOLLEY, H. W., SCOTT, R. B., and BRICKWEDDE, F. G.   1948.   J. Research Natl. Bur. Standards, **41**, 379.

A STUDY OF METHODS FOR OBTAINING HIGH RESOLUTION WITH A PAIR SPECTROMETER[1]

G. A. BARTHOLOMEW, P. J. CAMPION, AND K. ROBINSON

ABSTRACT

Methods of improving the resolution and line shape of a flat magnetic field pair spectrometer with the aid of specially designed detector apertures are described. The performance of two such apertures is described in detail. The theoretical line shape and resolution for one type of aperture are calculated and compared with experiment.

I. INTRODUCTION

In the energy region above 1.02 Mev the process of pair production may be used for the measurement of energies and intensities of γ-rays. The pair spectrometer, first described by McDaniel, von Dardel, and Walker (1947) and Walker and McDaniel (1948), employing 180° deflection of the pair electrons in a uniform magnetic field has been used by a number of workers (Rutherglen, Rae, and Smith 1951; Terrell 1950; Balzer *et al.* 1958; Knoepfel *et al.* 1959; see also the compilation by Bartholomew and Higgs 1958) and, where sources of sufficient intensity have been available, good resolution and considerable accuracy of energy measurement have been obtained.

A full account of the performance of a pair spectrometer as an absolute instrument in the measurement of γ-ray energies and intensities has been given by Kinsey and Bartholomew (1953). In that report the dependence of the shape of the γ-ray coincidence peak, the resolution, and peak counting rate, on the various instrumental variables such as counter aperture dimensions and radiator thickness were described for an instrument using, as counter apertures, rectilinear slit jaws of the minimum thickness required to stop electrons in the energy range of interest, ≲ 8 Mev.

In the 180°, flat magnetic field pair spectrometer of conventional design, a broad radiator is mounted in an axial plane between the pole faces of an electromagnet. Pairs produced by γ-rays incident on the radiator are detected in coincidence, after 180° deflection, by two detectors placed with their apertures in the plane one on each side of the radiator.* At relativistic velocities the sum of the moduli of the momenta of the pair electrons is essentially independent of the division of the total kinetic energy between the electrons. Hence it follows that the same magnetic field which transmits to the detectors electron pairs produced near the center of the radiator with nearly equal momentum division will simultaneously transmit electron pairs of the same

*A modification of this geometry involving a curved radiator has been described by Alburger (1956). This refinement which was suggested to improve the detection of a divergent γ-ray beam emitted from a point source was not studied in the present investigation, in which well-collimated γ-ray beams were incident normally on the radiator.

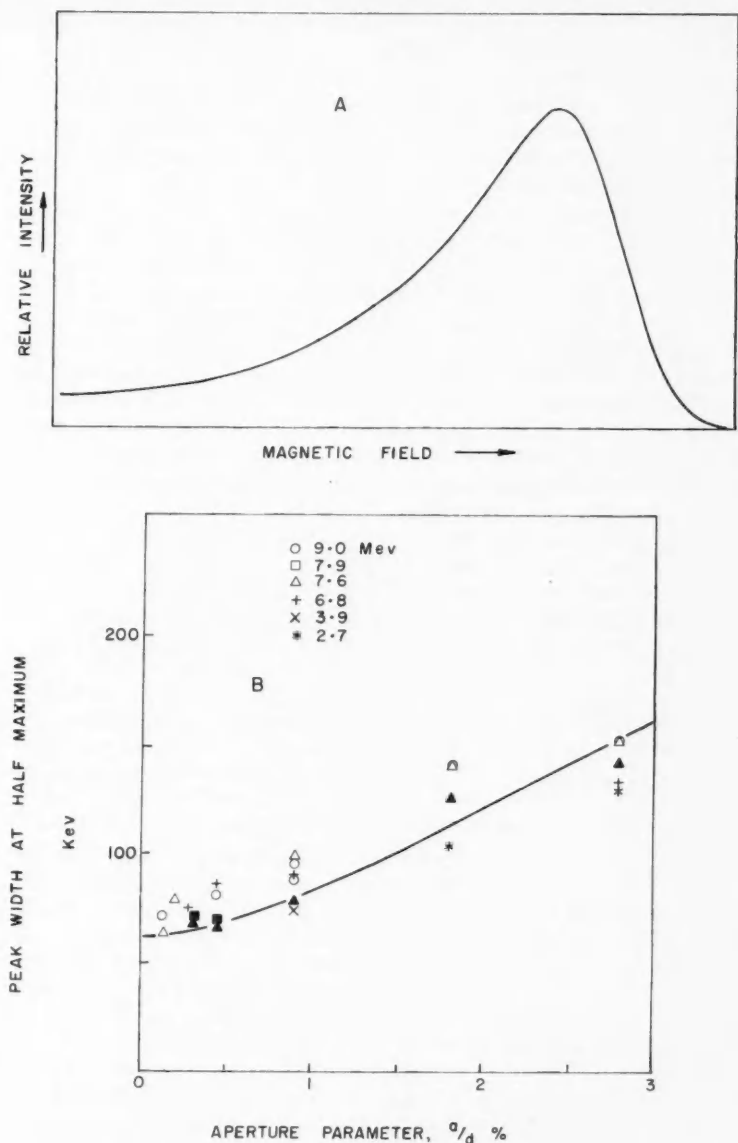FIG. 1. Characteristics of peak shape obtained with thin counter apertures. Curve A shows the shape of the coincidence peak at 9 Mev. Curve B (Kinsey and Bartholomew 1953) gives the width of the coincidence peak at half maximum as a function of the slit width *a* measured as a fraction of the distance *d* from the slit to the axis of the magnet. The points are experimental; the full line is a theoretical curve for 8 Mev.

total energy and the appropriate momentum division produced at other positions on the radiator. Since, moreover, as shown by Bethe and Heitler (1934), the distribution of the number of pair events as a function of the energy of the positron is nearly flat, at least for high γ-ray energies, it follows that (for slit jaws of minimum thickness) different parts of an extended radiator will contribute roughly equal amounts to the total counting rate, a fact which has been verified experimentally (Kinsey and Bartholomew 1953).

The shape of the coincidence peak obtained with the use of thin slits is characterized by a sharply falling slope toward high magnetic fields and a more gently falling slope merging into a long tail toward low magnetic fields. A typical peak shape, which is essentially independent of γ-ray energy, is shown in Fig. 1A. In Fig. 1B, a plot is given of peak width at half maximum as a function of aperture width for slits with thin jaws. This curve shows that the peak width approaches a limit of about 70 kev as the aperture width approaches zero, and the experimental points show that the peak width is nearly independent of γ-ray energy. It has been shown (Kinsey and Bartholomew 1953) that the peak shape may be calculated by assuming in the first approximation that the slits are infinitely long and of zero jaw thickness and later correcting the results for finite length and thickness.

In the present report we describe two refinements of design of the counter apertures which lead to improvements in line shape and resolution (full width of a line at half-maximum intensity divided by the energy). One aperture design has the virtue that calculations of peak shape can be readily made for the case where the radiator is restricted to a point at the center of symmetry. It would appear to provide the optimum counting efficiency that can be achieved under these geometrical conditions. In practice this slit is useful only where very high resolutions are required; for poorer resolution superior counting efficiencies are obtained with apertures which can be used with extended radiators. The second aperture described in this report is of the latter type.

II. SLIT DESIGN

It is convenient to begin with the consideration of a point radiator and to modify conclusions at a later stage, where necessary, by introducing the extension of the radiator. For simplicity we consider the point radiator placed half way between the counters. As a further simplification, for theoretical consideration of slit design we ignore scattering and energy loss in the radiator.

It may be easily demonstrated that the use of slits with thin jaws must lead to a tail of essentially unlimited length extending toward low magnetic fields. For simplicity, we consider only those orbits lying in the median plane of the magnet, Fig. 2. Let O be the point radiator and S_+ the positron slit of aperture width, a, at distance, d, from O. It is clear that the centers of curvature of all orbits passing through S_+ must lie within the band of width $a/2$ at distance $d/2$ from O. This band we shall call the domain of centers of curvature or dcc. Orbits of positrons of momentum p_+ entering S_+ at a magnetic field H must have centers of curvature lying on the arcs A and A' (of the circle with radius $R_+ = p_+e(Hc)^{-1}$ centered at O, where p_+ is the momentum of the positron,
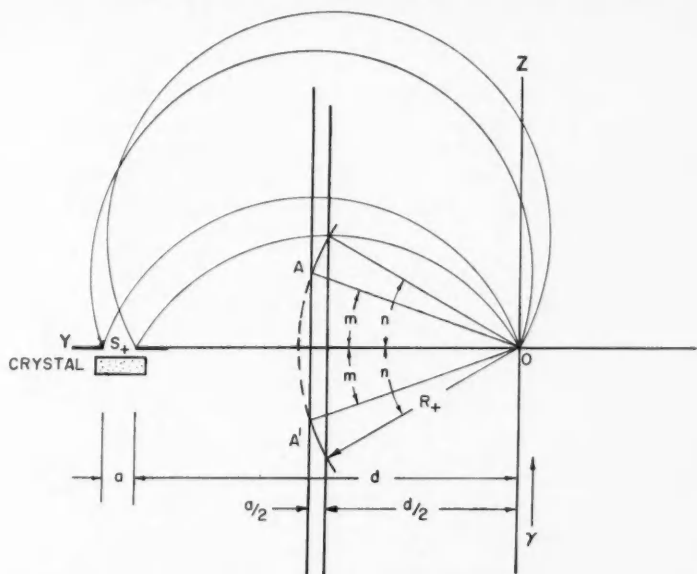
FIG. 2.   Geometry for thin slits and orbits of radius R_+ lying in the plane perpendicular to the magnetic field. The γ-ray is directed along the Z axis. The band at $y = d/2$ is the domain of centers of curvature of all orbits which can reach the detector from the radiator at O.

e is the electronic charge, c is the velocity of light, and H is the magnetic field) which lie inside the dcc. The angle of emission, θ_+, of the positrons with respect to the γ-ray direction falls in the range $m < \theta_+ < n$ defined by these arcs as shown in Fig. 2 where $\cos m = (d+a)/2R_+$ and $\cos n = d/2R_+$. In order for coincidences to occur, similar restrictions must apply simultaneously to θ_- and R_- for the paired electron. The maximum field at which coincidences can occur, H_0, is that for which $R_+ = R_- = d/2$.

Now, the coincidence counting rate in counts per quantum at a field H from a γ-ray of energy α striking a radiator containing C atoms per square centimeter is*

$$(1) \qquad I(\alpha, H) = C \iiint \sigma \left(\cos \theta_+, \cos \theta_-, p_+, \alpha\right) d \cos \theta_+ \, d \cos \theta_- \, dp_+$$

where σ represents the differential pair cross section and where the integrals extend over all values of $\cos \theta_+$, $\cos \theta_-$, and p_+ consistent with both R_+ and R_- simultaneously intersecting the dcc for positrons and electrons respectively. We see, therefore, that since the dcc extends indefinitely in the $\pm Z$ directions, coincidences may in principle occur at all values of H below the maximum field, H_0. The relative magnitude of the counting rate at larger values of R_+ and R_-, i.e., low H, is determined by the value of σ at large θ_+ and θ_-. In

*We continue to restrict ourselves to two dimensions.

practice, for thin slits it is largely the decrease of σ as θ_+ and θ_- increase which is responsible for the decrease in counting rate for values of H below the value corresponding to the maximum rate. The differential cross section σ is of such a shape that only modest improvements in resolution are obtained as the width a is reduced as shown in Fig. 1B. However, the finite thickness of the jaws of the slit limits the dcc for large R and this tends to reduce the relative size of the low-field tail. The dcc diagram corrected for slit jaw thickness, t, is shown in Fig. 3, in which the ratios a/d and t/d have been exaggerated
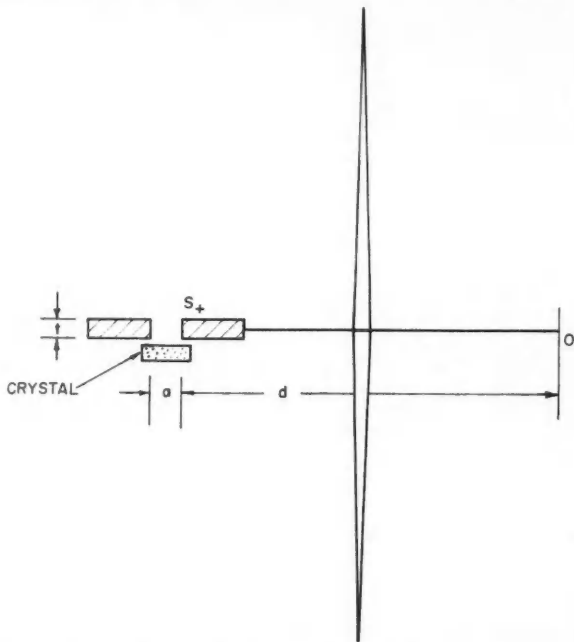
FIG. 3. Type-1 slits showing the effect of the finite slit thickness on the domain of centers of curvature. The needle-shaped area includes the centers of curvature of all orbits which can reach the detector from O.

for illustrative purposes. This reduction of the low-field tail is greatest at low γ-ray energies where the mean angle, $\theta_\pm$ is relatively large (Kinsey and Bartholomew 1953). The combined effects of the pair angular distribution at high energies and the finite slit thickness at low energies fortuitously produce the observed energy-independent line width (Fig. 1B). Slits of zero thickness would give much poorer resolution at low energies. We shall refer to the slits of Fig. 3 as type-1 slits.

The dcc diagram which is useful in determining the limits of integration for calculation of peak shape provides a simple graphical method of assessing the relative merits of different types of slit. For example, one type of slit (hereafter referred to as type-2) which has proved very useful experimentally is shown in

Fig. 4. This slit has jaws some five times thicker than the maximum useable aperture width and the inner surfaces of the jaws are curved with a radius equal to d. The slits are mounted with their exit apertures in the plane of the radiator. It is apparent from the limited range of the dcc that this type of slit
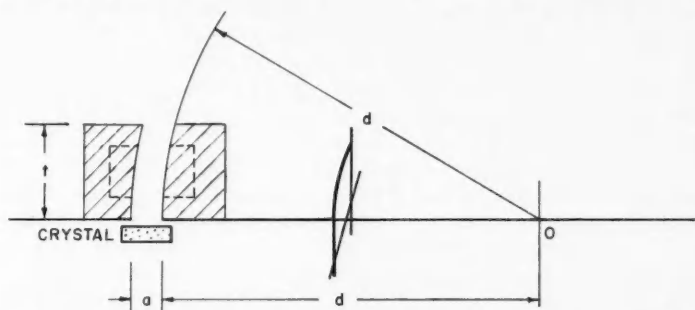
FIG. 4.   Type-2 slits showing the domain of centers of curvature. Both jaws are thick and are placed with one edge in the plane of the radiator. The aperture is curved with radius d. The ratios t/d and a/d are exaggerated for illustrative purposes. The broken lines indicate the positions of milled channels to reduce electron scattering.

will produce a peak with only a small tail toward low magnetic fields. This slit has the disadvantage that, due to lack of symmetry in the shape of the dcc, line shape calculations, even for a point radiator, are very complicated.

It is not difficult to see with the aid of the dcc diagram that, in the two dimensional case and for a point radiator, the slit design which gives the greatest transmission consistent with a high resolution and the smallest possible low-field tail is that shown in Fig. 5. The inner jaw of the slit is thin
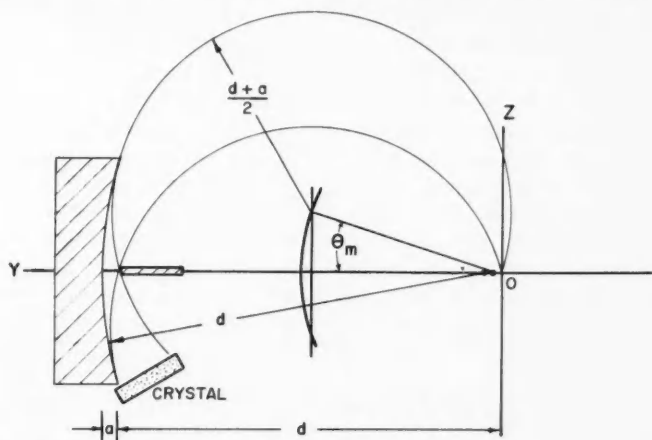
FIG. 5.   Slit giving optimum peak shape showing the domain of centers of curvature. The inner jaw is of minimum thickness. The outer jaw is curved with radius d. The ratio a/d is exaggerated for illustrative purposes.

and therefore, for all allowed values of R_+, the range of integration over $\cos \theta_+$ is as large as possible. The outer jaw has a radius of curvature d and thickness $(8a_m d)^{1/2}$ where a_m is the maximum required value of the slit width, a. For all values of $a \leqslant a_m$ this jaw ensures that there will be a maximum contribution from orbits with $R_+ = (d+a)/2$ but no contribution from orbits with larger radii. The limiting emission angle θ_m is given approximately by $\cos \theta_m = 1-\delta$ where $\delta = a/d$. Considering both electrons, no coincidences will occur for fields below the field H_{min} corresponding to $R_+ + R_- = d+a$. Pairs detected at this field like those detected at H_0 must have equal momentum, p_0, for both electrons. Specifically this field is $H_{min} \simeq H_0 (1-\delta)$.

Because of the high degree of symmetry possessed by these slits the derivation of an expression for the line profile is relatively straightforward. Following a procedure similar to that outlined by Kinsey and Bartholomew (1953) for the calculation of the line profile for thin slits, we may rewrite (1) including the limits of integration applicable to the two-dimensional slits of Fig. 5.

$$(2) \quad I(\alpha,\omega,\delta) = 2C \int_0^\zeta \int_{1-\omega+z}^1 \int_{1-\omega-z}^1 \sigma(\cos \theta_+, \cos \theta_-, \alpha)\, d\cos \theta_+\, d\cos \theta_-\, dz$$

where

$$\omega = \frac{H_0 - H}{H_0}$$

is the magnetic field parameter,

$$z = \left| \frac{p_0 - p_+}{p_0} \right|$$

is the displacement of momentum from equal momentum division, and

$$\zeta = \omega \qquad \text{for } 0 < \omega < \delta/2,$$
$$= \delta - \omega \qquad \text{for } \delta/2 < \omega < \delta,$$
$$= 0 \qquad \text{for } \delta < \omega.$$

Turning next to consider directions of electron emission out of the YZ plane (Fig. 6), we derive the shape of the aperture in the XY plane which preserves the angular limits imposed by the geometry of Fig. 4 regardless of the azimuthal angles $\phi_\pm$. The required geometry is clearly that which transmits all orbits which leave the radiator within a cone of apex angle 2θ as shown in Fig. 6. We wish, therefore, to find the boundaries of the region containing the intersections with the XY plane of orbits which are emitted from O within the cone defined by $\cos \theta_m = 1-\delta$. The co-ordinates of the intersection of a positron orbit with the XY plane are

$$(3) \qquad x_+ = \frac{2p_+ c}{eH} \sin \theta_+ \cos\phi_+ \cot^{-1}(\tan \theta_+ \sin\phi_+),$$

$$(4) \qquad y_+ = \frac{2p_+ c}{eH} \cos \theta_+.$$
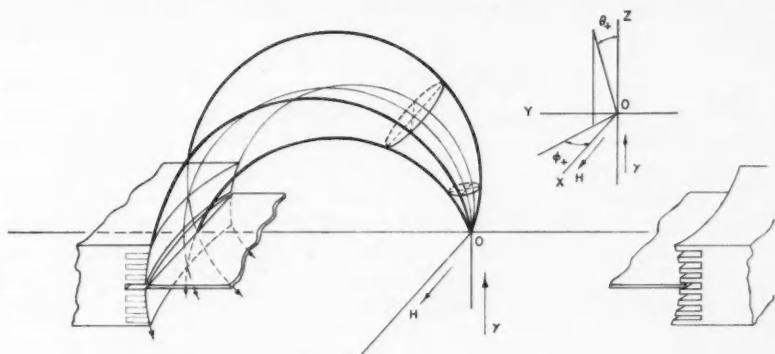
FIG. 6.   Type-3 slits showing limiting orbits transmitted for $\cos \theta_m = 1 - \delta$. The inner slit jaw has minimum thickness and a rectilinear edge at a distance d from O. The radius of curvature of the outer jaw in the YZ plane is d while that in the XY plane is $\pi^2 d/4$. The thickness of the outer jaw is $(8a_m d)^{1/2}$.

In order to determine the shape of the inner slit jaw we consider the trajectories with $\cos \theta = 1 - \delta$ which are transmitted at H_{min}. As mentioned above, such pairs have $p_+ = p_- = p_0$. From eq. 4 the locus of the intersections with the XY plane of all positron trajectories satisfying these conditions is given by

$$(5) \qquad\qquad y_+ = \frac{2p_0 c}{eH_0} .$$

This value of y_+ is identical with that for the orbit which is transmitted at the highest field for which coincidences can occur, namely $y_+ = d$. Thus the inner slit jaw must be a straight edge perpendicular to OY at a distance d from O.

In order to determine the shape of the outer jaw in the XY plane we consider the trajectories with $\phi_+ = 0$ transmitted at $H = H_{min}$. The locus of the intersections of these trajectories is given in the approximation $a \ll d$ by the expressions

$$(6) \qquad\qquad x_+ = \frac{\pi}{2} d(1+\delta) \sin \theta_+,$$

$$(7) \qquad\qquad y_+ = d(1+\delta) \cos \theta_+.$$

These equations define an ellipse which, in the same approximation, may be replaced by a circle of radius

$$(8) \qquad\qquad R = \frac{\pi^2 d}{4}$$

centered on the Y axis. The required aperture in the XY plane is then a segment of this circle of length $\pi(2ad)^{1/2}$.

We are therefore led to a doubly curved outer slit jaw with radii of curvature $\pi^2 d/4$ in the XY plane and d in the YZ plane. It may be shown that to a good

approximation, the same curvatures are required in neighboring planes parallel to the XY and YZ planes respectively. Such an outer jaw, which has a cross section in the YZ plane identical with that in Fig. 5, coincides closely with the envelope of all orbits leaving O within the cone of apex half-angle $\cos^{-1}(1-\delta)$. The acceptance solid angle defined by this cone is $\sim 2\pi\delta$ steradians. The positron beam transmitted by this aperture is illustrated by five limiting orbits in Fig. 6. We shall refer to this aperture as type-3 slits.

In the absence of perturbing effects such as electron scattering, the line profile obtained in practice with type-3 slits is given by (2) with the function σ representing the differential cross section for pair production for $p_+ = p_-$, integrated over ϕ_+ and ϕ_-. The differential cross section given by Bethe and Heitler (1934) with $p_\pm = p_0$ may be integrated over $\phi_\pm$ analytically to give*

$$(9) \qquad \sigma(x,y,\alpha) = -\frac{Z^2 r_0^2}{8\alpha^2 S^2 137} P(x,y,\alpha),$$

where

$$P(x,y,\alpha) = \frac{4}{(S-x)(S-y)} - \frac{1}{(A^2-B^2)^{1/2}}\left[\frac{1-x^2}{(S-x)^2} + \frac{1-y^2}{(S-y)^2} + \frac{4(S^2+A)}{(S-x)(S-y)}\right]$$
$$+ \frac{S^2 A}{(A^2-B^2)^{3/2}}\left[\frac{1-x^2}{(S-x)^2} + \frac{1-y^2}{(S-y)^2} - \frac{2(2-x^2-y^2-2A)}{(S-x)(S-y)}\right],$$

$$A = S^2 + \tfrac{1}{2} + \frac{xy}{2} - S(x+y),$$

$$B = \tfrac{1}{2}[(1-x^2)(1-y^2)]^{\frac{1}{2}},$$

$$S = \left[1 - \left(\frac{2}{\alpha}\right)^2\right]^{-\frac{1}{2}},$$

and where $x = \cos\theta_+$, $y = \cos\theta_-$, $\alpha = h\nu/m_0 c^2$,   and $r_0 = e^2/m_0 c^2$.

The line profiles, $I(\alpha,\omega,\delta)/C$, for γ-ray energies of 3 and 12 Mev calculated using (2) with $Z = 79$, $\delta = 0.02$, and σ given by (9) are shown in Fig. 7. It is to be noted that, unlike the profile for type-1 slits, the low field side of the peak has a slope comparable to or even greater than that of the high field side. The low field side intersects the ω-axis as expected at $H_{\min} = H_0 (1-\delta)$. The resolution is approximately one half the base width, i.e. $\delta/2$. In spite of the large change in the angular distribution function (9) between 3 and 12 Mev, the two curves are remarkably similar, indicating that with type-3 apertures the line profile is determined largely by the slit geometry and only weakly by the differential pair cross section. That this is indeed the case is clearly demon-

---

*It may be shown that negligible error is introduced by assuming that the differential cross section applicable at equal momentum division also holds for the small departures from equal division represented by the limits ζ in (2). However, due to failure of the Born approximation, for the practical case of a gold radiator and low electron energies this formula can give only an approximate representation of the true distribution.

At equal momentum division the energy differential, dE_0, appearing in the original Bethe–Heitler expression is related to dz by $dE_0 = \alpha/(2S^2)dz$. The factor $\alpha/(2S^2)$ is included in eq. 9.
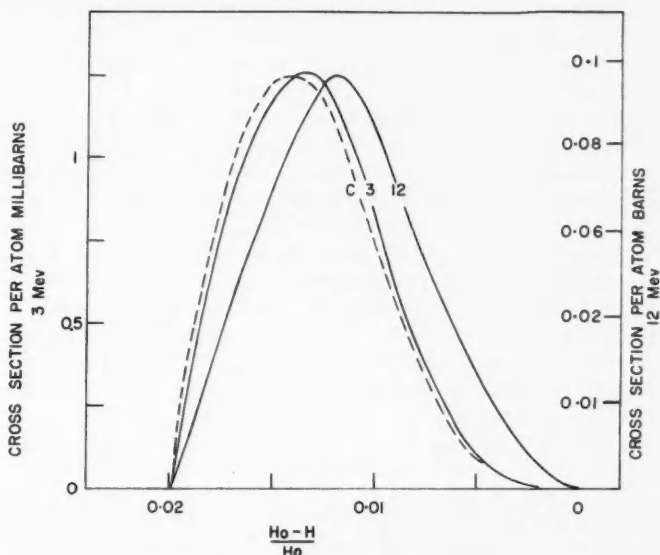
FIG. 7. The theoretical peak shapes for a flat angular distribution (broken curve) and for the Bethe–Heitler (1934) angular distribution at 3 and 12 Mev (full curves) for type-3 slits with $\delta = 0.02$. Separate ordinates are given for the 3- and 12-Mev curves. The curve for the flat distribution is normalized to the same peak height as for the full curves.

strated by calculating the peak shape for $\sigma(x,y,\alpha) = $ constant. The result of such a calculation is shown by the broken curve C in Fig. 7. As a consequence of this insensitivity to the angular distribution the resolution is given approximately by $\delta/2$ at all energies, a deduction which has been verified by calculations at several energies between 2 and 20 Mev. It also follows that the line shape is relatively insensitive to processes which tend to distort the distribution such as poor γ-ray collimation and inhomogeneities in the magnetic field. The net result of such effects is to reduce the transmission but leave the resolution unaltered. However, energy loss by scattering of the electrons in the radiator can cause a broadening of the peak. Scattering of electrons by the walls of the vacuum chamber and by the slit jaws and transmission of electrons through the jaws can of course also contribute to broadening.

Figure 7 also gives the theoretical absolute cross sections, per atom of a gold radiator, for the peaks at 3 and 12 Mev. The theoretical absolute peak counting efficiency with a 5 mg per cm^2 gold point-radiator at 7.38 Mev for type-3 slits at 1.6% resolution is 1.2×10^{-6} counts per photon which is to be compared with 2.4×10^{-7} counts per photon calculated by Kinsey and Bartholomew (1953) for type-1 slits and the same energy and resolution. The theoretical variation of the peak efficiency with energy for type-3 slits is similar to that calculated by Kinsey and Bartholomew for type-1 slits, the greatest departure being at 5 Mev where the ratio of the efficiency to that at 2.75 Mev is some 15% greater for type-3 slits than for type-1 slits.

The preceding slit design is based on the assumption of a point radiator situated in the median plane half way between the slits. It is to be expected that contributions from other parts of an extended radiator will tend to broaden the coincidence peak. Some broadening is caused by the fact that, for pairs with unequal momentum division, the sum of the moduli of the momenta is not quite equal to that for pairs with equal momentum division. This effect and its bearing on the determination of the practical dimensions of the radiator are discussed in detail by Kinsey and Bartholomew (1953). Further broadening of the theoretical line shape will occur for type-3 slits because the slit jaws, which are designed specifically for a central point radiator, provide imperfect baffling for electron orbits originating elsewhere on the radiator. It is also to be expected that the peak counting efficiency will decrease as the point of origin of the pair is moved away from the center of the radiator. The magnitude of the latter effect is difficult to estimate theoretically and no attempt will be made to give such an estimate here. Some experiments which show the effect of the radiator size on the line shape are described below.

III. EXPERIMENTAL ARRANGEMENTS

The existing pair spectrometer (Kinsey and Bartholomew 1953) was used to test various properties of the three types of slit discussed above. The geometrical arrangement used for the comparison of type-1 and type-2 slits is shown in Fig. 8A. This configuration, with the exit apertures of the slits and the radiator placed on a diameter of the magnet pole face and the distance between the inner jaws of the slits equal to 22.675 cm, is the standard operating arrangement of the instrument. The type-1 slits were made of 0.15 cm thick gold, the type-2 slits of 1.3 cm thick Mallory 1000 Metal (a tungsten, nickel, copper alloy). Both were 3.2 cm long. Channels were milled in the type-2 slit
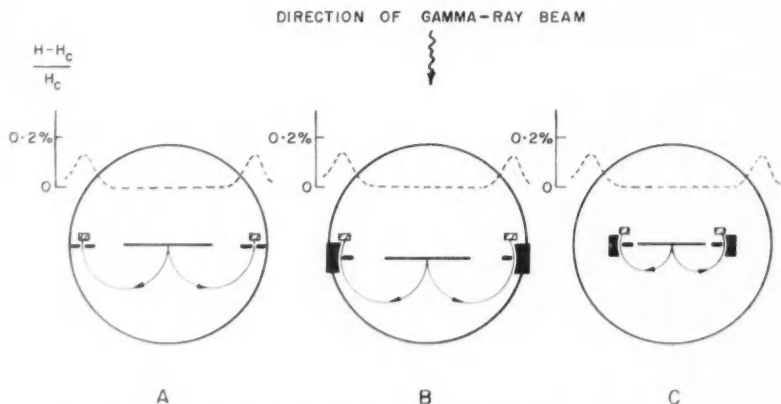
FIG. 8. Arrangements for testing slit geometries. The full circles represent the poles of the magnet. The relative magnetic field strength as a function of radius in the median plane is shown by the broken curves.

jaws, as illustrated by the broken lines in Fig. 4, in order to reduce the scattering of electrons. The radiator was a sheet of gold ~ 5 mg/cm² thick supported by an aluminum foil 2 mg/cm² thick. Since the positions of the stilbene crystals were rigidly fixed it was not convenient to use an identical geometry to test the type-3 slits. For this purpose, two different geometrical configurations, Figs. 8B and 8C, were employed. In the B arrangement, which makes use of the same stilbene detectors, the radiator was displaced away from the pole diameter by 2.4 cm and the separation of the inner jaws of the slits was increased to 23.767 cm. The slit jaws were made of Mallory Metal, the inner jaw being 0.2 cm thick and the outer 3.1 cm thick. A channel milled in the outer jaw allowed the aperture size to be varied by sliding the outer jaw over the fixed inner jaw, as shown in Fig. 6. Other channels were milled in the outer jaw to reduce electron scattering. With the geometry of Fig. 8B, however, the region of the magnetic field traversed by the electrons was somewhat different from that for arrangement A. (The relative magnetic field strength as a function of radius is shown as a broken curve superimposed on each diagram in Fig. 8.) Therefore, in order to obtain a fair comparison of the performance of type-3 slits under identical magnetic field conditions the third arrangement, Fig. 8C, was also employed. In this arrangement the separation of the inner jaws of the slits was reduced to 15.240 cm. Only type-1 and type-3 slits were compared in this geometry. Both types were made of Mallory Metal; the thin jaws were 0.2 cm thick and the thick jaws were 2.0 cm thick. For mechanical reasons, which prevented the use of light pipes in this arrangement, it was not possible to use scintillation detectors. These were replaced by small, thin-walled, flow-type proportional counters using argon and 10% methane at atmospheric pressure. For the arrangements A and B the maximum area of the incident γ-ray beam was 8 cm by 5 cm with the long direction perpendicular to the magnetic field; for arrangement C the corresponding dimensions were 8.0 cm and 3.8 cm. For certain measurements the effective radiator area was reduced by either stopping down the collimator or by reducing the size of the radiator itself.

IV. MEASUREMENTS

The test experiments were carried out with two objects in view. The first was to attempt to verify the concepts of slit design discussed in Section II. The measurement principally involved the comparison of the peak shape and resolution for type-3 slits with those predicted theoretically. In the very high resolution region it was difficult to make realistic comparisons owing to the presence of effects, other than slit geometry, which tend to limit the resolution and transmission in this region. Since the temporary arrangements used to test type-3 slits could not be adopted for normal operation of the spectrometer without major modifications, no attempt was made to determine experimentally the variation of either counting efficiency or toe correction* with energy. On the other hand, type-2 slits could be used for practical operation (see, for

---

*See Kinsey and Bartholomew (1953) for a discussion of the toe correction which enters in absolute determinations of γ-ray energies.

example, Knowles, Manning, Bartholomew, and Campion 1959). Unfortunately, as mentioned above, the theoretical line shape for type-2 slits is difficult to calculate and, in fact, no attempt has been made to compute it. Therefore, the second object of the test experiments was to determine empirically for type-2 slits the line shape, the variation of counting efficiency as a function of energy and resolution, the variation of resolution as a function of energy for a constant aperture width, and the magnitude and energy dependence of the toe correction.

A. Type-3 Slits

1. Line Shape

The coincidence peak obtained at 9 Mev with type-3 slits, in the arrangement B of Fig. 8, is shown by the experimental points and the dashed curve in Fig. 9. For this measurement the aperture parameter δ was 0.016 and the γ-ray beam dimensions were 5.7 cm by 5 cm. The peak shape obtained with type-1 slits and slightly poorer resolution (1.0%) is shown for comparison, curve B. The type-3 slits clearly produce a peak with a more symmetrical shape and a much-reduced low-field tail compared with that obtained with type-1 slits. The comparison also shows that the high-field sides of both peaks have similar shapes. This result is to be expected since the inner slit jaw, which defines the electron beam transmitted at fields near H_0, is the same for both types of slit. The line shapes at 6.76 and 7.64 Mev were also examined and found to be similar to that in Fig. 9 at the same resolution.

The theoretical line shape for $\delta = 0.016$ at 9 Mev calculated using (2) and (9) is shown as curve A, Fig. 9. Whereas the high-field side of the experimental peak agrees with the theoretical curve, both the maximum and the low-field sides are shifted to lower magnetic fields presumably because of the various effects discussed in Section 2 below. An example of the peak shape near the limit of resolution attainable with this type of slit and source strengths available from neutron capture γ-rays is shown by the broken curve, Fig. 10. The peak was produced by the intense 6.76-Mev γ-ray emitted in the $Ti^{48}(n,\gamma)Ti^{49}$ reaction and was obtained with $\delta = 0.0025$ and a γ-ray beam of dimensions 5 cm by 1 cm in geometry B, Fig. 8. The resolution obtained was 0.37% which is to be compared with the theoretical value of 0.12% calculated for this aperture and a point radiator. It is to be noted that even at this high resolution the high-field slope of the peak agrees well with that expected theoretically, shown in Fig. 10 as a full curve.

2. Resolution

The experimental peak in Fig. 9 has a half width of 0.95% which is about 0.15% greater than the corresponding theoretical curve, while in Fig. 10 the experimental peak is some three times wider than the theoretical curve. This loss of resolution and the appearance of a low-field tail are caused by pairs produced at points other than the center of the radiator, by scattering of electrons in the radiator and from the slit jaws, by energy loss in the radiator, and by the inhomogeneity of the magnetic field. Measurements with radiators of different areas suggest that the most important of these effects is probably the first. The mean energy-loss in the radiator is about 0.1%. The contributions
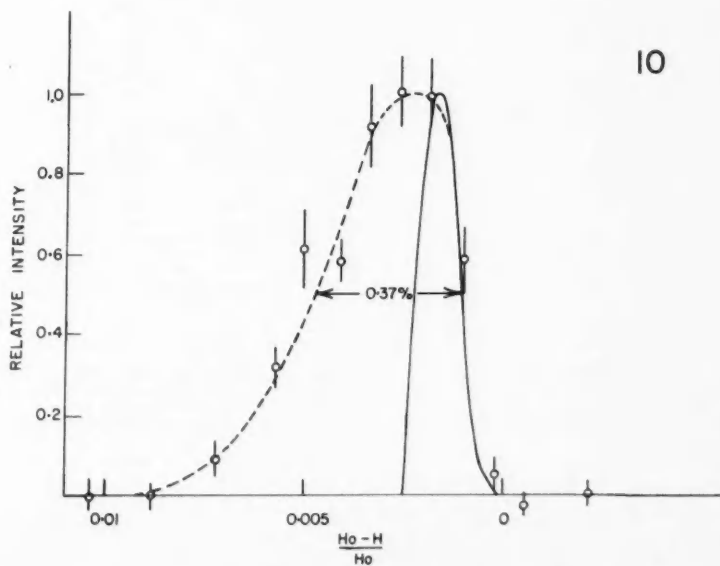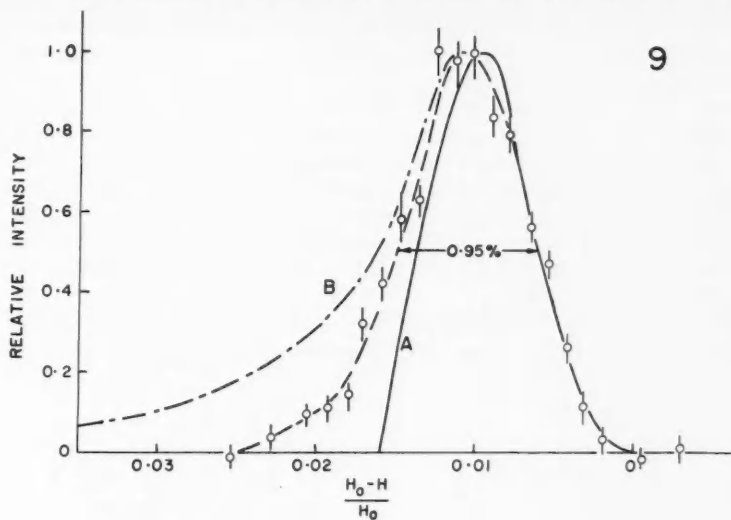
FIG. 9. The points are experimental results at 9.0 Mev for type-3 slits and radiator dimensions 5.7 cm by 5 cm with $\delta = 0.016$. The experimental peak shape for type-1 slits at similar resolution is shown by curve B. The theoretical peak shape for $\delta = 0.016$ and a point radiator is shown by curve A.

FIG. 10. The points are experimental results at 6.76 Mev for type-3 slits with $\delta = 0.0025$ and radiator dimensions 5 cm by 1 cm. The peak counting rate in this experiment was 14 counts per hour. The full curve shows the theoretical peak shape for $\delta = 0.0025$ and a point radiator.

from the other effects are more difficult to estimate but some reasons exist for assuming they are small. For example, it is to be noted that, in order for an electron of a given momentum to reach the detector, it must approach a type-3 slit within a small acceptance angle. Therefore, electrons which undergo changes of direction by traversing non-uniform regions of the field tend to be eliminated and do not in general contribute to the broadening of the peak to the degree allowed by type-1 slits. An indication that the broadening caused by inhomogeneities in the field is relatively unimportant is provided by the observation that the line shape for a given δ obtained with the improved magnetic field conditions of Fig. 8C showed no improvement over those obtained with arrangement B.

The variation of the resolution, W, as a function of δ is shown in Fig. 11. The full curve shows the theoretical resolution ($W = \delta/2$) while the broken

| γ-RAY ENERGY | RADIATOR SIZE | |
Mev	5·7 x 5 cm	5 x 1 cm
9 · 0	△	▲
7 · 63	○	●
6 · 75	□	■
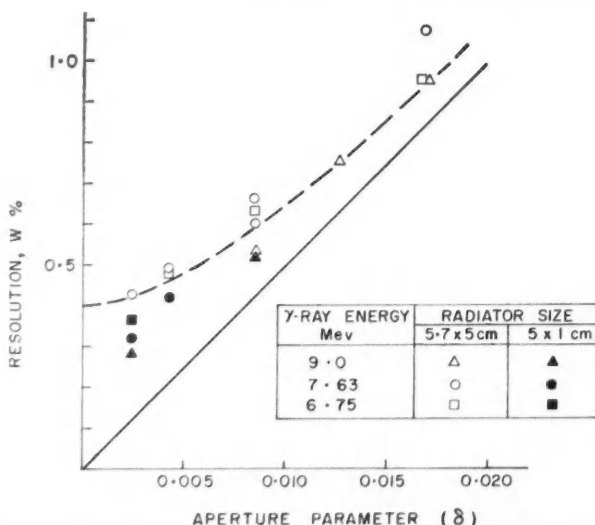
FIG. 11. Variation of the resolution W as a function of the aperture parameter for type-3 slits. The points show experimental results for energy and effective radiator size indicated in the table. The full curve gives the theoretical variation $W = \delta/2$, while the broken curve which corresponds more closely to the experimental points is given by $W^2 = (\delta/2)^2 + (0.004)^2$.

curve is that obtained when a constant 0.4% is added in quadrature to the theoretical resolution. The open and full points represent measurements with effective radiator dimensions 5.7 cm $\times$ 5 cm and 5 cm $\times$ 1 cm* respectively, where the first dimension in each case represents the length in the Y direction

*This radiator was chosen as a compromise between the necessity for maintaining a reasonable counting rate and the requirement that the radiator be substantially smaller than the standard 5.7 cm $\times$ 5 cm. It can be shown that contributions from parts of the radiator away from the median plane have a more serious effect on the peak shape than those in the median plane, hence the elongated shape.

(Fig. 6). Since the latter is by no means a point radiator we may infer that most of the remaining width is also probably caused by the radiator area.

The variation of the peak counting rate as a function of the resolution for type-3 slits at 6.76 Mev is shown in Fig. 12. The full curve which shows the theoretical dependence has been normalized to give the same peak counting rate at 1% resolution. The full points were obtained with arrangement B, the open points with arrangement C, Fig. 8. The discrepancy between the experimental results and the theoretical curve is, of course, caused by the same effects which caused the departure of the resolution from the theoretical value
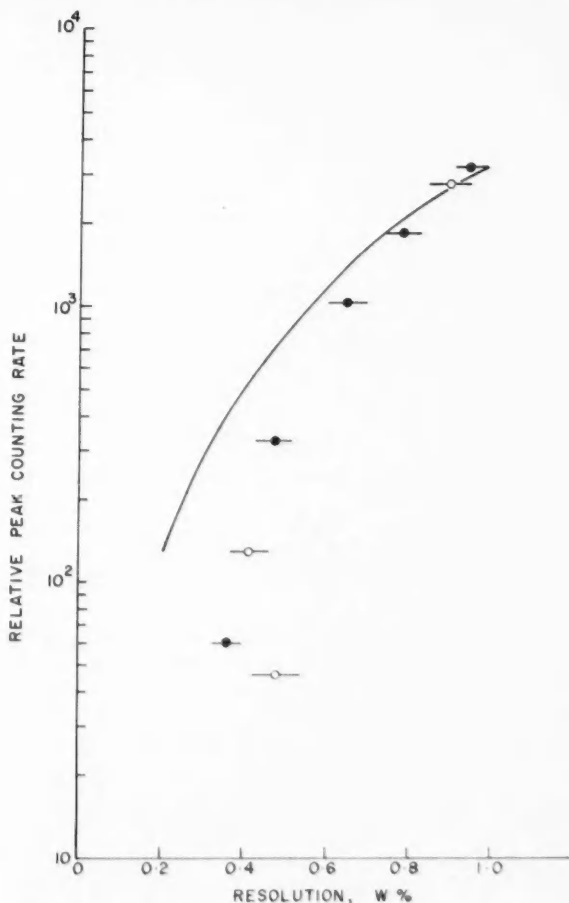
FIG. 12. Variation of the peak counting rate as a function of the resolution for type-3 slits at 6.76 Mev. The full points were obtained with experimental arrangement B and the open points with arrangement C of Fig. 8. The full curve shows the theoretical variation.

in Fig. 11. The discrepancy is enhanced in Fig. 12 because those effects which spoil the resolution also decrease the peak counting efficiency and because, as mentioned earlier, there are additional effects such as imperfect γ-ray collimation and magnetic field inhomogeneities which may reduce the peak intensity without seriously affecting the resolution.

B. *Type-2 Slits*

1. *Line Shape*

The line shape obtained with type-2 slits adjusted to give 1% resolution ($\delta = 0.013$) at 6.41 Mev is shown in Fig. 13. These slits produce a more
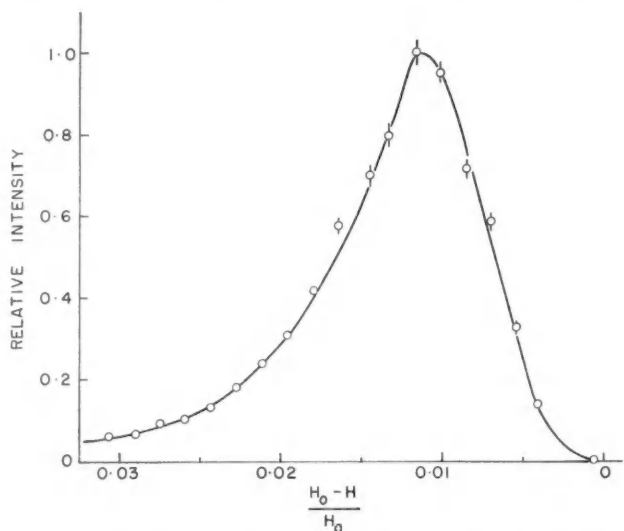
FIG. 13.   Experimental peak shape obtained with type-2 slits at 6.41 Mev and 1% resolution.

symmetrical line shape than that obtained with type-1 slits and, as with type-3 slits, the low-field tail is much reduced. Similar line shapes are observed at other energies.

2. *Resolution*

A demonstration of the superiority of type-2 slits relative to type-1 is given in Fig. 14 in which are plotted the full width of a peak at half maximum, W, and the area, A, of a peak of unit height as a function of γ-ray energy. The results are given for $\delta = 0.009$ for type-1 slits and 0.013 for type-2 slits. Under these conditions both slits give 1% resolution near 10 Mev. As the γ-ray energy decreases, type-1 slits provide nearly constant line width, 100 kev, while type-2 slits maintain a resolution which is very roughly a constant 1% of the energy. Furthermore, in the case of type-2 slits, within the limits of error, the area of a peak of unit height is identical with the width at half
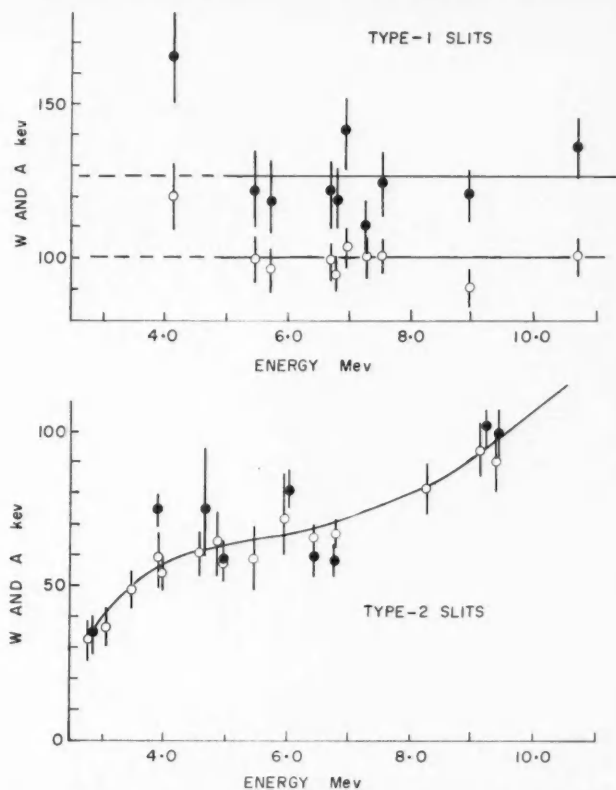
Fig. 14.   The resolution, W (open points), and the area of a peak of unit height, A (full points), as a function of γ-ray energy for type-1 slits with $\delta = 0.009$ and for type-2 slits with $\delta = 0.013$.

maximum at all energies as expected for a near-triangular-shaped peak. On the other hand, for type-1 slits, because of the additional area in the tail, the value of A is some 25% greater than W. Thus, the superiority of type-2 slits in resolving complex γ-ray spectra is derived not only from the improvement in the width at half height but also from the improved peak shape. An example of the improvement obtained at 3.918 Mev is shown in Fig. 15 where a reduction in W of almost a factor of three is achieved with only a 50% loss in peak counting rate.

3. Energy Dependence of the Counting Efficiency

The energy dependence of the peak counting efficiency for type-2 slits has not yet been investigated by the same methods that were used by Kinsey and Bartholomew (1953) for type-1 slits, i.e. by the measurement of the counting rates of γ-rays whose absolute intensities are deduced by other means. Instead,
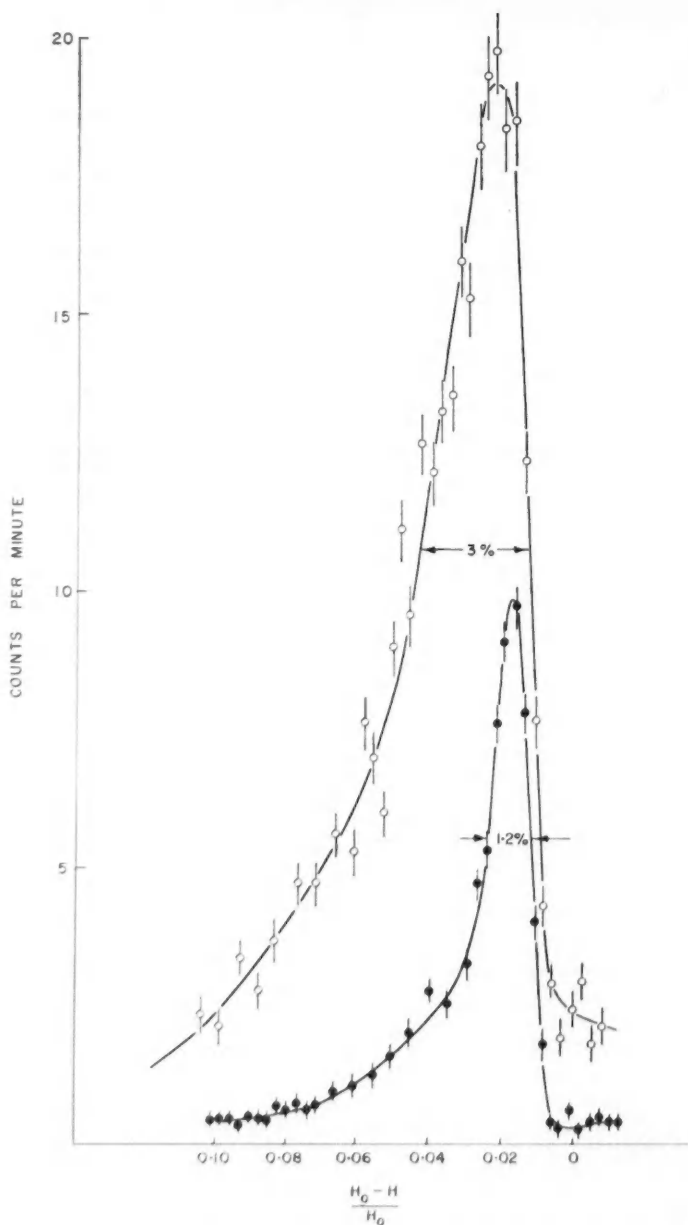
Fig. 15.   The 3.918-Mev γ-ray from the Mg²⁴(n,γ)Mg²⁵ reaction. The curve with 3% resolution was obtained with type-1 slits with δ = 0.009 while that with 1.2% resolution was obtained with type-2 slits with δ = 0.013.
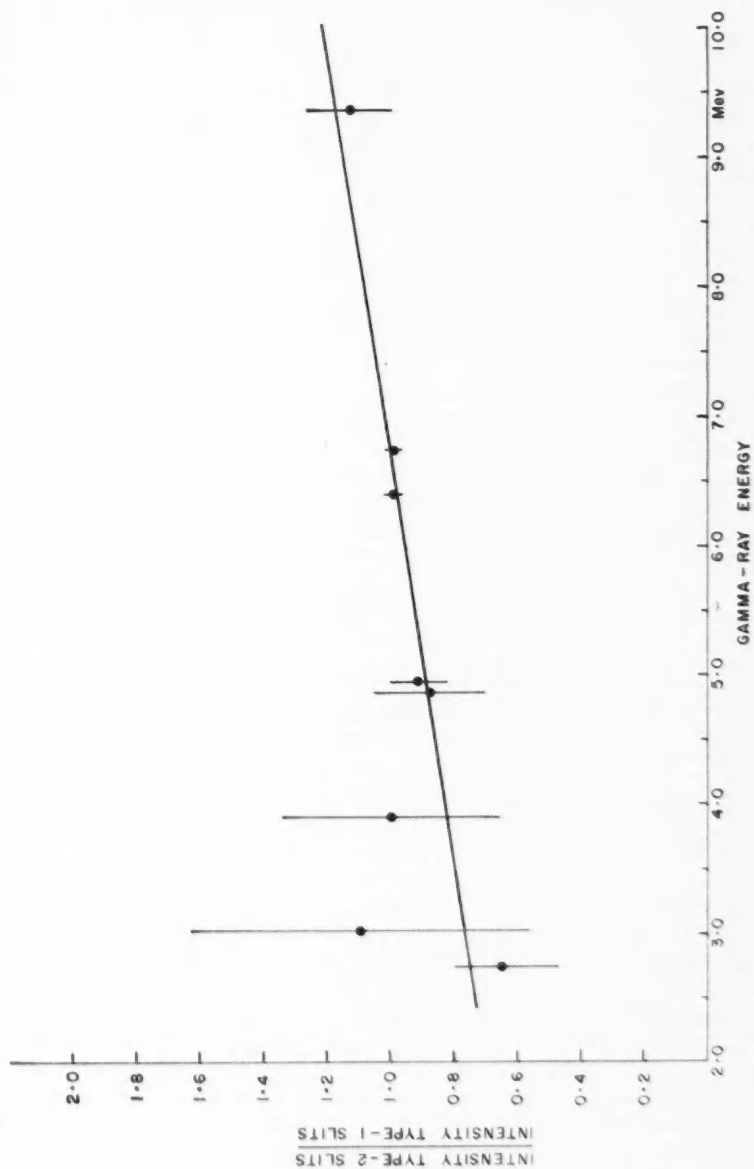
FIG. 16. Ratio of the peak counting rates for γ-rays measured with type-2 slits to those measured with type-1 slits as a function of energy, normalized to unity at 6.6 Mev.

a less precise determination of the efficiency function has been made by a comparison of the counting rates obtained with type-2 slits and those obtained with type-1 slits for a number of γ-ray energies. The results of such a comparison, giving the ratio of intensities for type-2 slits with $\delta = 0.013$ and type-1 slits with $\delta = 0.009$, normalized to unit ratio at 6.6 Mev, are shown in Fig. 16. Within the accuracy of the measurement the energy dependence of the peak counting efficiency for the two types of slit is the same although there is a suggestion, as shown by the straight line, that the energy variation for type-2 slits is possibly more rapid than for type-1. Since the absolute accuracy of the determination for type-1 slits is not high (Kinsey and Bartholomew 1953) a more precise comparison is hardly justified. In making intensity determinations using type-2 slits we have assumed that the efficiency curve of type-1 slits applies and have increased the probable error attributed to it by 5 to 10% to take account of the uncertainty of the comparison measurement.

4. Toe Correction

The energy dependence of the toe correction for type-2 slits was determined empirically by carefully measuring the extrapolated end point of the high-field side of the line for γ-rays whose energies had been accurately measured using type-1 slits. Because of this comparison procedure the accuracy of energy determinations by type-2 slits is always somewhat less than that for type-1. Within the limits of error of the measurements the toe correction was found to vary linearly with energy according to the relation

$$(10) \qquad \Delta E = (0.005 \pm 0.001)E$$

where E is the γ-ray energy.

C. The Efficiency-Resolution Functions for Types-1, -2, and -3 Slits

The experimental variations of peak counting rate as a function of resolution for each of the three types of slit using a broad radiator are compared in Fig. 17 for a γ-ray energy of 6.76 Mev. Types-1 and -2 were used in geometry A and type-3 in geometry B of Fig. 8. These measurements show that for values of the resolution between 1.4% and 0.6% the type-2 slits are the most efficient while in the range below 0.6% it is advantageous to use type-3. Above 1.4% resolution types-1 and -2 would appear to give comparable resolution. The relatively poor performance of type-3 slits at low resolution (large W), indicated in Fig. 17, may be caused by the fact that the line shape depends more strongly on the point of origin of the pairs for type-3 slits than for the other two types. Unfortunately counting rates did not permit comparisons with radiators of smaller size and therefore it was not possible to check the theoretical conclusion that type-3 slits should give the optimum performance for a point radiator at all values of resolution. The effect of the field inhomogeneities on the line shape using arrangement B (Fig. 8) was studied in additional experiments using arrangement C. In these experiments the performance of type-3 slits was observed to be similar to that in arrangement B indicating that the field effect was small.
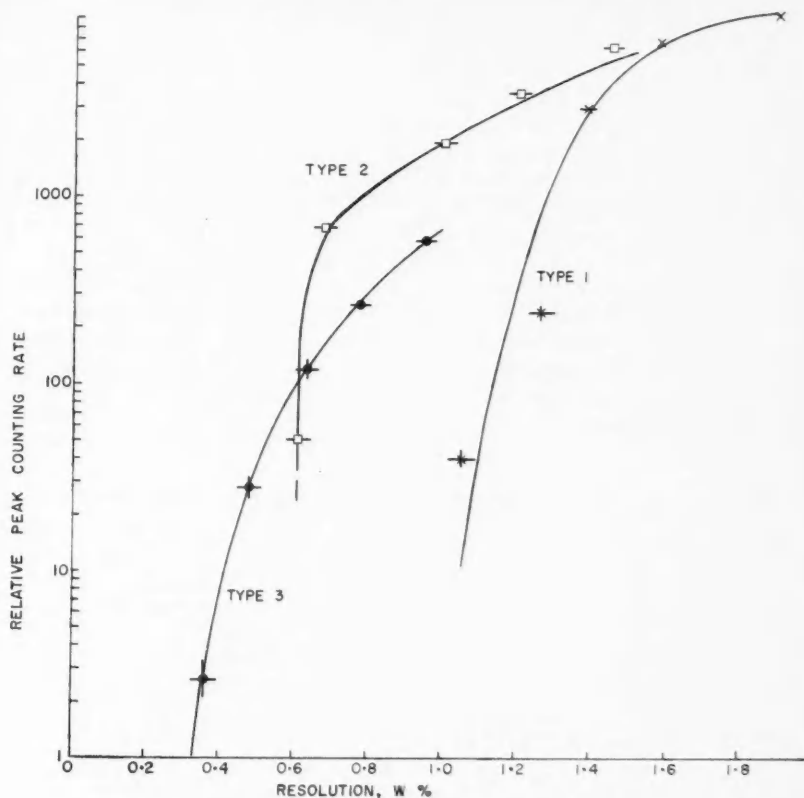
FIG. 17.   Relative peak counting rate as a function of resolution W for slits of types-1, -2, and -3. The curves were obtained at 6.76 Mev with geometries A and B of Fig. 8. The radiator size was 5.7 cm $\times$ 5 cm for all but the point at $W = 0.37\%$ for which the size was 5 cm $\times$ 1 cm.

V. CONCLUSION

By using specially designed counter apertures it is possible to improve the performance of a 180° flat field pair spectrometer beyond that attainable with conventional slits. Without attempting to give a rigorous proof we have argued that the type-3 apertures must provide the best performance, i.e. the ultimate transmission at any resolution, that can be achieved by a flat field spectrometer with a point radiator coplanar with the detector apertures. For the present instrument, however, which employs a broad radiator, type-2 slits are found to be more practicable, although, unlike type-3 slits, it is difficult to make line shape calculations for this design. In both types of slits a marked improvement in peak shape is achieved mainly by the reduction of the low-field tail which characterized the line profile produced by thin slits. In addition

the resolution is approximately constant with energy for both type-2 and type-3 slits. It would appear that in applications where poor resolution and high efficiency are required, type-1 slits with a broad radiator are probably no less efficient than more elaborate types. For somewhat better resolutions it is advantageous to retain the broad radiator and use thick jaws such as type-2 to reduce the low-field tail associated with the line profile. Still higher resolutions are obtained with type-3 slits and an extended radiator, while the highest resolutions can only be obtained with type-3 slits and radiators of small size.

ACKNOWLEDGMENTS

REFERENCES

ALBURGER, D. E.   1955.   *In* Beta- and gamma-ray spectroscopy, *edited by* K. Seigbahn (North-Holland Publishing Co., Amsterdam), p. 767.
BALZER, R., KNOEPFEL, H., STOLL, P., and WÖLFI, W.   1958.   Helv. Phys. Acta, **31**, 328.
BARTHOLOMEW, G. A. and HIGGS, L. A.   1958.   Atomic Energy of Canada Limited, Rept. A.E.C.L. 669.
BETHE, H. and HEITLER, W.   1934.   Proc. Roy. Soc. (London), A, **146**, 83.
KINSEY, B. B. and BARTHOLOMEW, G. A.   1953.   Can. J. Phys. **31**, 537.
KNOEPFEL, H., SHERRER, P., and STALL, P.   1959.   Z. Physik, **156**, 293.
KNOWLES, J. W., MANNING, G., BARTHOLOMEW, G. A., and CAMPION, P. J.   1959.   Phys. Rev. **114**, 1065.
McDANIEL, B., VON DARDEL, G., and WALKER, R.   1947.   Phys. Rev. **72**, 985.
RUTHERGLEN, J. G., RAE, E. R., and SMITH, R. D.   1951.   Proc. Phys. Soc. (London), A, **64**, 906.
TERRELL, J.   1950.   Phys. Rev. **80**, 1076.
WALKER, R. and McDANIEL, B.   1948.   Phys. Rev. **74**, 315.

KLEIN–DUNHAM POTENTIAL ENERGY FUNCTIONS IN SIMPLIFIED ANALYTICAL FORM[1]

W. R. JARMAIN

ABSTRACT

A simple formula, based originally on the work of Klein and Rees, is developed for calculating potential energy curves, except near the dissociation limit, for electronic states of diatomic molecules. Classical turning points $r_{1,2}$ are given as functions of vibrational quantum number ($V \equiv v + 1/2$), with coefficients depending on observed spectroscopic constants, in the form

$$\frac{r_{1,2}(V)}{r_e} = \left[\frac{S_1}{S_1 + S_2} + \left(\frac{f}{r_e} \right)^2 \right]^{1/2} \pm \frac{f}{r_e}$$

where

$$S_1(V) = 1 + \sum_{n=1}^{\infty} b_n V^n; \qquad S_2(V) = \sum_{n=1}^{\infty} d_n V^n;$$

$$\frac{f}{r_e} = 2 \left(\frac{B_e}{\omega_e} \right)^{1/2} V^{1/2} S_1(V).$$

For most states convergence is rapid, but as a rule more so for heavy molecules than for light molecules. Assuming it to be close to the 'true' potential, such a representation affords a convenient means of assessing the accuracy of the Morse or other empirical potential function. Morse curves have also been fitted by least squares to Klein–Rees turning points.

Term-by-term comparison between the inverted Dunham series and an equivalent form of the above has led to the surprising discovery that if Dunham's small correction terms are neglected, Klein and Dunham potentials are mathematically identical. This is contrary to the generally held belief that the two should be used in mutually exclusive regions. In the present form these series exhibit better behavior over a wider range than a series giving potential energy as a function of internuclear separation.

I. INTRODUCTION

In this laboratory's continuing program of computation (Nicholls 1958) of Franck–Condon factors (Bates 1952) for diatomic molecular transitions, the Morse (1929) function has consistently been used as a vibrational potential. While its limitations are of course recognized, the Morse potential has the advantage of leading to exact solutions of the Schrödinger wave equation, and of providing vibrational wave functions whose overlaps can be integrated analytically if a simple, usually valid, approximation is applied (Fraser and Jarmain 1953; Fraser 1954). Moreover, for most electronic states, a Morse model has been found to represent adequately the vibrational energy levels.

For some states, however, notably $B^2\Sigma^-$ of CH, a Morse potential has appeared to be seriously in error. Consequently the writer was led to a study of the Klein–Rydberg (1932, 1931) method for constructing potential curves

through Rees's (1947) analytical treatment of it. Based on these authors' work, new expressions were derived for the classical turning points in terms of vibrational quantum number, with the coefficients involving combinations of standard spectroscopic constants. The approach taken was more general than that of Rees, in that it was not restricted to an energy expression cubic in the vibrational quantum number. The resulting formulae have also facilitated tremendously the calculation of accurate potentials, with the possible exceptions of those cases where only two vibrational constants are known, or the higher constants are insignificant.

A corresponding power series expansion for potential energy as a function of internuclear distance was next set up. Rather unexpectedly, it was discovered that the modified Klein–Rydberg–Rees method produces a potential which is mathematically identical with Dunham's (1932) first approximation! (That is, as is customary, Dunham's Y_{ij} are assumed to be given with sufficient accuracy by just the first terms of the respective power series in B_e^2/ω_e^2.) It seems to have been fairly generally but erroneously believed before that the methods of Klein and Dunham are not equivalent; on the contrary that the former should be used for higher quantum numbers and the latter near the minimum.

The principal purpose of this paper is to present formulae from which potential curves can rapidly be constructed over an extended range (usually) of vibrational quantum number v, and to indicate applications that are being made or are contemplated.

II. DEVELOPMENT OF EXPRESSIONS RELATING CLASSICAL TURNING POINTS AND VIBRATIONAL QUANTUM NUMBER

The modification to be described in detail here was developed a few years ago (Jarmain 1956). It should be emphasized, however, that recent re-examination of Klein's (1932) paper has revealed that the working formulae given below can be derived from two of his equations.*

For the maximum and minimum values, $r_{1,2}$, of the interatomic distance for a molecule vibrating with an energy U, Klein gives

$$(1) \qquad r_{1,2}(U) = \left(\frac{f}{g} + f^2\right)^{1/2} \pm f$$

where f and g are defined in terms of the auxiliary function

$$S(U,\kappa) = \frac{1}{\pi(2\mu)^{\frac{1}{2}}} \int_0^{I'} [U - E(I,\kappa)]^{1/2} dI.$$

In this, $E(I,\kappa)$ is the sum of vibrational and rotational energies for any level up to U; action variable $I = h(v+1/2)$; $\kappa = [J(J+1)h^2]/8\pi^2\mu$; J is the rotational quantum number; μ is the reduced mass of the molecule; and $I = I'$ when $E = U$. Then

*See Klein (1932), equations (13) and (18).

$$f = \frac{\partial S}{\partial U}\bigg]_{\kappa=0} \quad \text{and} \quad g = -\frac{\partial S}{\partial \kappa}\bigg]_{\kappa=0}.$$

Putting $V = v+1/2$ and differentiating under the integral sign,

(2)
$$f(U) = \frac{h}{2\pi(2\mu)^{\frac{1}{2}}} \int_0^{V'} [U-E(V,\kappa)]^{-1/2}dV$$

$$g(U) = \frac{h}{2\pi(2\mu)^{\frac{1}{2}}} \int_0^{V'} \frac{\partial E}{\partial \kappa}[U-E(V,\kappa)]^{-1/2}dV$$

evaluated at $\kappa = 0$ for the case of no rotation. The implication in writing V as the variable of integration is that the vibrational quantum number is not formally restricted to discrete values.

Usually, for the vibrating rotator (Herzberg 1950),

(3) $E(V,\kappa) = (\omega_e V-\omega_e x_e V^2+\omega_e y_e V^3-\omega_e z_e V^4+ \ldots)$
$$+[B_v J(J+1)-D_v J^2(J+1)^2+ \ldots]$$

where

$$B_v = B_e-\alpha_e V+\gamma_e V^2 \ldots$$
$$D_v = D_e+\beta_e V+ \ldots .$$

Thus,

$$E(V,\kappa) = (\omega_e V-\omega_e x_e V^2+ \ldots)+q\kappa(B_e-\alpha_e V+\gamma_e V^2 \ldots)$$
$$-q^2\kappa^2(D_e+\beta_e V \ldots)$$

in which $q = 8\pi^2\mu/h^2$. For U, ω_e, $\omega_e x_e$, B_e, etc., in wave numbers, and B_e taken to the quadratic term, equations (2) can be written

$$f = N \int_0^{V'} [U-(\omega_e V-\omega_e x_e V^2+ \ldots)]^{-1/2}dV$$

(4) $g = \frac{1}{N} \left\{ B_e \int_0^{V'} [U-(\omega_e V-\omega_e x_e V^2+ \ldots)]^{-1/2}dV-\alpha_e \int_0^{V'} V[U-(\omega_e V \right.$

$$\left. -\omega_e x_e V^2+ \ldots)]^{-1/2}dV+\gamma_e \int_0^{V'} V^2[U-(\omega_e V-\omega_e x_e V^2+ \ldots)]^{-1/2}dV \right\}$$

where $N = (h/8\pi^2\mu c)^{1/2} = r_e B_e^{\frac{1}{2}}$, and f and g are in C.G.S. units. These integrands become infinite at the upper limit, of course, but the integrals nevertheless exist.

Although the following scheme can be perfectly general, suppose that the vibrational energy is satisfactorily represented by a quartic in V. Then the radical expression appearing in equations (4) is

(5) $(U-\omega_e V+\omega_e x_e V^2-\omega_e y_e V^3+\omega_e z_e V^4)^{-1/2} \equiv [(V'-V)F(V)]^{-1/2}$

where

$$F(V) = (\omega_e-\omega_e x_e V'+\omega_e y_e V'^2-\omega_e z_e V'^3) - (\omega_e x_e-\omega_e y_e V'+\omega_e z_e V'^2) V$$
$$+(\omega_e y_e-\omega_e z_e V') V^2-\omega_e z_e V^3.$$

Since integrals of the form

$$\int_0^{V'} V^n [V' - V]^{-1/2} dV, \quad n \text{ a positive integer,}$$

have known values,* namely

$$2\left[\frac{2.4.6. \ \ldots \ 2n}{3.5.7. \ \ldots \ (2n+1)} \right] (V')^{n+1/2},$$

the procedure suggested is to expand $[F(V)]^{-1/2} = G(V)$ in Maclaurin's series. Successive derivatives of G with respect to V are as follows:

$$G'(V) = -1/2G\left(\frac{F'}{F}\right) = -1/2Ga_0, \quad \text{say}$$

$$(6) \quad G''(V) = -1/2G\left[\frac{F''}{F} - 3/2\left(\frac{F'}{F}\right)^2\right] = -1/2Gb_0$$

$$G'''(V) = -1/2G\left[\frac{F'''}{F} - 9/2\left(\frac{F'}{F}\right)\left(\frac{F''}{F}\right) + 15/4\left(\frac{F'}{F}\right)^3\right] = -1/2Gc_0$$

and so on, F and all of its derivatives to be evaluated at $V = 0$, which corresponds to the minimum of the potential curve. It should be noted that a_0, $b_0, c_0, \ldots$ depend upon V'. Set

$$\rho = \int_0^{V'} G(V)(V'-V)^{-1/2}\,dV, \qquad \delta = \int_0^{V'} V\,G(V)(V'-V)^{-1/2}\,dV,$$

$$\epsilon = \int_0^{V'} V^2 G(V)[V' - V]^{-1/2}\,dV,$$

with

$$G(V) = G(0) + G'(0)V + G''(0)\frac{V^2}{2!} + G'''(0)\frac{V^3}{3!} + \ldots \ .$$

Whenever, as is generally so, $\omega_e \gg |\omega_e x_e| \gg |\omega_e y_e| \gg |\omega_e z_e|$, this expansion can safely be assumed to have a negligible remainder after a limited number of terms for some desired accuracy over any reasonable range of V (see Section VII). Performing the integrations, we obtain

$$\rho = 2G(0)\ V'^{\frac{1}{2}}\left(1 - \frac{a_0}{3}\ V' - \frac{2b_0}{15}\ V'^2 - \frac{4c_0}{105}\ V'^3 \ldots\right),$$

$$(7) \qquad \delta = \frac{4}{3}G(0)\ V'^{3/2}\left(1 - \frac{2a_0}{5}\ V' - \frac{6b_0}{35}\ V'^2 - \frac{16c_0}{315}V'^3 \ldots\right),$$

$$\epsilon = \frac{16}{15}G(0)\ V'^{5/2}\left(1 - \frac{3a_0}{7}\ V' - \frac{4b_0}{21}\ V'^2 - \frac{40c_0}{693}\ V'^3 \ldots\right).$$

For most states, terms of such series are found to diminish rapidly as the power of V' increases, even for V' values which are a fairly large fraction of the possible maximum short of dissociation.

*Klein worked out integrals of identical type, but in terms of a different variable.

Returning to equation (1) we substitute $f = N\rho$ and $g = 1/N(B_e\rho - \alpha_e\delta + \gamma_e\epsilon)$ and get

$$(8) \qquad r_{1,2}(V') = N[(C+\rho^2)^{1/2}\pm\rho]$$

in which

$$C = \left(B_e - \alpha_e\frac{\delta}{\rho} + \gamma_e\frac{\epsilon}{\rho}\right)^{-1}$$

and functional dependence of r on U is implied through V'. Note that the width of the potential curve so described is just $2N\rho$ and the center, i.e. $(r_1+r_2)/2$, is $N(C+\rho^2)^{1/2}$, at any chosen level. Approximately, for very small V', $C = 1/B_e$, but with increasing V', $\alpha_e(\delta/\rho)$ and (to a lesser extent) $\gamma_e(\epsilon/\rho)$ become significant even for $B_e \gg |\alpha_e| \gg |\gamma_e|$, because C is usually dominant over ρ^2.

It would now appear that an assumed potential, such as Morse, which implies an α_e (Dunham 1932; Pekeris 1934), will have a central axis which is in error more or less according to the deviation of the theoretical α_e from the observed value. There is a similar but ordinarily less important effect with γ_e. Numerical checks indicate that these deviations often represent a more serious source of error than stopping at a quadratic or cubic in the energy polynomial, unless the energy levels are poorly fitted thereby. The width of the potential curve depends on the vibrational constants and one rotational constant, B_e.

As has been stressed elsewhere (Coolidge, James, and Vernon 1938; Hulburt and Hirschfelder 1941; Chamberlain and Roesler 1955) it is, in general, unsafe to use vibrational constants outside the range of observed energy levels from which they were derived. If this point is kept in mind, there should be no serious objection to a potential curve based on accurately fitted polynomials rather than on the numerical energies themselves. The case of marked change in the rate of convergence of the vibrational levels (Birge 1929; Gaydon 1947), necessitating the use of two or more sets of 'constants', will be discussed in Section III.

Equation (8) can be applied directly to the construction of normal potential curves, but a more convenient form is obtained by writing $r_{1,2}$ as an explicit function of V. If we drop the prime on V, tedious but straightforward reduction leads to

$$(9) \qquad \frac{r_{1,2}(V)}{r_e} = \left[\frac{S_1}{S_1+S_2}+\left(\frac{f}{r_e}\right)^2\right]^{1/2}\pm\frac{f}{r_e}$$

where

$$S_1(V) = 1+\frac{5}{6}kV+\left[\frac{43}{40}k^2-\frac{11}{10}m\right]V^2+\left[\frac{177}{112}k^3-\frac{81}{28}km+\frac{93}{70}n\right]V^3$$

$$+\left[\frac{2867}{1152}k^4-\frac{311}{48}k^2m+\frac{1487}{420}kn+\frac{331}{168}m^2\right]V^4+\left[\frac{11531}{2816}k^5-\frac{101527}{2464}k^3m\right.$$

$$\left.+\frac{29627}{3696}k^2n+\frac{19205}{528}km^2-\frac{47821}{4620}mn\right]V^5+\ldots.$$

$$\frac{f(V)}{r_e} = 2\left(\frac{B_e}{\omega_e}\right)^{1/2} V^{1/2} S_1(V),$$

$$S_2(V) = -\frac{2}{3}\left(\frac{\alpha_e}{B_e}\right) V + \left[-\frac{3}{5} k \left(\frac{\alpha_e}{B_e}\right) + \frac{8}{15}\left(\frac{\gamma_e}{B_e}\right)\right] V^2 +$$

$$\left[\left(-\frac{23}{28} k^2 + \frac{29}{35} m\right)\left(\frac{\alpha_e}{B_e}\right) + \frac{52}{105} k \left(\frac{\gamma_e}{B_e}\right)\right] V^3 + \left[\left(-\frac{4721}{2520} k^3 + \frac{481}{210} km - \frac{65}{63} n\right)\right.$$

$$\times\left(\frac{\alpha_e}{B_e}\right) + \left(\frac{73}{105} k^2 - \frac{44}{63} m\right)\left(\frac{\gamma_e}{B_e}\right)\right] V^4 + \left[\left(-\frac{1451}{704} k^4 + \frac{9847}{1848} k^2 m - \frac{1327}{462} kn\right.\right.$$

$$\left.-\frac{1061}{660} m^2\right)\left(\frac{\alpha_e}{B_e}\right) + \left(\frac{1513}{1386} k^3 - \frac{2278}{1155} km + \frac{68}{77} n\right)\left(\frac{\gamma_e}{B_e}\right)\right] V^5 + \ldots,$$

in which

$$k = \frac{\omega_e x_e}{\omega_e}, \qquad m = \frac{\omega_e y_e}{\omega_e}, \qquad n = \frac{\omega_e z_e}{\omega_e}.$$

Once the coefficients of powers of V in (9) have been worked out for a given state, the determination of turning points at a specified level takes only a few minutes on a desk calculator. Equation (9) can also be employed formally for non-integral v, and thus the potential curve can be interpolated in a consistent manner between energy levels. It will be observed that the co-efficients of (9) are made up of terms which, apart from numerical multipliers, regularly decrease by one order of magnitude (e.g. $\omega_e x_e/\omega_e$) for each increase of unity in the power of V. Convergence of the series shown is found to be considerably more rapid than that of Dunham's (1932) $U(r)$. Terms in V^4 and higher appearing in S_1 and S_2 are frequently negligible but for a few exceptional states (e.g. C_2, $B^3\Pi_g$) they are large enough even for moderately low v (say 5) so that convergence can not be depended upon. The above formulation is then not applicable beyond the lowest few levels. In Section VI proof will be given that Dunham's first approximation to the relationship between potential energy and internuclear distance is mathematically identical with equation (9). The magnitude of a Dunham correction to the linear term of (9) for N_2 and OH ground states will also be indicated.

Potential curves constructed here have each been carried arbitrarily no higher than a level whose energy is roughly half the dissociation energy. Equation (9) is not expected to be valid near the dissociation limit.

III. CHANGES IN THE RATE OF CONVERGENCE OF THE VIBRATIONAL ENERGY LEVELS

When a single power series fails to represent adequately the observed vibrational energy levels, it is necessary to employ two or more sets of vibrational constants over appropriate ranges of V. To illustrate, if a 'discontinuity' occurs in the neighborhood of V_1, $0 < V_1 < V_2$, for turning points corresponding to V_2 equations (4) become

$$f = N\left\{ \int_0^{V_1} [U - (\omega_{e_1}V - (\omega_e x_e)_1 V^2 + (\omega_e y_e)_1 V^3 - (\omega_e z_e)_1 V^4)]^{-1/2} \, dV \right.$$

$$\left. + \int_{V_1}^{V_2} [U - (\omega_{e_2}V - (\omega_e x_e)_2 V^2 + (\omega_e y_e)_2 V^3 - (\omega_e z_e)_2 V^4)]^{-1/2} \, dV \right\}$$

$$(10) \quad g = \frac{1}{N}\left\{ B_e \left[\int_0^{V_1} (U - \omega_{e_1}V + \ldots)^{-1/2} dV + \int_{V_1}^{V_2} (U - \omega_{e_2}V + \ldots)^{-1/2} dV \right] \right.$$

$$- \alpha_e \left[\int_0^{V_1} (U - \omega_{e_1}V + \ldots)^{-1/2} V dV + \int_{V_1}^{V_2} (U - \omega_{e_2}V + \ldots)^{-1/2} V dV \right]$$

$$\left. + \gamma_e \left[\int_0^{V_1} (U - \omega_{e_1}V + \ldots)^{-1/2} V^2 dV + \int_{V_1}^{V_2} (U - \omega_{e_2}V + \ldots)^{-1/2} V^2 dV \right] \right\}$$

where ω_{e_1}, $(\omega_e x_e)_1$, ... apply below V_1 and ω_{e_2}, $(\omega_e x_e)_2$, ... above it. Thus

$$f = N(\rho_1 + \rho_2) \text{ and } g = \frac{1}{N}[B_e(\rho_1 + \rho_2) - \alpha_e(\delta_1 + \delta_2) + \gamma_e(\epsilon_1 + \epsilon_2)]$$

with ρ_2, δ_2, ϵ_2 derived from integration over the interval V_1 to V_2. Equation (8) now reads

$$(11) \quad r_{1,2}(V) = N\left\{ \left[\left(B_e - \alpha_e \frac{\delta_1 + \delta_2}{\rho_1 + \rho_2} + \gamma_e \frac{\epsilon_1 + \epsilon_2}{\rho_1 + \rho_2} \right)^{-1} + (\rho_1 + \rho_2)^2 \right]^{1/2} \pm (\rho_1 + \rho_2) \right\}.$$

Reduction to a form analogous to (9) has not been carried out.

IV. KLEIN–DUNHAM AND MORSE POTENTIAL FUNCTIONS FOR N_2, $X^1\Sigma_g^+$ AND OH, $X^2\Pi_i$

A formula derived from equation (9) but more suitable for comparison with a Morse or other empirical potential is

$$(9') \quad \frac{r_{1,2}(V)}{r_e} = 1 + \left[2\left(\frac{B_e}{\omega_e}\right) + \frac{1}{3}\left(\frac{\alpha_e}{B_e}\right) \right] V + \left[\frac{10}{3} k \left(\frac{B_e}{\omega_e}\right) - 2\left(\frac{B_e}{\omega_e}\right)^2 - \frac{2}{3}\left(\frac{\alpha_e}{\omega_e}\right) \right.$$

$$\left. + \frac{1}{45} k \left(\frac{\alpha_e}{B_e}\right) + \frac{1}{6}\left(\frac{\alpha_e}{B_e}\right)^2 - \frac{4}{15}\left(\frac{\gamma_e}{B_e}\right) \right] V^2 + \ldots$$

$$\pm 2\left(\frac{B_e}{\omega_e}\right)^{1/2} V^{1/2} \left[1 + \frac{5}{6} kV + \left(\frac{43}{40} k^2 - \frac{11}{10} m\right) V^2 + \ldots \right].$$

Table I shows classical turning points, centers, and half-widths for the lowest 20 vibrational levels of the ground state $X^1\Sigma_g^+$ of N_2 as computed from (i) formula (9') and (ii) the Morse function with a dissociation energy of $\omega_e^2/4\omega_e x_e$. As can be seen, discrepancies are small at lower levels but generally increase with the quantum number, and are greater for r_1 than for r_2. For this state equation (9') is (in angstroms)

$$\frac{r_{1,2}(V)}{1.094} = \begin{array}{l} 1 + 4.805 \times 10^{-3} \, V + 2.64 \times 10^{-5} \, V^2 + 1.89 \times 10^{-7} \, V^3 \\ \qquad\qquad\qquad\qquad\qquad\qquad + 4.2 \times 10^{-10} V^4 + \ldots \\ \pm 5.837 \times 10^{-2} \, V^{\frac{1}{2}} (1 + 5.105 \times 10^{-3} \, V + 3.68 \times 10^{-5} \, V^2 + 2.0 \times 10^{-8} V^3 \\ \qquad\qquad\qquad\qquad\qquad\qquad\qquad - 1.9 \times 10^{-9} \, V^4 \ldots). \end{array}$$

TABLE I

Turning points, centers, and half-widths (Å) N_2 $X^1\Sigma_g^+$

Vibrational quantum number	Klein–Dunham formula (9)				Morse			
	r_1	r_2	Center	Half-width	r_1	r_2	Center	Half-width
0	1.051_4	1.141_9	1.096_7	$.045_2$	1.051_2	1.141_8	1.096_5	$.045_3$
1	1.023_1	1.180_8	1.102_0	$.078_8$	1.022_7	1.180_4	1.101_6	$.078_9$
2	1.005_0	1.209_6	1.107_3	$.102_3$	1.004_4	1.209_0	1.106_7	$.102_3$
3	0.991_1	1.234_4	1.112_8	$.121_6$	0.990_2	1.233_6	1.111_9	$.121_7$
4	0.979_6	1.256_9	1.118_3	$.138_6$	0.978_4	1.255_9	1.117_2	$.138_8$
5	0.970	1.278	1.124	$.154$	0.968	1.277	1.123	$.154$
6	0.961	1.298	1.129	$.168$	0.959	1.296	1.128	$.169$
7	0.953	1.317	1.135	$.182$	0.951	1.315	1.133	$.182$
8	0.946	1.336	1.141	$.195$	0.944	1.334	1.139	$.195$
9	0.940	1.354	1.147	$.207$	0.937	1.352	1.145	$.207$
10	0.934	1.372	1.153	$.219$	0.931	1.369	1.150	$.219$
11	0.928	1.389	1.159	$.230$	0.925	1.387	1.156	$.231$
12	0.923	1.406	1.165	$.242$	0.920	1.404	1.162	$.242$
13	0.918	1.423	1.171	$.252$	0.915	1.421	1.168	$.253$
14	0.914	1.440	1.177	$.263$	0.910	1.438	1.174	$.264$
15	0.910	1.457	1.183	$.274$	0.906	1.454	1.180	$.274$
16	0.906	1.473	1.190	$.284$	0.902	1.471	1.186	$.285$
17	0.902	1.490	1.196	$.294$	0.897	1.488	1.193	$.295$
18	0.899	1.507	1.203	$.304$	0.894	1.504	1.199	$.305$
19	0.895	1.523	1.209	$.314$	0.890	1.521	1.205	$.315$

In Table II similar numbers are given for the lowest seven levels of OH, $X^2\Pi_i$. Equation (9') for this state reads

$$\frac{r_{1,2}(V)}{0.9706} = \begin{aligned} &1+2.271\times10^{-2}\,V+4.19\times10^{-4}\,V^2+7.1\times10^{-6}\,V^3+5.5\times10^{-7}V^4+\ldots \\ &\pm1.421\times10^{-1}\,V^{\frac{1}{2}}(1+1.924\times10^{-2}\,V+3.07\times10^{-4}\,V^2+2.4\times10^{-5}V^3 \\ &\qquad\qquad\qquad\qquad\qquad\qquad\qquad\qquad\qquad\qquad+1.3\times10^{-6}\,V^4+). \end{aligned}$$

It is noticeable that coefficients for the light molecule OH (large B_e/ω_e) are larger than those for N_2. Spectroscopic constants have been taken from Herzberg (1950) and Chamberlain and Roesler (1955). It is expected that one or two additional potential curves, constructed by means of (9), will be published in a more detailed scientific report (Jarmain 1959), now in preparation.

TABLE II

Turning points, centers, and half-widths (Å) OH $X^2\Pi_i$

Vibrational quantum number	Klein–Dunham formula (9)				Morse			
	r_1	r_2	Center	Half-width	r_1	r_2	Center	Half-width
0	0.883_3	1.080_2	0.981_7	$.098_5$	0.882_7	1.079_7	0.981_2	$.098_5$
1	0.830_7	1.178_5	1.004_6	$.173_9$	0.829_2	1.177_2	1.003_2	$.174_0$
2	0.799	1.257	1.028	$.229$	0.797	1.256	1.026	$.229$
3	0.776	1.330	1.053	$.277$	0.773	1.328	1.051	$.277$
4	0.758	1.399	1.079	$.321$	0.754	1.398	1.076	$.322$
5	0.743	1.468	1.105	$.363$	0.739	1.468	1.104	$.364$
6	0.731	1.537	1.134	$.403$	0.726	1.539	1.132	$.406$

Some 25 potentials for various states of N_2, N_2^+, NO, OH, O_2, and C_2 are at present on hand.

It is instructive at this point to write down the Morse function expanded in the form (9'). If we solve for the turning points and develop logarithms in series, the result is

$$
(12) \quad \frac{r_{1,2}(V)}{r_e} = \begin{aligned} &1+2\left(\frac{B_e}{\omega_e}\right)^{1/2} k^{1/2}V + 2\left(\frac{B_e}{\omega_e}\right)^{1/2} k^{3/2}V^2 + \frac{8}{3}\left(\frac{B_e}{\omega_e}\right)^{1/2} k^{5/2}V^3 + \ldots \\ &\pm 2\left(\frac{B_e}{\omega_e}\right)^{\frac{1}{2}} V^{\frac{1}{2}}\left(1+\frac{5}{6}kV+\frac{43}{40}k^2V^2+\frac{177}{112}k^3V^3+\ldots\right). \end{aligned}
$$

The series giving the half-width is identical with that in (9') if $\omega_e y_e = \omega_e z_e = 0$, as is true for the Morse model. Rees (1947) of course previously demonstrated that the Morse curve has the same half-width 'f' as does a Klein potential. Also, if the theoretical α_e and γ_e implied by the Morse function (Dunham 1932; Pekeris 1934) should happen to coincide with the experimental values, the coefficients of V and V^2 in (12) can be shown to be the same as those in (9'). For rotation–vibration coupling with a Morse potential function

$$
\alpha_e = \frac{6B_e^2}{\omega_e}\left[-1+\left(\frac{\omega_e x_e}{B_e}\right)^{1/2}\right]
$$

$$
\gamma_e = \frac{6B_e^3}{\omega_e^2}\left[5-10\left(\frac{\omega_e x_e}{B_e}\right)^{1/2}+\frac{23}{4}\left(\frac{\omega_e x_e}{B_e}\right)-\frac{7}{6}\left(\frac{\omega_e x_e}{B_e}\right)^{3/2}\right].
$$

In practice the above proviso will seldom if ever be satisfied exactly but sometimes to a good approximation. Thus, the Morse curve may occasionally be very close to the 'true' potential. For the particular states considered here, (12) becomes respectively

$$
\frac{r_{1,2}(V)}{1.094} = \begin{aligned} &1+4.569\times10^{-3}\,V+2.80\times10^{-5}\,V^2+2.29\times10^{-7}\,V^3+\ldots \\ &\pm 5.837\times10^{-2}\,V^{\frac{1}{2}}(1+5.105\times10^{-3}\,V+4.03\times10^{-5}\,V^2 \\ &\hspace{4cm}+3.6\times10^{-7}V^3+\ldots) \end{aligned}
$$

and

$$
\frac{r_{1,2}(V)}{0.9706} = \begin{aligned} &1+2.159\times10^{-2}\,V+4.98\times10^{-4}\,V^2+1.53\times10^{-5}\,V^3+\ldots \\ &\pm 1.421\times10^{-1}\,V^{\frac{1}{2}}(1+1.924\times10^{-2}\,V+5.73\times10^{-4}\,V^2 \\ &\hspace{4cm}+1.9\times10^{-5}V^3+\ldots). \end{aligned}
$$

V. FITTING MORSE FUNCTIONS TO KLEIN-DUNHAM DATA

As mentioned earlier, computation of Franck–Condon factors in this department and elsewhere (Bates 1949) has been based on the Morse model. Analytic integration of overlaps of Morse wave functions has been made possible through an approximation (Fraser and Jarmain 1953; Fraser 1954) involving the parameters α_i appearing in the functions

$$
U_i(r) = D_i[1-\exp-\alpha_i(r-r_{e_i})]^2.
$$

Formulae developed by this procedure have been programmed for an electronic computer,[*] and finally r-centroid analyses (Nicholls and Jarmain 1956) have been based on the same forms.

It seems desirable, therefore, to examine whether an artificial Morse function can be satisfactorily fitted to Klein–Dunham turning points for an electronic state where the standard Morse curve is a poor representation. In the Morse function, as is well known, there are three disposable parameters, which except for negative $\omega_e x_e$ can be taken to be (Herzberg 1950)

$$\alpha(A^{-1}) \equiv 0.24354(\mu_A \omega_e x_e)^{1/2}, \qquad K \equiv \frac{\omega_e}{\omega_e x_e}, \qquad \text{and } r_e(A).$$

It is the first two of these which can readily be adjusted in a least-squares fitting operation, r_e being unaltered. Only a few such fits have been attempted but it certainly is feasible for some states to improve the Morse description of the potential in this way.

When the Morse representation, adjusted as above, is unacceptable over even a small range of quantum numbers it may be necessary to resort to completely numerical methods, if accurate wave functions are required. The problem is difficult but a finite difference approach with the aid of a large scale computer could be tried, with a good chance of success.

VI. EQUIVALENCE OF KLEIN AND DUNHAM POTENTIALS

The power series assumed by Dunham (1932) to describe the relationship between effective potential energy U and internuclear separation r for a rotating vibrator is of the form

$$(13) \qquad U = a_0 R^2 (1 + a_1 R + a_2 R^2 + a_3 R^3 + \ldots)$$

where

$$R = \frac{r - r_e}{r_e}, \qquad a_0 = \frac{\omega_e^2}{4B_e},$$

ω_e is the classical frequency of small oscillations (cm^{-1}), and

$$B_e = \frac{h}{8\pi^2 \mu c r_e^2}.$$

Dunham solved Schrödinger's wave equation for this potential by the W.K.B. method and found the corresponding energy level equation in terms of the a's in (13) in the following form:

$$(14) \qquad F_{v,J} = \sum_{ij} Y_{ij}(v + 1/2)^i J^j (J+1)^j.$$

In particular

$$Y_{10} = \omega_e \left[1 + \frac{B_e^2}{4\omega_e^2} \left(25a_4 - \frac{95}{2} a_1 a_3 - \frac{67}{4} a_2^2 + \frac{459}{8} a_1^2 a_2 - \frac{1155}{64} a_1^4 \right) \right] \sim \omega_e.$$

*FERUT, formerly at the University of Toronto.

The first fifteen Y_{ij} were set up in this way by considering vibration and rotation in turn. It is evident that Y_{10}, the coefficient of $(v+1/2)$, is not equal to ω_e, but differs from it by terms in B_e^2/ω_e^2. As Dunham showed, we can get a first approximation to the values of the a's by regarding each Y_{ij} as being given experimentally, and by neglecting the small correction terms. These a's can then be used to calculate the correction terms with adequate accuracy. In effect each coefficient in (13) is made up of a major part, arising originally from a phase integral which coincides with that given by the Bohr–Sommerfeld theory, and minor parts due to integrals of lesser importance. Although Dunham's method is generally satisfactory for determination of accurate potential energy functions (Sandeman 1940; Hulburt and Hirschfelder 1941), the series is ordinarily convergent only near the potential minimum, as the following equation for N_2, $X^1\Sigma_g^+$ might suggest

$$U = 6.925\times10^5 R^2(1-2.820R+5.148R^2-8.301R^3+14.40R^4\ldots).$$

By inversion of Dunham's series

$$(15) \qquad R = \pm\left(\frac{U}{a_0}\right)^{\frac{1}{2}}\left[1\pm c_1\left(\frac{U}{a_0}\right)^{\frac{1}{2}}+c_2\left(\frac{U}{a_0}\right)\pm c_3\left(\frac{U}{a_0}\right)^{3/2}+\ldots\right]$$

in which the c_i are combinations of the a's in (13). Now for turning points on the normal potential curve, we have

$$U = \omega_e V-\omega_e x_e V^2+\omega_e y_e V^3-\omega_e z_e V^4+\ldots$$

Substituting in (15), treating powers of $(U/a_0)^{1/2}$ as binomial expansions, and reducing, we obtain

$$
\begin{aligned}
(16)\quad R = {} & sc_1 V-[skc_1-s^2c_3]\,V^2+[smc_1-2s^2kc_3+s^3c_5]\,V^3-[snc_1-s^2(k^2+2m)c_3 \\
& +3s^3kc_5-s^4c_7]\,V^4+\ldots \pm s^{1/2}V^{1/2}\Bigg\{1-\left[\frac{k}{2}-sc_2\right]V-\left[\frac{k^2}{8}-\frac{m}{2}\right. \\
& \left.+\frac{3}{2}\,skc_2-s^2c_4\right]V^2-\left[\frac{k^3}{16}-\frac{km}{4}+\frac{n}{2}-\left(\frac{3k^2}{8}+\frac{3m}{2}\right)sc_2+\frac{5}{2}\,s^2kc_4-s^3c_6\right]V^3 \\
& -\left[\frac{5k^4}{128}-\frac{3k^2m}{16}+\frac{kn}{4}+\frac{m^2}{8}-\left(\frac{k^3}{16}-\frac{3km}{4}-\frac{3n}{2}\right)sc_2-\left(\frac{15k^2}{8}+\frac{5m}{2}\right)s^2c_4\right. \\
& \left.+\frac{7}{2}\,s^3kc_6-s^4c_8\right]V^4\Bigg\}+\ldots
\end{aligned}
$$

where $s = 4(B_e/\omega_e)$ and k, m, and n are as defined previously.

By putting into (16) expressions for the c_i in terms of spectroscopic constants it is possible to show that (9') and (16) are identical at least as far as (16) is written, providing only the major parts of the c_i are used. That is, to a first and usually satisfactory approximation, Klein's potential is exactly the same as Dunham's! Although certainly there has been some awareness that Klein and Dunham potentials are similarly based (Coolidge, James, and Vernon 1938; Vanderslice. Mason, Maisch, and Lippincott 1959), there has apparently been no previous recognition of their complete equivalence within the above

terms of reference. In fact it has generally been considered that Klein's potential should not be used at low energy levels because of its semiclassical foundations and partially graphical development, while Dunham's series, which normally converges only in the neighborhood of the minimum, is appropriate in the very region where Klein's is not. A general proof of this identity, in the sense of avoiding term-by-term comparison, is now being sought. It is of course clear on the vibrational side that Klein's action integral together with his use of half integral quantum numbers is of precisely the same effect as Dunham's first two W.K.B. integrals. On the other hand it is not obvious that their methods of including the rotational contributions are mathematically equivalent.

Expressions for the c_i needed in equation (16) have been taken from the useful work of Sandeman (1940)

$$c_1 = \frac{1}{2} + \frac{1}{12}\left(\frac{\omega_e}{B_e}\right)\left(\frac{\alpha_e}{B_e}\right)$$

$$c_2 = \frac{1}{3}\left(\frac{\omega_e x_e}{B_e}\right)$$

$$c_3 = 0.5 - 2c_1 + 0.6c_2 + 1.5c_1^2 + 0.8c_1c_2 - \frac{1}{60}\left(\frac{\omega_e}{B_e}\right)^2\left(\frac{\gamma_e}{B_e}\right)$$

$$c_4 = 1.8c_2^2 - 0.1\left(\frac{\omega_e}{B_e}\right)\left(\frac{\omega_e y_e}{B_e}\right)$$

$$14c_5 = (9 + 10c_1)c_4 - 2(14 - 21c_1 - 11c_2)c_3 + (17 - 12c_1 - 6c_2 - 33c_1^2 - 18c_1c_2)c_2$$
$$- 14(3 - 5c_1 + 2c_1^2)c_1 + 7$$

$$7c_6 = 30c_2c_4 - 27c_2^3 + 0.2\left(\frac{\omega_e}{B_e}\right)^3\left(\frac{\omega_e z_e}{\omega_e}\right)$$

$$21c_7 = 14(1 + c_1)c_6 - 7(6 - 9c_1 - 7c_2)c_5 + (27.5 - 26c_1 - 27c_2 + 29c_3 - 43.5c_1^2$$
$$- 60c_1c_2)c_4 - (63 - 210c_1 - 14c_2 - 31.5c_3 + 126c_1^2 + 147c_1c_2 + 65c_2^2)c_3 + (38.5$$
$$- 105c_1 - 2.5c_2 - 35c_1^2 + 24c_1c_2 + 13.5c_2^2 + 98c_1^3 + 97.5c_1^2c_2 + 54c_1c_2^2)c_2 - (84 - 220.5c_1$$
$$+ 210c_1^2 - 52.5c_1^3)c_1 + 10.5$$

$$c_8 = 5c_2c_6 + \frac{50}{21}c_4^2 - 15c_2^2c_4 + 9c_2^4$$

wherein all c_i after c_2 are dependent on the lower ones, and constants of higher order than $\omega_e z_e$ and γ_e have been set at zero. Also useful for computation but inferior to (9) is a slight rearrangement of (15)

$$(17) \quad R_{1,2} = c_1 t^2 + c_3 t^4 + c_5 t^6 + c_7 t^8 + \ldots \pm t(1 + c_2 t^2 + c_4 t^4 + c_6 t^6 + c_8 t^8 + \ldots)$$

where $t = (U/a_0)^{1/2}$, but it requires evaluation of powers of U, whereas earlier forms could make use of tabulated powers of V.

For hydrogen and some hydrides it may be necessary to apply Dunham corrections to the coefficients in the working formulae. Following Sandeman (1940), the Y_{ij} of equation (14) may be split into components

$$(18) \qquad Y_{ij} = x_{ij} + y_{ij} + z_{ij} + \ldots,$$

x_{ij} being the major part and y_{ij} and z_{ij} small corrections decreasing successively in a ratio of the order of B_e^2/ω_e^2. For all but the most precise work it is sufficient to use only the first corrections y_{ij} which are calculated in the manner outlined above for the a's. In equation (9′), the correction to the largest term (linear one) $\sim -6 \times 10^{-8}$ for N_2, $X^1\Sigma_g^+$, and $\sim -2 \times 10^{-5}$ for OH, $X^2\Pi_i$.

VII. SPECIAL CASE—VIBRATIONAL ENERGY QUADRATIC IN V

For some of the electronic states for which at present only two vibrational constants are tabulated, the following formulation, equivalent to that of Rees (1947), may be advantageous. The integrals appearing in equations (4) can here be evaluated exactly without resorting to expansion in series. We find that

$$f = \frac{r_e B_e^{1/2}}{(\omega_e x_e)^{1/2}} \ln\left[\frac{(\omega_e^2 - 4\omega_e x_e U)^{1/2}}{\omega_e - (4\omega_e x_e U)^{1/2}}\right]$$

$$(19) \qquad = \frac{r_e B_e^{1/2}}{(\omega_e x_e)^{1/2}} \ln\left[\left(1 + \sqrt{\frac{U}{D}}\right)^{1/2}\left(1 - \sqrt{\frac{U}{D}}\right)^{-1/2}\right]$$

$$g = \frac{1}{2 r_e B_e^{1/2}(\omega_e x_e)^{3/2}} \ln\left[\frac{(\omega_e^2 - 4\omega_e x_e U)^{1/2}}{\omega_e - (4\omega_e x_e U)^{1/2}}\right]\left\{\left[2\omega_e x_e B_e - \alpha_e \omega_e + \frac{\gamma_e(3\omega_e^2 - 4\omega_e x_e U)}{4\omega_e x_e}\right]\right.$$

$$\left. + (4\omega_e x_e U)^{1/2}\left[\alpha_e - \frac{3\omega_e \gamma_e}{4\omega_e x_e}\right]\right\}$$

where the dissociation energy

$$D = \frac{\omega_e^2}{4\omega_e x_e}.$$

$r_{1,2}$ are then determined by substitution in equation (1).

Very recently, potential curves for a number of electronic states of N_2 and NO have been constructed by Vanderslice *et al.* (1959), using a series of quadratic energy expressions and the Rydberg–Klein–Rees method. Their procedure limits to two the number of both vibrational and rotational 'constants', and allows ω_e, $\omega_e x_e$, B_e, and α_e to vary with the energy level. Insofar as comparison is possible with results obtained here their turning points are consistently a little towards higher r values. Deviations are largely in the centers of these curves, however, good agreement appearing in the widths. Presumably then the discrepancies can be attributed to different utilization of the rotational data.

The relations (19) are valid only for positive $\omega_e x_e$, and thus do not hold for the upper states of the main systems of the alkali-metal hydrides (Almy

and Beiler 1942; Gaydon 1947). In these cases f and g are given in terms of inverse sine functions instead of logarithms. Such difficulty is not encountered in the use of equations (9) or (17).

Convergence of the series in (9') for a quadratic energy expression can be confirmed by combining (19) and (1), applying known convergent expansions and reducing. This procedure shows term-by-term identity of formulae based on Maclaurin's series on the one hand and exact closed form integrals on the other. Furthermore there is no reason to suppose that the inclusion of *small* higher-order vibrational constants could cause divergence for any level whose energy is less than about half the energy at the dissociation limit.

ACKNOWLEDGMENTS

REFERENCES

ALMY, G. M. and BEILER, A. C. 1942. Phys. Rev. **61**, 476.
BATES, D.R. 1949. Proc. Roy. Soc. (London), A, **196**, 217.
——— 1952. Monthly Notices Roy. Astron. Soc. **112**, 614.
BIRGE, R. T. 1929. Trans. Faraday Soc. **25**, 707.
CHAMBERLAIN, J. W. and ROESLER, F. L. 1955. Astrophys. J. **121**, 541.
COOLIDGE, A. S., JAMES, H. M., and VERNON, E. L. 1938. Phys. Rev. **54**, 726.
DUNHAM, J. L. 1932. Phys. Rev. **41**, 713, 721.
FRASER, P. A. 1954. Proc. Phys. Soc. (London), A, **67**, 939.
FRASER, P. A. and JARMAIN, W. R. 1953. Proc. Phys. Soc. (London), A, **66**, 1145, 1153.
GAYDON, A. G. 1947. Dissociation energies (Chapman and Hall, Ltd., London).
HERZBERG, G. 1950. Molecular spectra and molecular structure. I. Spectra of diatomic molecules (D. Van Nostrand Company, Inc., New York).
HULBURT, H. M. and HIRSCHFELDER, J. O. 1941. J. Chem. Phys. **9**, 61.
JARMAIN, W. R. 1956. Unpublished.
——— 1959. Sci. Rept. No. 3, Contract AF 19(604)-4560. In preparation.
KLEIN, O. 1932. Z. Physik, **76**, 226.
MORSE, P. M. 1929. Phys. Rev. **34**, 57.
NICHOLLS, R. W. 1958. Ann. géophys. **14**, 208.
NICHOLLS, R. W. and JARMAIN, W. R. 1956. Proc. Phys. Soc. (London), A, **69**, 253.
PEKERIS, C. L. 1934. Phys. Rev. **45**, 98.
REES, A. L. G. 1947. Proc. Phys. Soc. (London), A, **59**, 998.
RYDBERG, R. 1931. Z. Physik. **73**, 376.
SANDEMAN, I. 1940. Proc. Roy. Soc. (Edinburgh), **60**, 210.
VANDERSLICE, J. T., MASON, E. A., MAISCH, W. G., and LIPPINCOTT, E. R. 1959. J. Molecular Spectroscopy, **3**, 17.

THE GAMMA-NEUTRON CROSS SECTION FOR N^{14} [1]

J. D. King, R. N. H. Haslam, and R. W. Parsons[2]

ABSTRACT

The reaction $N^{14}(\gamma,n)N^{13}$ has been studied by irradiating dicyandiamide in the X-ray beam of a 25-Mev betatron and measuring the residual activity with a sodium iodide crystal system. The photoneutron cross section shows maxima at 11.7, 13.2, 15.2, 19.5, and 22.8 Mev, the last two being in the giant resonance region. The integrated cross section from threshold to the beginning of the giant resonance region is 1.8 Mev-mb, and this is compared with a recent theoretical prediction. During the course of the experiment, accurate measurements were made of the half-life of N^{13} and it was found to be 9.93 ± 0.05 minutes.

INTRODUCTION

In a recent paper, Fujii (1959) has developed a theory to explain the low energy photodisintegration of C^{13}, N^{14}, and F^{19}. He postulates that these nuclei have a central core and one or more relatively loosely bound nucleons. At energies well below the giant resonance region, photodisintegration is assumed to occur by the excitation of the extra nucleon without disturbing the central core. Such a mechanism, which was originally postulated by Guth and Mullin (1949) to explain the photodisintegration of Be^9 at low energies, is quite different from those postulated by either Goldhaber and Teller (1948) or Wilkinson (1956) to explain the existence of the giant resonance; the Goldhaber and Teller model assumes simultaneous excitation of all nucleons, which oscillate as two interpenetrating fluids, while Wilkinson assumes the excitation of single nucleons deep in the nuclear core.

According to the Fujii (1959) model, N^{14} consists of a C^{12} core and an extra neutron and proton, both of which are in $1p_{1/2}$ states; at low energies, photodisintegration is accomplished by electric dipole absorption resulting in the emission of the loosely bound neutron or proton in a d wave. It has been shown (Carver *et al.* 1954) that this extra-nucleon model is not applicable to Be^9 because, at 6 Mev, the (γ,n) reaction for Be^9 proceeds through the ground state in less than 20% of the cases. However, such a model may be better for N^{14}, since, according to shell theory, a C^{12} core would have two completely filled levels, the $1s_{1/2}$ and the $1p_{3/2}$. The last neutron and proton in N^{14} both go into otherwise unoccupied states, the $1p_{1/2}$. The Be^8 core, on the other hand, is not saturated and the last neutron in Be^9 goes into the already partially filled $1p_{3/2}$ state. Fujii predicts that the probability of the electric dipole transition, and hence the cross section for $N^{14}(\gamma,n)N^{13}$ should have a peak value for an incident photon energy of 13.5 Mev. The height of this peak is expected to be 15 mb and its half width 0.9 Mev.

The reaction $N^{14}(\gamma,n)N^{13}$ has been studied experimentally in this laboratory by Johns *et al.* (1951), Horsley *et al.* (1952), Chidley and Katz (1955), and

Chidley (1956). All agree that there is at least one peak well below the giant resonance region, but the measurements are not of sufficient accuracy to provide a check of the theoretical predictions. Since 1956 the energy stability of the betatron with which the measurements were made has been improved, and more satisfactory counting equipment, using scintillation crystals instead of a Geiger counter, has been constructed. It, therefore, seemed worth while to make a further detailed study of this reaction in order to obtain results which are sufficiently precise to be compared with the theoretical predictions.

EXPERIMENTAL PROCEDURE

Reagent quality dicyandiamide, $C_2H_4N_4$, was pressed into disks of diameter 4.5 cm and thickness 1.2 cm; the mean weight of the samples was 24.86 g, the maximum deviation from this value being 0.03 g. The disks were irradiated in the X-ray beam of the University of Saskatchewan betatron at regular intervals of approximately 0.2 Mev from 10.5 to 25 Mev. In addition, in the region from threshold to 16 Mev extra measurements were made to provide data at 0.1-Mev intervals. The energy stability of the betatron was checked regularly by irradiating samples of boric acid at 17.23 Mev and measuring the induced 2.1-minute β^+ activity from O^{15}; the drift was less than 10 kev at 17.23 Mev during the course of the experiment. The dose was measured in terms of the charge passed to a condenser by an aluminum-walled ionization chamber mounted in the X-ray beam; the condenser was shunted by a resistance whose value was chosen to compensate for the decay of the sample activity during the irradiation. The dosimeter had previously been calibrated against a Victoreen thimble in an 8-cm lucite block.

After being irradiated, the samples were placed between two 2 in. × 2 in. NaI crystals mounted on RCA 5819 photomultiplier tubes. The photomultipliers were connected to a conventional coincidence circuit of resolving time 0.57 μsec, for detecting the photons resulting from the annihilation of the positrons emitted by the N^{13}. Above 12 Mev, at least 10,000 coincidences and 40,000 single channel counts were recorded in a 10-minute counting period; at high energies up to 160,000 coincidences were recorded for each point. Paralysis and resolving time corrections were applied to all points, the total correction never exceeding 2%.

The scale of the yield curve was determined by comparing the yields from thin samples of copper and dicyandiamide at 22 Mev with the aid of a flow counter (Roalsvig and Haslam 1959); the yield from the reaction $Cu^{63}(\gamma,n)Cu^{62}$ was assumed to be 2.25×10^8 disintegrations per mole per 100 r (Roalsvig *et al.* 1959).

Since dicyandiamide contains carbon, above 18.72 Mev the reaction $C^{12}(\gamma,n)C^{11}$ will produce a positron emitter of half-life 20.5 minutes which contributes to the observed activity. A correction for this was determined experimentally at 1-Mev intervals by following the sample activity for 62 minutes and analyzing the resulting decay curve into its two components by the method of least squares.

RESULTS

Before the carbon correction can be determined, the half-life of N^{13} must be known accurately. It was measured by irradiating a dicyandiamide sample at 18 Mev and counting for nine periods of 8 minutes each, with an interval of 1 minute between counting periods. From the measurements, the half-life of N^{13} was estimated to be 9.92 minutes. This is considerably smaller than the values $10.08 \pm .04$ and $10.05 \pm .03$ minutes reported by Wilkinson (1955) and Churchill (1953) respectively, but is close to the value of $9.96 \pm .03$ minutes reported by Arnell *et al.* (1958).

The half-life measurements were therefore repeated under different conditions. In order to reduce the effect of possible impurities, which were assumed to be oxygen, iron, phosphorus, and potassium, irradiations were performed at 15 Mev and 12.4 Mev, but the results for the half-life of the sample activity were in all cases close to 9.92 minutes. In a typical experiment, 543,929 single-channel counts and 118,485 coincidences were observed in the first 8-minute counting period. In order to determine the purity of the sample, a chemical analysis was made and it was concluded that the amounts of potassium and phosphorus were insignificant and that the amount of iron was less than 0.1% by weight. This is much too small to account for the observed discrepancy. In addition, half-life measurements were performed with a 2π proportional flow counter instead of the sodium iodide crystal system, and also with samples of ammonium sulphate instead of dicyandiamide. All sets of measurements were analyzed by the method of least squares, and it was concluded that the half-life of N^{13} is 9.93 ± 0.05 minutes, no systematic dependence on the sample, irradiation energy, or method of detection being noted. This figure was, therefore, used in estimating the carbon correction at energies above 18.72 Mev.

In Fig. 1, the yield, A, of N^{13} per unit monitor response is plotted as a function of the maximum energy E_m in the X-ray spectrum; the carbon correction has already been applied. The smooth curve is an analytic function $y = ax^2 + bx^3 + cx^4$ where $x = E_m - 10.55$, the constants a, b, and c being chosen so that y roughly fits the yield curve. The deviations $A - y$ of the experimental points from the smooth curve are shown in Fig. 2. In order to verify the presence of the fine structure which is apparent in this curve, the measurements were repeated after an interval of approximately 2 months with improved counting statistics; the two sets of results were in very good agreement.

The full curve in Fig. 2 was drawn only after a consideration of both sets of data; in particular, the detailed structure in the regions 11.25 to 12.50 Mev, 13.20 to 16.25 Mev, and 17.90 to 23.80 Mev was apparent from both sets of measurements. The true yield curve was then assumed to be the sum of the analytic curve y and the smoothed deviation curve.

The cross section was obtained from the smoothed yield curve by the inverted matrix method of Penfold and Leiss (1958) using bin widths of 0.5 and 0.2 Mev; the results are shown in Figs. 3 and 4 respectively. From Fig. 3,
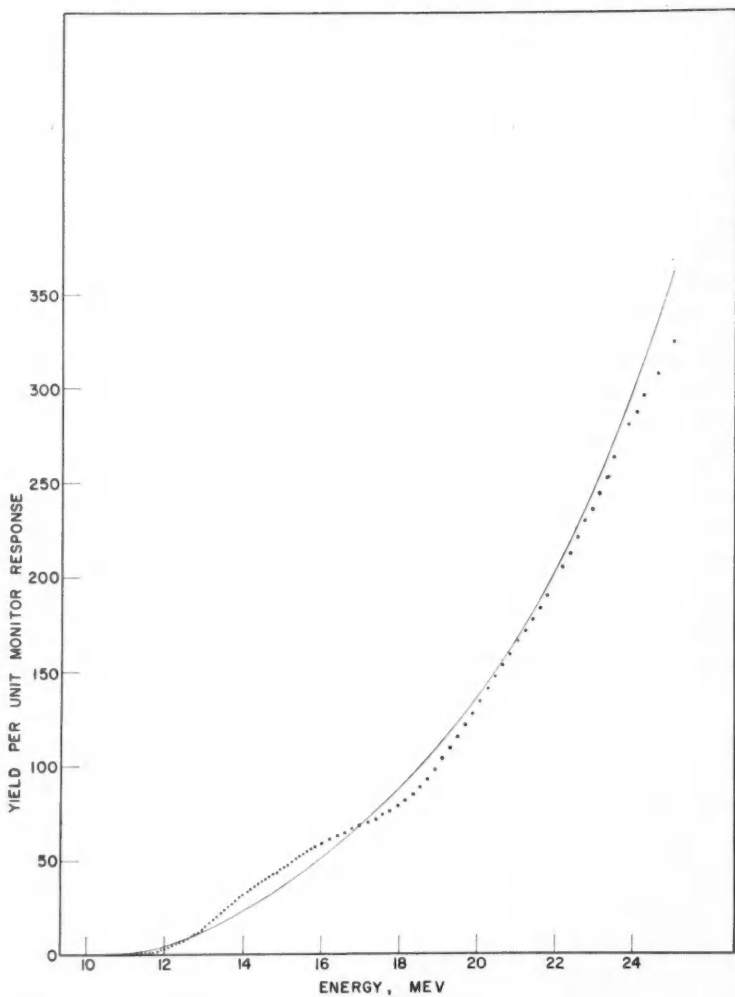
Fig. 1.   Yield, A, of N^{13} per unit monitor response as a function of photon energy. The full curve is an analytic function of the form $y = ax^2 + bx^3 + cx^4$.
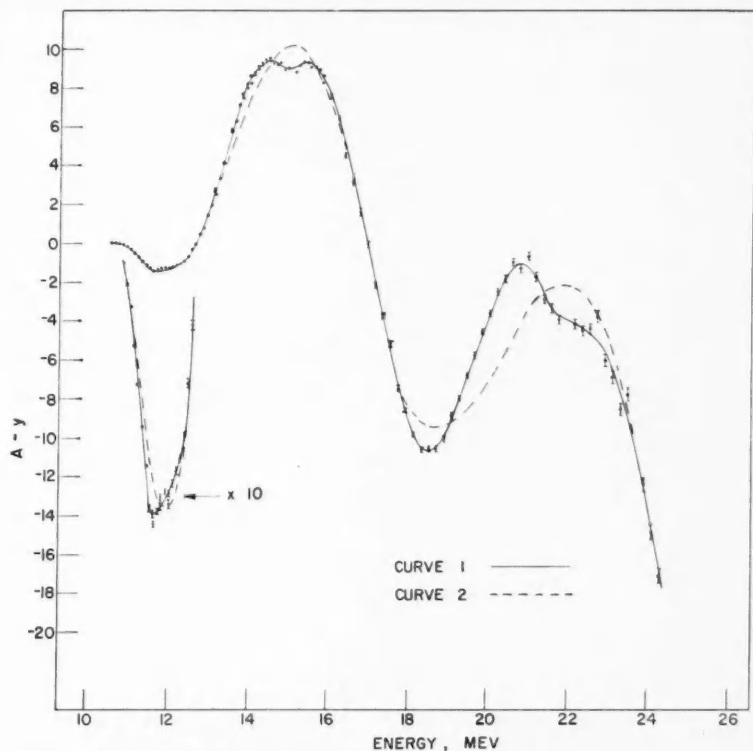
FIG. 2. Deviations of the experimental points from the smooth curve, y. Where the standard deviation is not shown, it is of the order of, or less than, the radius of the dot. The solid line, curve 1, is a smooth curve through the deviations. The dashed line, curve 2, shows the deviations from the smooth curve, y, of an artificially prepared yield curve which is close in shape to the experimental curve, but which gives, on analysis, only a single broad peak at 14 Mev and another at 22 Mev.

the cross section is seen to have peaks at 13.2, 15.2, 19.5, and 22.8 Mev, and there is some evidence for a small peak at 11.7 Mev. It is seen from Fig. 4 that the analysis with a bin width of 0.2 Mev confirms the presence of these peaks, and brings out more detail of the one at 11.7 Mev; that this small peak is largely smoothed out in the analysis using a 0.5 Mev bin is not surprising.

In order to determine whether any of the above peaks in the cross section were not genuine but had been introduced by an incorrect smoothing procedure, an attempt was made to find the smooth yield curve which is closest in shape to the observed yield and which gives, on analysis, only a single broad peak at 14 Mev and another at 22 Mev. This was done by a trial and error method involving the use of the first differences of the yield curve. The
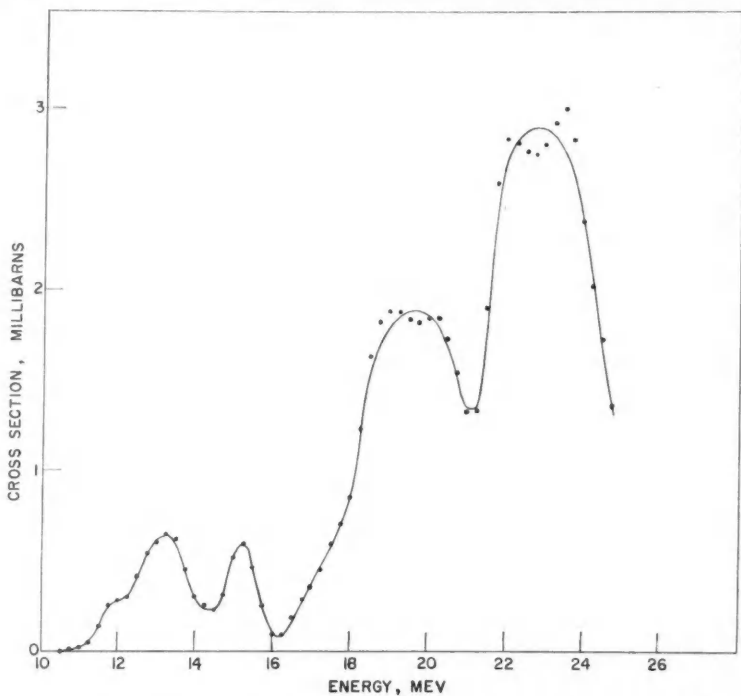
FIG. 3.   The cross section for $N^{14}(\gamma, n)N^{13}$ using a bin width of 0.5 Mev.

deviations of the artificially prepared yield curve from the analytic function y are shown by the dashed curve in Fig. 2. A simple statistical analysis was made in order to determine whether the artificial curve gives a reasonable fit to the observed yield points, results being summarized in Table I. The

TABLE I

Statistical analysis to confirm the presence of fine structure in the deviation curve of Fig. 2

Energy interval, Mev	Intrinsic % deviation	R.M.S. % deviation from curve 1	R.M.S. % deviation from curve 2
11.25–12.50	0.7	2.4	14.3
13.20–16.25	0.22	0.31	1.59
17.90–23.80	0.18	0.22	1.37

intrinsic percentage deviation is calculated by combining the statistical fluctuations inherent in each count with an estimate of the error involved in the reading of the dose. The latter involved reading a helipot which was
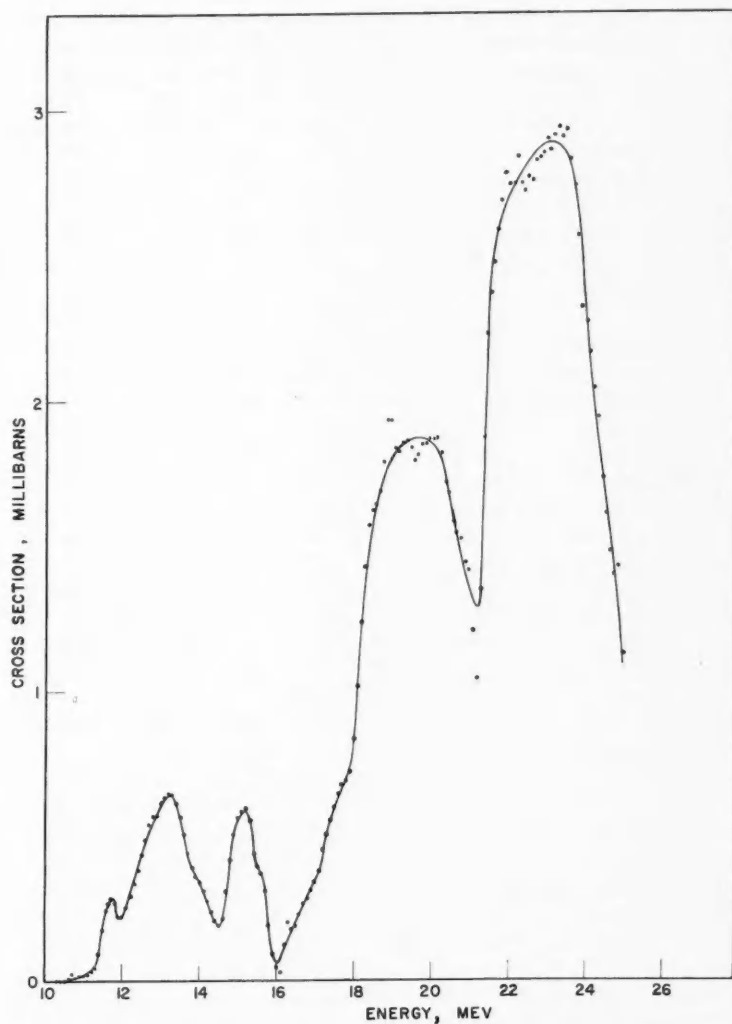
FIG. 4.   The cross section for $N^{14}(\gamma,n)N^{13}$ using a bin width of 0.2 Mev.

graduated to read from 1 to 1000; it was assumed that this could be done to $\pm 1/2$ division. From Table I, it is seen that curve 1 is a more justifiable representation of the observations than the artificial curve 2; this, combined with the fact that the experimental points are randomly distributed about curve 1 but not about curve 2, and also that the details shown in curve 1 were well reproduced when the measurements were repeated, suggests that the fine structure shown in Figs. 3 and 4 is indeed genuine.

DISCUSSION

It is tempting to interpret the two peaks at 19.5 and 22.8 Mev as the components of a split giant resonance; such a splitting was predicted by Okamoto (1958) and Danos (1958) for deformed nuclei and has been verified for several intermediate and high mass nuclei by several observers (Fuller and Weiss 1958; Spicer *et al.* 1958; Parsons and Katz 1959; Parsons 1959). According to the Danos (1958) theory, the intrinsic quadrupole moment would be of the order of 0.08 barn, a figure which is not inconsistent with values deduced by other methods (Bassompierre 1955; Mizushima 1957). Such an intrinsic quadrupole moment in a nucleus containing only 14 nucleons implies, classically, a high deformation; the ratio of the major and minor axes of the nucleus, assumed spheroidal, is approximately 1.2. This may not be surprising for although N^{14} lies midway between C^{12} and O^{16}, both of which are presumably spherical, it seems reasonable to assume that the addition or subtraction of a neutron and proton from small spherical nuclei could result in a considerable deformation.

However, the above interpretation is open to serious objection, since the theory of Danos should be applied to the total photon absorption cross section and the (γ,n) cross section accounts for only 15 to 20% of the total cross section (Ferguson *et al.* 1954; Wright *et al.* 1956). Competition from the (γ,np) and (γ,p) reactions could seriously affect the shape of the (γ,n) cross section, in which case the application of the Danos theory to this reaction would have little meaning.

The yield at 22 Mev was found to be 3.81×10^6 neutrons per mole per 100 r, a value considerably larger than the figure 2.38×10^6 reported by Johns *et al.* (1951). However, the peak value of the cross section determined from the present work is 2.9 mb, in close agreement with the value of 2.84 mb reported previously. The disappearance of the discrepancy is due to the fact that the inverted matrix method of analysis yields lower values for the cross section than the photon difference method that was used in the earlier work.

Instead of one peak below the giant resonance, as predicted by Fujii (1959), the present work shows three. The total integrated cross section from threshold to 16 Mev is 1.8 Mev-mb which is much smaller than the value of 13.5 Mev-mb predicted by Fujii. However, Fujii assumes complete overlap of the initial and final state wave functions of the "core", thus neglecting any polarization of the "core" by the extra neutron. Taking this effect into consideration would lower the theoretical value for the total integrated cross section. The small peak at 11.7 Mev was also found by Chidley (1956), but he did not resolve the two peaks at 13.2 and 15.2 Mev. The latter, however,

are confirmed by preliminary measurements of the spectrum of the neutrons emitted when nitrogen is exposed to 17 Mev bremsstrahlung (Kowalski 1959). They correspond to excited states of the N^{14} nucleus. This is also confirmed by the work of Johansson (1959), who finds that the cross section for the reaction N$^{14}(\gamma,p)$C^{13} shows peaks at these energies. All these peaks presumably correspond to resonance absorption of photons, but it is not possible to interpret any of them in terms of the Fujii (1959) theory since the predicted integrated cross section is too large. However, it should be possible to determine, from measurements of the angular distribution of the neutrons emitted in various energy ranges, whether photodisintegration in this energy region proceeds by an electric dipole transition as predicted by Fujii or by magnetic dipole and electric quadrupole transitions as predicted by Blatt and Weisskopf (1952).

ACKNOWLEDGMENTS

REFERENCES

ARNELL, S. E., DUBOIS, J., and ALMÉN, O. 1958. Nuclear Phys. **6**, 186.
BASSOMPIERRE, A. 1955. Compt. rend. **240**, 285.
BLATT, J. M. and WEISSKOPF, V. F. 1952. Theoretical nuclear physics (John Wiley & Sons, Inc., New York), p. 654.
CARVER, J. H., KONDAIAH, E., and McDANIEL, B. D. 1954. Phil. Mag. **45**, 948.
CHIDLEY, G. B. 1956. Ph.D. thesis, University of Saskatchewan, Saskatoon, Saskatchewan.
CHIDLEY, G. B. and KATZ, L. 1955. Phys. Rev. **99**, 1646.
CHURCHILL, J. L. W., JONES, W. M., and HUNT, S. E. 1953. Nature, **172**, 460.
DANOS, M. 1958. Nuclear Phys. **5**, 23.
FERGUSON, G. A., HALPERN, J., NATHANS, R., and YERGIN, P. F. 1954. Phys. Rev. **95**, 776.
FUJII, S. 1959. Progr. Theoret. Phys. **21**, 511.
FULLER, E. G. and WEISS, M. S. 1958. Natl. Bur. Standards, Rept. 5687.
GOLDHABER, M. and TELLER, E. 1948. Phys. Rev. **74**, 1046.
GUTH, E. and MULLIN, C. J. 1949. Phys. Rev. **76**, 234.
HORSLEY, R. J., HASLAM, R. N. H., and JOHNS, H. E. 1952. Can. J. Phys. **30**, 159.
JOHANSSON, S. 1959. Private communication.
JOHNS, H. E., HORSLEY, R. J., HASLAM, R. N. H., and QUINTON, A. 1951. Phys. Rev. **84**, 856.
KOWALSKI, S. B. 1959. Private communication.
MIZUSHIMA, M. 1957. Phys. Rev. **105**, 1262.
OKAMOTO, K. 1958. Phys. Rev. **110**, 143.
PARSONS, R. W. 1959. Can. J. Phys. **37**, 1344.
PARSONS, R. W. and KATZ, L. 1959. Can. J. Phys. **37**, 809.
PENFOLD, A. S. and LEISS, J. E. 1958. Analysis of photo cross sections (Physics Research Laboratory, University of Illinois, Chicago).
ROALSVIG, J. P. and HASLAM, R. N. H. 1959. Can. J. Phys. **37**, 499.
ROALSVIG, J. P., HASLAM, R. N. H., and McKENZIE, D. J. 1959. Can. J. Phys. **37**, 607.
SPICER, B. M., THIES, H. H., BAGLIN, J. E., and ALLUM, F. R. 1958. Australian J. Phys. **11**, 298.
WILKINSON, D. H. 1955. Phys. Rev. **100**, 32.
———— 1956. Physica, **22**, 1039.
WRIGHT, I. F., MORRISON, D. R. O., REID, J. M., and ATKINSON, J. R. 1956. Proc. Phys. Soc. A, **69**, 77.

THEORY OF THE INFRARED AND RAMAN SPECTRA OF SOLID PARAHYDROGEN[1]

J. VAN KRANENDONK

ABSTRACT

The theory of the rotational and vibrational energy bands in solid hydrogen, developed previously, is applied to the interpretation of the infrared and Raman spectra of solid parahydrogen. A comparison of the theory with the experimental results yields information about the nature of the rotational and vibrational motions of the molecules in the solid, and about the anisotropic intermolecular forces. A calculation of the intensity of the infrared rotational and vibrational lines is given, which is based on the induction mechanisms introduced previously to explain the induced absorption in gaseous hydrogen. Satisfactory agreement with the experimental values is obtained. The importance of the interaction between other than nearest neighboring molecules, and of the interference effects affecting the single transitions, is pointed out. A frequency analysis is given of the infrared and Raman rotational and vibrational lines in the solid, and a consistent theory of the shifts and splittings of the various lines is obtained. Empirical values of the rotational and vibrational coupling constants are derived and compared with the theoretical values.

1. INTRODUCTION

The general theory of the infrared spectra of homonuclear diatomic molecules induced by the intermolecular forces, which was developed previously (Van Kranendonk 1957), is applied here to the infrared spectrum of solid hydrogen. This spectrum has been studied experimentally in great detail by Allin, Gush, Hare, and Welsh (1957, 1958), and by Gush, Hare, Allin, and Welsh (1960). To this latter paper we will refer as I. Our object is to interpret the experimental data on solid parahydrogen in terms of the intermolecular induction effects introduced previously to explain the pressure-induced infrared spectrum of gaseous hydrogen (Van Kranendonk 1958, 1959a; Van Kranendonk and Kiss 1959). The Raman spectrum of solid hydrogen, which has been studied experimentally by Bhatnagar, Allin, and Welsh (1960), will also be discussed.

One of the most interesting aspects of the infrared and Raman spectra of solid hydrogen is revealed by the high resolution data which indicate the existence of rotational and vibrational exciton bands in solid hydrogen. The theory of these energy bands has recently been developed in some detail (Van Kranendonk 1959b; we refer to this paper as II); in the present paper this theory is applied to the interpretation of the rotational and vibrational spectra of solid hydrogen. In this way detailed information is obtained about the anisotropic intermolecular forces in solid hydrogen, which are responsible for the appearance of the energy bands, and about the nature of the rotational and vibrational motions of the molecules in the solid.

There is a characteristic difference between the Raman spectrum on the one hand and the induced infrared spectrum on the other. The intensities in the

Raman spectrum are determined by the matrix elements of the polarizability of the medium. This polarizability may be assumed to be equal to the sum of the polarizabilities of the individual molecules, and the effect of the inter-molecular interaction on the polarizability may be neglected. (The internal field effect due to the long-range dipole-dipole interaction should of course be taken into account.) The activation mechanism for the Raman spectrum is therefore a property of the individual molecules, and in the Raman spectrum of the solid the intermolecular forces come into play only in so far as they affect the rotational and vibrational motions of the molecules. We also remark that, since the polarizability is independent of the intermolecular separations, the translational motions of the molecules, in this case the lattice vibrations, are not Raman active and do not appear at all in the Raman spectrum. In the infrared spectrum, on the other hand, the intensities are governed by the dipole moment of the medium. Because of the homonuclear character of the molecules, the dipole moment vanishes in the absence of the intermolecular interaction. The infrared spectrum of solid hydrogen is therefore a purely induced spectrum arising from the dipole moments induced by the inter-molecular forces in all pairs of interacting molecules. The characteristic property of this induced absorption is the strong dependence of the induced dipole moments on the intermolecular separations. The dipole moments vanish for distances beyond two or three molecular diameters, and increase very rapidly with decreasing intermolecular separations. As a result, the translational motion of the molecules plays an important role in the induced infrared absorption. Quite generally, the integrated intensities in induced infrared spectra are given by configurational integrals involving the con-figurational distribution function of the molecules (Van Kranendonk 1957). The induced absorption therefore reflects an important statistical property of the medium. In solid hydrogen the most prominent part of the spectrum is the phonon spectrum, appearing both in the rotational and in the rotation–vibrational spectrum, as is evident from the experimental data (cf. I). The discussion of these phonon spectra is reserved for a future publication; at present we discuss only the pure rotational and vibrational parts of the spectrum, which correspond to transitions in which no change in the state of the lattice vibrations is involved. We accordingly assume that the centers of mass of the molecules are held fixed at the sites of a rigid lattice.

Another important property of the induced infrared spectra is the appearance of the cancellation effect in dense media (Allin, Gush, Hare, and Welsh 1957, 1958; Van Kranendonk 1957, 1959a). The dipole moments induced by the intermolecular interaction between a molecule and its neighboring molecules tend to cancel one another. This cancellation is the more complete the higher the symmetry of the surrounding configuration of a molecule. The cancellation effect affects only the single transitions. The double and higher transitions which involve a change of state in two or more molecules are not affected by the cancellation effect in the approximation that there is no correlation between the rotational and vibrational motions in different molecules. The existence of rotational and vibrational energy bands in solid hydrogen shows that such

correlations are present in the solid. Nevertheless, we shall show that the integrated intensity due to double and higher transitions is not affected by the cancellation effect. In the solid the single transitions are therefore relatively much weaker than the double transitions. These conclusions are borne out by the detailed calculations presented below, and are in accord with the experimental results obtained by Gush, Allin, Hare, and Welsh (1960).

In Section 2 we discuss the rotational Raman spectrum, and in Section 3 the rotational infrared spectrum. In Section 4 the double rotational transitions are considered. In Sections 5 and 6 the Raman and infrared vibrational spectra are discussed. Finally, in Section 7 an analysis of the rotational and vibrational frequencies is presented.

2. THE ROTATIONAL RAMAN SPECTRUM

As explained in the introduction, we ignore the lattice vibrations, and we consider a crystal of pure parahydrogen with a rigid hexagonal close-packed lattice structure, containing N molecules and $\frac{1}{2}N$ unit cells. The position vectors of the corners of the unit cells are denoted by $\mathbf{R}_i (i = 1, \ldots, \frac{1}{2}N)$, and the position of the second molecule in a unit cell, relative to the corner, is given by τ. The corners of the unit cells are called α sites, and the sites inside the unit cells β sites. In the ground state, which is the only occupied state at all temperatures to be considered, all the molecules are in the $v = 0, J = 0$ state. This state is non-degenerate, and we denote its wave function by

$$(1) \qquad \psi_0 = \psi_0(r_1, \ldots, r_N; \quad \omega_1, \ldots, \omega_N),$$

where r_i and $\omega_i \equiv (\theta_i, \phi_i)$ indicate the internuclear separation and the orientation of the internuclear axis of the ith molecule. We assume periodic boundary conditions; the state (1) is then invariant for all the covering operations of the lattice, and in particular for all the lattice translations. As shown in II, the excited rotational states of solid parahydrogen are broadened by the anisotropic intermolecular forces into rotational energy bands corresponding to travelling rotational excitations. The wave functions of these excited states describe coherent rotational motions of the molecules. For $J = 2$, for example, the 10 eigenfunctions belonging to $\mathbf{k} = 0$, where $\mathbf{k}$ is the wave vector of the rotational excitons, are given by (cf. II, eq. (12))

$$(2) \qquad \psi_m^\pm(0) = N^{-1/2} \sum_i [\varphi_m(\mathbf{R}_i) \pm \varphi_m(\mathbf{R}_i + \tau)].$$

Here $m = 2, \ldots, -2$ is the magnetic quantum number relative to the hexagonal axis, and $\varphi_m(\mathbf{R})$ is the state in which the molecule at $\mathbf{R}$ is in the rotational state $2,m$ and all the other molecules are not rotating. In the states $\psi_m^+(0)$ all the molecules are rotating in phase with one another, whereas in the states $\psi_m^-(0)$ the two molecules in a unit cell are rotating with a relative phase difference equal to π. The $5N$ states corresponding to the presence of one $J = 2$ rotational exciton form a band of states the total width of which was estimated in II to be about 20 cm^{-1}. The next higher set of excited states corresponds to the presence of two $J = 2$ excitons, and forms a band with a width equal to twice that of the single exciton band, etc.

We now consider the pure rotational Raman spectrum of solid parahydrogen, which has been observed with high resolution by Bhatnagar, Allin, and Welsh (1960). The intensity due to the creation of single $J = 2$ rotational excitons is determined by the matrix elements of the polarizability between the ground state (1) and the $J = 2$ energy band eigenfunctions $\psi_m^\pm(\mathbf{k})$,

$$(3) \qquad \langle \psi_0 | \sum_i \, [\alpha(\mathbf{R}_i) + \alpha(\mathbf{R}_i + \boldsymbol{\tau})] | \psi_m^\pm(\mathbf{k}) \rangle.$$

$\alpha(\mathbf{R})$ is a component of the polarizability tensor of the molecule at $\mathbf{R}$, and we have assumed in (3) that the polarizability is equal to the sum of the polarizabilities of the separate molecules. The matrix elements (3) are different from zero only for $\mathbf{k} = 0$, since the first two factors in (3) are invariant for the lattice translations. Thus in the Raman scattering processes only $\mathbf{k} = 0$ rotational excitons are created. In reality the wave vector of the created excitons is not exactly zero, but has a finite value following from the conservation of energy and wave vector. However, the wave lengths of the incident and scattered photons are large compared with the lattice constant, as has been assumed in writing (3), and the $\mathbf{k}$ of the exciton is then effectively zero. For $\mathbf{k} = 0$ the exciton states $\psi_m^+(0)$ and $\psi_m^-(0)$ are even and odd respectively with respect to an inversion at a point midway between the two molecules in a unit cell (cf. II). Consequently only the transitions to the even states, $\psi_m^+(0)$, are Raman active. According to II, eq. (28), these states form a triplet the energies of which are given by

$$(4) \qquad E_m^+ = (0.903)a_m\epsilon,$$

where $m = 0, \pm1, \pm2$; ϵ is the quadrupolar coupling constant

$$(5) \qquad \epsilon = Q^2/5a^5,$$

Q being the quadrupole moment of the molecules, and a the lattice constant; and $a_{\pm2} = 1$, $a_{\pm1} = -4$, $a_0 = 6$. The energies (4) are measured from the energy the $J = 2$ level would have in the absence of the anisotropic intermolecular forces responsible for the rotational energy band. This energy does not coincide with the energy of the corresponding level in a free molecule, because the equilibrium internuclear distance in a molecule in the solid is slightly larger than in a free molecule. This is a result of the isotropic intermolecular forces, as will be discussed in Section 7. Finally, the wave functions of the states (4) are of the form (2) with m referring to the hexagonal axis.

The three Raman active levels (4) give rise to a three-component $S_0(0)$ Raman line. This Raman triplet has been observed by Bhatnagar, Allin, and Welsh (1960), who give the following experimental values for the Raman frequency shifts of these lines:

$$(6) \quad S_0^\alpha(0) = 351.84 \text{ cm}^{-1}; \qquad S_0^\beta(0) = 353.85 \text{ cm}^{-1}; \qquad S_0^\gamma(0) = 355.83 \text{ cm}^{-1}.$$

The separations between the lines are given by

$$(7) \qquad \begin{cases} \Delta_1 = S_0^\beta(0) - S_0^\alpha(0) = 2.01 \text{ cm}^{-1}, \\ \Delta_2 = S_0^\gamma(0) - S_0^\beta(0) = 1.98 \text{ cm}^{-1}. \end{cases}$$

According to the theoretical formula (4), Δ_1 and Δ_2 should be exactly equal. Let us first ignore the small difference between the values of Δ_1 and Δ_2 given in (7), and use the average value $\Delta = 2.00$ cm^{-1}. Using (4), we then get $\Delta = 5(0.903)\epsilon$, from which we derive the empirical value $\epsilon = 0.443$ cm^{-1} for the coupling constant ϵ. If we assume that the anisotropic forces responsible for the splitting Δ are purely quadrupolar, we can calculate ϵ from (5) by using the theoretical value of James and Coolidge (1938) for the quadrupole moment, $Q = 0.45 ea_0^2$, and the experimental value, $a = 7.09a_0$, for the lattice constant, which can be calculated from the known density of solid hydrogen. In this way we obtain the value $\epsilon = 0.50$ cm^{-1}. The discrepancy between the empirical value, $\epsilon = 0.443$ cm^{-1}, and the theoretical value, $\epsilon = 0.50$ cm^{-1}, may be due to inaccuracies in the values of Q and a. However, we consider this to be unlikely, because the value of Q used here leads to values of the intensities of the induced spectra in gaseous hydrogen that are in close agreement with the experimental values (Van Kranendonk 1958; Van Kranendonk and Kiss 1959). It is therefore more probable that the discrepancy is an indication that the anisotropic forces are not exclusively of quadrupolar origin. We therefore investigate the effect of other types of anisotropic forces on the energy levels belonging to $\mathbf{k} = 0$.

The most general expression for the potential of the intermolecular forces between two hydrogen molecules in the ground vibrational state can be written as a sum of terms of the form

$$(8) \qquad V_{l_1 l_2} = 4\pi\epsilon(R) \sum_n a_n Y_{l_1}^n(\omega_1) Y_{l_2}^n(\omega_2)^*$$

over all integer values of l_1 and l_2. Because of the homonuclear character of the molecules, only even values of l_1 and l_2 occur. The constants a_n satisfy the relation $a_n = a_{-n}$. The term $l_1 = l_2 = 0$ gives the isotropic part of the potential. The terms corresponding to $l_1 + l_2 = 2$ vanish when summed over all pairs of molecules in a crystal with hexagonal symmetry. The first non-vanishing contribution to the anisotropic forces in solid hydrogen therefore comes from the terms corresponding to $l_1 + l_2 = 4$. The quadrupolar coupling corresponds to $l_1 = l_2 = 2$, and for $\epsilon = Q^2/5R^5$ the constants a_n have the values $a_2 = 1$, $a_1 = -4$, $a_0 = 6$. The most general term (8) corresponding to $l_1 = l_2 = 2$ contains three arbitrary parameters, and besides the quadrupolar coupling there are therefore two other types of anisotropic force with $l_1 = l_2 = 2$. In this connection it is more convenient to rewrite (8) in the following form:

$$(9) \qquad V_{l_1 l_2} = 4\pi \sum_j \epsilon_j \alpha_j f_{j,0}(\omega_1, \omega_2),$$

where $f_{j,0}$ is a normalized function transforming as an eigenfunction of J^2 and J_z belonging to the eigenvalues j and 0 respectively, where $\mathbf{J} = \mathbf{J}_1 + \mathbf{J}_2$ is the total internal rotational angular momentum of the two molecules. The index j in (9) runs over the even values comprised in $l_1 + l_2, \ldots, |l_1 - l_2|$. The odd values of j in (9) give no contribution, because the interaction (9) should be invariant for an inversion at a point midway between the two molecules. The coefficients in (8) and (9) are related by the equation

$$(10) \quad \begin{cases} \epsilon a_n = (-1)^n \sum_j C(22j; n, -n)\epsilon_j \alpha_j = \sum_j \epsilon_j a_n(j), \\ a_n(j) \equiv (-1)^n C(22j; n, -n)\alpha_j, \end{cases}$$

where $C(j_1 j_2 j_3; m_1, m_2)$ is a Clebsch–Gordan coefficient (Rose 1957). The quadrupolar coupling corresponds to $j = 4$ (cf. II), and the two other types of coupling to $j = 2$ and $j = 0$. We choose the constants α_j such that $a_2(j) = 1$ for all j; $a_n(4) \equiv a_n$ are the quadrupolar constants already introduced in eq. (4). In this way we get

$$(11) \quad \begin{cases} \alpha_4 = \sqrt{70}, & a_2(4) = 1, & a_1(4) = -4, & a_0(4) = 6, \\ \alpha_2 = \sqrt{7}/2, & a_2(2) = 1, & a_1(2) = -\tfrac{1}{2}, & a_0(2) = -1, \\ \alpha_0 = \sqrt{5}, & a_2(0) = 1, & a_1(0) = 1, & a_0(0) = 1. \end{cases}$$

The energies, $E_m^{\pm}$, of the ten $J = 2$ rotational exciton levels belonging to $\mathbf{k} = 0$, resulting in the presence of the coupling (9) between all pairs of molecules in the solid, can be calculated along the lines indicated in II, Section 3. We omit the details of the calculation and give only the result which is

$$(12) \quad E_m^{\pm} = \sum_j \epsilon_j a_m(j)(S_j^{\alpha} + S_j^{\beta}).$$

S_j^{α} and S_j^{β} are lattice sums over the α and β sites respectively. For $j = 4$, these sums have been evaluated in II; for $j = 2$ and $j = 0$, we take into account only the contribution from nearest neighbors, because all other forces are of shorter range than the quadrupolar forces corresponding to $j = 4$. In this way we obtain

$$(13) \quad \begin{cases} S_4^{\alpha} = 2.550, & S_2^{\alpha} = -3, & S_0^{\alpha} = 6, \\ S_4^{\beta} = -1.647, & S_2^{\beta} = 3, & S_0^{\beta} = 6. \end{cases}$$

This concludes the discussion of the terms with $l_1 = l_2 = 2$. We next investigate the terms corresponding to $l_1 = 4$, $l_2 = 0$ and $l_1 = 0$, $l_2 = 4$. This interaction is of the nature of a crystalline field interaction, the sum over all pairs of molecules being equal to a sum of terms each depending on the orientation of only one molecule. Assuming only nearest neighbor interaction, and denoting the constant $\epsilon(a)a_0$ in (8) by ϵ_c, we get for the potential of the ith molecule:

$$(14) \quad \begin{aligned} V_c(\boldsymbol{\omega}_i) &= (4\pi)^{1/2}\epsilon_c \sum_m \sum_j D_{m0}^4(\phi_{ij}, \theta_{ij}, \gamma_{ij}) Y_4^m(\boldsymbol{\omega}_i) \\ &= (7/6)(4\pi)^{1/2}\epsilon_c Y_4^0(\boldsymbol{\omega}_i), \end{aligned}$$

where the D_{m0}^4 are representation coefficients of the rotation group, and $(\phi_{ij}, \theta_{ij}, \gamma_{ij})$ are the Eulerian angles of a rotation that takes the hexagonal axis into the axis connecting molecule i to molecule j. The effective crystalline field is thus a fourth-order axially symmetric field. This field is, of course, not a real electric field, because it represents anisotropic van der Waals interaction. The matrix of the total crystalline field interaction between the 10

exciton states belonging to $\mathbf{k} = 0$ is diagonal, and the diagonal elements are given by

$$(15) \qquad \langle \psi_m^\pm(0) \, | \sum_i V_c(\omega_i) | \psi_m^\pm(0) \rangle \; = \; (7/6)(4\pi)^{1/2}\epsilon_c \langle 20|40|20 \rangle = \tfrac{1}{6}a_m(4)\epsilon_c.$$

The quadrupolar constants $a_m(4)$ appear here because of the fact that both the quadrupolar and the crystalline field interactions are pure $j = 4$ interactions.

Finally, we consider the terms (8) with $l_1 + l_2 > 4$. It is easy to show that these terms have no non-vanishing matrix elements within the manifold of states corresponding to the presence of one $J = 2$ exciton. Configurational interaction, i.e. admixtures of states corresponding to values of $J \neq 2$, can be shown to be negligible for all of the interactions considered here, because of the large unperturbed energy differences involved.

We thus arrive at the conclusion that in the presence of the most general anisotropic forces in solid hydrogen, the energies of the ten $J = 2$ exciton levels belonging to $\mathbf{k} = 0$ are given by

$$(16) \qquad \begin{cases} E_m^+ = (0.903\epsilon + \tfrac{1}{6}\epsilon_c)a_m + 12\epsilon_0, \\[2mm] E_m^- = (4.20\epsilon + \tfrac{1}{6}\epsilon_c)a_m - 6a_m(2)\epsilon_0, \end{cases}$$

where $\epsilon = \epsilon_4$ is the quadrupolar coupling constant, and where the constants $a_m = a_m(4)$ and $a_m(2)$ are given by (11). For the separations (7) between the components of the Raman triplet we obtain from (16)

$$(17) \qquad\qquad \Delta_1 = \Delta_2 = 5(0.903\epsilon + \tfrac{1}{6}\epsilon_c).$$

It is not possible to obtain empirical values of ϵ and ϵ_c separately, unless the Raman $S_1(0)$ triplet could be resolved experimentally (cf. Section 5). An estimation of the value of ϵ_c can be obtained by using in (17) the theoretical value, $\epsilon = 0.50$ cm^{-1}, for ϵ. Using the experimental value, $\Delta = 2.00$ cm^{-1} for the splitting (7), we get in this way $\epsilon_c = -0.31$ cm^{-1}.

We remark that even in the presence of the most general anisotropic forces the relation $\Delta_1 = \Delta_2$ holds good, whereas experimentally a small difference of 0.03 cm^{-1} between Δ_1 and Δ_2 has been found (cf. eq. (7)). The theoretical result $\Delta_1 = \Delta_2$ is valid for arbitrary intermolecular forces in an ideal lattice. The observed small difference between Δ_1 and Δ_2 is therefore presumably due to a deviation from perfect symmetry, either because of the presence of the lattice vibrations, or because of lattice imperfections.

3. THE ROTATIONAL INFRARED SPECTRUM

The infrared spectrum of hydrogen is optically active in virtue of the existence of electric dipole moments induced by the intermolecular forces. The intensities in the rotational spectrum depend on the induced rotational dipole moment which is equal to the expectation value of the total dipole moment operator of the molecules over the ground electronic state and over the ground vibrational states of the molecules. For a pair of hydrogen molecules, the

induced rotational moment is a function of the orientations, ω_1 and ω_2, of the molecules and of their separation, R, which can be expanded as follows (Van Kranendonk and Kiss 1959):

$$(18) \qquad \mu_\kappa(\omega_1, \omega_2; R) = 4\pi \sum_{\lambda_1 \dots \mu_2} C_\kappa(\lambda_1\mu_1\lambda_2\mu_2; R) \, Y_{\lambda_1}^{\mu_1}(\omega_1) \, Y_{\lambda_2}^{\mu_2}(\omega_2).$$

In the present paper we use for all spherical harmonics and spherical components of vectors the phases $i^{|m|+m}$ (cf. Rose 1957). The index κ in (18) thus refers to the spherical components $\mu_0 = \mu_z$, $\mu_{\pm 1} = \mp(\mu_x \pm i\mu_y)/\sqrt{2}$.

For the quadrupolar induction effect the non-vanishing coefficients in the expansion (18) are given by (Van Kranendonk and Kiss 1959):

$$(19) \qquad \begin{cases} C_0(2000) = \dfrac{3}{\sqrt{5}} \dfrac{Q\alpha}{R^4}, & C_1(2100) = -\dfrac{3}{\sqrt{15}} \dfrac{Q\alpha}{R^4}, \\[2ex] C_1(2120) = -\dfrac{4\sqrt{3}}{15} \dfrac{Q\gamma}{R^4}, & C_1(222-1) = \dfrac{\sqrt{2}}{15} \dfrac{Q\gamma}{R^4}, \end{cases}$$

plus 10 other coefficients following from (19) by means of the symmetry relations

$$(20) \qquad \begin{cases} C_\kappa(\lambda_1\mu_1\lambda_2\mu_2) = -C_\kappa(\lambda_2\mu_2\lambda_1\mu_1), \\[1ex] C_\kappa(\lambda_1\mu_1\lambda_2\mu_2) = C_{-\kappa}(\lambda_1-\mu_1\lambda_2-\mu_2)^*. \end{cases}$$

α is the average polarizability, and γ is the anisotropy of the polarizability of a hydrogen molecule. For the overlap induction effect the non-vanishing coefficients are given by

$$(21) \qquad \begin{cases} C_\kappa(2\kappa 00) = -C_\kappa(002\kappa) = \xi_\kappa \exp(-R/\rho), \\[1ex] \xi_0 - \dfrac{2}{\sqrt{3}} \xi_1 = \lambda e\sigma \exp(\sigma/\rho), \end{cases}$$

where $\sigma = 2.93$ Å is the Lennard–Jones molecular diameter. From the rotational spectrum in gaseous hydrogen, a value of λ can be derived, giving $\lambda = 0.8 \times 10^{-4}$ (Van Kranendonk and Kiss 1959).

We assume that in the solid the induction effects are additive, so that the total induced dipole moment is given by the sum of the moments (18) over all pairs of molecules (cf. Van Kranendonk 1959a). The intensity of absorption due to single rotational transitions $J = 0 \to J = 2$ depends on the matrix elements,

$$(22) \qquad \langle \psi_0 | \mu_\kappa | \psi_m^\pm(\mathbf{k}) \rangle,$$

of the total moment μ_κ between the ground state ψ_0, and the single $J = 2$ exciton states $\psi_m^\pm(\mathbf{k})$. Since the first two factors in (22) are invariant for the lattice translations, transitions occur only to the states $\mathbf{k} = 0$. In reality the $\mathbf{k}$ vector of an exciton created in an absorption process must be equal to the $\mathbf{k}$ vector of the absorbed photon. However, the wave length of the photon is large compared with the lattice spacing, and the $\mathbf{k}$ of the excitons may be

taken to be zero. We have the further selection rule that transitions are possible only to the odd states $\psi_m^-(0)$, in consequence of the fact that μ_κ is odd under an inversion at a point midway between the two molecules in a unit cell. To obtain the selection rule for m, we must evaluate the matrix elements (22), because we are dealing with a repeated representation (cf. II). This can be done most easily by transforming the spherical harmonics appearing in the wave functions $\psi_m^-(0)$ (cf. eq. (2)) from the hexagonal axis to the inter-molecular axes as quantization axes by means of the relation (cf. Rose 1957)

$$(23) \qquad Y_l^m(\theta,\phi) = \sum_{m'} D_{mm'}^l(\alpha\beta\gamma)^* Y_l^{m'}(\theta',\phi'),$$

where θ, ϕ are polar angles relative to the hexagonal axis, and θ', ϕ' are defined relative to the relevant intermolecular axis. We first calculate the matrix elements to the localized rotational excitation states $\varphi_m(\mathbf{R})$. This gives

$$(24) \qquad \langle\psi_0|\mu_\kappa|\varphi_m(\mathbf{R}_i)\rangle = \sum_{j\rho} (-1)^\rho C_\rho(2\rho00; R_{ij}) \, D_{\kappa\rho}^1(\mathbf{a}_{ij})^* D_{m,-\rho}^2(\mathbf{a}_{ij})^*,$$

where $\mathbf{a}_{ij}$ in the argument of the representation coefficients denotes a rotation that takes the hexagonal axis into the direction of the vector $\mathbf{R}_{ij} = R_{ij} \, \mathbf{a}_{ij}$ that connects the ith to the jth molecule. The sum over j in (24) runs over all the molecules $j \neq i$, and the quantities C_ρ are given by (19) and (21). With the help of the Clebsch–Gordan series (Rose 1957), we reduce (24) to

$$(25) \qquad \langle\psi_0|\mu_\kappa|\varphi_m(\mathbf{R}_i)\rangle = \sum_{j\rho l} (-1)^\rho \left(\frac{4\pi}{2l+1}\right)^{1/2}$$
$$\times C(12l; \kappa m) \, C(12l; \rho, -\rho) \, C_\rho(2\rho00; R_{ij}) \, Y_l^{\kappa+m}(\theta_{ij}, \phi_{ij}),$$

where θ_{ij}, ϕ_{ij} are the polar angles of $\mathbf{R}_{ij}$ relative to the hexagonal axis as polar axis. When we combine (25) with the corresponding expression for $\varphi_m(\mathbf{R}_i + \tau)$, we get

$$(26) \qquad \langle\psi_0|\mu_\kappa|\psi_m^-(0)\rangle = N^{1/2} \sum_{i\rho l} (-1)^\rho \left(\frac{4\pi}{2l+1}\right)^{1/2}$$
$$\times C(12l; \kappa m) \, C(12l; \rho, -\rho) \, C_\rho(2\rho00; R_i) \, Y_l^{\kappa+m}(\theta_i, \phi_i).$$

Use has been made of the fact that the vectors connecting an α site to the neighboring sites are the opposites of those connecting a β site to its neighbors. As a consequence of this, the sum over l in (26) runs only over the possible odd values, i.e. $l = 1, 3$. The sum over i in (26) runs over all the neighboring sites of an α molecule, and $\mathbf{R}_i = (R_i, \theta_i, \phi_i)$ is a position vector from this molecule. Because of the presence of a trigonal axis in the crystal, the expression (26) vanishes unless $\kappa + m = 0$, ± 3. However, for $\kappa + m = 0$ the terms $l = 1, 3$ are zero because of the presence of the symmetry element σ_h. We thus get a non-vanishing matrix element only for $\kappa + m = \pm 3$, so that only the term $l = 3$ in (26) survives. The component μ_1 of the dipole moment gives rise to the transitions to the state $\psi_2^-(0)$, and the component μ_{-1} to the state $\psi_{-2}^-(0)$. The $S_0(0)$ line contains only the ± 1 components, and is accordingly polarized

perpendicularly to the hexagonal axis. In contradistinction to the Raman spectrum, where the three even $\mathbf{k} = 0$ levels are all active, only one of the three odd $\mathbf{k} = 0$ levels is infrared active. The fact that the two odd levels corresponding to $m = 0$, ± 1 are inactive in the infrared is due to the symmetry properties of the crystal. These symmetry properties do not affect the Raman lines, since the Raman activation mechanism is a property of the individual molecules.

The matrix elements (26) corresponding to $\kappa = 1$, $m = 2$ and $\kappa = -1$, $m = -2$ are equal, and are given by

$$(27) \quad \langle \psi_0 | \mu_1 | \psi_2^-(0) \rangle = \langle \psi_0 | \mu_{-1} | \psi_{-2}^-(0) \rangle$$

$$= N^{1/2} \left(\frac{12\pi}{35} \right)^{1/2} \sum_i \left[C_0(2000; R_i) - \frac{2}{\sqrt{3}} C_1(2100; R_i) \right] Y_3^3(\theta_i, \phi_i).$$

From this expression it is evident that molecules lying on opposite sides of the central molecule give no contribution to the induced absorption. This is an example of the cancellation effect which reduces the intensity of the single transitions. If each molecule were at a center of inversion symmetry, the expression (27) would vanish identically. The fact that the $S_0(0)$ line appears at all in the infrared is therefore evidence for the fact that solid parahydrogen has a hexagonal rather than a cubical close-packed structure. This is in accord with the Röntgen measurements made by Keesom, De Smedt, and Mooy (1935), which were, however, not entirely conclusive. A neutron diffraction experiment on solid hydrogen would therefore be of interest.

The integrated intensity of the $S_0(0)$ line can be calculated from (17), or, alternatively, by using the theorem of spectroscopic stability which states that the total intensity due to all possible transitions $J = 0 \rightarrow J = 2$ is invariant for perturbations removing the degeneracy of the states, i.e. in our case for the anisotropic interaction responsible for the energy band formation. When we neglect the contribution from the overlap induction effect, which amounts to 7% of the total intensity, we get for the integrated absorption coefficient per molecule per unit volume,

$$(28) \qquad \bar{\alpha}[S_0(0)] = \frac{V}{N} \int \bar{A}(\nu) d\nu = 5\pi^3 S_1^2 \frac{Q^2 \alpha^2}{ha^8}.$$

$\bar{A}(\nu)$ is the absorption coefficient per wave length, ν is the frequency (in sec^{-1}), and S_1 denotes the lattice sum

$$(29) \qquad S_1 = \sum_i' \left(\frac{a}{R_i} \right)^4 \sin^3 \theta_i \exp (3i\phi_i).$$

When one restricts the sum in (29) to the six nearest β sites of the central α molecule, one obtains $S_1 = 1.155$, whereas the true value, obtained with the help of the summation method developed by Nyboer and De Wette (1957), is equal to $S_1 = 0.701$. The intensity (28) of the $S_0(0)$ line is therefore reduced by a factor 0.37 because of the dipole moments induced by the central quadrupole in more distant than nearest neighboring molecules. The induction

in about two to three hundred neighbors contributes significantly to the intensity of the $S_0(0)$ line. Using the experimental value $\alpha = 5.7a_0^3$ and the theoretical value $Q = 0.45\ ea_0^2$, we get from (28):

$$(30) \qquad\qquad \bar{a}[S_0(0)] = 0.77 \times 10^{-13}\ \text{sec}^{-1}\ \text{cm}^3.$$

The experimental value obtained by Kiss (1959) is 0.52×10^{-13} sec^{-1} cm^3, which is about 30% lower than the theoretical value (30). This discrepancy is probably due to the fact that the $S_0(0)$ line is very sharp, so that the measurements have not been done with sufficient resolving power. It is also possible that the intensity measurements are affected by the circumstance that the $S_0(0)$ line shows complete polarization perpendicularly to the hexagonal axis. If the specimen were a single crystal with the hexagonal axis aligned perpendicularly to the direction of incidence of the beam, the observed absorption would be a factor $3/4$ smaller than for incident isotropic radiation to which (30) applies. Further experiments are required to settle these points, and to make a more accurate verification of the expression (28) possible.

We next discuss the frequency of the $S_0(0)$ line. According to the expression (16) for the energy, $E_{\pm 2}^-$, of the infrared active level, the frequency of the $S_0(0)$ line is shifted by the anisotropic intermolecular forces by an amount equal to

$$(31) \qquad\qquad 4.20\epsilon + \tfrac{1}{6}\epsilon_c - 6\epsilon_2.$$

Using the theoretical value $\epsilon = 0.50$ cm^{-1}, and the empirical value $\epsilon_c = -0.31$ cm^{-1} derived from the rotational Raman data (cf. Section 2), and neglecting the coupling constant ϵ_2, we obtain for the frequency shift (31) the value 2.05 cm^{-1}. According to the Raman measurements of Stoicheff (1957), the rotational frequency in the gas is equal to 354.38 cm^{-1}. According to the calculations presented in Section 7, this value is decreased in the solid by the isotropic intermolecular forces to 353.7 cm^{-1}. The frequency shift (31) due to the anisotropic forces is measured from this value of 353.7 cm^{-1}. The final value for the frequency of the $S_0(0)$ line in the solid is therefore equal to 355.7. cm^{-1}. This is in satisfactory agreement with the experimental value of (355.6 ± 0.3) cm^{-1} obtained by Kiss (1959). Within the experimental accuracy there is therefore no indication for a non-vanishing value of the coupling constant ϵ_2, i.e. for the presence of a $j = 2$ anisotropic coupling. We can also compare the $S_0(0)$ infrared line with the $S_0(0)$ Raman line in the solid. With the help of (16), one can calculate the frequency of the $S_0(0)$ infrared line from that of one of the components of the Raman line, e.g. the $S_0^\beta(0)$ line. In this way we obtain

$$(32)\ \ \bar{\nu}_{\text{IR}} = \bar{\nu}_{\text{R}} - (0.903\epsilon + \tfrac{1}{6}\epsilon_c) - 12\epsilon_0 + 4.20\epsilon + \tfrac{1}{6}\epsilon_c - 6\epsilon_2 = (355.5 - 12\epsilon_0 - 6\epsilon_2)\text{cm}^{-1}.$$

In combination with the experimental value of (355.6 ± 0.3) cm^{-1}, and the result derived from (31) that ϵ_2 is negligible, we see from (32) that the coupling constant ϵ_0 is also very small. In the following we therefore neglect the $j = 0$ and $j = 2$ anisotropic forces, and we assume that there is present only the quadrupolar coupling, and possibly a small $j = 4$ crystalline field type of anisotropic interaction.

4. THE DOUBLE ROTATIONAL INFRARED TRANSITIONS

Because of the existence of terms corresponding to $\lambda_1 = \lambda_2 = 2$ in the expansion (18) of the induced dipole moment, which are due to the anisotropy of the polarizability, double rotational transitions are possible in the infrared. These transitions correspond to the simultaneous creation of two rotational excitons, and give rise to the $S_0(0) + S_0(0)$ line in solid parahydrogen, which has been observed by Kiss (1959). Although this line arises from the small coefficients $\lambda_1 = \lambda_2 = 2$ in (18), its intensity is of the same order of magnitude as that of the single $S_0(0)$ line, because the double transitions are not affected by the cancellation effect (Van Kranendonk 1957). The width of the $S_0(0) + S_0(0)$ line is an order of magnitude larger than that of the $S_0(0)$ line, because the translational symmetry now demands only that the total wave vector of the two excitons be zero. The wave vector of the relative motion of the two excitons need not vanish, and can range over the entire Brillouin zone. The $S_0(0) + S_0(0)$ line therefore extends over a frequency range corresponding to twice the width of the single $J = 2$ exciton band, i.e. according to II over about 40 cm^{-1}. Experimentally it is difficult to estimate the total extent of the line, because it is superimposed on the strong phonon spectrum. However, the experimental half-width of the line is about 20 cm^{-1} (Kiss 1959), which agrees well with the theoretical value of 40 cm^{-1} for the total extent of the line.

The motion of two excitons is described by a wave function $U_{mm'}(\mathbf{R}_{i\gamma}, \mathbf{R}_{i'\gamma'})$ the square of which gives the probability of finding the excitons at $\mathbf{R}_{i\gamma}$ and $\mathbf{R}_{i'\gamma'}$ with z components of angular momentum equal to m and m' respectively. The wave equation for this function contains two terms of the nature of the left-hand side of the wave equation II, eq. (7) for a single exciton, which can be interpreted as the kinetic energy terms for the translational motion of the two excitons, plus a term which describes the interaction between the two excitons (Van Kranendonk 1955). This interaction contains an infinitely strong repulsive core for $\mathbf{R}_{i\gamma} = \mathbf{R}_{i'\gamma'}$, corresponding to the fact that the two excitons cannot be located on one and the same molecule, plus terms describing the interaction between the excitons when they occupy neighboring molecules, which have the form of spin–spin coupling terms. At present we will not try to solve this wave equation, nor will we try to discuss the interesting question whether there exist bound states of the two excitons. We will therefore not write down the wave equation explicitly.

To calculate the integrated intensity of the $S_0(0) + S_0(0)$ line, we make use again of the theorem of spectroscopic stability which states that the total intensity may be calculated with the help of unperturbed wave functions, i.e. with localized rotational excitations. The contribution to the total intensity of the pair of molecules at $\mathbf{R}_i$ and $\mathbf{R}_j$ is proportional to

$$(33) \qquad \sum_{\kappa mm'} |\langle \psi_0 | \mu_\kappa | \varphi_{mm'}(\mathbf{R}_i, \mathbf{R}_j) \rangle|^2 = \sum_{\kappa mm'} |C_\kappa(2m2m'; R_{ij})|^2.$$

The integrated absorption coefficient per molecule per unit volume is accordingly given by

$$(34) \qquad \tilde{\alpha}[S_0(0)+S_0(0)] = \frac{4\pi^3}{3h} \sum_{\kappa mm'} \sum_i |C_\kappa(2m2m';R_i)|^2.$$

The sum over i runs over all the molecules except the central molecule, and R_i is the distance from the central molecule. The characteristic difference between (34) and the corresponding expression (28) for the single rotational line is that (34) depends on a sum of squared terms, whereas (28) depends on the square of a sum of terms over all molecules. The single transitions therefore show interference effects, leading to the cancellation effect, whereas the double transitions do not show such interference effects. Using the values (19) for the coefficients C_κ, we get

$$(35) \qquad \tilde{\alpha}[S_0(0)+S_0(0)] = \frac{352}{225} \pi^3 S_2 \frac{Q^2\gamma^2}{ha^8},$$

where S_2 denotes the lattice sum

$$(36) \qquad S_2 = \sum_i{}' (a/R_i)^8 = 12.80.$$

With the experimental value $\gamma = 1.6a_0^3$ (Volkmann 1935), and $Q = 0.45ea_0^2$, the numerical value of (35) becomes equal to

$$(37) \qquad \tilde{\alpha}[S_0(0)+S_0(0)] = 0.49\times10^{-13}\,\text{sec}^{-1}\,\text{cm}^3.$$

This value is in satisfactory agreement with the experimental value obtained by Kiss (1959), which is equal to about $0.6\times10^{-13}\,\text{sec}^{-1}\,\text{cm}^3$. The accuracy of the experimental value is not very great because of the uncertainty involved in the separation of the line from the overlapping phonon spectrum. It is therefore not possible as yet to obtain a reliable value of γ from these measurements.

5. THE RAMAN VIBRATIONAL SPECTRUM

The fundamental vibrational spectrum of solid parahydrogen arises from transitions between the ground state and the excited states containing one $v = 1$ vibrational excitation and zero, one, or more $J = 2$ rotational excitations. The pure vibrational level $v = 1$, $J = 0$ is broadened by the intermolecular forces into a vibrational exciton band corresponding to travelling vibrational excitations (cf. II). The energies of the two levels belonging to $\mathbf{k} = 0$ are given by

$$(38) \qquad E^+(0) = -6\epsilon', \quad E^-(0) = 0,$$

where ϵ' is the vibrational coupling constant (cf. II). The energies (38) are measured from the energy the $v = 1$, $J = 0$ level would have in the solid for $\epsilon' = 0$. This energy differs from the corresponding energy in a free molecule by an amount equal to $-2018\mu_1$, where μ_1 is a dimensionless constant characterizing the effect of the isotropic intermolecular forces on the rotation–vibrational properties of the molecules in the solid (cf. Section 7). As we will show presently, an empirical value of μ_1 can be obtained from the frequency of the $S_1(0)$ line, giving $\mu_1 = 4.4\times10^{-3}$.

In the pure $v = 1$ vibrational Raman processes, again only $\mathbf{k} = 0$ excitons are created, and only the even level, $E^+(0)$, of the two levels (38) is Raman active. The fundamental vibrational Raman spectrum therefore consists of only one line, the $Q_1^+(0)$ line, the frequency of which is given by

(39) $\bar{\nu}[Q_1^+(0)] = (4161.1 - 2018\mu_1 - 6\epsilon')$ cm^{-1} $= (4152.2 - 6\epsilon')$ cm^{-1},

in which 4161.1 cm^{-1} is the experimental value of the vibrational frequency in the gas obtained by Stoicheff (1957). Equating (39) to the experimental value for this frequency obtained by Bhatnagar, Allin, and Welsh (1960), which is 4149.81 cm^{-1}, we obtain the value $\epsilon' = 0.40$ cm^{-1} for the vibrational coupling constant. This value is in satisfactory agreement with the theoretical value, $\epsilon' = 0.5$ cm^{-1}, obtained in II by estimating the dependence of the dispersion forces on the internuclear distances in the molecules. The close agreement between the two values of ϵ' shows that the main contribution to the vibrational coupling in the solid comes from the dispersion forces.

The excited states with $v = 1$, $J = 2$ form a band of states corresponding to travelling rotational and vibrational excitations, with an over-all width equal to 20 cm^{-1} (width of the $J = 2$ band) plus 2.4 cm^{-1} (width of the $v = 1$ band), and a $5N$-fold degenerate "impurity" level, corresponding to bound $v = 1$, $J = 2$ excitations, lying below the band. As shown in II, these bound $v = 1$, $J = 2$ excitations do not travel through the lattice because there are no inter-molecular forces of appreciable magnitude which depend both on the inter-nuclear separations and on the orientations of the molecules. The $v = 1$, $J = 2$ energy band levels are Raman inactive in the approximation that the polarization is not affected by the intermolecular interaction, because in these energy band states the $v = 1$ and $J = 2$ excitations are always located on different molecules. Only the bound $v = 1$, $J = 2$ states are Raman active, and these give rise to the $S_1(0)$ Raman line. According to the calculations presented in II, the $v = 1$, $J = 2$ bound level is shifted away from the $v = 1$, $J = 2$ energy band by the quadrupolar forces by an amount equal to $168\epsilon^2/W_0$. Using the theoretical value, $\epsilon = 0.50$ cm^{-1}, for the quadrupolar coupling constant, and the experimental value, $W_0 = 18.0$ cm^{-1}, for the rotation-vibrational interaction constant (Stoicheff 1957), we obtain for this shift the value -2.3 cm^{-1}. An additional shift equal to $-2157\mu_1$ is caused by the iso-tropic intermolecular forces (cf. Section 7); the shift in W_0 caused by these forces is negligible. Collecting these results, we obtain the following expression for the frequency of the $S_1(0)$ Raman line:

(40) $\bar{\nu}[S_1(0)] = (4497.5 - 2157\mu_1 - 2.3)$ cm^{-1},

where the frequency of the $S_1(0)$ line in the gas, 4497.5 cm^{-1}, has been calculated from the band constants given by Stoicheff (1957). The frequency of the $S_1(0)$ Raman line in solid parahydrogen has been measured by Bhatnagar, Allin, and Welsh (1960), and amounts to 4485.8 cm^{-1}. Using this value, we obtain from (40) the value $\mu_1 = 4.4 \times 10^{-3}$ for the constant μ_1. This value of μ_1 has been used in (39) to obtain a value for the vibrational coupling constant ϵ'. The value so obtained agrees well with the theoretical value of ϵ'. If we had

neglected the shift of 2.3 cm^{-1} occurring in (40), we would have obtained a value of ϵ' which is a factor of 10 smaller than the theoretical value. In this way we therefore obtain indirect evidence for the correctness of the value of 2.3 cm^{-1} for the shift of the impurity level, and hence a verification of the impurity calculation presented in II. This shift of 2.3 cm^{-1} is due to the quadrupolar forces, and is a result of the fact that the $J = 2$ rotational excitation spends part of its time on one of the non-vibrating molecules rather than on the central vibrating molecule to which it is bound.

Just as the $S_0(0)$ line, the $S_1(0)$ Raman line is also split into three components by the anisotropic intermolecular forces, but the separation is an order of magnitude smaller than for the $S_0(0)$ line. The bound $v = 1$, $J = 2$ level is split into a triplet by the crystalline field type of anisotropic force which is given by (14). The resulting energy shifts are readily calculated and are given by

$$(41) \qquad\qquad E_m = \tfrac{1}{6}\epsilon_c\, a_m(4).$$

With the value $\epsilon_c = -0.31$ cm^{-1} obtained from the splitting of the $S_0(0)$ line (cf. Section 2), we get

$$E_{\pm 1} = 0.2 \text{ cm}^{-1}, \qquad E_{\pm 2} = 0.05 \text{ cm}^{-1}, \qquad \text{and} \qquad E_0 = -0.3 \text{ cm}^{-1}.$$

In addition to these shifts the levels are shifted slightly by the quadrupolar forces. These shifts have been calculated in II for the case that there is no crystalline field present. However, the crystalline field does not change the wave functions of the excitons, and the shifts calculated in II therefore apply also to the present case. They are given by $-(D_m - 168)\epsilon^2/W_0$, where

$$D_0 = 177, \qquad D_{\pm 1} = 162, \qquad \text{and} \qquad D_{\pm 2} = 169.5.$$

The energy shifts of the three components into which the bound $v = 1$, $J = 2$ level is split are therefore given by

$$(42) \quad E_{\pm 1} = +0.3 \text{ cm}^{-1}, \qquad E_{\pm 2} = -0.05 \text{ cm}^{-1}, \qquad E_0 = -0.4 \text{ cm}^{-1}.$$

The triplet is thus inverted compared to the $S_0(0)$ triplet (cf. eq. (4)). The separations in the triplet (42) are given by $\Delta'_1 = \Delta'_2 = 0.35$ cm^{-1}. Because of the uncertainty in the value of ϵ_c, the values (42) only indicate the order of magnitude of the splitting. It would be interesting if the $S_1(0)$ Raman line could be measured at high resolution. As we show in the next section, only the level $E_{\pm 2}$ is infrared active. Everything else being assumed to be the same, the Raman $S_1(0)$ line should therefore be broader than the infrared $S_1(0)$ line. This seems to be borne out by the experimental data, providing some evidence for the existence of the splitting (42).

6. THE VIBRATIONAL INFRARED SPECTRUM

As in the case of the rotational spectrum discussed in Section 3, the vibrational infrared spectrum is induced by the intermolecular forces. We assume that in the solid the induction effects are additive, and that the total dipole moment is equal to the sum over all pairs of molecules of the moments induced

in isolated pairs. These induced pair moments have been studied in some detail (Van Kranendonk 1957, 1958) in connection with the infrared spectrum in gaseous hydrogen. For a pair of molecules 1, 2 the "moment" corresponding to molecule 1 making the vibrational transition is equal to the derivative of the pair dipole moment with respect to the internuclear separation in molecule 1. We denote this moment by **M**, and expand it in the usual way:

$$(43) \qquad M_\kappa(\omega_1, \omega_2; R) = 4\pi \sum_{\lambda_1 \ldots \mu_2} D_\kappa(\lambda_1 \mu_1 \lambda_2 \mu_2; R) \ Y_{\lambda_1}^{\mu_1}(\omega_1) \ Y_{\lambda_2}^{\mu_2}(\omega_2).$$

The most important non-vanishing coefficients D_κ are given by (Van Kranendonk 1958):

$$(44) \qquad \begin{cases} D_0(0000) = \xi \exp(-R/\rho), \\[2mm] D_0(2000) = +\dfrac{3}{\sqrt{5}} \dfrac{Q'\alpha}{R^4}, \qquad D_{\pm 1}(2\pm 100) = -\dfrac{3}{\sqrt{15}} \dfrac{Q'\alpha}{R^4}, \\[2mm] D_0(0020) = -\dfrac{3}{\sqrt{5}} \dfrac{Q\alpha'}{R^4}, \qquad D_{\pm 1}(002\pm 1) = +\dfrac{3}{\sqrt{15}} \dfrac{Q\alpha'}{R^4}. \end{cases}$$

The coefficient $D_0(0000)$ arises from the overlap induction effect, and the other six coefficients are due to the quadrupolar induction effect.

We consider first the pure vibrational lines corresponding to transitions from the ground state ψ_0 to the single $v = 1$ vibrational energy band states. Only the $E^-(0)$ level in this band is infrared active in absorption, as follows from the fact that the total induced dipole moment is translational invariant, and odd with respect to an inversion at a point midway between an α and a β molecule in a unit cell. The resulting line will be denoted by $Q_1^-(0)$ in contradistinction to the vibrational Raman line, which is denoted by $Q_1^+(0)$. The integrated intensity of the $Q_1^-(0)$ line may be calculated in terms of localized vibrational excitations. The matrix element of the total dipole moment μ_κ to the state $\psi_1(\mathbf{R}_i)$, in which the molecule at $\mathbf{R}_i$ is in the $v = 1$ state, is given by

$$(45) \qquad \langle \psi_0 | \mu_\kappa | \psi_1(\mathbf{R}_i) \rangle = \kappa_1 D_0(0000) \sum_j D_{\kappa 0}^1(\mathbf{a}_{ij})^*,$$

in which $\kappa_1 = (h/8\pi^2 m \nu_0)^{\frac{1}{2}}$, the $D_{\kappa 0}^1$ are representation coefficients of the rotation group (cf. eq. (29)) and the sum runs over all the molecules $j \neq i$. In a close-packed hexagonal lattice, this sum vanishes. This is partly due to the cancellation effect, and partly to the presence of the symmetry elements C_3 and σ_h. If the central molecule is an α molecule, the first effect makes the sum over the neighboring α molecules vanish, whereas the sum over the neighboring β molecules is equal to zero because of the incompatibility of $D_{\kappa 0}^1$ with the symmetry elements C_3 and σ_h possessed by the β sublattice. In pure parahydrogen the intensity of the $Q_1^-(0)$ line is therefore equal to zero. This conclusion is in accord with the observations of Gush, Hare, Allin, and Welsh (1959), which show that the intensity of the $Q_1^-(0)$ line approaches zero with vanishing ortho-concentration.

We next consider the S branch arising from transitions to the states $v = 1$, $J = 2$. The transitions to the $v = 1$, $J = 2$ energy band correspond to the

simultaneous creation of a $v = 1$ vibrational exciton and a $J = 2$ rotational exciton. The translational symmetry demands only that the total $\mathbf{k}$ vector of the two excitons be zero, but the $\mathbf{k}$ vector describing the relative motion of the two excitons can range over the entire Brillouin zone. The resulting absorption band therefore extends over a range of frequencies lying between the width of the $J = 2$ and the sum of the widths of the $J = 2$ and $v = 1$ bands, i.e. between about 20 cm^{-1} and 22.4 cm^{-1}, depending on whether the maxima and minima in the two bands occur at the same place or in widely different places of the Brillouin zone. Experimentally (cf. I), the $Q_1(0) + S_0(0)$ band extends over a frequency range of about (22 ± 2) cm^{-1}, in good agreement with the theoretical estimate given above. In the $v = 1$, $J = 2$ band the two excitons are never located on the same molecule, because the bound states corresponding to such situations are contained in the "impurity" levels lying below the band. In this sense the transitions to the $v = 1$, $J = 2$ band are double transitions. The transitions to the bound $v = 1$, $J = 2$ states are also infrared active, and give rise to the sharp $S_1(0)$ line (cf. I).

We first discuss the intensities of the $S_1(0)$ and $Q_1(0) + S_0(0)$ lines. The excited states corresponding to these lines arise out of the $5N^2$-fold degenerate $v = 1$, $J = 2$ level by the action of the anisotropic intermolecular forces and the rotation–vibrational coupling in a molecule, as explained in II. In virtue of the spectroscopic stability, the sum of the integrated intensities of the $S_1(0)$ and $Q_1(0) + S_0(0)$ lines is not affected by this removal of the degeneracy of the $v = 1$, $J = 2$ level. The total integrated intensity may therefore be calculated with the help of unperturbed wave functions, i.e. in terms of localized vibrational and rotational excitations. The moment corresponding to the molecule at $\mathbf{R}_i$ making the vibrational transition is given by

$$(46) \qquad \mathbf{M}_i = \sum_j{}' \mathbf{M}(\omega_i, \omega_j; \mathbf{R}_{ij}),$$

where the sum runs over all the molecules $j \neq i$, and where the pair moment for $i = 1$, $j = 2$ is given by (43). The matrix elements of the moment (46) corresponding to single transitions are given by

$$(47) \quad \langle \psi_0 | M_{i\kappa} | \varphi_m(\mathbf{R}_i) \rangle = \sum_{\rho=0,\pm1} (-1)^\rho \sum_j{}' D_\rho(2\rho00; R_{ij})\, D^1_{\kappa\rho}(\mathbf{a}_{ij})^* D^2_{m,-\rho}(\mathbf{a}_{ij})^*,$$

where the $D_\rho(2\rho00; R_{ij})$ are the expansion coefficients (44), and the other symbols are defined in eq. (24). The matrix elements corresponding to double transitions are given by

$$(48) \quad \langle \psi_0 | M_{i\kappa} | \varphi_m(\mathbf{R}_j) \rangle = \sum_{\rho=0,\pm1} (-1)^\rho\, D_\rho(2\rho00; R_{ij}) D^1_{\kappa\rho}(\mathbf{a}_{ij})^* D^2_{m,-\rho}(\mathbf{a}_{ij})^*.$$

The characteristic difference between (47) and (48) is that (47) contains a sum of terms over all the neighboring molecules, whereas (48) does not. The parts of the induced dipole moments responsible for the single transitions therefore show interference effects, leading to the cancellation effect, whereas the parts of the moments responsible for the double transitions do not show such inter-

ference effects. The integrated intensities can be calculated from (47) and (48) by performing the same type of calculation as was done in Section 3 for the rotational spectrum. The contribution of the matrix elements (47) to the integrated absorption coefficient per molecule per unit volume is given by

$$(49) \qquad \bar{\alpha}_1 = 5\pi^3 S_1^2 \kappa_1^2 \frac{Q'^2 \alpha^2}{ha^8},$$

where S_1 denotes the lattice sum (29), and $\kappa_1^2 = h/8\pi^2 m\nu_0$, m and ν_0 being the reduced mass and the frequency of the molecular vibration. The contribution of the matrix elements (48) is given by

$$(50) \qquad \bar{\alpha}_2 = 8\pi^3 S_2 \kappa_1^2 \frac{Q^2 \alpha'^2}{ha^8},$$

where S_2 denotes the lattice sum (36). The role of the cancellation effect is clearly displayed by (49) and (50). The intensity (49) due to single transitions is proportional to the square of the lattice sum S_1 which is a small quantity because of a cancellation of terms. The intensity (50) due to double transitions depends on the lattice sum S_2 which is equal to a sum of squared terms and is large. The cancellation effect makes the intensity due to single transitions a factor $8S_2/5S_1^2 \simeq 42$ smaller than it would otherwise have been.

The sum of the integrated intensities of the $S_1(0)$ and $Q_1(0)+S_0(0)$ lines is given by the sum of (49) and (50),

$$(51) \qquad \bar{\alpha}[S_1(0)]+\bar{\alpha}[Q_1(0)+S_0(0)] = \frac{\pi^3 \kappa_1^2}{ha^8}[5S_1^2 Q'^2 \alpha^2 + 8S_2 Q^2 \alpha'^2].$$

This expression is still exact, as far as the calculation of the intensity for given dipole moments is concerned. To calculate the separate intensities of the $S_1(0)$ and $Q_1(0)+S_0(0)$ lines, it is necessary to calculate the wave function describing the relative motion of the vibrational and rotational exciton in the bound state. We do not attempt such a calculation at present, and we introduce the assumption that the rotational excitation in the bound state is completely localized on the vibrating molecule. It is difficult to estimate the accuracy of this approximation as far as the calculation of the intensity is concerned. The energy of the bound state changes by only about 10% when account is taken of the fact that the excitation is not completely localized (cf. II). One might be inclined to think that the spreading out of the wave function of the excitons would strongly affect the intensity of the $S_1(0)$ line, because the transition to the bound state would partly become a double rather than a single transition. However, this is not so, because even in a spread out bound state the rotational motions of the molecules involved would be completely coherent, and the transition would be fully affected by the cancellation effect. The error introduced by our approximation should therefore not be much larger than about 10%. When we assume that the bound states are completely localized, the intensity of the $S_1(0)$ line is given by (49), since the wave functions are then equal to the unperturbed wave functions used in (47). By subtracting (49)

from (51), we see that in the same approximation the expression (50) is equal to the integrated intensity of the $Q_1(0) + S_0(0)$ band. For the constants appearing in (51) we use the following values. For α and α' we use the experimental values, $\alpha = 5.7a_0^3$ and $\alpha' = 4.0a_0^2$. The value of α' is obtained from the average experimental value of the matrix element of the polarizability, $\alpha_{01} = 0.10 \times 10^{-24}$ cm^3 (Terhune and Peters 1959), by means of the relation $\alpha_{01} = \alpha'(h/8\pi^2 m \nu_0)^{\frac{1}{2}}$, where m is the mass of a proton, and ν_0 is the frequency of the 0–1 vibrational transition. For Q we use the theoretical value of James and Coolidge (1938), $Q = 0.45ea_0^2$. The value of Q' has also been calculated by James and Coolidge, and is $Q' = 0.30ea_0$. However, a careful analysis of the intensities of the single and double transitions in the induced vibrational spectrum in gaseous hydrogen, carried out by Hunt (1959), has shown that this value of Q' is too small. The value derived from the intensities in the gas is $Q' = 0.54ea_0$, and we accordingly use this value in our calculations of the intensities in the solid. From (49), (50), and (51) we thus obtain:

$$(52) \quad \begin{cases} \tilde{\alpha}[S_1(0)] + \tilde{\alpha}[Q_1(0) + S_0(0)] = 0.48 \times 10^{-13} \, \text{sec}^{-1} \, \text{cm}^3, \\ \tilde{\alpha}_1 : \tilde{\alpha}_2 = (0.0240)(Q'\alpha/Q\alpha')^2 = 1:14. \end{cases}$$

The value of the total intensity is in satisfactory agreement with the experimental value, which is 0.45×10^{-13} sec^{-1} cm^3 (cf. I). The ratio of the intensities would be 1:46 if the value of Q' of James and Coolidge (1938) were used. The experimental value of this ratio is 1:15, and is in good agreement with the calculated value (52) based on the value of Q' derived from the spectrum in the gas.

The frequency of the $S_1(0)$ infrared line coincides with the frequency (40) of the $S_1(0)$ Raman line in the approximation that the small splitting (42) produced by the crystalline field and the quadrupolar forces is neglected. When this splitting is taken into account, the infrared line shifts by -0.05 cm^{-1} (only the $m = \pm 2$ level is infrared active in absorption, cf. Section 3) whereas the Raman line splits more or less symmetrically about the $m = \pm 2$ level (cf. (42)). Experimentally, the $S_1(0)$ Raman line has not yet been resolved. The center of the line should therefore coincide with the position of the infrared line, and this is what has been observed (cf. I). This result verifies our conclusion that the bound $v = 1$, $J = 2$ excitations do not travel through the lattice and are accordingly not broadened into an energy band.

7. ROTATION–VIBRATIONAL FREQUENCY ANALYSIS

To calculate the shifts produced by the intermolecular forces in the rotation–vibrational frequencies of the molecules, it is necessary to have a consistent set of formulae expressing the rotation–vibrational band constants in terms of the mechanical properties of the molecules. We first discuss free hydrogen molecules. For a given value, J, of the rotational angular momentum the effective potential for the radial motion is given by (cf. Pauling and Wilson 1935)

(53) $U(r) = hc\omega(\tfrac{1}{2}\xi^2 + \lambda_1\xi^3 + \lambda_2\xi^4 + \ldots) + \tfrac{1}{2}hc\omega J(J+1)(-2\lambda^3\xi + 3\lambda^4\xi^2 + \ldots),$

where

(54) $\xi = \dfrac{r - r_e}{l}, \qquad l = \left(\dfrac{\hbar}{m\omega}\right)^{1/2}, \qquad \lambda = \dfrac{l}{r_e}.$

For the low-lying vibrational states l is of the order of magnitude of the ampli-
tude of vibration. The variable ξ is therefore of the order of unity, and λ is the
expansion parameter in the expansion of the rotation–vibrational interaction
arising from the variation of the centrifugal force over the amplitude of
vibration. The constants $\lambda_1, \lambda_2, \ldots$ are the anisotropy constants. Two expansions
are involved in (53), and in principle these two expansions are independent
of each other, i.e. it is possible to have a large anisotropy and a small rotation–
vibrational interaction, or vice versa. In hydrogen the situation is such that
λ_n and λ^n are of the same order of magnitude, so that there is effectively only
one expansion parameter. To conform to standard notation we introduce the
dimensionless anisotropy constants

(55) $a_n = 2\lambda_n/\lambda^n,$

which are of order unity. The non-vanishing band constants appearing in the
various orders λ^n are given in Table I together with their orders of magnitude

TABLE I

Band constants in order λ^n

n	Band constants	cm^{-1}
0	ω_e	10^3
2	$\omega_e x_e, B_e$	10^2
4	$\omega_e y_e, \alpha_e$	1
6	$\omega_e z_e, D_e, \gamma_e$	10^{-2}
8	$\omega_e a_e, \epsilon_e, \beta_e$	10^{-3}
10	$\omega_e b_e, \eta_e, \delta_e, H_e$	10^{-5}

which clearly show the progressive nature of the successive approximations
obtained in this way. For the accuracy required in our work it is necessary to
go to the 6th order involving eight band constants. The quantities ω_e/ω;
$\omega_e x_e/\lambda^2\omega$, $B_e/\lambda^2\omega$; $\omega_e y_e/\lambda^4\omega$, $\alpha_e/\lambda^4\omega$; etc. are power series in ascending powers of
λ^4 starting with terms of order unity, which have been calculated by Dunham
(1932). To obtain a consistent approximation, we should take into account in
these series the terms of order 1 and λ^4. However, to make the analysis not too
involved, we neglect the terms in λ^4 in these series, and in this way we obtain
the following set of relations:

(56)
$$
\begin{cases}
\omega_e = \omega, & \omega_e x_e = \tfrac{3}{4}\lambda^2\omega A_{20}(2), \\[4pt]
B_e = \tfrac{1}{2}\lambda^2\omega, & \omega_e y_e = \tfrac{1}{8}\lambda^4\omega A_{30}(4), \\[4pt]
\alpha_e = \tfrac{3}{2}\lambda^4\omega A_{11}(1), & \omega_e z_e = \tfrac{5}{16}\lambda^6\omega A_{40}(6), \\[4pt]
D_e = \tfrac{1}{2}\lambda^6\omega, & \gamma_e = \tfrac{3}{4}\lambda^6\omega A_{21}(3).
\end{cases}
$$

The quantities $A_{20}(2)$, etc. are algebraic expressions in the anisotropy constants a_n, and the numbers in the parentheses indicate the number of constants involved. We use the experimental values of Stoicheff (1957) for the quantities in the left-hand sides of (56). There is no experimental evidence for a non-vanishing value of $\omega_e z_e$ and we therefore put $\omega_e z_e = 0$. From B_e we obtain

$$(57) \qquad \lambda^2 = 2B_e/\omega_e = 2.765 \times 10^{-2}.$$

The constant $D_e = \frac{1}{2}\lambda^6\omega_e$ is equal to 0.0465 cm^{-1}, whereas the experimental value is 0.0468 cm^{-1}. The constant a_1 can be determined from α_e, a_2 from $\omega_e x_e$, etc., as has been done by Stoicheff (1957), giving

$$(58) \qquad a_1 = -1.598, \qquad a_2 = 1.868, \qquad a_3 = -2.072, \qquad a_4 = 2.261.$$

Because we have restricted ourselves in (56) to the first non-vanishing terms, the values (58) do not represent the true values of the constants a_n, but are chosen such that (56) gives exact values for $\omega_e x_e$, $\omega_e y_e$, α_e, and γ_e.

We now investigate the effect of the terms $f(r_1)+f(r_2)$ appearing in the potential of the intermolecular forces (cf. II, eq. (33)) on the rotational and vibrational properties of the molecules. In the solid these terms give rise to an additional term of the form $U'(r)$ in the potential energy of each molecule. We develop $U'(r)$ in powers of $r-r_e$, giving

$$(59) \qquad U'(r) = -hc\omega(\mu_1\xi+\mu_2\xi^2+\ldots),$$

where $\mu_1, \mu_2, \ldots$ are dimensionless force constants. In the calculation of the effect of (59) on the band constants of the molecule, we retain only the terms linear in μ_1. Eventually it will be necessary to take into account the higher order terms in $\mu_1^2, \mu_2, \ldots$, but for our present work the first approximation linear in μ_1 suffices. Eliminating the term in $U(r)+U'(r)$ linear in $r-r_e$ we find, after some straightforward calculations, the following expressions for the resulting changes in the mechanical constants of the molecules:

$$(60) \qquad \begin{cases} \Delta r_e = \mu_1 l, & \Delta\omega = \dfrac{3}{2}\mu_1\lambda a_1\omega, \\[2mm] \Delta l = -\dfrac{3}{4}\mu_1\lambda a_1 l, & \Delta\lambda = -\mu_1\lambda^2(1+\tfrac{3}{4}a_1), \\[2mm] \Delta a_1 = \mu_1\lambda(a_1-3a_1^2+4a_2), & \Delta a_2 = \mu_1\lambda(2a_2-3a_1a_2+5a_3), \\[2mm] \Delta a_3 = \mu_1\lambda(3a_3-\dfrac{15}{2}a_1a_3+6a_4), & \Delta a_4 = \mu_1\lambda(4a_4-9a_1a_4). \end{cases}$$

The resulting changes in the band constants (56) are readily evaluated, and are given by

$$(61) \qquad \begin{cases} \Delta\omega_e = -1754\mu_1, & \Delta\omega_e x_e = 33.0\mu_1, \\[2mm] \Delta B_e = -20.2\mu_1, & \Delta\omega_e y_e = -61.2\mu_1, \\[2mm] \Delta\alpha_e = 0.695\mu_1, & \Delta\gamma_e = -0.944\mu_1, \\[2mm] & \Delta D_e = 0.0092\mu_1. \end{cases}$$

The value of μ_1 can be determined from the observed frequency of the $S_1(0)$ line and the calculated shift of this line due to the quadrupolar forces (cf. Section 5). This leads to the value $\mu_1 = 4.4 \times 10^{-3}$ used in the preceding sections. A theoretical estimate of μ_1 can be obtained by assuming that the force μ_1 comes from the dispersion forces, and using for the constant C in the potential, $V = -C/R^6$, of these forces the approximate expression (cf. II)

$$(62) \qquad C = \frac{3}{2} \frac{E_1 E_2}{E_1 + E_2} \alpha_1 \alpha_2.$$

The quantity μ_1 is then given by

$$(63) \qquad \mu_1 = (3l/4hc\omega a^6)(E\alpha\alpha' + \tfrac{1}{2}E'\alpha^2) \sum_i{}' (a/R_i)^6,$$

the numerical value of which is equal to about 7×10^{-3}. This value is of the same order of magnitude as the semiempirical value of 4.4×10^{-3}; the discrepancy between the two values may be due to the neglect of the terms in $\mu_1^2, \mu_2, \ldots$ in (61), or to the neglect of the contribution of the overlap forces to the theoretical value (63). We shall, however, not investigate these points here. We remark only that in connection with the frequency analysis discussed here it would be interesting if accurate experimental values for the infrared and Raman frequencies in the overtone region could be obtained.

REFERENCES

ALLIN, E. J., GUSH, H. P., HARE, W. F. J., and WELSH, H. L.   1957.   Phys. Rev. **106**, 1101.
———— 1958.   Nuovo cimento Suppl. **9**, 77.
BHATNAGAR, S. S., ALLIN, E. J., and WELSH, H. L.   1960.   Can. J. Phys. To be published.
DUNHAM, J. L.   1932.   Phys. Rev. **41**, 721.
GUSH, H. P., HARE, W. F. J., ALLIN, E. J., and WELSH, H. L.   1960.   Can. J. Phys. **38**, 176.
HUNT, L. J.   1959.   Ph.D. Thesis, University of Toronto, Toronto, Ontario.
JAMES, H. M. and COOLIDGE, A. S.   1938.   Astrophys. J. **87**, 438.
KEESOM, W. H., DE SMEDTT, J., and MOOY, H. H.   1935.   Commun. Kamerlingh Onnes Lab. Univ. Leiden, **209d**.
KISS, Z. J.   1959.   Ph.D. Thesis, University of Toronto, Toronto, Ontario.
NYBOER, B. R. A. and DE WETTE, F.   1957.   Physica, **23**, 309.
PAULING, L. and WILSON, E. B.   1935.   Introduction to quantum mechanics (McGraw-Hill Book Co., New York).
ROSE, M. E.   1957.   Elementary theory of angular momentum (John Wiley & Sons, Inc., New York).
STOICHEFF, B. P.   1957.   Can. J. Phys. **35**, 730.
TERHUNE, R. W. and PETERS, C. W.   1959.   J. Mol. Spectroscopy, **3**, 138.
VAN KRANENDONK, J.   1955.   Physica, **21**, 749.
———— 1957.   Physica, **23**, 825.
———— 1958.   Physica, **24**, 347.
———— 1959a.   Physica, **25**, 337.
———— 1959b.   Physica, **25**. To be published.
VAN KRANENDONK, J. and KISS, Z. J.   1959.   Can. J. Phys. **37**, 1187.

TRANSITION INTENSITIES AND CONVERSION COEFFICIENTS IN Dy[160] [1]

M. A. Clark

ABSTRACT

K

-

conversion

coefficients for gamma transitions in Dy[160] have been measured

and the transition multipolarities determined as follows (E_γ, α_K, multipolarity):
86.7 kev, 1.5 (E2); 197 kev, 1.6×10^{-1} (E2); 216 kev, 4.0×10^{-2} (E1); 299 kev,
1.3×10^{-2} (E1); 880 kev, 3.1×10^{-3} (E2); (962+966) kev, 2.5×10^{-3} (E2);
1179 kev, 6.6×10^{-4} (E1); 1205 kev, 4.6×10^{-4} (E1); 1273 kev, 6.1×10^{-4} (E1);
1315 kev, 3.9×10^{-4} (E1). Relative transition intensities are compared with the
predictions of the Unified Model of Bohr and Mottelson and the asymmetric
rotor theory of Davydov and Filippov. Transition intensities from the 966-kev
level to members of the ground state rotational band suggest the asymmetric
rotor interpretation.

INTRODUCTION

For some time the unified model of Bohr and Mottelson[2] has received
experimental confirmation in the rotational and vibrational behavior of nuclei.
Nuclei in the mass range $150 < A < 190$ have been of particular interest
since in these occur large departures from spherical symmetry which are such
a striking feature of the collective behavior of the nucleons.

Recently Davydov and Filippov (1958) have taken a somewhat different
point of view regarding the energy levels and transitions in even–even nuclei.
They employ an asymmetric rotor model of the nucleus in which the condition
of axial symmetry inherent in the unified model has been relaxed. Rotational
states on this model give levels in even–even nuclei which include positive-
parity states described by the unified model as γ-vibrations. Some experimental
evidence has appeared in support of their theory (Van Patter 1959; Mac-
Donald 1959; DeMille et al. 1959). Considerable agreement is found with their
predictions of transition intensities from the first and second 2+ excited states
in even–even nuclei over a wide range of atomic masses. This agreement is
quite good well outside the mass region where large nuclear distortions are
found.

The beta decay of Tb[160] feeds levels in Dy[160] well above the ground state
and results in a large number of gamma rays which cascade through levels in
Dy[160], making possible interesting tests of the theories.

Many workers have studied the Tb[160] beta decay.[3] The present paper
describes the measurement of transition intensities and conversion coefficients
in Dy[160] which have previously been reported only very briefly (Clark and
Knowles 1957). Some evidence is found which favors the asymmetric rotor
theory.

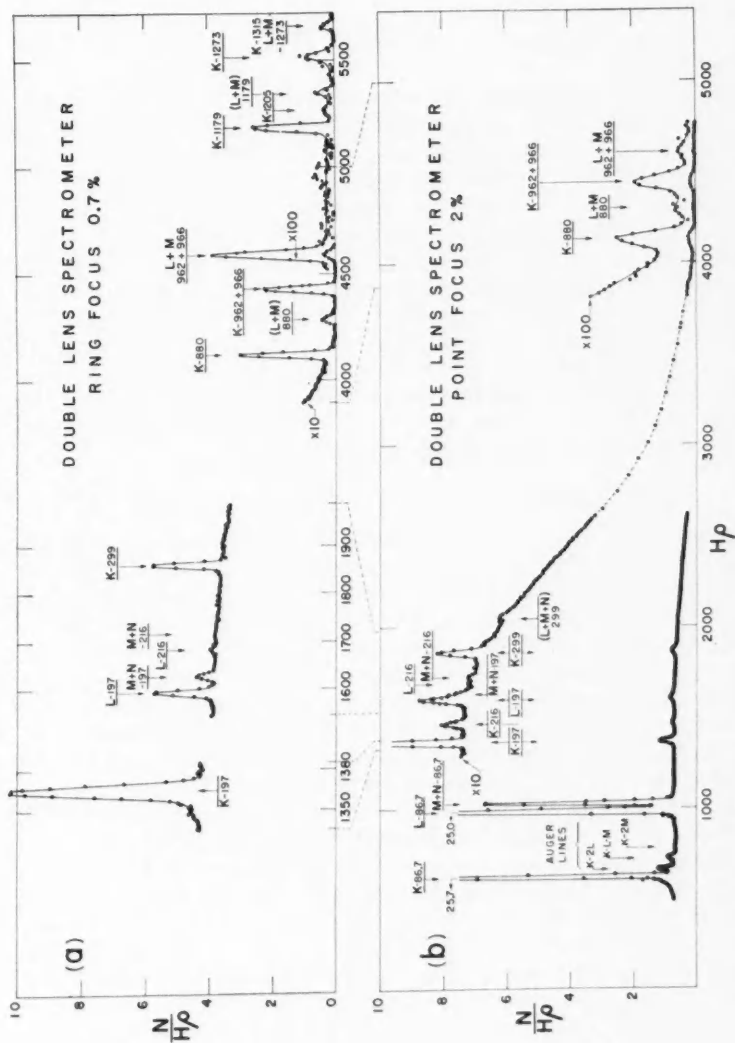
Figs. 1(a) and 1(b). Conversion-electron spectra in the decay of Tb[160]. Counting errors are smaller than the plotted points except in the region of high momentum where an obvious scatter in the background shows the statistical fluctuations.

CONVERSION-ELECTRON MEASUREMENTS

Sources for the study of conversion electrons were prepared by irradiating milligram quantities of terbium oxide in the NRX reactor to about 150 curies/g specific activity and subliming a portion of this material under vacuum onto 200 microgram/cm^2 aluminum foils through holes 1 to 3 mm in diameter.

Studies of the conversion-electron spectrum were made using two magnetic electron spectrometers: a conventional lens spectrometer operated at 2% resolution (Bell and Graham 1952) and a ring-focus double-lens spectrometer operated at 0.7% resolution (Elliott *et al.* 1954). Typical results are shown in Figs. 1(a) and 1(b). Conversion-line intensities after decay corrections are given in Table I. In the case of the K 86.7-kev line, whose energy is 33 kev, corrections for absorption in the 200 microgram/cm^2 foil covering the stilbene scintillation detector and for the pulse height distribution in the latter amounted to about 17% in magnitude. The absorption and pulse-height-distribution corrections were determined as a function of momentum by a study of the counter pulse height distributions for various spectrometer settings down to 15 kev with and without an extra 200 microgram/cm^2 foil over the counter. For all other conversion lines these corrections were less than a few per cent in magnitude.

GAMMA-RAY INTENSITY MEASUREMENTS

Gamma-ray relative intensities were measured by means of a 2 in. by 2 in. NaI(Tl) scintillation detector, a curved-crystal gamma-ray spectrometer, and the ring-focus electron spectrometer with Pb and U photoelectric converters.

Figure 2(a) shows the gamma-ray spectrum of Tb^{160} obtained using the NaI scintillation detector optically coupled to an RCA 6342 photomultiplier whose output was displayed on an Atomic Instrument 20-channel pulse height analyzer. The latter was operated with a biasing arrangement to study 100 separate pulse height channels, 20 at a time. For the gamma-ray measurement a beta source used for the conversion measurements was employed, the beta rays and conversion electrons being stopped by 1/4 in. of lucite. The source and lucite were placed 9 inches from the detector, and a conical collimator allowed gamma rays to strike only the front face of the NaI crystal. The arrangement was carefully calibrated for the variation with energy of the pulse height spectrum shape due to monoenergetic gamma rays. This calibration employed sources of Hg^{203} (279 kev), Au^{198} (411 kev), Cu^{64} (511 kev), Cs^{137} (662 kev), Zn^{65} (1119 kev), and Na^{22} (511 and 1277 kev). Absorption corrections were required for the lucite beta-ray absorber, the aluminum crystal cover, and the magnesium oxide layer over the NaI crystal. These corrections were 10% or less in magnitude for all but the 86.7-kev gamma ray (21%) and the K X rays (40%). The intensity ratio obtained for the 511- and 1277-kev gamma rays from the Na^{22} calibration source, after all corrections, was 1.77±.12 with all errors included. Various workers have measured the electron-capture-to-positron-decay ratio for Na^{22} (Strominger *et al.* 1958) from which one derives

a gamma-ray ratio $1.78\pm.02$. The agreement here is well within the estimated error of 7% in our measurement. The fitting of the more complex Tb^{160} spectrum introduces further error, and the final gamma-ray intensities are considered to be known to about 15%. This figure is intended to represent a standard deviation taking into account systematic errors.
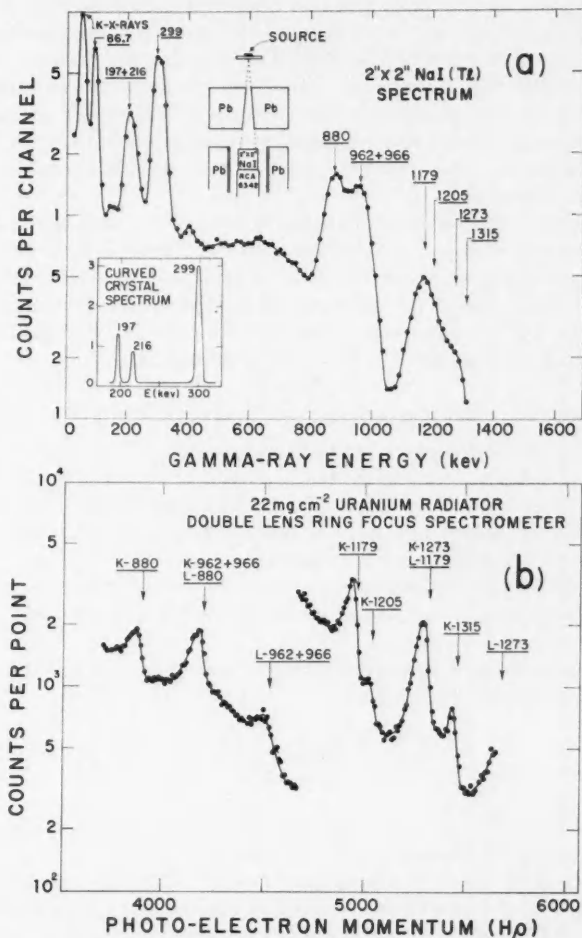
FIG. 2. (a) The gamma-ray spectrum of Tb^{160} obtained with a 2 in. $\times$ 2 in. NaI(Tl) scintillation spectrometer. Except where shown, errors are smaller than the plotted points. The inset shows a portion of the spectrum as observed with a curved-crystal gamma-ray spectrometer.

(b) A portion of the photoelectron spectrum of the gamma rays of Tb^{160} obtained from a 22 mg/cm² uranium radiator. Total counts per point are plotted as ordinate.

A number of the intense gamma-ray peaks were not well separated in the NaI crystal spectrum. Accordingly their relative intensities were determined using instruments of higher resolution over more limited ranges of energy.

The high-energy gamma-ray relative intensities were studied by means of photoelectrons ejected from 2-mm diameter radiators of uranium and lead 22 mg/cm^2 and 20 mg/cm^2 thick, respectively. A Tb^{160} source of about 5-mc strength was used, and the beta rays and conversion electrons were absorbed by about 500 mg/cm^2 copper placed between the source and the radiators. The Co^{60} gamma rays of energies 1172 kev and 1332 kev span the region of interest rather well, and therefore a 5-mc source of Co^{60} was used with the same radiators to check the variation of photoelectron intensity with energy. Figure 2(b) shows the photoelectron spectrum obtained with the uranium radiator. Results of the measurements with both uranium and lead radiators were combined to get relative intensities.

Measurements of the relative intensities of the gamma rays below 300 kev in energy were also made using a 100-mc source of Tb^{160} and a curved-crystal gamma-ray spectrometer (Knowles 1957; Clark and Knowles 1957) (see insert in Fig. 2(a)). One of the main results of these quartz-crystal measurements was the relative intensity of the 197-kev and 216-kev gamma rays which were unresolved in the 2 in.×2 in. NaI spectrometer.

K-CONVERSION COEFFICIENTS AND GAMMA-RAY MULTIPOLARITIES

K-conversion coefficients were obtained as follows:

(a) K-conversion-line intensities were normalized to the total number of K-shell vacancies created (i.e. ΣI_K). The curved-crystal gamma-ray spectrometer revealed no low-energy gamma rays of appreciable intensity whose K-conversion lines would have been missed.

(b) The gamma-ray intensities were also normalized to the number of K-shell vacancies (i.e. $I_{K\,X\,ray}/\omega_F$ where ω_F is the fluorescent yield for the K shell).

(c) K-conversion coefficients were then obtained by taking the ratios of these normalized intensities; thus

$$\alpha_K = \frac{I_K}{I_\gamma} \cdot \frac{I_{K\,X\,ray}}{\omega_F \cdot \Sigma I_K}.$$

The value of ω_F for Dy ($Z = 66$) is 0.926 (Wapstra et al. 1959). The error in this value is negligible compared with our intensity errors.

Table I contains the K-conversion-coefficient values, the errors being a combination of the errors in the various intensities already discussed. For comparison of the results with theoretical conversion coefficients we plot in Fig. 3 the experimental coefficients as well as the curves for E1, E2, and M1 transitions from the work of Sliv (1958). The calculations of Rose (1958) give substantially identical results in this case. The lowness of the experimental points in the high-energy region suggests a possible systematic error of the

TABLE I

E_γ	I_γ (per dis.)*	I_K (per dis.)†	I_L (per dis.)†	I_{M+N} (per dis.)†	Total I (per dis.), %	α_K§	Multipolarity
K X rays	2.0(-1)						
86.7	1.37(-1)	2.06(-1), 10%	3.04(-1)	9.5(-2)	74	1.5(0), 21%	E2
197	4.5(-2)	7.4(-3)	3.16(-3)	8.2(-4), 7%	5.6	1.6(-1), 20%	E2
216	3.5(-2)	1.4(-3)	1.4(-4), 22%		3.7	4.0(-2), 20%	E1
299	2.7(-1)	3.5(-3)	~6(-4), 20% ($L+M+N$)		27	1.3(-2), 20%	E1
393	~1(-2)	~2.2(-4)			~1	<2(-2)	E1(E2)
765	<√2 2(-2)	—			—		
880	3.06(-1)	9.4(-4)			31	3.1(-3)	E2
962 ‡	1.1(-1) } ‡3.58(-1)	2.7(-4) } ‡9.1(-4)			11	2.5(-3), 20%	E2
966 }	2.5(-1) }	6.4(-4) }			26	2.6(-3), 20%	E1
1179	1.56(-1)	1.03(-4), 7%			15.6	6.6(-4), 20%	E1
1205	2.6(-2)	1.2(-5), 35%			2.6	4.6(-4), 40%	E1
1273	8.5(-2)	5.2(-5), 10%			8.5	6.1(-4), 20%	E1
1315	3.4(-2)	1.3(-5), 35%			3.4	3.9(-4), 40%	E1

*Errors in gamma-ray intensities, as discussed in the text, are considered to be less than about 15%. The numbers in parentheses give powers of 10.

†Errors shown are for cases limited in accuracy primarily by counting statistics. The remaining intensities are considered to be known to about 5%. We estimate in addition an error of about 10% in the determination of the area under the continuous beta-ray spectrum, including scattering effects in the spectrometer. The errors in the conversion-line intensities should be combined with this 10% error to obtain errors in absolute intensity.

‡These lines were not separated in this work. They have been split up by means of ratios obtained from the work of Bäckström et al. (1959) for the gamma rays and Ewan et al. (1959) for the conversion lines.

§Errors in the K-conversion coefficients include errors in the gamma-ray intensities, the conversion-line intensities, and in the K X-ray intensity. The error in fluorescent yield is negligible in comparison.
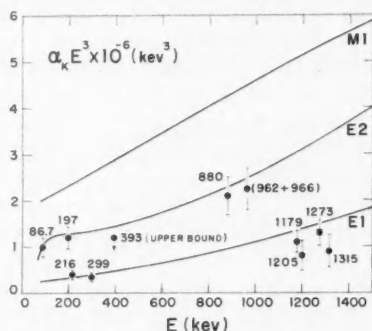
Fig. 3. K-conversion coefficients for Dy[160] transitions compared with theoretical coefficients due to Sliv (1958). Note that in the ordinate an E^3 dependence has been removed for convenience.

order of 10% in the data. There is no ambiguity regarding multipole assignments (except for the 393-kev transition where only a limit is available) and the assignments are listed in Table I. The (962+966)-kev gamma-ray intensity has been split up by means of the relative intensities of Bäckström et al. (1959). The (962+966)-kev K-conversion intensity has been split up by means of the relative intensities of Ewan et al. (1959). The two transitions have the same value of α_K within the errors. No evidence for $M1$ or $M2$ admixture can be found in any of the conversion coefficients within the accuracy of the measurements. The assignments are in agreement with those of Nathan (1957) with the exception of the 1205-kev and 1315-kev transitions which he did not observe. They have, however, been studied by Bäckström et al. (1959), whose results agree with the $E1$ assignments determined here.

LEVEL ASSIGNMENTS AND TRANSITION INTENSITIES

The transitions studied in this work can be placed unambiguously in the level scheme shown in Fig. 4, which is consistent with the work of both Nathan and Bäckström. Recently Ewan et al. (1959) have obtained powerful independent evidence for this level scheme primarily on the basis of high-precision measurements of conversion-line momenta. The spin and parity assignments follow from the observed multipolarities and the gross features of the relative transition intensities.

The levels at 86.7 kev and 284 kev, as pointed out by many investigators, have all the properties of a rotational band based on the ground state.

Transition intensities from the $2+$ level at 966 kev to the ground state band have been discussed previously (Nathan 1957; Clark and Knowles 1957; Grigorev et al. 1958) in terms of the unified model. We have re-evaluated the reduced transition probabilities since our previous publication (Clark and Knowles 1957) taking into account the presence of the two transitions of 962 kev and 966 kev as mentioned above. Assuming pure $E2$ radiation for the 966-kev transition, the theoretical conversion coefficient, and our absolute

LEVELS IN Dy^{160}
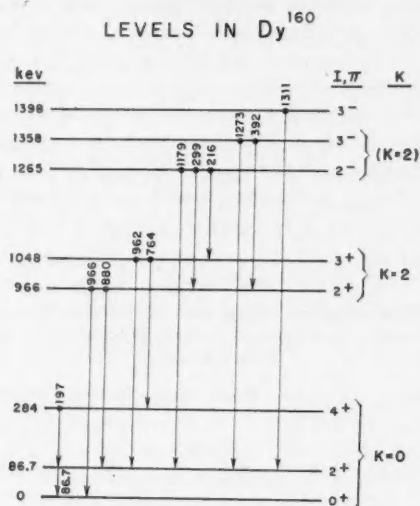
FIG. 4.   Level scheme of Dy160 (Nathan 1957; Bäckström et al. 1959; Ewan et al. 1959).

TABLE II

Gamma-ray transitions from the 966-kev level

E_γ, kev	Transition	Relative reduced $E2$ transition probabilities				
		$K = 0$	$K = 2$	Asymmetric rotor	This expt.	Nathan expt.
966	$2+ \rightarrow 0+\ (E2)$	1	1	1	1	1
880	$2+ \rightarrow 2+\ (E2)$	1.43	1.43	1.9	1.9 ± 0.3	2.4
682	$2+ \rightarrow 4+\ (E2)$	2.57	.07		$<0.09^*$	0.012

*Limit obtained from 2 in. × 2 in. NaI spectrometer.

conversion-line intensity as split up according to the high-resolution results of Ewan et al. we obtain the reduced transition probabilities given in Table II. Here the error is conservative, as systematic errors should be small in the measurement of relative intensities separated only 10% in energy. There is clearly a fair agreement with the unified model based on a $K = 2$ assignment for the 966-kev level. However, a discrepancy exists which seems outside experimental error.

In the same table are listed theoretical values based on the asymmetric rotor theory (Davydov and Filippov 1958). In this the condition of axial symmetry (inherent in the unified model) has been relaxed. The agreement of our experimental result with the prediction of the asymmetric rotor theory is rather good. Van Patter (1959) in a survey of similar transitions over a wide range of nuclides has listed considerable evidence supporting this theory of Davydov and Filippov.

Transitions from the 1048-kev level are rather weak, and our data on these are meager. As already described, the intensity of the 962-kev transition has been derived from the conversion intensities of Ewan *et al.* at high resolution, taking into account the relative gamma intensities measured by Bäckström. The 764-kev transition to the 4+ state was observed in the analysis of the 2 in.×2 in. NaI scintillation-counter data, but its intensity is known from this only within about a factor of two. In Table III are the predictions of the unified model for a $K = 2$ assignment as well as our experimental results and those of Nathan. A value of 2 for K seems reasonable from these data.

TABLE III

Gamma-ray transitions from the 1048-kev level

E_{γ}, kev	Transition	Relative reduced $E2$ transition probabilities				
		$K_i = 1$	$K_i = 2$	$K_i = 3$	This expt.	Nathan expt.
	$I_i \rightarrow I_f$ K_f					
962	3+ → 2+ 0	1	1	1	1	1
765	3+ → 4+ 0	2.5	0.4	0	$.25^{+.3}_{-.1}$	0.77

The $E1$ transitions from the 1265-kev level to the 966-kev and 1048-kev levels are of interest since the latter two appear to satisfy the requirements of members of a $K = 2$ vibrational band. In Table IV we present the relative reduced transition probabilities as predicted by the unified model for both

TABLE IV

Gamma-ray transitions from the 1265-kev level

E_{γ}, kev	Transition	Relative reduced $E1$ transition probabilities			
		$K_i = 1$	$K_i = 2$	This expt.	Nathan expt.
	$I_i \rightarrow I_f$ K_f				
299	2− → 2+ 2	1	1	1	1
216	2− → 3+ 2	2	0.5	0.34±0.07	0.38
1179	2− → 2+ 0			0.01±0.002	0.009*

*Derived from conversion-line intensities and assuming pure $E1$ radiation.

$K = 1$ and $K = 2$, assuming $K = 2$ for the final levels in both cases. Our experimental results are given, as well as those of Nathan. There is not complete agreement with the theoretical values, but an assignment of $K = 2$ is highly favored over $K = 1$. The transition probability for the 1179-kev gamma ray (Table IV) shows a retardation of at least 80/1 over the 299-kev gamma ray, which supports the $K = 2$ assignment, since for $\Delta K = 2$ the 1179-kev ($E1$) transition is K-forbidden. An assignment of $K = 0$ is thus also ruled out for the 1265-kev level, since in this case the transition would be allowed by the K-selection rules.

DISCUSSION

The transitions in Dy¹⁶⁰ support to a considerable degree the unified-model description of rotational and vibrational levels in even–even nuclei. The ground state ($K = 0$) rotational band is clearly established. The levels (966, 2+) and (1048, 3+) appear from our data to form members of a $K = 2$ gamma-vibrational band, though the evidence for $K = 2$ for the 1048-kev level is not entirely conclusive. It is more definite than from the results of Nathan (1957), who first suggested this possibility. Nathan also proposed that the (1265, 2−) and (1358, 3−) levels are members of an octupole band ($K = 2$). Such a $K = 2$ assignment for the 1265-kev level seems likely from our intensity data. We have no evidence for the K value of the (1398 kev, 3−) level. Bäckström et al. (1959) have given transition intensities from the 1398-kev level to the 2+ and 4+ levels in the ground state band which support for the former an assignment $K = 0$.

Possible differences from the predictions of the unified model do appear. The transition intensities from the 966-kev level favor the asymmetric rotor theory of Davydov and Filippov (1958). The $E1$ transition intensities from the 1265-kev level differ from the $K = 2$ predictions outside the experimental error and Nathan's results suggest the same discrepancy. Regardless of the validity of the asymmetric rotor theory, it would seem that we have evidence for the partial failure of K as a good quantum number in vibrational excitations. Further tests of this point would be interesting, and would require accurate intensities for some of the weaker transitions.

REFERENCES

ALDER, K., BOHR, A., HUUS, T., MOTTELSON, B., and WINTHER, A. 1956. Revs. Modern Phys. **28**, 432.
BÄCKSTRÖM, G., LINDSKOG, J., BERGMAN, O., BASHANDY, E., and BÄCKLIN, A. 1959. Arkiv Fysik, **15**, 121.
BELL, R. E. and GRAHAM, R. L. 1952. Phys. Rev. **86**, 212.
CLARK, M. A. and KNOWLES, J. W. 1957. Bull. Am. Phys. Soc. Ser. II, **2**, 231.
DAVYDOV, A. S. and FILIPPOV, G. F. 1958. J. Exptl. Theoret. Phys. (U.S.S.R.) **35**, 440.
DE MILLE, G. R., KAVANAGH, T. M., MOORE, R. B., WEAVER, R. S., and WHITE, W. 1959. Can. J. Phys. **37**, 1036.
ELLIOTT, L. G., PRESTON, M. A., and WOLFSON, J. L. 1954. Can. J. Phys. **32**, 153.
EWAN, G. T., GRAHAM, R. L., and GEIGER, J. S. 1959. Bull. Am. Phys. Soc. Ser. II, **4**, 292, and unpublished results.
GRIGOREV, E. P., DZHELEPOV, B. S., ZOLOTAVIN, A. V., KRAFT, O. E., KATSIK, B., and PEKER, L. 1958. Bull. acad. U.S.S.R. **22**, 101.
KNOWLES, J. W. 1957. Gamma ray crystal spectroscopy. Atomic Energy of Canada Limited Report No. GPI-42.
MACDONALD, N. 1959. Nuclear Phys. Submitted.
NATHAN, O. 1957. Nuclear Phys. **4**, 125.
ROSE, M. E. 1958. Internal conversion coefficients (North-Holland Pub. Co., Amsterdam).
SLIV, L. A. and BAND, I. M. 1958. Tables of internal conversion coefficients (Academy of Science U.S.S.R. Press, Moscow).
STROMINGER, D., HOLLANDER, J. M., and SEABORG, G. T. 1958. Revs. Modern Phys. **30**, 585.
VAN PATTER, D. M. 1959. Bull Am. Phys. Soc. Ser. II, **4**, 233.
WAPSTRA, A. H., NIJGH, G. J., and VAN LIESHOUT, R. 1959. Nuclear spectroscopy tables (North-Holland Pub. Co., Amsterdam).

THE SCATTERING OF A PLANE WAVE BY A
ROW OF SMALL CYLINDERS[1]

R. F. MILLAR

ABSTRACT

Consideration is given to the scattering of a plane wave by N cylinders equi-spaced in a row. The problems associated with scatterers, both "soft" and "hard" in the acoustical sense, are treated. An application of Green's theorem together with the appropriate boundary condition on the cylinders leads to a set of simultaneous integral equations in the unknown function on the cylinders.

Solutions in the form of series in powers of a small parameter δ (essentially the ratio of cylinder dimension to wavelength) are assumed. In the case of elliptic cylinders, the integral equations are reduced to sets of linear algebraic equations. Only for the first term in the solution for "soft" cylinders is it necessary to solve N simultaneous equations in N unknowns; all other equations involve essentially only one unknown. Far-fields and scattering cross sections are calculated. The case of two "soft" cylinders is given particular attention.

Conditions for justification of the neglect of higher-order terms are discussed. It is found that all terms but the first (in either problem) may be neglected if $\delta \ll 1$ and $(N-1)/(ka)$ is sufficiently small. (Here a is the spacing between centers of adjacent cylinders, and k is the wave number.) For this reason these solutions are most useful when the number of cylinders is small.

INTRODUCTION

The scattering of plane waves by cylinders has been the subject of many investigations. Most of the recent advances in this connection have been made by Twersky (1952) and Karp (1955), who consider the effects of inter-action between cylinders, although from somewhat different points of view. The solution given by Karp is subject to the restriction that the minimum spacing between cylinders is very much greater than the wavelength and cross-sectional dimensions of the cylinders, and requires knowledge of the solution for an isolated cylinder of similar form. Twersky's method of solution, although in theory quite general, is of most practical importance when the cylinder spacing is very much greater than the wavelength.

The perturbation method to be presented here has been employed in one form or another by several authors, but so far as is known, not to problems in multiple scattering. The formulation of the problem is similar to that presented by Row (1955), but the methods of solution differ. Although this type of analysis is also applicable in the study of scattering by small, three-dimensional objects, only the two-dimensional problems associated with perfectly "hard" or "soft" scatterers (or their electromagnetic analogues) will be considered. In order to further simplify the analysis, it is assumed that the cylinders (finite in number) form a grating, with equal spacing between elements, although neither restriction is essential. The wavelength

is of necessity much greater than the cross-sectional dimensions of the cylinders, but the separation between scatterers is not necessarily much greater than the wavelength.

The boundary condition assumed on the cylinders is the vanishing of either (1) the total wave function (u), or (2) its normal derivative $(\partial u/\partial n)$. An application of Green's theorem leads in each problem to a set of simultaneous integral equations for the unknown distributions on the cylinders. In both cases, the integral equations are reduced to linear algebraic equations when the assumption is made that the unknowns may be expanded in series in powers of a small parameter (δ) which involves the ratio of cylinder dimension to wavelength (see, for example, Bouwkamp 1953, where diffraction by a narrow slit is treated in this manner). Analytic evaluation of the first terms is carried out for the case of identical cylinders of elliptical section, of which circular cylinders and strips are particular examples. The scattering cross sections of the structure are found, and certain special cases are considered.

When the normal derivative of the wave function vanishes on the cylinders, it is found that, to a first approximation, each cylinder scatters independently of the others, but interaction effects are apparent even in the first approximation when the wave function vanishes on the cylinders.

<div align="center">PROBLEM (1): $u = 0$ ON THE CYLINDERS</div>

Derivation of the Integral Equations

Let the cylinders be arranged so that their generators lie parallel to the x axis of a rectangular Cartesian co-ordinate system (see Fig. 1). At the moment, the shapes of the cylinders will be unspecified, but it is assumed that some point interior to each, termed the center, lies on the positive y axis, with the origin of co-ordinates situated at the center of the first cylinder C_1. The center of the νth cylinder, C_ν, has co-ordinates $[(\nu-1)a, 0]$ in the (y,z) system. Here a is the distance between centers of successive scatterers, and the subscript ν runs from 1 to N, where N is the number of cylinders.

Let the total wave function be $u = u^1 + u^s$ where $u^1 = e^{ik(y\cos\alpha + z\sin\alpha)}$ is the incident plane wave whose propagation vector makes an angle α with the
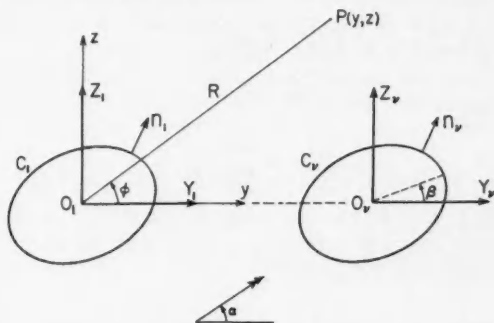

FIG. 1. Geometrical configuration of cylinders, and symbols employed in the analysis.

positive y axis, and u^s is the scattered field which satisfies an appropriate radiation condition. (The time-dependence factor $e^{i\omega t}$ is understood to multiply all field quantities.)

If $P(y,z)$ is a point exterior to $C_1, C_2, \ldots C_N$ then, since $(\nabla^2 + k^2)u^s(P) = 0$, an application of Green's theorem in the region bounded by the contours $C_1, C_2, \ldots C_N$, a small circle C_P about P, and a large circle C_0 enclosing C_P, $C_1, \ldots C_N$ leads to the following expression for $u^s(P)$:

$$(1) \qquad u^s(P) = \frac{i}{4} \sum_{\nu=1}^{N} \int_{C_\nu} \left[u^s \frac{\partial}{\partial n_\nu} H_0^{(1)}(kr_\nu) - H_0^{(1)}(kr_\nu) \frac{\partial u^s}{\partial n_\nu} \right] ds_\nu,$$

where n_ν is the unit normal drawn outward from C_ν and r_ν is the distance from P to the point of integration on C_ν. The integral along C_0 becomes vanishingly small as C_0 recedes to infinity.

Since $u^s = -u^i$ on C_ν,

$$(2) \qquad u^s(P) = -\frac{i}{4} \sum_{\nu=1}^{N} \int_{C_\nu} \left[u^i \frac{\partial}{\partial n_\nu} H_0^{(1)}(kr_\nu) + H_0^{(1)}(kr_\nu) \frac{\partial u^s}{\partial n_\nu} \right] ds_\nu.$$

If, now, P tends to a point P_Λ on the λth cylinder, then in a similar manner it may be shown that

$$(3) \qquad \sum_{\nu=1}^{N} \int_{C_\nu} H_0^{(1)}(kr_{\nu\Lambda}) \chi_\nu ds_\nu = -4iu^i(P_\Lambda) - \sum_{\nu=1}^{N} \int_{C_\nu} H_0^{(1)}(kr_{\nu\Lambda}) \frac{\partial u^i}{\partial n_\nu} ds_\nu,$$

where $\Lambda = 1, 2, \ldots N$, and $\chi_\nu \equiv \partial u^s / \partial n_\nu$. Here, and in future, an upper case Greek subscript will refer to a fixed point on the corresponding cylinder. Thus $r_{\nu\Lambda}$ is the distance between a fixed point on C_λ and a point of integration on C_ν. In the derivation of equations (3), use has been made of the following relationships in order to eliminate normal derivatives of Hankel functions:

$$\int_{C_\nu} \left[u^i \frac{\partial}{\partial n_\nu} H_0^{(1)}(kr_{\nu\Lambda}) - H_0^{(1)}(kr_{\nu\Lambda}) \frac{\partial u^i}{\partial n_\nu} \right] ds_\nu = \begin{cases} 2iu^i(P_\Lambda) & \nu = \lambda, \\ 0 & \nu \neq \lambda. \end{cases}$$

The equations (3) form a set of N simultaneous integral equations in the unknowns χ_ν. At least two methods of approach to their solution appear feasible. Although only one of these will be employed here, an outline of the alternative seems worth while. This may be found in the Appendix.

Let it be assumed that

$$(4) \qquad b\chi_\nu = \sum_{n=0}^{\infty} a_n^\nu \delta^n,$$

where $\delta = kb \ll 1$, and b is a characteristic dimension of the cylinder. For $\nu = \lambda$, the Hankel function appearing in equations (3) may be written (see for example, Bouwkamp 1953) as

$$(5) \qquad H_0^{(1)}(kr_{\lambda\Lambda}) = H_0^{(1)}(\delta R_{\lambda\Lambda}) = \frac{2i}{\pi} \left(\psi_0 + \psi_1 \delta^2 + \psi_2 \delta^4 + \ldots \right),$$

where

$$(6) \quad \begin{cases} \psi_0 = p + \log |2R_{\lambda\lambda}|, \\[2mm] \psi_n = \dfrac{(-1)^n R_{\lambda\lambda}^{2n}}{2^{2n}(n!)^2}\left(p - 1 - \tfrac{1}{2}\ldots - \dfrac{1}{n} + \log |2R_{\lambda\lambda}|\right), \qquad n > 0, \\[2mm] p = \log\left(\dfrac{\gamma\delta}{4}\right) - i\dfrac{\pi}{2}, \end{cases}$$

and $\log \gamma = 0.5772157\ldots$ is Euler's constant.

If, on the other hand, (y_ν, z_ν) are co-ordinates of a point on C_ν, then

$$y_\nu = (\nu-1)a + bY_\nu, \qquad z_\nu = bZ_\nu,$$

where (Y_ν, Z_ν) are normalized co-ordinates with origin O_ν at the center of C_ν (see Fig. 1). When $\nu \neq \lambda$, the first terms in the Taylor series for $H_0^{(1)}(kr_{\nu\Lambda})$ about $\delta = 0$ are

$$(7) \quad H_0^{(1)}(kr_{\nu\Lambda}) = H_0^{(1)}(|\nu-\lambda|ka) - \epsilon_{\nu\lambda} H_1^{(1)}(|\nu-\lambda|ka)(Y_\nu - Y_\lambda)\delta + O(\delta^2),$$

where

$$(8) \quad \epsilon_{\nu\lambda} = \begin{cases} 1 & \nu > \lambda, \\ -1 & \nu < \lambda. \end{cases}$$

Since $H_0^{(1)}(kr_{\nu\Lambda})$ is, for $\nu \neq \lambda$, an analytic function of δ except when $kr_{\nu\Lambda} = 0$, it is easily shown that the series (7) is convergent if $|\nu-\lambda|a > b[(Y_\nu - Y_\lambda)^2 + (Z_\nu - Z_\Lambda)^2]^{\frac{1}{2}}$. In particular, if d_ν is the minimum diameter of the circle centered at O_ν and circumscribing C_ν, $\nu = 1, 2, \ldots N$, and if $d = \underset{\nu=1,2,\ldots N}{\text{Max.}}\ d_\nu$, then the series (7) is convergent if $a > d$. The convergence is rapid when $a \gg d$, and becomes progressively slower as a approaches d.

If $u^1(P_\Lambda)$ is written in the form

$$(9) \quad u^1(P_\Lambda) = \sum_{n=0}^{\infty} u_n^1(P_\Lambda)\delta^n,$$

and the coefficients A_n^Λ are defined by the relationship

$$(10) \quad -4i\, u^1(P_\Lambda) - \sum_{\nu=1}^{N}\int_{C_\nu} H_0^{(1)}(kr_{\nu\Lambda})\frac{\partial u^1}{\partial n_\nu}\,ds_\nu = \sum_{n=0}^{\infty} A_n^\Lambda \delta^n,$$

then, since $u_0^1(P_\Lambda)$ is independent of P_Λ (and so $A_0^\Lambda = -4i\,u_0^1(P_\Lambda)$), the following equations are satisfied by a_0^ν:

$$(11) \quad \frac{2i}{\pi b}\int_{C_\lambda} a_0^\lambda \psi_0(\lambda, \Lambda)\,ds_\lambda + \frac{1}{b}\sum_{\nu\neq\lambda} H_0^{(1)}(|\nu-\lambda|ka)\int_{C_\nu} a_0^\nu ds_\nu = -4i\,u_0^1(P_\Lambda),$$
$$\lambda, \Lambda = 1, 2, \ldots N.$$

The equating of terms of order δ leads to a similar set of equations for a_1^ν. Because

$$\frac{\partial u_0^1}{\partial n_\nu} = 0,$$

$$(12) \quad \sum_{\nu \neq \lambda} \int_{C_\nu} \left[H_0^{(1)}(|\nu - \lambda|ka) \frac{\partial u_1^1}{\partial n_\nu} - \epsilon_{\nu\lambda} H_1^{(1)}(|\nu - \lambda|ka)(Y_\nu - Y_\lambda) \frac{\partial u_0^1}{\partial n_\nu} \right] ds_\nu$$

$$= \sum_{\nu \neq \lambda} H_0^{(1)}(|\nu - \lambda|ka) \int_{C_\nu} \frac{\partial u_1^1}{\partial n_\nu} ds_\nu.$$

Since u_1^1 is a solution of the Laplace equation, the integral on the right-hand side of equation (12) may be shown to vanish for all ν; therefore

$$(13) \qquad A_1^\Lambda = -4i\, u_1^1(P_\Lambda) - \frac{2i}{\pi} \int_{C_\lambda} \psi_0(\lambda, \Lambda) \frac{\partial u_1^1}{\partial n_\lambda} ds_\lambda,$$

and

$$(14) \quad \frac{2i}{\pi b} \int_{C_\lambda} a_1^\lambda \psi_0(\lambda, \Lambda) ds_\lambda + \frac{1}{b} \sum_{\nu \neq \lambda} H_0^{(1)}(|\nu - \lambda|ka) \int_{C_\nu} a_1^\nu ds_\nu$$

$$= -4i\, u_1^1(P_\Lambda) - \frac{2i}{\pi} \int_{C_\lambda} \psi_0(\lambda, \Lambda) \frac{\partial u_1^1}{\partial n_\lambda} ds_\lambda + \frac{1}{b} \sum_{\nu \neq \lambda} \epsilon_{\nu\lambda} H_1^{(1)}(|\nu - \lambda|ka)$$

$$\times \int_{C_\nu} (Y_\nu - Y_\Lambda) a_0^\nu ds_\nu, \qquad \lambda, \Lambda = 1, 2, \ldots N.$$

The similarity between the left-hand sides of equations (11) and (14) is at once evident; this is a characteristic of the integral equations for terms of all orders.

In order to proceed further, it appears necessary to be more specific in regard to the shape of the cylinders. In the following section, the coefficients a_0^ν, a_1^ν will be determined for identical cylinders of elliptical form, with particular attention being given to the case $N = 2$.

Solution of the Integral Equations for Elliptic Cylinders

To determine the functions a_0^ν, a_1^ν for elliptic cylinders, it is first necessary to find a suitable representation for $\psi_0(\lambda, \Lambda)$. If a point has Cartesian co-ordinates (y, z) with respect to O_1, then the transformation to elliptic co-ordinates (μ_ν, θ_ν) with respect to O_ν is (see Fig. 1)

$$y = (\nu - 1)a + b(\cosh \mu_\nu \cos \theta_\nu \cos \beta - \sinh \mu_\nu \sin \theta_\nu \sin \beta),$$
$$z = b(\cosh \mu_\nu \cos \theta_\nu \sin \beta + \sinh \mu_\nu \sin \theta_\nu \cos \beta),$$

and a point on C_ν is determined by (Y_ν, Z_ν) where

$$(15) \qquad \begin{cases} Y_\nu = \cosh \mu \cos \theta_\nu \cos \beta - \sinh \mu \sin \theta_\nu \sin \beta, \\ Z_\nu = \cosh \mu \cos \theta_\nu \sin \beta + \sinh \mu \sin \theta_\nu \cos \beta. \end{cases}$$

Here μ is the constant value of μ_ν on each cylinder, β is the inclination of the major axes to the y axis, and $2b$ is the distance between foci of the ellipse.

It may be shown (see, for example, Morse and Feshbach 1953) that, in terms of the elliptical co-ordinates defined above,

$$(16) \qquad \psi_0(\lambda, \Lambda) = p + \mu - 2 \sum_{n=1}^\infty \frac{e^{-n\mu}}{n} (\cosh n\mu \cos n\theta_\lambda \cos n\theta_\Lambda$$

$$+ \sinh n\mu \sin n\theta_\lambda \sin n\theta_\Lambda).$$

Also,

$$(17) \begin{cases} u_0^1(P_\Lambda) = e^{i(\Lambda-1)ka \cos \alpha}, \\ u_1^1(P_\Lambda) = ie^{i(\Lambda-1)ka \cos \alpha} [\cosh \mu \cos \theta_\Lambda \cos(\alpha-\beta) + \sinh \mu \sin \theta_\Lambda \sin (\alpha-\beta)]. \end{cases}$$

Since

$$(18) \qquad\qquad ds_\nu = b(\cosh^2 \mu - \cos^2 \theta_\nu)^{\frac{1}{2}}d\theta_\nu,$$

the functions α_0^ν defined by

$$(19) \qquad\qquad \alpha_0^\nu = (\cosh^2 \mu - \cos^2 \theta_\nu)^{\frac{1}{2}} a_0^\nu$$

satisfy the equations

$$(20) \qquad \frac{2i}{\pi} \int_0^{2\pi} \alpha_0^\lambda \psi_0(\lambda, \Lambda)d\theta_\lambda + \sum_{\nu \neq \lambda} H_0^{(1)}(|\nu - \lambda|ka) \int_0^{2\pi} \alpha_0^\nu d\theta_\nu$$

$$= -4ie^{i(\Lambda-1)ka \cos \alpha}, \qquad\qquad \lambda, \Lambda = 1, 2, \ldots N.$$

When the representation (16) for $\psi_0(\lambda,\Lambda)$ is employed, it is seen that the α_0^ν are constants (that is, independent of θ_ν), determined by the following set of simultaneous linear algebraic equations:

$$(21) \quad \frac{2i}{\pi} (p+\mu)\alpha_0^\lambda + \sum_{\nu \neq \lambda} H_0^{(1)}(|\nu - \lambda|ka)\alpha_0^\nu = -\frac{2i}{\pi} e^{i(\lambda-1)ka \cos \alpha}, \quad \lambda = 1, 2, \ldots N.$$

The determinant of this system is

$$(22) \quad D_N \equiv \begin{vmatrix} \frac{2i}{\pi} (p+\mu) & H_0^{(1)}(ka) & H_0^{(1)}(2ka) & \ldots & H_0^{(1)}[(N-1)ka] \\ H_0^{(1)}(ka) & \frac{2i}{\pi} (p+\mu) & H_0^{(1)}(ka) & \ldots & H_0^{(1)}[(N-2)ka] \\ \vdots & \vdots & \vdots & & \vdots \\ H_0^{(1)}[(N-1)ka] & H_0^{(1)}[(N-2)ka] & H_0^{(1)}[(N-3)ka] & \ldots & \frac{2i}{\pi} (p+\mu) \end{vmatrix}.$$

It would be of interest to know whether D_N possesses, when $\delta > 0$, any zeros for real values of ka. For $N = 2$, it may be shown that the conditions for such a zero are

$$J_0(ka) = \pm 1, \qquad Y_0(ka) = \pm\frac{2}{\pi}\left[\mu + \log\left(\frac{\gamma\delta}{4}\right)\right],$$

and these imply that $ka = \delta = 0$, a solution of no significance. On the other hand, if $N > 2$, and ka is large, then it may be shown that no zeros exist; for

$$D_N = A^{N-2}\{A^2 - [(N-1)H_1^2 + (N-2)H_2^2 + \ldots + 1 \cdot H_{N-1}^2] + O[(ka)^{-3/2}]\}$$

where

$$A \equiv \frac{2i}{\pi} (p+\mu), \qquad H_n \equiv H_0^{(1)}(nka) \sim \left(\frac{2}{\pi nka}\right)^{\frac{1}{2}} e^{inka - \frac{1}{4}\pi i}.$$

The condition $D_N = 0$ is thus equivalent to

$$A^2 = [(N-1)H_1^2 + \ldots + 1 \cdot H_{N-1}^2] + O[(ka)^{-3/2}].$$

But

$$|(N-1)H_1^2 + \ldots + 1 \cdot H_{N-1}^2| \lesssim \frac{2}{\pi ka}\left[1 + N\left(\tfrac{1}{2} + \tfrac{1}{3} + \ldots + \frac{1}{N-1}\right)\right],$$

so the right-hand side of the above equation is less than unity if ka is sufficiently large, while $|A^2| > 1$. Therefore under these circumstances $D_N \neq 0$ for real, positive δ.

In the subsequent work, it will be assumed that $D_N \neq 0$ for the chosen values of ka and δ.

The solution of equations (21) is readily found for sufficiently small N. For example, if $N = 1$,

$$(23) \qquad \alpha_0^1 = -\frac{1}{p+\mu},$$

while, if $N = 2$,

$$(24) \qquad \begin{cases} \alpha_0^1 = [4(p+\mu) + 2\pi i e^{ika\cos a} H_0^{(1)}(ka)]/D_2 \\ \alpha_0^2 = [4(p+\mu)e^{ika\cos a} + 2\pi i H_0^{(1)}(ka)]/D_2. \end{cases}$$

The real and imaginary parts of $\tfrac{1}{2}\pi\alpha_0^1$ (equations (24)) are, in Fig. 2, plotted as functions of ka and α, for $\delta e^\mu = 0.01$.

It may be observed (see equations (21)) that, in general, the α^r are functions of

$$p+\mu\left[= \log\left(\frac{kbe^\mu}{4}\right) - \tfrac{1}{2}\pi i\right],$$

and are independent of the angle of inclination β. Further, it may be shown that $2be^\mu$ is equal to the sum of the lengths of the major and minor axes of the ellipse. Thus, insofar as the shape of the ellipse is concerned, the solution α_0^r is dependent only on the sum of the lengths of the major and minor axes.

The first-order equations (14) may be solved in much the same manner once the integrals appearing in the right-hand sides have been evaluated. Since

$$ds_\lambda \frac{\partial}{\partial n_\lambda} = d\theta_\lambda \frac{\partial}{\partial \mu_\lambda},$$

a simple calculation gives

$$\frac{2i}{\pi}\int_{C_\lambda} \psi_0(\lambda, \Lambda) \frac{\partial u_1^1}{\partial n_\lambda} ds_\lambda = 4e^{-\mu}\sinh\mu\cosh\mu\cos(\theta_\Lambda - \alpha + \beta)e^{i(\Lambda-1)ka\cos a},$$

while

$$\int_{C_\nu} (Y_\nu - Y_\Lambda)a_0^r ds_\nu = -2\pi\alpha_0^r(\cosh\mu\cos\theta_\Lambda\cos\beta - \sinh\mu\sin\theta_\Lambda\sin\beta).$$

If functions α_1^r are defined by

$$(25) \qquad \alpha_1^r = (\cosh^2\mu - \cos^2\theta_r)^{\frac{1}{2}} a_1^r,$$
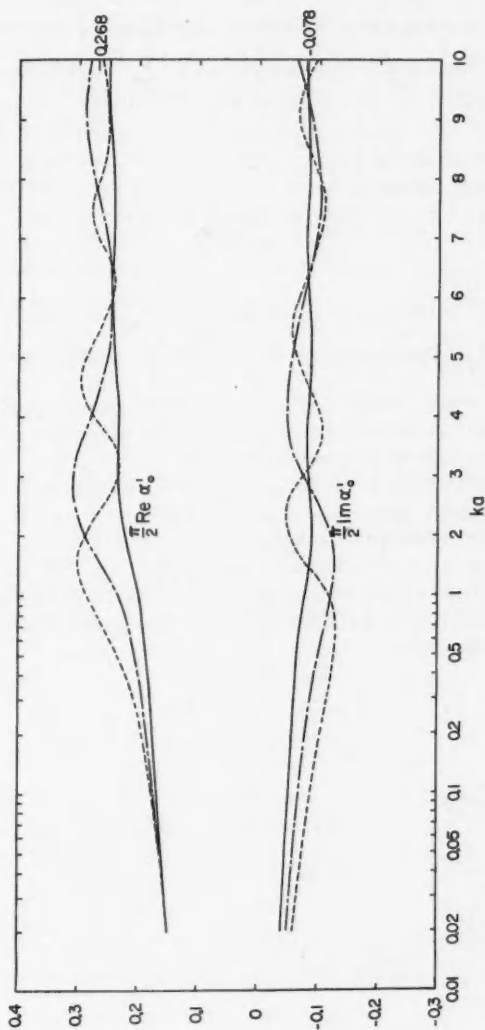
FIG. 2. Real and imaginary parts of $\frac{1}{2}\pi\alpha_0^i$ as functions of ka for $N = 2$, $\delta\epsilon'' = 0.01$, and different angles of incidence α, calculated from equation (24). The limiting value $(0.268 - i0.078)$ of $\frac{1}{2}\pi\alpha_0^i$ as ka tends to infinity is also shown. Note that the ka scale is logarithmic for $ka < 1$.

$---\ \alpha = 0°$, $\ -\ -\ -\ \alpha = 90°$, $\ ----\ \alpha = 180°$.

then the first-order equations (14) become

$$(26) \quad \frac{2i}{\pi} \int_0^{2\pi} \alpha_1^{\lambda} \psi_0(\lambda, \Lambda) d\theta_\lambda + \sum_{\nu \neq \lambda} H_0^{(1)}(|\nu - \lambda|ka) \int_0^{2\pi} \alpha_1^{\nu} d\theta_\nu$$

$$= 4e^{-\mu}[\cosh^2 \mu \cos \theta_\Lambda \cos (\alpha - \beta) + \sinh^2 \mu \sin \theta_\Lambda \sin (\alpha - \beta)]e^{i(\Lambda-1)ka \cos \alpha}$$

$$- 2\pi(\cosh \mu \cos \theta_\Lambda \cos \beta - \sinh \mu \sin \theta_\Lambda \sin \beta) \sum_{\nu \neq \lambda} \alpha_0^{\nu} \epsilon_{\nu\lambda} H_1^{(1)}(|\nu - \lambda|ka),$$

$$\lambda, \Lambda = 1, 2, \ldots N,$$

where $\epsilon_{\nu\lambda}$ is defined by equation (8).

The solution of these equations is

$$(27) \quad\quad\quad\quad \alpha_1^{\lambda} = \beta_1^{\lambda} \cos \theta_\lambda + \gamma_1^{\lambda} \sin \theta_\lambda,$$

where

$$(28) \quad \begin{cases} \beta_1^{\lambda} = ie^{i(\lambda-1)ka \cos \alpha}\cosh \mu \cos (\alpha - \beta) - \tfrac{1}{2}\pi ie^{\mu} \cos \beta \sum_{\nu \neq \lambda} \alpha_0^{\nu} \epsilon_{\nu\lambda} H_1^{(1)}(|\nu - \lambda|ka), \\ \gamma_1^{\lambda} = ie^{i(\lambda-1)ka \cos \alpha}\sinh \mu \sin (\alpha - \beta) + \tfrac{1}{2}\pi ie^{\mu}\sin \beta \sum_{\nu \neq \lambda} \alpha_0^{\nu} \epsilon_{\nu\lambda} H_1^{(1)}(|\nu - \lambda|ka). \end{cases}$$

At this point it is worth while to consider the relative magnitudes of α_0^{λ}, α_1^{λ} in order to determine under what circumstances the first-order terms may be neglected in comparison with those of zero order.

The sum in equations (28) is an interaction contribution, and may, for small ka, or for sufficiently large N and certain values of α and ka, become exceedingly large. The coefficients of higher powers of δ, too, will be large, and the condition $\delta \ll 1$ is not sufficient to ensure that the first one or two terms in the series provide an accurate approximation to the exact solution.

Consider first the case of small ka. Then the sum in equations (28) dominates, and a rough calculation gives

$$\left| \frac{\alpha_1^{\lambda}\delta}{\alpha_0^{\lambda}} \right| \lesssim \frac{\pi}{2} \delta e^{\mu}(N-1)|H_1^{(1)}(ka)|.$$

Thus

$$\left| \frac{\alpha_1^{\lambda}\delta}{\alpha_0^{\lambda}} \right| \ll 1 \quad \text{if} \quad |H_1^{(1)}(ka)| \ll \frac{2}{\pi \delta e^{\mu}(N-1)}.$$

Since $ka \ll 1$, this condition is equivalent to

$$\delta e^{\mu}(N-1) \ll ka.$$

If, for example, $\delta e^{\mu} = 0.01$, and $N = 2$, then the first-order term may be neglected when $ka \gtrsim 0.1$, and equations (24) provide a good approximation to the solution.

If $ka \gg 1$, so

$$\alpha_0^{\lambda} \doteq -(p+\mu)^{-1}e^{i(\lambda-1)ka \cos \alpha},$$

then the sum in equations (28) is at most of order $|p+\mu|^{-1}[(N-1)/(ka)]^{\frac{1}{2}}$. In this case, a criterion for the neglect of terms other than zero order would

appear to be $\delta e^{\mu}[(N-1)/(ka)]^{\frac{1}{2}} \ll 1$, as well as $\delta \ll 1$. This point has been stressed by Twersky (1952), to whom the reader is referred for a much more complete discussion. In either case, it seems necessary to keep the ratio $(N-1)/(ka)$ small, or else to decrease δ accordingly.

Before proceeding with the calculation of the scattered far-fields, the second problem, in which $\partial u/\partial n = 0$ on the cylinders will be considered.

PROBLEM (2): $\partial u/\partial n = 0$ ON THE CYLINDERS

Derivation and Solution of the Integral Equations

The configuration of Fig. 1 will be retained in this discussion. As in the case just considered, a set of simultaneous integral equations will be derived for the unknown distribution on the scatterers, and this will be solved approximately for small, identical elliptic cylinders.

The scattered field u^{s} at a point P exterior to all the cylinders is (see equation (1)):

$$(29) \qquad u^{s}(P) = \frac{i}{4} \sum_{\nu=1}^{N} \int_{C_{\nu}} \left[u^{s} \frac{\partial}{\partial n_{\nu}} H_{0}^{(1)}(kr_{\nu}) + H_{0}^{(1)}(kr_{\nu}) \frac{\partial u^{i}}{\partial n_{\nu}} \right] ds_{\nu}.$$

When the point P lies on C_{λ},

$$(30) \qquad u^{s}(P_{\Lambda}) = \frac{i}{2} \sum_{\nu=1}^{N} \int_{C_{\nu}} \left[u^{s} \frac{\partial}{\partial n_{\nu}} H_{0}^{(1)}(kr_{\nu\Lambda}) + H_{0}^{(1)}(kr_{\nu\Lambda}) \frac{\partial u^{i}}{\partial n_{\nu}} \right] ds_{\nu}.$$

In equation (30), the integral involving the normal derivative of $H_{0}^{(1)}(kr_{\lambda\Lambda})$ is to be interpreted as a Cauchy principal value.

If the value of u^{s} on C_{ν} is denoted by ϕ_{ν}, then the following set of simultaneous linear integral equations is obtained for the unknowns ϕ_{ν}:

$$(31) \qquad \phi_{\Lambda} - \frac{i}{2} \sum_{\nu=1}^{N} \int_{C_{\nu}} \phi_{\nu} \frac{\partial}{\partial n_{\nu}} H_{0}^{(1)}(kr_{\nu\Lambda}) ds_{\nu}$$
$$= \frac{i}{2} \sum_{\nu=1}^{N} \int_{C_{\nu}} H_{0}^{(1)}(kr_{\nu\Lambda}) \frac{\partial u^{i}}{\partial n_{\nu}} ds_{\nu}, \qquad \Lambda = 1, 2, \ldots N.$$

The above equations differ in certain respects from the set (equations (3)) considered previously. The unknown distribution on the cylinders appears outside the integral as well as under the sign of integration, and the kernels are normal derivatives rather than Hankel functions alone. Nevertheless the same procedure that was employed in the solution of the first problem may be followed here to obtain an approximate solution for small elliptic scatterers.

In terms of the elliptic co-ordinates introduced at an earlier point, the equations (31) may be re-written as

$$(32) \qquad \phi_{\Lambda} - \frac{i}{2} \sum_{\nu=1}^{N} \int_{0}^{2\pi} \phi_{\nu} \frac{\partial}{\partial \mu_{\nu}} H_{0}^{(1)}(kr_{\nu\Lambda}) d\theta_{\nu}$$
$$= \frac{i}{2} \sum_{\nu=1}^{N} \int_{0}^{2\pi} H_{0}^{(1)}(kr_{\nu\Lambda}) \frac{\partial u^{i}}{\partial \mu_{\nu}} d\theta_{\nu}, \qquad \Lambda = 1, 2, \ldots N.$$

If it is recalled that the integral involving $\partial H_0^{(1)}(kr_{\lambda\Lambda})/\partial\mu_\lambda$ is a principal value (so that $\theta_\lambda \neq \theta_\Lambda$), it is not difficult to show that the normal derivative of the Hankel function is well behaved throughout the interval of integration. In fact,

$$\frac{\partial}{\partial\mu_\lambda} H_0^{(1)}(kr_{\lambda\Lambda}) = -\frac{kb^2}{r_{\lambda\Lambda}} H_1^{(1)}(kr_{\lambda\Lambda}) \sinh 2\mu \sin^2 \tfrac{1}{2}(\theta_\lambda - \theta_\Lambda),$$

$$r_{\lambda\Lambda}^2 = 4 \sin^2 \tfrac{1}{2}(\theta_\lambda - \theta_\Lambda)[\sin^2 \tfrac{1}{2}(\theta_\lambda + \theta_\Lambda) + \sinh^2\mu],$$

and if $kr_{\lambda\Lambda} \ll 1$, while $\theta_\lambda \neq \theta_\Lambda$, $\partial H_0^{(1)}(kr_{\lambda\Lambda})/\partial\mu_\lambda$ is proportional to

$$\sinh 2\mu[\sinh^2\mu + \sin^2 \tfrac{1}{2}(\theta_\lambda + \theta_\Lambda)]^{-1}.$$

Appropriate expansions for $\partial H_0^{(1)}(kr_{\nu\Lambda})/\partial\mu_\nu$ may be obtained by the differentiation of equations (5) and (7). In the latter case, where $\nu \neq \lambda$,

$$(33) \qquad \frac{\partial}{\partial\mu_\nu} H_0^{(1)}(kr_{\nu\Lambda}) = -\epsilon_{\nu\lambda} H_1^{(1)}(|\nu - \lambda|ka)\, \delta$$

$$\times (\sinh\mu \cos\theta_\nu \cos\beta - \cosh\mu \sin\theta_\nu \sin\beta) + O(\delta^2),$$

where once again μ is equal to the constant value of μ_ν on C_ν.

To determine $\partial H_0^{(1)}(kr_{\lambda\Lambda})/\partial\mu_\lambda$, consideration of $\partial\psi_0(\lambda,\Lambda)/\partial\mu_\lambda$ is required. Here it is necessary to assume at the outset that $\mu_\lambda \neq \mu_\Lambda$. It is immaterial whether μ_λ is taken to be greater than or less than μ_Λ. In the following analysis, it will be assumed that $\mu_\lambda < \mu_\Lambda = \mu$, and thus $\psi_0(\lambda,\Lambda)$ is determined by equation (16) with μ replaced by μ_λ in $\cosh n\mu$ and $\sinh n\mu$. Then,

$$\frac{\partial}{\partial\mu_\lambda} \psi_0(\lambda,\Lambda) = -2 \sum_{n=1}^{\infty} e^{-n\mu} (\sinh n\mu_\lambda \cos n\theta_\lambda \cos n\theta_\Lambda$$

$$+ \cosh n\mu_\lambda \sin n\theta_\lambda \sin n\theta_\Lambda).$$

The summation may be performed, after which it is seen that

$$(34) \qquad \frac{\partial}{\partial\mu_\lambda} \psi_0(\lambda,\Lambda)\bigg|_{\mu_\lambda = \mu} = \tfrac{1}{2} + \sum_{n=1}^{\infty} e^{-2n\mu} \cos n(\theta_\lambda + \theta_\Lambda).$$

Let the right-hand sides of equations (32) be expanded in the form

$$\sum_{n=0}^{\infty} B_n^\Lambda\, \delta^n.$$

With the aid of equations (5), (16), and (17), it may be seen that

$$(35) \qquad \begin{cases} B_0^\Lambda = 0, \\ B_1^\Lambda = 2ie^{i(\Lambda-1)ka\cos\alpha}e^{-\mu}\sinh\mu\cosh\mu\cos(\theta_\Lambda - \alpha + \beta), \\ \quad . \\ \quad . \\ \qquad . \quad . \end{cases}$$

Finally, if ϕ_ν is assumed to be expressible in the form

$$(36) \qquad \phi_\nu = \sum_{n=0}^{\infty} b_n^\nu \delta^n,$$

where the coefficients b_n^ν are functions of θ_ν with period 2π, it follows that

(37)
$$
\begin{cases}
b_0^\Lambda + \dfrac{1}{\pi} \int_0^{2\pi} b_0^\lambda \left[\dfrac{1}{2} + \sum_{n=1}^{\infty} e^{-2n\mu} \cos n(\theta_\lambda + \theta_\Lambda) \right] d\theta_\lambda = 0, \\[2ex]
b_1^\Lambda + \dfrac{1}{\pi} \int_0^{2\pi} b_1^\lambda \left[\dfrac{1}{2} + \sum_{n=1}^{\infty} e^{-2n\mu} \cos n(\theta_\lambda + \theta_\Lambda) \right] d\theta_\lambda \\[2ex]
\quad + \dfrac{i}{2} \sum_{\nu \neq \lambda} \epsilon_{\nu\lambda} H_1^{(1)}(|\nu - \lambda| ka) \int_0^{2\pi} b_0^\nu d\theta_\nu = B_1^\Lambda, \\[1ex]
\quad \cdot \\
\quad \cdot \\
\quad \cdot \quad \cdot
\end{cases}
$$

The equations (37) may be solved by expanding the unknowns in Fourier series in θ_ν and evaluating the integrals. The solution is

(38)
$$
\begin{cases}
b_0^\nu = 0, \\[1ex]
b_1^\nu = ie^{i(\nu-1)ka \cos \alpha}[\sinh \mu \cos \theta_\nu \cos (\alpha - \beta) + \cosh \mu \sin \theta_\nu \sin (\alpha - \beta)], \\[1ex]
\quad \cdot \\
\quad \cdot \\
\quad \cdot \quad ,
\end{cases}
\qquad \nu = 1, 2, \ldots N,
$$

and

(39)
$$
\phi_\nu = i\delta e^{i(\nu-1)ka \cos \alpha}[\sinh \mu \cos \theta_\nu \cos (\alpha - \beta)
$$
$$
+ \cosh \mu \sin \theta_\nu \sin (\alpha - \beta)] + O(\delta^2).
$$

To a first approximation each cylinder scatters independently if the terms designated $O(\delta^2)$ are truly negligible. In this connection, it should be noted that conditions on the present solution analogous to those which follow equations (28) may also be obtained, although interaction effects do not become apparent until higher-order terms are considered.

FAR-FIELDS AND SCATTERING CROSS SECTIONS

The determination of the scattered far-fields through equations (2) and (29) (for problems (1) and (2), respectively) involves a relatively simple calculation. If (R,ϕ) denote polar co-ordinates of the far-field point (see Fig. 1), so $R \gg Na$, $kR \gg 1$, then the distance r_ν from a point on C_ν to the far-field point is $r_\nu = R_\nu - b(Y_\nu \cos \phi + Z_\nu \sin \phi)$, where R_ν represents the distance from the center of C_ν to (R,ϕ); thus $R_\nu = R - (\nu-1)a \cos \phi$, $\nu > 1$; $R_\nu = R$, $\nu = 1$.

Problem (1): $u = 0$ *on the Cylinders*

In this case, it is readily shown that

$$
\int_{C_\nu} u^1 \frac{\partial}{\partial n_\nu} H_0^{(1)}(kr_\nu) ds_\nu \sim \frac{e^{ikR}}{\sqrt{(kR)}} O(\delta^2),
$$

$$
\int_{C_\nu} H_0^{(1)}(kr_\nu) \frac{\partial u^s}{\partial n_\nu} ds_\nu \sim \frac{e^{ikR}}{\sqrt{(kR)}} [2\sqrt{(2\pi)} e^{-\frac{1}{4}\pi i} e^{-i(\nu-1)ka \cos \phi} \alpha_0^\nu + O(\delta^2)],
$$

so

$$(40) \qquad u \sim e^{ik(y\cos\alpha+z\sin\alpha)} - \left(\frac{\pi}{2}\right)^{\frac{1}{2}} e^{\frac{1}{4}\pi i}\, \frac{e^{ikR}}{\sqrt{(kR)}} \cdot \left[\sum_{\nu=1}^{N} \alpha_0^\nu e^{-i(\nu-1)ka\cos\phi} + O(\delta^2)\right].$$

If u is interpreted as the x component of an E-polarized electromagnetic field, then, on a large circle of radius R enclosing all the cylinders, the component of the complex Poynting vector in the direction of the outward normal is

$$\frac{i}{\omega\mu_0}\, u\, \frac{\partial u^*}{\partial R},$$

and the scattered power per unit length of the cylinders is equal to

$$P = \frac{\pi^2}{2\omega\mu_0}\,\mathrm{Re}\sum_{\nu,\,\eta=1}^{N} \alpha_0^\nu \alpha_0^{\eta*}\, J_0[ka(\nu-\eta)] + O(\delta^2).$$

Here starred (*) quantities represent complex conjugates, μ_0 is the permeability of free space, and $J_0(z)$ is the zero-order Bessel function. It follows that $\sigma_N^{(1)}$, the scattering cross section per unit length of the N cylinders (defined as the ratio of P to the power flow in the incident field through unit area perpendicular to the direction of propagation), is determined by

$$(41) \qquad \sigma_N^{(1)} = \frac{\pi^2}{k}\left[\mathrm{Re}\sum_{\nu,\,\eta=1}^{N} \alpha_0^\nu \alpha_0^{\eta*}\, J_0[ka(\nu-\eta)] + O(\delta^2)\right].$$

$\sigma_N^{(1)}$ also denotes the scattering cross section for cylinders that are "soft" in the acoustical sense.

Examples

$N = 1$. From equations (23) and (41),

$$(42) \qquad \sigma_1^{(1)} = \frac{\pi^2}{k}\left\{\frac{1}{\left[\log\left(\dfrac{\gamma\delta e^\mu}{4}\right)\right]^2 + \dfrac{\pi^2}{4}} + O(\delta^2)\right\}.$$

If the ellipse degenerates into a strip of width $2b$ ($\mu = 0$), then, for any inclination to the y axis,

$$(43) \qquad \sigma_{1\,\mathrm{STRIP}}^{(1)} = \frac{\pi^2}{k}\left\{\frac{1}{\left[\log\left(\dfrac{\gamma\delta}{4}\right)\right]^2 + \dfrac{\pi^2}{4}} + O(\delta^2)\right\},$$

a result which has been obtained previously on a number of occasions (see, for example, Bouwkamp 1954).

For the case of a circular cylinder of radius r_0,

$$(44) \qquad \sigma_{1\,\mathrm{CIRCLE}}^{(1)} = \frac{\pi^2}{k}\left\{\frac{1}{\left[\log\left(\dfrac{\gamma\delta'}{2}\right)\right]^2 + \dfrac{\pi^2}{4}} + O(\delta'^2)\right\},$$

where $\delta' = kr_0$.

It will be observed that $\sigma_1^{(1)}$ is, to a first approximation, independent of the

angles of incidence (α) and inclination (β), and depends only on δe^{μ}. Thus a small circular cylinder scatters the same power as a strip whose width is twice the diameter of the cylinder.

$N = 2$. Some algebraic manipulation leads from equations (24) and (41) to

$$(45) \quad \sigma_2^{(1)} = \frac{8\pi^2}{k} \Big(\mathrm{Re}\{[4|p+\mu|^2 + \pi^2|H_0^{(1)}(ka)|^2][1 + J_0(ka) \cos{(ka \cos \alpha)}]$$

$$+ 4\pi i[J_0(ka) + \cos{(ka \cos \alpha)}](p^*+\mu)H_0^{(1)}(ka)\} /$$

$$\{|4(p+\mu)^2 + \pi^2[H_0^{(1)}(ka)]^2|^2\} + O(\delta^2) \Big).$$

Discussion of this case becomes much more difficult for large values of N. However, if $ka \gg 1$, interaction and end effects may be usually disregarded, and the α_0^ν then differ from the value given by equation (23) only in a phase factor:

$$\alpha_0^\nu = -\frac{1}{p+\mu} e^{i(\nu-1)ka \cos \alpha}.$$

Needless to say, this will lead to the usual results of the single scattering approximation which have been discussed many times previously (for references, see Twersky 1952).

Problem (2): $\partial u / \partial n = 0$ *on the Cylinders*
In this case

$$(46) \quad \begin{cases} \displaystyle\int_{C_\nu} H_0^{(1)}(kr_\nu) \frac{\partial u^i}{\partial n_\nu} ds_\nu \sim -\sqrt{(2\pi)} e^{-\frac{1}{4}\pi i} \delta^2 \\ \qquad\qquad \cdot e^{i(\nu-1)ka\,(\cos \alpha - \cos \phi)} \sinh 2\mu \sin^2 \tfrac{1}{2}(\alpha - \phi) \dfrac{e^{ikR}}{\sqrt{(kR)}} + O(\delta^3), \\[1.5em] \displaystyle\int_{C_\nu} u^s \frac{\partial}{\partial n_\nu} H_0^{(1)}(kr_\nu) ds_\nu \sim \sqrt{(2\pi)} e^{-\frac{1}{4}\pi i}\delta^2 \\ \qquad\qquad \cdot e^{i(\nu-1)ka\,(\cos \alpha - \cos \phi)}[\sinh^2 \mu \cos{(\alpha - \beta)} \cos{(\phi - \beta)} \\ \qquad\qquad\qquad + \cosh^2 \mu \sin{(\alpha - \beta)} \sin{(\phi - \beta)}] \dfrac{e^{ikR}}{\sqrt{(kR)}} + O(\delta^3), \end{cases}$$

so

$$(47) \quad u^s \sim \tfrac{1}{2}\Big(\frac{\pi}{2}\Big)^{\frac{1}{2}} e^{\frac{1}{4}\pi i}\delta^2 \frac{e^{ikR}}{\sqrt{(kR)}} [\sinh^2 \mu \cos{(\alpha - \beta)} \cos{(\phi - \beta)}$$

$$+ \cosh^2 \mu \sin{(\alpha - \beta)} \sin{(\phi - \beta)} - \sinh 2\mu \sin^2 \tfrac{1}{2}(\alpha - \phi)]$$

$$\cdot \sum_{\nu=1}^{N} e^{i(\nu-1)ka\,(\cos \alpha - \cos \phi)} + O(\delta^3),$$

and the scattered field becomes vanishingly small as δ tends to zero.

If u now represents the x component of an H-polarized electromagnetic field, or the cylinders are "hard" in the acoustical sense, then the scattering cross section per unit length ($\sigma_N^{(2)}$) is

$$(48) \quad \sigma_N^{(2)} = \frac{\pi^2 \delta^4}{8k} \operatorname{Re} \sum_{\nu,\, \eta=1}^{N} \Bigg(\{ e^{2\mu} \sinh^2 \mu \cos^2 (\alpha-\beta)[J_0(\zeta) - \cos 2\beta J_2(\zeta)]$$

$$+ e^{2\mu} \cosh^2 \mu \sin^2 (\alpha-\beta)[J_0(\zeta) + \cos 2\beta J_2(\zeta)] + \tfrac{1}{2} \sinh^2 2\mu J_0(\zeta)$$

$$+ \tfrac{1}{2} e^{2\mu} \sinh 2\mu \sin 2(\alpha-\beta) \sin 2\beta J_2(\zeta) - 2i e^{\mu} \sinh 2\mu$$

$$\times [\sinh \mu \cos (\alpha-\beta) \cos \beta - \cosh \mu \sin(\alpha-\beta) \sin \beta] J_1(\zeta) \} e^{-i\zeta \cos \alpha} + O(\delta) \Bigg),$$

where $\zeta = (\nu-\eta)ka$.

Since

$$\sum_{\nu,\, \eta=1}^{N} J_{2n}[(\nu-\eta)ka] e^{-i(\nu-\eta)ka \cos \alpha} = 2 \sum_{\nu=1}^{N-1} (N-\nu) J_{2n}(\nu ka) \cos (\nu ka \cos \alpha) + \begin{cases} N, n=0 \\ 0, \ n \neq 0 \end{cases}$$

$$\sum_{\nu,\, \eta=1}^{N} J_{2n+1}[(\nu-\eta)ka] e^{-i(\nu-\eta)ka \cos \alpha} = -2i \sum_{\nu=1}^{N-1} (N-\nu) J_{2n+1}(\nu ka) \sin (\nu ka \cos \alpha),$$

equation (48) may be rewritten as

$$(49) \quad \sigma_N^{(2)} = \frac{\pi^2 \delta^4}{8k} \Bigg(e^{2\mu} \sinh^2 \mu \cos^2(\alpha-\beta) \Bigg\{ N + 2 \sum_{\nu=1}^{N-1} (N-\nu)[J_0(\nu ka)$$

$$- \cos 2\beta J_2(\nu ka)] \cdot \cos (\nu ka \cos \alpha) \Bigg\} + e^{2\mu} \cosh^2 \mu \sin^2(\alpha-\beta)$$

$$\times \Bigg\{ N + 2 \sum_{\nu=1}^{N-1} (N-\nu)[J_0(\nu ka) + \cos 2\beta J_2(\nu ka)] \cdot \cos (\nu ka \cos \alpha) \Bigg\} + \tfrac{1}{2} \sinh^2 2\mu$$

$$\times \Bigg\{ N + 2 \sum_{\nu=1}^{N-1} (N-\nu) J_0(\nu ka) \cos (\nu ka \cos \alpha) \Bigg\} + e^{2\mu} \sinh 2\mu \sin 2(\alpha-\beta) \sin 2\beta$$

$$\times \sum_{\nu=1}^{N-1} (N-\nu) J_2(\nu ka) \cos (\nu ka \cos \alpha) - 4e^{\mu} \sinh 2\mu \, [\sinh \mu \cos(\alpha-\beta) \cos \beta$$

$$- \cosh \mu \sin (\alpha-\beta) \sin \beta] \cdot \sum_{\nu=1}^{N-1} (N-\nu) J_1(\nu ka) \sin (\nu ka \cos \alpha) + O(\delta) \Bigg).$$

Thus

$$(50) \quad \begin{cases} \sigma_N^{(2)} \text{ STRIPS} = \dfrac{\pi^2 \delta^4}{8k} \Bigg(\sin^2(\alpha-\beta) \Bigg\{ N + 2 \sum_{\nu=1}^{N-1} (N-\nu)[J_0(\nu ka) + \cos 2\beta J_2(\nu ka)] \\ \qquad\qquad\qquad\qquad\qquad\qquad \cdot \cos (\nu ka \cos \alpha) \Bigg\} + O(\delta) \Bigg), \\[3mm] \sigma_N^{(2)} \text{ CIRCLES} = \dfrac{3\pi^2 \delta'^4}{4k} \Bigg(N + 2 \sum_{\nu=1}^{N-1} (N-\nu) J_0(\nu ka) \cos (\nu ka \cos \alpha) \\ \qquad\qquad - \dfrac{4}{3} \cos 2\alpha \sum_{\nu=1}^{N-1} (N-\nu) J_2(\nu ka) \cos (\nu ka \cos \alpha) \\ \qquad\qquad\qquad - \dfrac{8}{3} \cos \alpha \sum_{\nu=1}^{N-1} (N-\nu) J_1(\nu ka) \sin (\nu ka \cos \alpha) + O(\delta') \Bigg). \end{cases}$$

If $ka \gg 1$, equations (49) become (if the sums are negligible in comparison with N)

$$(51) \qquad \sigma_N^{(2)} \sim N\sigma_1^{(2)},$$

and

$$(52) \qquad \begin{cases} \sigma_{1\,\text{STRIP}}^{(2)} = \dfrac{\pi^2 \delta^4}{8k} [\sin^2 (\alpha-\beta) + O(\delta)], \\[2ex] \sigma_{1\,\text{CIRCLE}}^{(2)} = \dfrac{3\pi^2 \delta'^4}{4k} [1 + O(\delta')]. \end{cases}$$

The first of equations (52) has been obtained, for $\alpha = \frac{1}{2}\pi$, $\beta = 0$, a number of times (see, for example, Bouwkamp 1954), and higher-order terms in the series have been given by de Hoop (1955).

The neglect of higher-order terms in the series for $\sigma_N^{(2)}$ (and $\sigma_N^{(1)}$) is, of course, dependent upon satisfaction of the conditions discussed in the paragraphs following equations (28). In particular, for the present case, and $ka \gg 1$,

$$(53) \quad \sigma_N^{(2)} = \text{Re}\, \frac{\pi^2 \delta^4}{8k} \{e^{2\mu} \sinh^2 \mu \cos^2 (\alpha-\beta)[N + 4 \cos^2\beta\, G_0]$$

$$+ e^{2\mu} \cosh^2 \mu \sin^2 (\alpha-\beta)[N + 4\sin^2\beta\, G_0] + \tfrac{1}{2}\sinh^2 2\mu[N + 2G_0]$$

$$- e^{2\mu} \sinh 2\mu \sin 2(\alpha-\beta) \sin 2\beta G_0 + 4ie^{\mu}\sinh 2\mu[\sinh \mu \cos (\alpha-\beta)$$

$$\times \cos \beta - \cosh \mu \sin (\alpha-\beta) \sin \beta]G_1 + O(\delta)\},$$

where

$$(54) \quad G_n \equiv G_n(N, ka, \cos\alpha)$$

$$= \left(\frac{2}{\pi ka}\right)^{\frac{1}{2}} \left[N + \frac{i}{ka}\frac{d}{d(\cos\alpha)}\right] \sum_{\nu=1}^{N-1} \frac{e^{i\nu ka \cos\alpha}}{\sqrt{\nu}} \cos\left[\nu ka - (n+\tfrac{1}{2})\frac{\pi}{2}\right].$$

The magnitude of the sum appearing in G_n must be sufficiently small in order that the neglect of higher-order terms in $\sigma_N^{(2)}$ be justified. In this connection, the reader is again referred to the paper of Twersky (1952).

CONCLUDING REMARKS

Although the analysis in the present paper has been confined to problems in which u or $\partial u/\partial n$ vanish on the cylinders, there appears to be no reason why scattering by cylinders (or small three-dimensional objects), upon which are satisfied more general impedance-type boundary conditions (and which may be distributed in a more general fashion), should not be considered in a similar manner.

An application of the principle of images to the foregoing results will, when $\beta = 0$ or $\frac{1}{2}\pi$, lead to the solutions for scattering from an infinite "hard" or "soft" plane screen upon which is situated a number of semi-elliptical ridges whose dimensions are much less than the wavelength.

The method described here is evidently most appropriate when the number of scatterers is small; for it has been seen that when N is large, the smallness of δ is itself insufficient to ensure that a good approximation to the solution will be provided by the first one or two terms in the series.

Finally, it should be noted that the solutions obtained above may be only asymptotic as δ tends to zero, since they are not power series in the strict sense. On the other hand, for three-dimensional problems, a convergent series solution would be expected.

ACKNOWLEDGMENTS

REFERENCES

BAKER, B. B. and COPSON, E. T. 1950. The mathematical theory of Huygens' principle (Oxford University Press), p. 177.
BOUWKAMP, C. J. 1953. Diffraction theory, a critique of some recent developments, New York University, Mathematics Research Group, Research Report No. EM-50.
—— 1954. Repts. Progr. in Phys. **17**, 35.
DE HOOP, A. T. 1955. Proc. Koninkl. Ned. Akad. Wetenschap., B, **58**, 401.
KARP, S. N. 1955. Diffraction by an infinite grating of arbitrary cylinders. New York University, Inst. of Mathematical Sciences, Division of Electromagnetic Research, Research Report No. EM-85.
MORSE, P. M. and FESHBACH, H. 1953. Methods of theoretical physics (McGraw-Hill Book Co., Inc., New York), p. 1202.
ROW, R. V. 1955. J. Appl. Phys. **26**, 666.
TWERSKY, V. 1952. J. Appl. Phys. **23**, 1099.

APPENDIX

AN ALTERNATIVE METHOD OF SOLUTION TO EQUATIONS (3)

Suppose that the Green's function $G_\lambda(P,Q)$ for diffraction by C_λ is known. $G_\lambda(P,Q) = 0$ when P is on C_λ, and $G_\lambda(P,Q) \sim (2i/\pi) \log |PQ|$ as P tends to Q.

If Green's theorem is now applied in the region exterior to C_λ and a small circle C_Q about Q, then

$$0 = \int_{C_\lambda + C_Q} \left[G_\lambda(P,Q) \frac{\partial}{\partial n} H_0^{(1)}(k|OP|) - H_0^{(1)}(k|OP|) \frac{\partial}{\partial n} G_\lambda(P,Q) \right] ds,$$

where $|OP|$ is the distance from the integration point P to some point O within C_λ.

Thus,

$$H_0^{(1)}(k|OQ|) = \frac{i}{4} \int_{C_\lambda} H_0^{(1)}(k|OP|) \frac{\partial}{\partial n_\lambda} G_\lambda(P,Q) \, ds_\lambda.$$

If now the point O is permitted to approach C_λ, and Q lies on the surface of C_r, $\lambda \neq \nu$, then in the notation that has been previously employed,

$$(A1) \qquad H_0^{(1)}(kr_{\nu\lambda}) = \frac{i}{4} \int_{C_\lambda} H_0^{(1)}(kr_{\lambda\lambda}) \frac{\partial}{\partial n_\lambda} G_\lambda(P_\lambda, Q_\nu) ds_\lambda, \qquad \nu \neq \lambda.$$

Equation (A1) is an example of the well-known relationship which expresses a radiative wave function, non-singular in a region, in terms of its boundary values and the appropriate Green's function.

With the aid of the transformation (A1), the equations (3) may be rewritten as

$$(\text{A2}) \qquad \int_{C_\lambda} ds_\lambda H_0^{(1)}(kr_{\lambda\Lambda})\left[\frac{\partial u}{\partial n_\lambda}+\frac{i}{4}\sum_{\nu\neq\lambda}\int_{c_\nu}\frac{\partial u}{\partial n_\nu}\frac{\partial}{\partial n_\lambda}G_\lambda(P_\lambda,\,Q_\nu)ds_\nu\right]$$
$$= -4iu^i(P_\Lambda), \qquad\qquad \lambda,\Lambda = 1,2,\dots N$$

where $u = u^i + u^s$.

Each of the equations (A2) has the form of the equation for scattering by C_λ alone. Suppose, when all cylinders but C_λ have been removed, that the value of $\partial u/\partial n_\lambda$ on C_λ is U_λ. Then the solution of equations (A2) is

$$(\text{A3}) \qquad \frac{\partial u}{\partial n_\lambda}+\frac{i}{4}\sum_{\nu\neq\lambda}\int_{c_\nu}\frac{\partial u}{\partial n_\nu}\frac{\partial}{\partial n_\lambda}G_\lambda(P_\lambda,Q_\nu)ds_\nu = U_\lambda, \qquad \lambda = 1,2,\dots N.$$

Equations (A3) may be solved by successive substitutions with $\partial u/\partial n_\lambda = U_\lambda$ as a first approximation. The series for $\partial u/\partial n_\lambda$ may be shown to converge as geometric progressions for sufficiently large spacing between cylinders, since

$$\frac{\partial G_\lambda}{\partial n_\lambda}(P_\lambda,Q_\nu) = O(|P_\lambda Q_\nu|^{-\frac{1}{2}})$$

as $|P_\lambda Q_\nu|$ tends to infinity. The first approximation leads to the results of independent scattering, while interaction effects are included in higher-order approximations. The resemblance which this approach bears to that of Karp (1955) is evident. A particular application will be found in the work of Baker and Copson (1950) on the infinite slit.

A solution of equations (A3) by perturbation methods appears to be possible. If the functions involved are assumed to be expansible in powers of some small parameter, then equations (A3) may be reduced to sets of integral equations of the potential type. Since, however, knowledge of the Green's function is necessary in this approach, the perturbation method is more readily applicable to equations (3) as they stand.

ALPHA DECAY AND FISSION OF ALIGNED NUCLEI[1]

N. R. STEENBERG AND R. C. SHARMA

ABSTRACT

The theory of the angular distribution of alpha particles and of fission fragments
from nuclei aligned at low temperatures is presented. Very explicit results are
obtained in the high temperature approximation. These are directly dependent
upon the branching which takes place to the various allowed partial waves. This
branching is influenced by the nuclear shape, but it is shown that for this problem
the effect of penetrating a spheroidal barrier is not critical. An application is
made to the experimental work so far available and the result is reasonably
satisfactory.

SECTION 1. INTRODUCTION

The phenomenon of nuclear alignment at low temperatures is by now
familiar. Early experiments involved observations on β and γ radiations
alone. Recently observations have been made on α particles and fission frag-
ments (Dabbs *et al.* 1956; Roberts *et al.* 1956, 1958). This paper presents a
theoretical analysis of the emission of α particles and fission fragments from
oriented nuclei. To obtain nuclear data such as nuclear shape and surface
conditions they must first be disentangled from purely geometrical factors
which are troublesome but contain no real physics.

It would be intuitively expected that α particles from nuclei whose spins
are preferentially oriented would be emitted anisotropically. Similarly it would
be expected that if oriented nuclei were allowed to undergo slow neutron
induced fission the fragments would show a definite angular distribution with
respect to the axis of alignment. A bonus is provided when the same nuclide
does both, e.g. U^{233}, for then it is possible to compare both effects independently
of the degree of alignment.

It will be helpful to have in mind the experimental arrangement envisaged.
The nucleus under study must have a spin $I > \frac{1}{2}$. Even–even nuclei are thus
excluded. It is introduced into a suitable salt and the temperature is reduced
until the nuclear spins become oriented along a crystal axis of magnetic
symmetry. The relative population of all the magnetic substates is then
altered from the statistical value $1/(2I+1)$. Orientation takes place through
hyperfine coupling of the nuclear magnetic moment to the magnetic field
of the electrons, or coupling of the quadrupole moment to the crystalline
electric field, or both.

For heavily ionizing particles a detector must be placed in the cryostat to
observe emissions along, and perpendicular to, the axis of alignment. For
fission the cryostat and specimen are exposed to a flux of slow neutrons. Here
the detector must be able to discriminate against all but fission fragments.

The angular distribution of either α particles or fission fragments is governed
by two factors:

(*a*) purely geometric ones which can be regarded solely as consequences
of the conservation of angular momentum, and

(b) physical parameters such as the hyperfine coupling and especially the branching ratios to the various accessible final states.

For α decay of an odd nucleus two types of branching must be distinguished (see Fig. 1):

(a) branching to various energy and spin states of the daughter, and

(b) in a transition to a single energy state of the daughter branching among the various allowable α particle partial waves (l values).
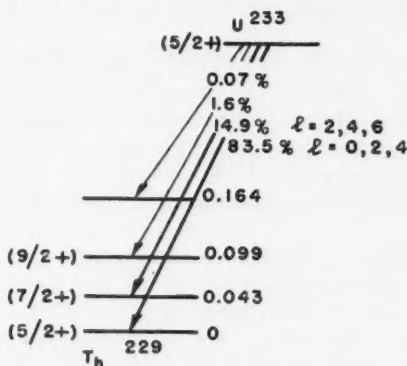

FIG. 1. Alpha decay scheme of U²³³ (Strominger et al. 1958).

Both types are expected to reflect conditions at the nuclear surface. Our particular interest is in 'favored' transitions (Bohr, Fröman, and Mottelson 1955) in which the odd nucleon is not involved and K, the projection of the nuclear spin on the body axis, is unchanged.

It may be noted here that the branching process may also be divided into two parts:

(a) the initial distribution of α particles on the nuclear surface, and

(b) the penetration of the spheroidal nuclear barrier which may favor some modes at the expense of others.

Most α emitters are in the region of strong prolate distortion. The difficult problem of branching in the α decay of distorted nuclei has been discussed extensively (see Rasmussen and Segall 1956; Pennington and Preston 1958; and references quoted there) but no clear picture has yet emerged. Fortunately the angular distribution can be discussed without explicitly introducing the effects of asphericity.

In Section 2 the theory of α decay of oriented nuclei is presented with an illustrative example. Simple and very explicit formulae are given for the high temperature approximation. In Section 3, the penetration of a spheroidal barrier is considered. It is shown that the part of the branching (amongst the various l values to a given final state of the daughter) which is induced by barrier penetration can reasonably be estimated on the basis of a spherical barrier. In other words the effect of asphericity lies mainly in its influence

on the relative amplitudes of the partial waves at the nuclear surface and
does not otherwise enter into the angular distribution. It should be borne in
mind that the clear-cut boundary between an inside region and an exterior
(Coulomb) region at a sharp spheroidal nuclear surface is somewhat artificial.

In Section 4 the theory of fission of an oriented nucleus by slow neutrons
is presented with an illustrative example. The anisotropy for α decay and
fission of the same nuclide are then compared. In Section 5 an application
is made to the only experimental evidence now available, the α decay and
fission of U^{233} and the α decay of Np^{237}.

SECTION 2. ALPHA DECAY OF ORIENTED NUCLEI

The angular distribution of α particles from oriented nuclei can be dealt
with in several ways in varying degrees of abstractness (Brussaard and
Tolhoek 1958; Rose 1956). The following is perhaps the simplest approach
possible. The only concept involved is the conservation of angular momentum.
It is similar to previous treatments of emissions from oriented nuclei (Steen-
berg 1952, 1954).

Consider a transition in which an oriented nucleus of spin I ($\geqslant 1$) goes
to a state of the daughter nucleus of spin I_1. (By suitably biasing the detector
we can in principle observe one α group at a time.)

It is assumed that there is one axis of magnetic symmetry (the z axis)
along which the nucleus is aligned. It then follows that the statistical matrix
for the nucleus is diagonal in a representation in which I_z is diagonal. In
other words we can treat each magnetic substate for which $I_z = M$ ($\hbar$ units)
separately.

Conservation of angular momentum then demands that the wave function
ψ_I^M of the system, daughter nucleus plus α particle, coming from an emitting
state for which $I_z = M$ have the following form:

$$(2.1) \qquad \psi_I^M(\mathbf{x}, r\theta\phi) = \sum_{l=|I_1-I|}^{I_1+I} \frac{u_{lI_1}(r)}{r} \sum_{m=-l}^{l} C_{M\ M-m\ m}^{I\ I_1\ l} X_{I_1}^{M-m}(\mathbf{x}) Y_l^m(\theta\phi)$$

where

$X_{I_1}^{M-m}(\mathbf{x})$ = wave function of daughter nucleus,

$\mathbf{x}$ = spin and space co-ordinates of daughter nucleus,

$C_{M\ M-m\ m}^{I\ I_1\ l}$ = Clebsch–Gordan coefficient adding states of angular momenta
l and I_1 to form a state of spin I. Note that the indices are
written in reversed order to those of Biedenharn (1952).

For large r, $u_{lI_1}(r)$ has an asymptotic form

$$u_{lI_1}(r) = g_{lI_1} e^{iF_l(r)}/k^{\frac{1}{2}}$$

where k = momentum of α particle, $F_l(r)$ = propagating part.

Our interest is in the ratios g_{lI_1}/g_{0I_1} or rather in the normalized ratios
$f_{lI_1} = g_{lI_1}/(\sum_l |g_{lI_1}|^2)^{\frac{1}{2}}$, the l sum extending over permitted values. The f_{lI_1}'s
are the physically interesting parameters.

It may be noted that all the admissible u_{lI_1}'s may be quite comparable in magnitude in contrast to the case of γ radiation where mixtures (except $E2$ and $M1$) can be neglected.

The angular distribution of α particles from the state (equation (2.1) above) is

$$(2.2) \qquad I_M(\theta) = \int |\psi_I^M(\mathbf{x},\theta)|^2 \, d\mathbf{x}.$$

In Appendix I it is shown that this can be reduced to the following form

$$(2.3) \qquad I_M(\theta) = 1 + \sum_{k=2,4,\ldots}^{2I} \Pi_k(M\,I) F_k(I\,I_1) P_k(\cos\theta)$$

where $\Pi_k(M\,I)$ is given in Appendix I and in particular

$$\Pi_2(M\,I) = 3M^2 - I(I+1),$$

$$P_k(\cos\theta) = \text{the Legendre polynomial,}$$

and

$$F_k(I\,I_1) = (2k+1)(2I+1)\left(\frac{(2I-k)!}{(2I+k+1)!}\right)^{\frac{1}{2}} k! \sum_{ll'} f_{lI_1} f_{l'\,I_1}^* \sqrt{(2l+1)}\, C_{000}^{l'kl}$$
$$\times W(l' I_1 k I : Il),$$

$W(abcd:ef) = $ Racah coefficient.

Let $W_M^{(0)}(T)$ be the probability that a nucleus is in a substate M of the parent at a temperature T. $W_M^{(0)}$ is a diagonal element of the density matrix ρ referring to the nucleus alone $W_M^{(0)} = (M|\rho|M)$ and $\sum_M W_M^{(0)} = 1$. $W_M^{(0)}$ has been extensively treated elsewhere (Steenberg 1953). The angular distribution (to one daughter state) is then

$$(2.4) \qquad I(\theta) = \sum_M W_M^{(0)} I_M(\theta)$$

or

$$(2.5) \qquad I(\theta) = 1 + \sum_k P_k(\cos\theta)\, F_k(I\,I_1) \sum_M W_M^{(0)} \Pi_k(M).$$

In experiments the 'high' temperature region is the most accessible and can be measured most accurately. Furthermore it contains all the nuclear information obtainable from alignment experiments. The high temperature region is defined by the convergence of an expansion of $\rho = \exp(-\mathfrak{H}/kT)$ in powers of $1/kT$. $\mathfrak{H}$ is the spin Hamiltonian responsible for nuclear orientation. For some simple cases of nuclear alignment it is possible to work out $I(\theta)$ explicitly for arbitrary temperatures in either form (2.4) or (2.5) (Brussaard and Tolhoek 1958). However, for those methods of nuclear alignment used so far this is impracticable. The coupling of the nucleus to the lattice may also involve dipole–dipole and exchange interactions between the ions and may be temperature dependent (solid state effects, see Steenberg 1953). These cannot

be included in a calculation of $I(\theta)$ for arbitrary temperatures. Thus we confine ourselves here to the high temperature approximation, that is, retaining only the first non-vanishing terms in the expansion of ρ.

It is then found that in all cases of angular distributions (in parity conserving transitions!) $W_M^{(0)}$ can be put in the form

$$(2.6) \qquad W_M^{(0)} = (2I+1)^{-1}[1+\delta\Pi_2(M\,I)].$$

The parameter δ depends on the method of nuclear alignment and may be complex. For the case of interest here, quadrupole coupling to the crystalline field plus magnetic dipole coupling to the ionic spin, the spin Hamiltonian is (Bleaney et al. 1954)

$$(2.7) \qquad \mathfrak{H} = A\,S_z I_z + B(S_x I_x + S_y I_y) + Q[3I_z^2 - I(I+1)].$$

A and B are the dipole coupling constants, S is the 'ionic' spin, and Q is the quadrupole coupling constant,

$$(2.8) \qquad Q = -e(q/4I(2I-1))\partial E_z/\partial z,$$

$$q = \text{nuclear quadrupole moment},$$

$$E_z = \text{crystalline electric field}.$$

(Our definition is that of Pound (1950) and differs by a factor 3 from that often quoted.) Here the parameter has the form

$$(2.9) \qquad \delta = -\frac{Q}{kT} + \frac{(A^2-B^2)}{24(kT)^2} + \frac{10Q^2}{(kT)^2}.$$

It may be noted that from equation (2.6) if $\delta > 0$ the nuclear spins are predominantly along the axis of alignment and if $\delta < 0$ they are predominantly perpendicular to it.

With $W_M^{(0)}$ given by (2.6) and $I(\theta)$ in the form (2.5) we can make use of the orthogonality of the Clebsch–Gordan coefficients in the form

$$\sum_M \Pi_k(M)\Pi_2(M) = \delta_{k2}(2I+1)(2I+3)(2I-1)I(I+1)/5$$

to obtain the high temperature approximation to $I(\theta)$, that is

$$(2.10) \qquad I^{I_1}(\theta) = 1 + \delta P_2(\cos\theta)G_2(I\,I_1),$$

$$(2.11)\ G_2(I\,I_1) = \sqrt{I(I+1)(2I+3)(2I+1)(2I-1)}\sum_{ll'} f_l f_{l'}^*\, C_{0\ 00}^{l'\ 2\ l}\, W(l'\,I_1 2I:Il).$$

Where branches occur to several daughter states with relative intensities $i(I_1)$ and no discrimination is made then the flux of each must be added to form the total angular distribution $I_{tot}(\theta)$ as follows:

$$I_{tot}(\theta) = \sum_{I_1} i(I_1) I^{I_1}(\theta)$$

$$(2.12) \qquad I_{tot}(\theta) = 1 + \delta P_2(\cos\theta)G_2\,(\text{total})$$

where $\qquad G_2\,(\text{total}) = \sum_{I_1} i(I_1)G_2(I\,I_1)$

and

$$\sum_{I_1} i(I_1) = 1.$$

The expressions (2.10), (2.11) agree essentially with Rose (1956) upon reduction of the statistical tensor. He confines himself, however, to S and D waves alone.

The parameter used to express experimental results is the ratio $R_\alpha = I(0)/I(\pi/2)$ of the intensities parallel and perpendicular to the axis of the alignment:

(2.13) $$R_\alpha = 1 + (3/2)\delta G_2 \text{ (total)}$$

to the first order in δ. The anisotropy ϵ is defined as $\epsilon = R_\alpha - 1 = 3\delta G_2/2$. Thus if $\delta G_2 > 0$ there is an excess of α radiation in the direction of the axis of alignment and if $\delta G_2 < 0$ there is an excess perpendicular to it.

2.1 Illustrative Examples

In order to illustrate the theory developed above we apply it to some specific examples.

Firstly consider the case of pure radiation, that is, where only one value of l contributes in a transition to a single daughter state. This is represented in equation (2.11) by $f_l = 1$ and all other $f_{l'} = 0$. Such a situation could occur where $I_1 = \frac{1}{2}$ and $I > 3/2$. Two classes may be distinguished which in a way represent extremes: (a) transition for which $I_1 = I \pm l$, "stretched" configurations, (b) transitions in which the spin does not change $I_1 = I$.

(a) For stretched configurations $G_2(I\,I_1)$ is always negative;

$$\text{for } I_1 = I - l, \qquad G_2 = -l(I-1)(2I+3)/(2l+3);$$

$$\text{for } I_1 = I + l, \qquad G_2 = -lI(2I-1)/(2l+3).$$

Here in both cases, for δ positive the α emission is predominantly in the direction perpendicular to the axis of alignment, i.e., from equation (2.10), $I(\pi/2) > I(0)$.

Physically this is understandable since $\mathbf{L}$ the orbital angular momentum vector of the emitted α particle must be predominantly parallel to the z axis. The direction of propagation is perpendicular to $\mathbf{L}$ and hence predominantly perpendicular to z. This is the demand of angular momentum conservation alone and is independent altogether of nuclear shape.

(b) For a transition in which the nuclear spin is unchanged $G_2(I\,I)$ is always positive with one exception ($I = 1$ and no parity change $G_2(I\,I) = -1$).

For $I_1 = I$, no parity change, $l = 2$,

$$G_2(I\,I) = (2I+5)(2I-3)/7.$$

($l = 2$ is the smallest value of l which can contribute to the anisotropy. This transition is the predominant group in a favored transition in the sense of Bohr, Fröman, and Mottelson 1955.)

For $I_1 = I$, parity change, $l = 1$

$$G_2(I\ I) = (2I+3)(2I-1)/5.$$

($l = 1$ is the smallest allowed value of l.) In both these cases the α emission is predominantly along the alignment axis.

As a further example and illustrating interference effects we choose the ground state transition from U^{233} (Strominger 1958)

$$(5/2+) \rightarrow (5/2+), \qquad l = 0, 2, 4$$

to Th^{229} (Fig. 1). From equation (2.10) the angular distribution is

(2.14) $I(\theta) = 1 + \delta P_2(\cos\theta) G_2(5/2\ 5/2)$

(2.15) $G_2(5/2\ 5/2) = \dfrac{20}{7}|f_2|^2 \pm 4\sqrt{14}\ |f_0 f_2| - \dfrac{20}{7}|f_4|^2 \pm \dfrac{36\sqrt{3}}{7}|f_2 f_4|.$

The sign of the anisotropy depends on the sign of δ (generally positive) and, if $f_0 > f_2 > f_4$, especially on the sign of the $f_0 f_2$ term. The expressions (2.14) and (2.15) agree with that of Brussaard and Tolhoek (1958) if their f_k is approximated for "high temperatures". The magnitudes and phases of the f_l's give information about the nuclear surface as discussed below. This expression, equation (2.15), will be referred to again in Section 5.

For an oriented prolate nucleus the body axis as well as the spin is mostly parallel to the z axis. Hill and Wheeler (1953) have pointed out that for a prolate spheroid the Coulomb barrier will be 'thinner' at the ends than at the middle. One would then expect a greatly enhanced emission at the poles of a prolate spheroid and hence parallel to the z direction contrary to the prediction of (a) above (and contrary to experiment as it happens).

For pure radiation no effect of asphericity can be incorporated into the theory. It is governed entirely by angular momentum conservation. Brussaard and Tolhoek (1958) have pointed out that it is mainly through the sign of $f_0 f_2$ term that information can be obtained about the distribution of the nascent α particle on the nuclear surface.

Briefly the argument is as follows. The wave function ψ_α describing the nascent α particle on the nuclear surface can be written as a series of Legendre polynomials in the body-fixed co-ordinate system,

(2.16) $\psi_\alpha = \displaystyle\sum_{l=0}^{2I} b_l P_l(\cos\theta'),$

where θ' = polar angle in the body-fixed system. (Equation (2.16) refers to α particles leading to the lowest member of a favored band. The original formulation is more general than this.) Considering the first two terms alone the distribution of ψ_α is

(2.17) $|\psi_\alpha|^2 = |b_0|^2 + 2|b_0 b_2|\cos\phi_{02} P_2(\cos\theta') + |b_2|^2(P_2(\cos\theta'))^2$

where ϕ_{02} = the relative phase of b_0 and b_2. According to Brussaard and Tolhoek (1958) ϕ_{02} is either 0 or π. Furthermore the relative phase of b_0 and b_2 is the same as the relative phase of f_0 and f_2, the probability amplitudes at great distance. In other words if $f_0 f_2^* = +|f_0 f_2|$ then $\phi_{02} = 0$. Equation (2.17) then

shows that $|\psi_\alpha|^2$ has a maximum at the poles of the prolate spheroid. If on the other hand (as seems experimentally to be the case) $f_0 f_2^* = -|f_0 f_2|$, and $\phi_{02} = \pi$, then $|\psi_\alpha|^2$ has a maximum around the waist of the spheroid. This choice of phase is favored by Pennington and Preston (1958) for even–even nuclei. (Note that because of a difference in definition of f_l these statements will appear reversed to those appearing in Brussaard and Tolhoek (1958).) For nuclear reactions Biedenharn and Rose (1953) give a very general proof, based on the reciprocity theorem, that the reduced matrix elements which here correspond to the f_l's must be real. Hence the relative phase of inter-fering partial waves must be exactly 0 or π. Whether this applies to α decay, however, is not clear.

SECTION 3.   PENETRATION OF A SPHEROIDAL BARRIER

It is not the intention here to go into detail on the theory of α emission from a distorted nucleus (see Pennington and Preston 1958). We do wish to show that in penetrating the barrier the effect of asphericity on the f_l's is small compared to that of the centrifugal term. For interest we will in Section 5 use the effect of the centrifugal barrier alone to estimate f_l's.

Recall that for a spherical nucleus the orbital angular momentum is a constant of motion so that we can represent an outgoing α particle of any l as

$$(3.1) \qquad \psi_\alpha{}_l^m = \frac{u_{l l_1}(r)}{r} Y_l^m(\theta \varphi).$$

$\theta \varphi$ refer to space-fixed axes and for large r

$$u_{l l_1}(r) = g_{l l_1} e^{i F_l(r)} k^{-\frac{1}{2}}.$$

The WKB approximation connects the outside amplitude $g_{l l_1}$ with the 'inside' amplitude

$$g_{l l_1}^{(\text{in})} \equiv u_{l l_1}(R_0)$$

at the point $r = R_0$

$$(3.2) \qquad g_{l l_1} = \sqrt{\frac{\kappa_l(R_0)}{k}} \, e^{-A_l} \, e^{i\pi/4} \, g_{l l_1}^{(\text{in})}$$

where

$$(3.3) \qquad \kappa_l^2(r) = \frac{2m}{\hbar^2} \left(V(r) + \frac{l(l+1)\hbar^2}{2mr^2} - E \right),$$

$V(r) = 2Ze^2/r$, $Z =$ atomic number of daughter, $E =$ particle energy, $E = \hbar^2 k^2/2m$, and

$$A_l = \int_{R_0}^{r'} \kappa_l(r) \, dr.$$

r' is the outside turning point where

$$\frac{2Ze^2}{r'} + \frac{l(l+1)\hbar^2}{2mr'^2} - E = 0.$$

However, r' is given very nearly by $r' = 2Ze^2/E$. The inside boundary is defined as the distance R_0 at which the potential departs substantially from the Coulomb form. Here no discontinuity is assumed at the nuclear surface (see for example Blatt and Weisskopf 1952). In such a case an inside wave with a definite propagation vector is implied and a transmission coefficient is defined. In equation (3.2) no assumption is made about the behavior inside $r = R_0$. Our interest is in the amplitude at that point.

The relative amplitude is given by

$$(3.4) \qquad \frac{g_{lI_1}}{g_{0I_1}} = e^{-(A_l - A_0)} \frac{g_{lI_1}^{(\text{in})}}{g_{0I_1}^{(\text{in})}}.$$

The small dependence on l which arises through $[\kappa_l(R_0)/\kappa_0(R_0)]^{\frac{1}{2}}$ is neglected.

It is shown in Appendix II that, using the fact that the centrifugal term $(\propto l(l+1))$ is small compared to the Coulomb term, equation (3.4) becomes (cf. Nosov 1957)

$$(3.5) \qquad \frac{g_{lI_1}}{g_{0I_1}} = e^{-l(l+1)\gamma/2} \frac{g_{lI_1}^{(\text{in})}}{g_{0I_1}^{(\text{in})}}$$

where

$$\frac{\gamma}{2} = \sqrt{\left\{ \frac{W}{V(R_0)} \left(1 - \frac{E}{V(R_0)} \right) \right\}}$$

$$W = \hbar^2/2mR_0^2.$$

Consider now a non-spherical nucleus. The nuclear 'surface' is now given by

$$R(\theta') = R_0[1 + \alpha P_2(\cos \theta')].$$

In what follows the body-fixed co-ordinate (z') system is assumed, θ' is the polar angle in the z' system. The Hamiltonian now contains the terms

$$(3.6) \qquad \Delta V(r,\theta') = \frac{e^2}{r^3} q\, P_2(\cos \theta').$$

$q = 6\alpha Z R_0^2/5$ is the intrinsic quadrupole moment and

$$\mathfrak{H}_{\text{rot}} = \hbar^2 \mathbf{I}_1^2/2\mathfrak{J}$$

where $\mathfrak{J}$ = moment of inertia. The term ΔV connects states for which $l' = l \pm 2, l$ so that equation (3.1) is no longer a solution. Instead linear combinations must be formed

$$\psi_\alpha = \sum_l \frac{u_{lI_1}(r)}{r} Y_l^0(\theta' \varphi')$$

referring to a transition leading to one member of a favored band. In favored transitions K the component of nuclear spin on the z' axis does not change and $K = I$, the initial spin, for a parent in the ground state. In the z' system therefore $m = 0$ only.

For an aspherical nucleus the f_i's are modified by redistribution of the flux amongst the various partial waves induced by ΔV as well as by attenuation within the barrier. The exact solution of the wave equation for $u_{l I_1}(r)$ involves coupled equations soluble only numerically (Rasmussen and Segall 1956). However, it can be shown (Sharma 1959; Fröman 1957) that if α is not too large the effect of ΔV is well represented by the angular dependence induced in $g_{l I_1}$ on penetrating a spheroidal barrier as follows, taking

$$(3.8) \qquad A_l(\alpha) = \int_{R(\theta)}^{r'} \left[\frac{2m}{\hbar^2} \left(V(r) + \frac{l(l+1)\hbar^2}{2mr^2} + \Delta V(r\theta') - E \right) \right]^{\frac{1}{2}} dr$$

and regarding the terms in $l(l+1)$ and ΔV small, equation (3.5) becomes (Appendix II)

$$(3.9) \qquad \frac{g_{l I_1}(\alpha)}{g_{0 I_1}(0)} = \exp\left[-l(l+1) \frac{\gamma}{2} \left(1 - \frac{\alpha P_2 (\cos\theta')}{2[1 - E/V(R_0)]} \right) \right] \frac{g_{l I_1}^{(\text{in})}}{g_{0 I_1}^{(\text{in})}}.$$

The value of $E/V(R_0)$ is of the order of $1/5$ for α emitters (see Section 5) hence for $\alpha \gtrsim 0.10$ the effect of ΔV is small compared to the effect of the centrifugal barrier. In Section 5 we will estimate g_l/g_0 omitting the term proportional to α.

It should be noted that the $u_{l I_1}(r)$, which is an exact solution of the wave equation, cannot have an angular dependence. The angular dependence in equation (3.9) represents the degree to which flux in a partial wave l is diverted into partial waves with $l' = l \pm 2$ while penetrating the barrier.

The above point of view is in contrast to that of Hill and Wheeler (1953), who predicted that distortion would produce a 16-fold increase in α emissions at the poles of a prolate nucleus (the thinnest part of the barrier). This was based on the comparison

$$(3.10) \quad \frac{g_0(\alpha)}{g_0(0)} = \exp\left\{ \alpha P_2(\cos\theta') \frac{4}{5} \sqrt{\frac{V(R_0)}{W} \left[1 - \frac{E}{V(R_0)} \right] \left[1 - \frac{E}{2V(R_0)} \right]} \right\}$$

(see Appendix II). This is in fact large but it implies the somewhat unrealistic assumption that before penetrating the spheroidal barrier the α particle starts as a spherically symmetrical ($l = 0$) wave 'inside' the nucleus.

SECTION 4. FISSION OF ALIGNED NUCLEI

The angular distribution of fission fragments with respect to the direction of the incident fast neutrons has been studied by Wilets and Chase (1956) and the analysis which follows is similar. We are to calculate the angular distribution, with respect to the axis of alignment, of fragments from slow neutron induced fission.

The assumptions that are made are as follows. An aligned target nucleus with spin I and z component M captures an S wave neutron and forms a fissioning nucleus with spin $I_2 = I \pm \frac{1}{2}$ and z component $M_2 = M \pm \frac{1}{2}$. The fissioning (and target) nucleus have a prolate shape and the wave function of the fissioning nucleus is

$$(4.1) \qquad \psi_{I_2}^{M_2\,K_2} = \sqrt{\frac{2I_2+1}{16\pi^2}}\left[\, \mathrm{X}_{K_2}(\mathbf{x})D_{M_2\,K_2}^{I_2}\pm \mathrm{X}_{-K_2}(\mathbf{x})D_{M_2-K_2}^{I_2}\right]$$

where $D_{MK}^{I}(\alpha\theta\gamma)$ = symmetric top wave function with $I_z = M$ and $I_{z'} = K$ (see Bohr 1952); $\alpha\theta\gamma$ = Euler angles of the axis of symmetry; $\mathrm{X}_{K_2}(\mathbf{x})$ = wave function of the particle structure. K_2 is the projection of I_2 on the body axis of the compound nucleus. If angular momentum in the body-fixed system is conserved $K_2 = K\pm\frac{1}{2}$ only. K is the projection of I on the body axis of the target nucleus, $K = I$.

The assumption that only one value of I_2 is involved has some justification although rather weak (Bohr 1956). It is this. At the saddle point most of the energy is bound up in energy of deformation. The nucleus passes the saddle point 'cold'. Thus the spectrum of fissioning states at the saddle point may be relatively simple and resemble that of the low-excited states of a strongly deformed nucleus. For simplicity it is assumed that only one value of I_2 is involved. The formalism may be readily generalized to include both allowed values. On the same basis the assumption that only one value of K_2 is involved is somewhat safer. For low excitation, states with differing K_2 will be much more widely separated than those of differing I_2.

The angular distribution of the body axis with respect to the z axis for the substate equation (4.1) is

$$(4.2) \qquad I_{M_2}^{K_2}(\theta) = \int |\psi_{I_2}^{M_2\,K_2}|^2\, d\mathbf{x}\,d\alpha\,d\gamma$$

$$= \frac{2I_2+1}{4}\left(|D_{M_2\,K_2}^{I_2}|^2+|D_{M_2-K_2}^{I_2}|^2\right)$$

since

$$\int d\mathbf{x}\,\mathrm{X}_{K_2'}^{*}(\mathbf{x})\,\mathrm{X}_{K_2}(\mathbf{x}) = \delta_{K_2K_2'}.$$

The fission fragments are assumed to recede along the body axis of the prolate spheroid, thus equation (4.2) is the angular distribution of the fission fragments. It is shown in Appendix III(a) that this can be reduced to

$$(4.3) \qquad I_{M_2}^{K_2} = \tfrac{1}{2}\left[1+(2I_2+1)\sum_{\nu=2,4\ldots} F_\nu(I_2)\Pi_\nu(M_2)\Pi_\nu(K_2)P_\nu\,(\cos\theta)\right]$$

where

$$F_\nu(I_2) = \frac{(2\nu+1)(\nu!)^2(2I_2-\nu)!}{(2I_2+\nu+1)!}$$

and Π_ν was defined in Section 2.

In Appendix III(b) it is shown that the relative population of the substates of the fissioning nucleus can be written

$$(4.4) \qquad W_{M_2}^{(2)} = \tfrac{1}{2}\sum_{M=M_2\pm\frac{1}{2}}|C_{M_2\ M\ M_2-M}^{I_2\ \ I\ \ \frac{1}{2}}|^2\,W_M^{(0)}.$$

$W_M^{(0)}$ was introduced in Section 2. The angular distribution of fission fragments is therefore

$$(4.5) \qquad I^{K_2}(\theta) = \sum_{M_2} W_{M_2}^{(2)} I_{M_2}^{K_2}(\theta).$$

As discussed in Section 2 the high temperature region is of greatest interest. Then, as before (equation (2.6))

$$W_M^{(0)} = (2I+1)^{-1}[1+\delta\,\Pi_2(M)].$$

Since

$$(4.6) \qquad \sum_M |C_{M_2\ M\ M-M_2}^{I_2\ I\ \frac{1}{2}}|^2 \Pi_2(M) = S_2(I_2\tfrac{1}{2}I)\Pi_2(M_2)$$

where

$$S_2(I_2\tfrac{1}{2}I) = (2I_2+1) \sqrt{\frac{(2I_2-2)!(2I+3)!}{(2I-2)!(2I_2+3)!}}\ W(I\tfrac{1}{2}2I_2:I_2I)$$

in particular

$$(4.7) \qquad S_2 = (2I-1)/(2I+1) \qquad \text{for } I_2 = I+\tfrac{1}{2}$$
$$S_2 = (2I+3)/(2I+1) \qquad \text{for } I_2 = I-\tfrac{1}{2}$$

it follows that the population of the substates of the fissioning nucleus is

$$(4.8) \qquad W_M^{(2)} = \frac{1}{2(2I+1)}\,[1+\delta S_2(I_2\tfrac{1}{2}I)\Pi_2(M_2)].$$

The angular distribution of fission fragments, equation (4.5), in the high temperature approximation becomes

$$(4.9) \qquad I^{K_2}(\theta) = \frac{(2I_2+1)}{4(2I+1)}\,[1+\delta S_2(I_2\tfrac{1}{2}I)\Pi_2(K_2)P_2\,(\cos\theta)]$$

since $F_2(I_2)\sum_{M_2}(\Pi_2(M_2))^2 = 1$. (For an explanation of the odd normalization see Appendix III(c).)

4.1 Illustrative Examples

To demonstrate the explicitness of the above formulation we apply them to a nucleus with spin $5/2$, U^{233}.

In the first instance let us assume the target nucleus is fully aligned (temperature saturation). This situation is nearly unattainable experimentally but it is instructive as will be seen. Here $W_M^{(0)} = \delta_{MI}$, i.e. the nuclear spin is parallel to the z axis. (This only occurs when the spin Hamiltonian is exactly diagonal in the M representation, e.g. in equation (2.9) B must vanish. The high temperature approximation is independent of this requirement.) We consider three alternatives: (a) $I_2 = I+\tfrac{1}{2}$, $K_2 = K+\tfrac{1}{2}$; (b) $I_2 = I+\tfrac{1}{2}$, $K_2 = K-\tfrac{1}{2}$; and (c) $I_2 = I-\tfrac{1}{2}$, $K_2 = K-\tfrac{1}{2}$. For U^{233} $I = 5/2+$ therefore (c) corresponds to $I_2 = 2+$ (S wave neutron) and $K_2 = 2$. The lowest excitation of an even–even nucleus would have $I_2 = 2+$, $K_2 = 0$. However (see Bohr 1956), after

an energy gap of about 1-Mev particle excitations are possible for which K_2 can have any value and $I_2 = K_2, K_2+1, K_2+2, \ldots$ with even parity. For (a) and (b) from equation (4.4) (dropping the factor $\frac{1}{2}$)

$$W_{M_2}^{(2)} = |C_{I+\frac{1}{2} I \frac{1}{2}}^{I+\frac{1}{2} I \frac{1}{2}}|^2 \delta_{M_2, I+\frac{1}{2}} + |C_{I-\frac{1}{2} I -\frac{1}{2}}^{I+\frac{1}{2} I}|^2 \delta_{M_2, I-\frac{1}{2}}$$

$$= \delta_{M_2 3} + \tfrac{1}{6} \delta_{M_2 2}, \qquad \text{for } I_2 = \tfrac{5}{2} + \tfrac{1}{2} = 3.$$

Then from equation (4.5) the angular distribution is

$$I^{K_2}(\theta) = (|D_{3 K_2}^3|^2 + |D_{3 -K_2}^3|^2) + \tfrac{1}{6}(|D_{2 K_2}^3|^2 + |D_{2 -K_2}^3|^2).$$

Explicit forms for the D_{MK}^I can be obtained from Sharp (1957) whence

(a) for $K_2 = 3$ $I(\theta) = 1 + 10 \cos^2 \theta + 5 \cos^4 \vartheta$,

(b) for $K_2 = 2$ $I(\theta) = 13 + 30 \cos^2 \theta - 35 \cos^4 \theta$.

These are illustrated in Fig. 2. In (a) there is a strong maximum in the direction of alignment, in (b) a shallow maximum around $\theta = 45°$. In (b) it should be
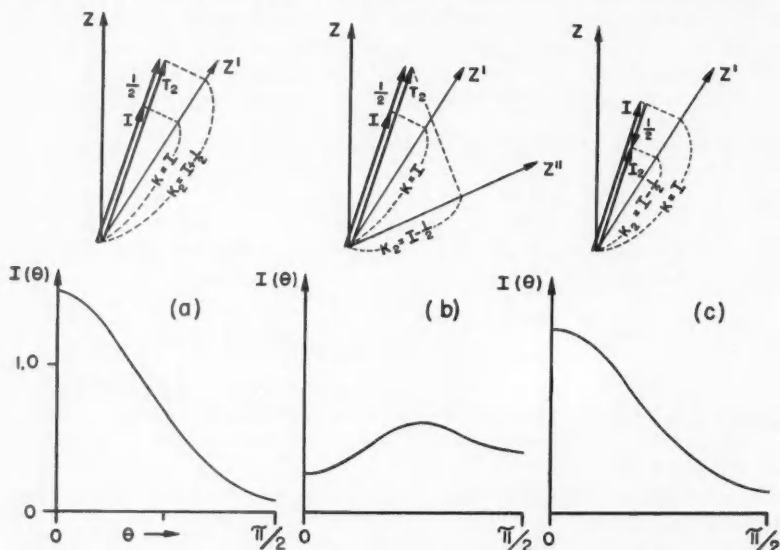
FIG. 2. Spin vectors and symmetry axis configurations (schematic) and corresponding angular distributions of fission fragments: (a) $I_2 = I + \frac{1}{2} = 3$, $K_2 = 3$; (b) $I_2 = 3$, $K_2 = 2$; (c) $I_2 = I - \frac{1}{2} = 2$, $K_2 = 2$. In (b) Z'' is the final position of the body axis.

noted that while the spin increases its component on the body axis diminishes. This can only be accomplished by a displacement of the z' axis as in Fig. 2(b). The relative occurrence of these modes will be governed by nuclear selection rules and the availability of such states at the saddle point.

For case (c) $I_2 = I - \frac{1}{2}$, $K_2 = K - \frac{1}{2}$ only, and $W_M^{(2)} = \delta_{M_2 I_2}$; then for $I = K = 5/2$

(c) $\qquad\qquad\qquad I(\theta) = 1 + 6\cos^2\theta + \cos^4\theta,$

which gives a less pronounced peak in the direction of alignment.

The high temperature expressions follow directly from equations (4.9) and (4.7), that is,

(4.10) $\qquad\qquad I(\theta) = 1 + \delta S_2(I_2\tfrac{1}{2}I)\Pi_2(K_2)P_2(\cos\theta).$

(We have dropped the statistical factor.)

$\qquad\qquad (a)\quad S_2(3\tfrac{1}{2}\,5/2)\Pi_2(3) = 10$

$\qquad\qquad (b)\quad S_2(3\tfrac{1}{2}\,5/2)\Pi_2(2) = \;\;0$

$\qquad\qquad (c)\quad S_2(2\tfrac{1}{2}\,5/2)\Pi_2(2) = \;\;8$

Both (a) and (c) are peaked in the z direction, (b) is (accidentally) isotropic. Figure 2 gives physical reasons for these.

4.2 Comparison of Fission and α Decay

For a nucleus which undergoes both α decay and fission in the same crystal (e.g. U^{233}) we can compare the anisotropies at high temperatures for the two processes.

In Section 2, equation (2.13), the anisotropy ϵ_α for decay was defined,

(4.11) $\qquad\qquad \epsilon_\alpha = (I(0)/I(\pi/2)) - 1 = (3/2)\delta G_2 \text{ (total)}.$

For fission fragments the same parameter can be defined

(4.12) $\qquad\qquad \epsilon_t = (3/2)\delta S_2(I_2\,\tfrac{1}{2}\,I)\Pi_2(K_2)$

to the first order in δ. The ratio of these quantities

(4.13) $\qquad\qquad \Re = \epsilon_t/\epsilon_\alpha = S_2(I_2\,\tfrac{1}{2}\,I)\Pi_2(K_2)/G_2 \text{ (total)}$

is independent of the alignment parameter δ which is valuable since this may be poorly known. The three alternatives discussed above are possible for the numerator of this fraction. In the experiment to be discussed in Section 5 $\Re$ was approximately $\Re = -1$.

SECTION 5. AN APPLICATION

The foregoing will now be applied to two cases for which experimental work has been done (Roberts *et al.* 1957b, 1958). These are U^{233} (α decay and fission) and Np^{237} (α decay). U^{233} has already been used as an illustrative example. We can now complete the calculation.

U^{233} Decay

The decay scheme was shown in Fig. 1. The experimental angular distribution was

$$I(\theta) = 1 - (0.063/T)P_2(\cos\theta).$$

The theoretical distribution for the ground state branch $(5/2+ \rightarrow 5/2+)$ was given in equation (2.14),

$$I^{5/2}(\theta) = 1 + \delta G_2(5/2\ 5/2)P_2(\cos\theta),$$

where

$$G_2(5/2\ 5/2) = \frac{20}{7}|f_2|^2 - \frac{20}{7}|f_4|^2 \pm 4\sqrt{14}\,|f_0 f_2| \pm \frac{36\sqrt{3}}{7}|f_2 f_4|.$$

To the first order in $1/T$, $\delta = -Q/kT$ (equation (2.9)). The coupling constant Q for U^{235} was obtained from specific heat measurements by Roberts *et al.* (1957a) in a salt similar to the cryogenic salt. It was found to be $Q^{235} = -.005$ cm^{-1} (this Q is one-third the value quoted due to a conventional difference in definition). The ratio of the quadrupole moments of U^{235} and U^{233} has been measured by Dorain *et al.* (1957) and found to be $q^{233}/q^{235} = 3.4/4.0$. Thus we take $Q^{233} = Q^{235} I(2I-1)q^{233}/I'(2I'-1)q^{235}$ where $I = 7/2$ and $I' = 5/2$ (cf. equation (2.8)). Hence $Q^{233} = -0.0089$ cm^{-1} and $\delta = -Q^{233}/kT = 0.0129/T$.

For a trial comparison we will estimate the f_l's from equation (3.5)

$$\left|\frac{g u_l}{g_{0 l}}\right|^2 = \exp\left\{-2l(l+1)\sqrt{\frac{W}{V(R_0)}\left[1-\frac{E}{V(R_0)}\right]}\right\}\left|\frac{g_{u_l}^{(\text{in})}}{g_{0 l}^{(\text{in})}}\right|^2$$

putting $|g_{u_l}^{(\text{in})}/g_{0 l}^{(\text{in})}| = 1$ for all l. This implies that all accessible l states for the α particle at the nuclear surface are equally likely. Then for $Z = 90$, $E = 4.82$ Mev, $R_0 = (9.76)10^{-13}$ cm (i.e. $R_0 = (1.40A+1.2)10^{-13}$ cm) we get $W = \hbar^2/2mR_0^2 = 0.055$ Mev and $V(R_0) = 2Ze^2/R_0 = 26.6$ Mev. The results are given in Table I.

TABLE I

$l =$	0	2	4	6
$|g_l/g_0|^2 =$	1	0.609	0.192	0.031
$|f_l|^2 =$	0.555	0.338	0.107	—

The largest term in $G_2(5/2\ 5/2)$ is the $f_0 f_2$ term and the sign must be taken as negative to obtain the correct sign for the anisotropy (excess in the equatorial plane). If the $f_2 f_4$ term is taken as negative $G_2(5/2\ 5/2) = -7.51$ and the predicted distribution is

$$I^{5/2}(\theta) = 1 - (0.096/T)P_2(\cos\theta).$$

The value $G_2(5/2\ 5/2) = -7.51$ is not far from the minimum possible value for this parameter obtainable by minimizing G_2 with respect to f_0, f_2, and f_4 subject to $\Sigma_l|f_l|^2 = 1$. If the $f_2 f_4$ term is taken positive $G_2(5/2\ 5/2) = -4.13$ and

$$I^{5/2}(\theta) = 1 - (0.053/T)P_2(\cos\theta).$$

The effect of the 15% branch to the $7/2+$ state should be included. The theoretical angular distribution to this first-excited state $I^{7/2}(\theta)$ is given by equation (2.10) with

$$G_2(5/2\ 7/2) = \frac{34}{7}|f_2|^2 - \frac{12}{7}\sqrt{55}\,|f_2 f_4| - \frac{126}{11}|f_4|^2 \pm \frac{12}{11}\sqrt{35}\,|f_4 f_6| - \frac{70}{11}|f_6|^2.$$

The $f_2 f_4$ term must be taken as negative. The f_i's are evaluated from Table I as shown in Table II.

TABLE II

$l =$	0	2	4	6
$|g_l/g_0|^2 =$	1	0.609	0.192	0.031
$|f_i|^2 =$	—	0.732	0.231	0.037

(The f_i's for the $5/2 \to 7/2$ group are negligibly affected by the energy difference of 43 kev.) This yields for $f_4 f_6$ negative $G(5/2\ \ 7/2) = -5.25$ and hence

$$I^{7/2}(\theta) = 1 - (0.675/T)P_2(\cos\theta).$$

The combined value $G(\text{total}) = (.85)(-7.51) + (.15)(-5.25) = -7.19$, hence

$$I_{\text{total}}(\theta) = (.85)I^{5/2}(\theta) + (.15)I^{7/2}(\theta) = 1 - (0.092/T)P_2(\cos\theta).$$

For the $f_4 f_6$ term positive this result becomes

$$I_{\text{total}} = 1 - (0.090/T)P_2(\cos\theta).$$

It has been suggested that partial waves with $l = 0$ and 2 (S and D waves) contribute almost exclusively to such transitions. In such a case

$$G_2(5/2\ \ 5/2) = (20/7)|f_2|^2 - 4\sqrt{14}|f_0 f_2|.$$

This can be minimized with respect to $|f_2|$ with $|f_0| = \sqrt{1-|f_2|^2}$. The minimum value of G_2 is -6.22 with $|f_2|^2 = 0.406$. For this value of G_2

$$I^{5/2}(\theta) = 1 - (0.080/T)P_2(\cos\theta).$$

For the 15% branch $l = 2$ only and

$$I^{7/2}(\theta) = 1 + \delta(34/7)P_2(\cos\theta) = 1 + (0.062/T)P_2(\cos\theta).$$

Thus for S and D waves alone $G(\text{total}) = -4.56$ and

$$I_{\text{total}}(\theta) = 1 - (0.059/T)P_2(\cos\theta).$$

This is the maximum possible value of the anisotropic term for S and D waves alone* (omitting the effect of the 1.6% branch to the 9/2 state) and is independent of any picture of barrier penetration or surface distribution. While it is markedly less than the experimentally observed value it depends on a value of Q determined by specific heat measurements. However, this result suggests that $l = 4$ waves do contribute to the decay.

*The above value disagrees with that obtained by Roberts et al. (1958) due to an error in their expression. Equation 16 of P/725, Proceedings of the Second Geneva Conference, Vol. 15, p. 322, should read

$$W(\theta) = 1 - \left[0.795\left(\frac{\delta^2}{1+\delta^2}\right) + 4.145\left(\frac{\delta}{1+\delta^2}\right) + 0.226\right]\frac{P}{kT}P_2(\cos\theta).$$

U^{233} *Fission*

The predicted angular distribution of fission fragments was given by equations (4.10) and (4.7). Using the value of δ used for the α decay, $\delta = (0.0129/T)$, we obtain

$$(a) \quad I_2 = 3, \quad K_2 = 3 \qquad I(\theta) = 1 + (0.128/T)P_2(\cos\theta),$$

$$(c) \quad I_2 = 2, \quad K_2 = 2 \qquad I(\theta) = 1 + (0.103/T)P_2(\cos\theta).$$

The experimental results are compatible with $I(\theta) = 1 + (0.06/T)P_2$.

Let us compare the fission and α decay results. The ratio of the anisotropies was given in equation (4.13)

$$\mathfrak{R} = S_2(I_2 \tfrac{1}{2} I)\Pi_2(K_2)/G_2 \text{ (total)}.$$

Experimentally $\mathfrak{R} \simeq -1$. We have two choices, (a) and (c), for the fission process $((b)$ yields zero) in the numerator. In the denominator we can use the value $G_2(\text{total}) = -7.19$ with all interference terms negative, used above for the α process and based on centrifugal barrier penetration alone. For this choice

$$(a) \quad \mathfrak{R} = -1.40,$$

$$(c) \quad \mathfrak{R} = -1.11.$$

These ratios depend on the f_i's chosen for the α process. However $|G_2|$ cannot exceed about 9.0. This suggests that if K_2 is limited to $K \pm \tfrac{1}{2}$ the fission proceeds predominantly through the $I_2 = 2$, $K_2 = 2$ state of the fissioning nucleus. A mixture of $I_2 = 3$, $K_2 = 3$ and $I_2 = 3$, $K_2 = 2$ would be compatible with a lesser value of $\mathfrak{R}$ although one would not expect two such states to be that close in energy. If K_2 is not limited then a mixture of $I_2 = 3$, $K_2 = 3$ and $I_2 = 2$, $K_2 = 0$ would serve.

If it is assumed that only $l = 0, 2$ waves contribute to the α process. We can compute $\mathfrak{R}$ using the minimum value of $G_2(\text{total}) = -4.56$. It is

$$(a) \quad \mathfrak{R} = -10/(4.56) = -2.20$$

or

$$(c) \quad \mathfrak{R} = -8/(4.56) = -1.75$$

which are rather too large. Recall that this ratio is independent of the measured value of Q and therefore it is again suggested that $l = 4$ waves contribute substantially to the α transition.

Np^{237} α *Decay*

The decay scheme of Np^{237} is shown in Fig. 3 (Strominger *et al.* 1958). This fits very well the type of transition discussed by Bohr, Fröman, and Mottelson (1955) in which the favored transition does not lead to the ground state. We therefore tentatively identify the 106-kev level as $7/2+$. Our interest is in
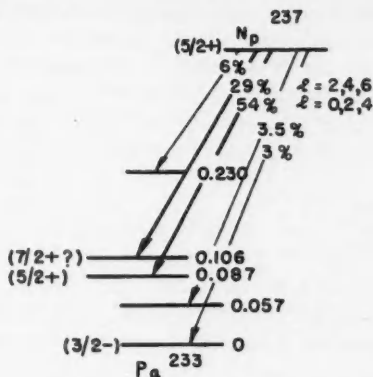
FIG. 3.   Alpha decay scheme of Np[237] (Strominger *et al.* 1958).

the principal branches, $5/2 \to 5/2$, 54% and $5/2 \to 7/2$, 29%. Experimentally the angular distribution of particles is reported as

$$I(\theta) = 1 - (0.068)P_2(\cos \theta)$$

at $T = 1.16°$ K (Roberts *et al.* 1956). Here the degree of nuclear alignment is known in more detail. For this nucleus in the salt used

$$\delta = -\frac{Q}{kT} + \frac{A^2 - B^2}{24k^2T^2} + \frac{10Q^2}{7k^2T^2}$$

(equation (2.9)). The parameters A, B, and Q were measured by Bleaney *et al.* (1954) and yield

$$\delta = (.0144/T) + (.0026/T^2) \quad \text{or} \quad \delta = 0.0143 \text{ at } T = 1.16° \text{ K}.$$

The parameters $G_2(5/2 \ 5/2)$ and $G_2(5/2 \ 7/2)$ have here the same form as for U[233]. Furthermore the $|f_i|$'s for $Z = 91$, $R_0 = 9.8 \times 10^{-13}$ cm, and $E = 4.78$ Mev differ negligibly from those for U[233]. Hence the G_2's have the following values:

   (a)   with the $f_2 f_4$ term negative $G_2 = -7.51$,

   (b)   with the $f_2 f_4$ term positive $G_2 = -4.13$.

(The $f_0 f_2$ term must be negative to obtain the correct sign of the anisotropy.) Using $\delta = 0.0143$ as above the 54% branch to the $5/2$ state has the following distributions:

   (a) $I^{5/2}(\theta) = 1 - (0.107)P_2(\cos \theta)$

   (b) $I^{5/2}(\theta) = 1 - (0.059)P_2(\cos \theta)$

at $T = 1.16°$ K.

The 29% branch to the 7/2 state must be included. The sign of the f_2f_4 term is determined by the choice already made for the 54% branch. With choice (*b*) the effect of the 29% branch is to reduce the anisotropy almost to zero. With choice (*a*) two alternatives remain for the sign of the f_4f_6 term. That is

$$\text{with } f_4f_6 \text{ negative} \qquad I^{7/2}(\theta) = 1 - 0.075 P_2(\cos \theta)$$

and

$$I_{\text{total}} = (0.65) I^{5/2}(\theta) + (0.35) I^{7/2}(\theta)$$
$$= 1 - 0.096 P_2(\cos \theta).$$

(the 54% and 29% branches are 65% and 35% of the total intensity in these two transitions), and with f_4f_6 positive $\qquad I^{7/2}(\theta) = 1 - 0.057 P_2(\cos \theta)$

and

$$I_{\text{total}}(\theta) = 1 - 0.090 P_2(\cos \theta).$$

The anisotropy predicted here is substantially greater than that observed experimentally. It must be recalled, however, that for Np^{237} several minor branches in the decay have been neglected and the identification of the 106-kev level in Pa^{233} as $7/2+$ is subject to experimental confirmation. For both U^{233} and Np^{237} the assumption that $|g_l^{(\text{in})}/g_0^{(\text{in})}|^2 = 1$ for all l is probably unrealistic. However, it is plain that minor adjustments of $|g_l^{(\text{in})}/g_0^{(\text{in})}|$ would bring the predicted anisotropy into agreement with that observed.

The angular distribution for the case of S and D waves alone with maximum anisotropy is

$$I^{5/2}(\theta) = 1 - (0.089) P_2(\cos \theta)$$
$$I^{7/2}(\theta) = 1 + (0.069) P_2(\cos \theta)$$

and

$$I_{\text{total}}(\theta) = (0.65) I^{5/2}(\theta) + (0.35) I^{7/2}(\theta)$$
$$= 1 - (0.047) P_2(\cos \theta)$$

for $T = 1.16°$ K. Again the maximum predicted anisotropy for S and D waves alone is less than that observed experimentally.

NOTE ADDED IN PROOF

Recently Pryce (Phys. Rev. Letters, **3**, 375, 1959) reports that the sign of the coupling constants for Np^{237} (and hence also for U^{233}) were incorrectly

chosen. The nuclear spins therefore lie across the alignment axis. To account for the observed angular distribution of α particles the sign of the $f_0 f_2$ term must be positive. To account for an axial predominance of fission fragments K_2 must be chosen as zero or one. The fissioning state could then be predominantly $I_2 = 2$, $K_2 = 0$. Such a choice implies that the nuclear symmetry axis reorients itself radically between capture of the neutron and the final separation of the fragments.

REFERENCES

BIEDENHARN, L. C. 1952. Tables of Racah coefficients, Oak Ridge National Laboratory Report 1098.
BIEDENHARN, L. C. and ROSE, M. E. 1953. Revs. Modern Phys. **25**, 729.
BLATT, I. M. and WEISSKOPF, V. J. 1952. Theoretical nuclear physics (John Wiley & Sons, New York).
BLEANEY, B., LLEWELLYN, P. M., PRYCE, M. H. L., and HALL, G. R. 1954. Phil. Mag. **45**, 992.
BOHR, A. 1952. Kgl. Danske Videnskab. Selskab., Mat.-fys. Medd. **26**, No. 14.
——— 1956. Proceedings of the First International Conference on the Peaceful Uses of Atomic Energy, Geneva, Vol. 2 (United Nations, New York), p. 151.
BOHR, A., FRÖMAN, P. O., and MOTTELSON, B. R. 1955. Kgl. Danske Vindenskab. Selskab., Mat.-fys. Medd. **29**, No. 10.
BRUSSAARD, P. J. and TOLHOEK, H. A. 1958. Physica, **24**, 233.
DABBS, J. W. T., ROBERTS, L. D., and PARKER, G. W. 1956. Bull. Am. Phys. Soc. Ser. II, **1** (4), 207.
DORAIN, P. B., HUTCHISON, C. A., JR., and WONG, E. 1957. Phys. Rev. **105**, 1307.
FRÖMAN, P. O. 1957. Kgl. Danske Videnskab. Selskab., Mat.-fys. Skr. **1**, No. 3.
HILL, D. L. and WHEELER, J. A. 1953. Phys. Rev. **89**, 1102.
NOSOV, V. G. 1957. Soviet Physics "Doklady", Am. Inst. of Physics translation **2**, 48.
PENNINGTON, E. M. and PRESTON, M. A. 1958. Can. J. Phys. **36**, 944.
POUND, R. V. 1950. Phys. Rev. **79**, 685.
RACAH, G. 1943. Phys. Rev. **63**, 367.
RASMUSSEN, J. O. and SEGALL, B. 1956. Phys. Rev. **103**, 1298.
ROBERTS, L. D., DABBS, J. W. T., and PARKER, G. W. 1956. Oak Ridge National Laboratory Report 2076, 3.
——— 1957a. Bull. Am. Phys. Soc. Ser. II, **2**, No. 1, 30.
——— 1957b. Oak Ridge National Laboratory Report 2430, 51.
——— 1958. Proceedings of the Second Geneva Conference on the Peaceful Uses of Atomic Energy, paper 725, Vol. **15**, 322.
ROSE, M. E. 1956. Oak Ridge National Laboratory Report 2076, 1.
SHARMA, R. C. 1959. Ph.D. Thesis, University of Toronto, Toronto, Ontario.
SHARP, W. T. 1957. Atomic Energy of Canada Ltd., Chalk River, Ont., Report A.E.C.L. No. 465.
STEENBERG, N. R. 1952. Proc. Phys. Soc. A, **65**, 791.
——— 1953. Proc. Phys. Soc. A, **66**, 399.
——— 1954. Phys. Rev. **93**, 678.
STROMINGER, D., HOLLANDER, J. M., and SEABORG, G. T. 1958. Revs. Modern Phys. **30**, 585.
WILETS, L. and CHASE, D. M. 1956. Phys. Rev. **103**, 1296.

APPENDIX I

The wave function for daughter nucleus plus outgoing α particle, equation (2.1), for $r \to \infty$ is

$$\psi_I^M(\mathbf{x}, \theta\varphi) = \sum_l \frac{u_{l l_1}(r)}{r} \sum_m C_{M\ M-m\ m}^{I\ I_1\ l} \mathbf{X}_{I_1}^{M-m}(\mathbf{x})\ Y_l^m(\theta\varphi).$$

The angular distribution equation (2.2) is

$$I_M(\theta) = \int |\psi_I^M|^2 d\mathbf{x}$$
$$= \sum_{l l'} f_{l l} f_{l' l_1}^* \sum_m C_{M\ M-m\ m}^{I\ I_1\ l} C_{M\ M-m\ m}^{I\ I_1\ l}\ (Y_{l'}^m)^* Y_l^m$$

where we have utilized the orthonormality of the daughter states in the form

$$\int (\mathbf{X}_{I_1 I'}^{M_1'}(\mathbf{x}))^* \, \mathbf{X}_{I_1}^{M_1}(\mathbf{x}) \, d\mathbf{x} = \delta_{M_1 M_1'} \delta_{I_1 I_1'}$$

and have multiplied by $kr^2/\Sigma |g_{lI_1}|^2$:

The following results are all obtainable by the methods of Racah (1943) (see also Biedenharn 1952):

$$(Y_{l'}^m)^* \, Y_l^m = \frac{1}{4\pi} \left(\frac{2l+1}{2l'+1} \right) \sum_{k=|l-l'|}^{l+l'} (2k+1) \, C_{m0m}^{l'kl} \, C_{000}^{l'kl} \, P_k(\cos\theta)$$

$$\sum_m C_{M\ M-m\ m}^{I\ I_1\ \ l} \, C_{M\ M-m\ m}^{I\ I_1\ \ l} \, C_{m0m}^{l'kl} = \sqrt{(2I+1)(2l'+1)} \, W(l'I_1 k I I l) \, C_{M0M}^{I\ k\ I}.$$

Hence using the properties

$$C_{0\ 00}^{l'\ 0\ l} = \delta_{ll'}, \ W(lI_1 0 II l) = [(2l+1)(2I+1)]^{-\frac{1}{2}} \quad \text{and} \quad \sum_l |f_l|^2 = 1,$$

$$I_M(\theta) = 1 + \sum_k (2k+1) \, C_{M\ 0\ M}^{I\ k\ I} \sqrt{2I+1} \sum_{ll'} f_l f_{l'}^* \sqrt{2l+1} \, C_{0\ 00}^{l'\ k\ l} \, W(l'I_1 k I:Il)$$

(the factor $1/4\pi$ has been dropped). The coefficient C_{M0M}^{IkI} can be written

$$C_M^{I\ k\ I} = k! \sqrt{2I+1} \left(\frac{(2I-k)!}{(2I+k+1)!} \right)^{\frac{1}{2}} \Pi_k(MI)$$

$$\Pi_k(MI) = \sum_\nu \frac{(-)^\nu (I+M)!(I-M)!k!}{[(k-\nu)!\nu!]^2 (I+M-\nu)!(I-M-k+\nu)!}$$

whence equation (2.3) follows.

APPENDIX II

We are to integrate

$$A_l(\alpha) = \int_{R(\theta)}^{r'} \left[\frac{2m}{\hbar^2} \left(V(r) + C_l(r) + \Delta V(r\theta') - E \right) \right]^{\frac{1}{2}} dr$$

where

$$V(r) = 2Ze^2/r, \qquad C_l(r) = l(l+1)\hbar^2/2mr^2,$$

$$\Delta V(r\theta') = \frac{3}{5} V(r) \left(\frac{R_0}{r} \right)^2 \alpha P_2(\cos\theta').$$

Expanding in powers of $(V-E)^{-1}$ and noting that $V(r)/E = r'/r$

$$A_l(\alpha) = \sqrt{\frac{2mE}{\hbar^2}} \int \sqrt{\frac{r'}{r} - 1} \left[1 + \left(\frac{C_l + \Delta V}{2E} \right) \left(\frac{r'}{r} - 1 \right)^{-1} + \dots \right] dr.$$

Now with

$$\frac{C_l}{E} = l(l+1) \frac{WE}{V(R_0)^2} \frac{1}{x^2},$$

$$\frac{\Delta V}{E} = \frac{3}{5} \left(\frac{E}{V(R_0)} \right)^2 \frac{\alpha P_2}{x^3}.$$

$$\sqrt{\frac{2mE}{\hbar^2}} = \frac{V(R_0)}{\sqrt{WE}}\frac{1}{r'},$$

$$x = r/r', \quad \text{and} \quad W = \hbar^2/2mR_0^2.$$

$A_l(\alpha)$ becomes

$$A_l(\alpha) = I_1 + I_2 + I_3$$

where

$$I_1 = \frac{V(R_0)}{\sqrt{WE}}\int_t^1 \sqrt{\frac{1-x}{x}}\,dx = \frac{V(R_0)}{\sqrt{WE}}[\cos^{-1}\sqrt{t}-\sqrt{t(1-t)}]$$

$$I_2 = \frac{l(l+1)}{2}\frac{\sqrt{WE}}{V(R_0)}\int_t^1 \sqrt{\frac{x}{1-x}}\frac{dx}{x^2} = \frac{l(l+1)}{2}\frac{\sqrt{EW}}{V(R_0)}2\sqrt{\frac{1-t}{t}}$$

$$I_3 = \frac{3}{10}\frac{E}{V(R_0)}\sqrt{\frac{E}{W}}\alpha P_2\int_t^1 \sqrt{\frac{x}{1-x}}\frac{dx}{x^3}$$

$$= \frac{E}{5\,V(R_0)}\sqrt{\frac{E}{V(R_0)}}\alpha\frac{P_2}{t}\sqrt{\frac{1-t}{t}}(2t+1)$$

and

$$t = R(\theta)/r' = R_0(1+\alpha P_2(\cos\theta'))/r'$$

$$R_0/r' = E/V(R_0).$$

Expanding t in powers of α we obtain

$$A_l(\alpha) = \frac{V(R_0)}{\sqrt{WE}}\left\{\cos^{-1}\sqrt{\frac{E}{V(R_0)}}-\sqrt{\frac{E}{V(R_0)}\left[1-\frac{E}{V(R_0)}\right]}\right\}$$

$$+l(l+1)\sqrt{\frac{W}{V(R_0)}-\left[1-\frac{E}{V(R_0)}\right]}\left\{1-\frac{\alpha P_2(\cos\theta')}{2[1-E/V(R_0)]}\right\}$$

$$-\frac{4\alpha P_2}{5}\sqrt{\frac{V(R_0)}{W}\left[1-\frac{E}{V(R_0)}\right]}\left[1-\frac{E}{2\,V(R_0)}\right].$$

Whence equations (3.5), (3.9), and (3.10) follow.

APPENDIX III

(a) From equation (4.2) we have

$$I_M^K(\theta) = \frac{(2I_2+1)}{4}(|D_{MK}^I|^2+|D_{M-K}^I|^2).$$

The properties of D_{MK}^I (see, for example, Sharp 1957) are such that

$$|D_{MK}^I|^2 = \sum_{\nu=0,1,2,3,\ldots} C_{M\ 0\ M}^{I\ \nu\ I}\,C_{K\ 0\ K}^{I\ \nu\ I}\,P_\nu(\cos\theta)\left(\frac{2\nu+1}{2I+1}\right).$$

Since

$$C_{-K\ 0\ -K}^{I\ \nu\ I} = (-)^\nu C_{K\ 0\ K}^{I\ \nu\ I}$$

$I_M^K(\theta)$ becomes

$$(A.1) \qquad I_M^K(\theta) = \tfrac{1}{2}\left[1 + (2I+1)\sum_{r=2,4,\ldots} F_r(I)\Pi_r(M)\Pi_r(K)P_r(\cos\theta)\right]$$

as given in equation (4.3).

(*b*) To show that the relative populations $W_{M_2}^{(2)}$ of a substate of the fissioning nucleus is

$$W_{M_2}^{(2)} = \tfrac{1}{2}\sum_M \left| C_{M_2\ M\ M_2-M}^{I_2\ I\ \frac{1}{2}} \right|^2 W_M^{(0)}$$

as in equation (4.4) we start from the fundamental relation that the mean value $\langle 0 \rangle$ of any quantum observable 0 is given by

$$\langle 0 \rangle = Tr(0\rho)/Tr\rho.$$

$Tr\rho$ is the trace (sum of the diagonal elements) of the density matrix ρ and ρ is defined such that $Tr\rho = 1$. $Tr(0\rho)$ is independent of representation hence we use the representation in which I_{2z} is diagonal with eigenvalues M_2. Then

$$Tr(0\rho) = \sum_{M_2} (M_2|0\rho|M_2) = \sum_{M_2 M_2'} (M_2|0|M_2')(M_2'|\rho|M_2).$$

Now a state $|I_2 M_2\rangle_f$ of the fissioning nucleus can be written as a superposition of the accessible target states $|I\,M\rangle_t$ and neutron states $|\tfrac{1}{2}m\rangle_n$

$$|I_2 M_2\rangle_f = \sum_{m=\pm\frac{1}{2}} C_{M_2\ M_2-m\ m}^{I_2\ I\ \frac{1}{2}}|I\ M_2-m\rangle_t|\tfrac{1}{2}m\rangle_n.$$

Hence

$$(M_2'|\rho|M_2) = \sum_{mm'} C_{M_2'\ M_2'-m'\ m'}^{I_2\ I\ \frac{1}{2}}\, C_{M_2\ M_2-m\ m}^{I_2\ I\ \frac{1}{2}}\, (M_2'-m',\, m'|\rho|M_2-m,\, m).$$

The density operator ρ can be written

$$\rho = \rho(\text{target})\rho(\text{neutron})$$

and

$$(M_2'-m'm'|\rho|M_2-mm) = (M_2'-m'|\rho(\text{target})|M_2-m)(m'|\rho(\text{neutron})|m).$$

For unpolarized neutrons

$$(m'|\rho(\text{neutron})|m) = \tfrac{1}{2}\delta_{mm'}.$$

For nuclear alignment with cylindrical symmetry $\rho(\text{nucleus})$ is diagonal in the representation with I_z for the target nucleus diagonal (the M representation). Hence

$$(M_2'|\rho|M_2) = \delta_{M_2 M_2'} W_{M_2}^{(2)}$$

where $W_{M_2}^{(2)}$ is the relative population of a magnetic substate of the fissioning nucleus

$$(A.2) \qquad W_{M_2}^{(2)} = \tfrac{1}{2}\sum_{M=M_2\pm\frac{1}{2}}\left| C_{M_2\ M\ M_2-M}^{I_2\ I\ \frac{1}{2}} \right|^2 W_m^{(0)}$$

and

$$W_M^{(0)} = (M|\rho(\text{nucleus})|M).$$

Finally

(A.3) $$Tr(0\rho) = \sum_{M_2} W_{M_2}^{(2)} (M_2|0|M_2)$$

and we identify $(M_2|0|M_2)$ as

$$(M_2|0|M_2) = \int |\psi_{I_2}^{M_2\,K_2}|^2 \, d\mathbf{x} \, d\alpha \, d\gamma$$

$$= I_{M_2}^{K_2}(\theta)$$

and $I(\theta) = Tr(0\rho)$ so that equation (4.5) follows.

(c) We now show that in general certain two physically obvious limiting conditions are met.

(i) The total flux is independent of the temperature. The total flux is by equation (A.3)

$$\int I(\theta) \sin \theta \, d\theta = \sum_{M_2} W_{M_2}^{(2)} \int I_{M_2}(\theta) \sin \theta \, d\theta = \sum_{M_2} W_{M_2}^{(2)}$$

since $$\int P_\nu(\cos \theta) \sin \theta \, d\theta = 0 \qquad \text{for } \nu > 0$$

and $$\int_0^\pi \sin \theta \, d\theta = 2.$$

Now by equation (A.2)

$$\sum_{M_2} W_{M_2}^{(2)} = \tfrac{1}{2} \sum_M W_M^{(0)} \sum_{M_2} |C_{M_2\ M\ M_2-M}^{I_2\ I\ \frac{1}{2}}|^2 = \frac{(2I_2+1)}{2(2I+1)}.$$

We now observe that only one value of I_2 of the two available $I_2 = I\pm\tfrac{1}{2}$ is considered, it being assumed that the other is excluded by nuclear selection rules. Hence the statistical factor $(2I_2+1)/2(2I+1)$. If, however, we sum over both values

(A.4) $$\sum_{I_2 M_2} W_{M_2}^{(2)} = \frac{1}{2(2I+1)} \sum_{I_2=I\pm\frac{1}{2}} (2I_2+1) = 1.$$

The statistical factor is retained in equation (4.9).

Equation (A.4) is the equivalent of the statement

$$Tr(\rho) = \sum_{I_2 M_2} W_{M_2}^{(2)} = 1.$$

(ii) For vanishing orientation (high temperatures) the angular distribution must be isotropic. For high temperature $W_M^{(0)} = 1/(2I+1)$, the statistical value. Hence by (A.1)

$$W_{M_2}^{(2)} = 1/2\,(2I+1) \quad \text{since} \quad \sum_M |C_{M_2\ M\ M_2-M}^{I_2\ I\ \frac{1}{2}}|^2 = 1.$$

Then by (A.1) and (A.3)

$$(A.5) \qquad I(\theta) = [4(2I+1)]^{-1}\sum_{M_2}1 = (2I_2+1)/4(2I+1)$$

since $\Sigma_M \Pi_\nu(M) = 0$ for $\nu > 0$. For high temperatures $I(\theta)$ given by equation (A.5) is independent of θ. The same results follow from equations (4.8) and (4.9), the high temperature approximations with $\delta = 0$.

USE OF RACAH ALGEBRA IN EVALUATING COMMUTATORS

M. J. ENGLEFIELD

Suppose $\mathbf{r}$ and $\mathbf{p}$ are the position and momentum vectors of a particle. The circular components of these vectors are obtained from the Cartesian components by the transformation

$$(1) \qquad r_1 = -i\sqrt{\tfrac{1}{2}}(r_x + ir_y), \qquad r_0 = ir_z, \qquad r_{-1} = i\sqrt{\tfrac{1}{2}}(r_z - ir_y).$$

The commutators of the r_λ and p_μ (λ, $\mu = 0$, ± 1) may be combined with certain Clebsch–Gordan coefficients to give the relations

$$\sum_\mu \langle 1\,\mu\,1\,\lambda-\mu | 1\,1\,L\lambda\rangle \cdot (r_\mu p_{\lambda-\mu} - p_{\lambda-\mu} r_\mu) = i\hbar\sqrt{3}\,\delta_{L,0}$$

$$(L = 0, 1, 2; \lambda = -L, -L+1, \ldots, L).$$

Now $\displaystyle\sum_\mu \langle 1\,\mu\,1\,\lambda-\mu | 1\,1\,L\lambda\rangle r_\mu p_{\lambda-\mu}$ is the λth component of the tensor product of rank L of $\mathbf{r}$ and $\mathbf{p}$. Denoting this by $\mathbf{r}\underset{\lambda}{\overset{L}{\circ}}\mathbf{p}$, the above equations are ·

$$(2) \qquad \mathbf{r}\underset{\lambda}{\overset{L}{\circ}}\mathbf{p} - (-1)^L\,\mathbf{p}\underset{\lambda}{\overset{L}{\circ}}\mathbf{r} = i\hbar\sqrt{3}\,\delta_{L,0}.$$

This is equivalent to the nine commutation relations between the components. The cases $L = 0, 1$ are respectively equivalent to $\mathbf{r}.\mathbf{p} - \mathbf{p}.\mathbf{r} = 3i\hbar$ and $\mathbf{r}\times\mathbf{p} + \mathbf{p}\times\mathbf{r} = 0$.

In general, a tensor of rank r is a quantity with $2r+1$ components which transform under rotations according to the $(2r+1)$-dimensional irreducible representation of the rotation group. If $S^{(s)}$ is of rank s, and $T^{(t)}$ of rank t, then

$$S^{(s)}\underset{\lambda}{\overset{L}{\circ}} T^{(t)} = \sum_\mu \langle s\,\mu\,t\,\lambda-\mu | stL\,\lambda\rangle\, S_\mu^{(s)} T_{\lambda-\mu}^{(t)} \qquad (\lambda = -L, -L+1, \ldots, L)$$

are the components of a tensor of rank L. This notation for the tensor product is due to Hope (1956).

Consider now the problem of obtaining the commutation relations between the components of the tensor of inertia of a system of N equal particles, and the corresponding functions of their momenta. Suppose $\mathbf{r}(i)$ and $\mathbf{p}(i)$ are the position and momentum vectors of the ith particle. The circular components of the tensor of inertia are

$$I^{(0)} = \sum_i \mathbf{r}(i)\overset{0}{\underset{}{\circ}}\mathbf{r}(i) \qquad \text{and} \qquad I_\lambda^{(2)} = \sum_i \mathbf{r}(i)\underset{\lambda}{\overset{2}{\circ}}\mathbf{r}(i);$$

the functions of the momenta are

$$K^{(0)} = \sum_i \mathbf{p}(i)\overset{0}{\underset{}{\circ}}\mathbf{p}(i) \qquad \text{and} \qquad K_\lambda^{(2)} = \sum_i \mathbf{p}(i)\underset{\lambda}{\overset{2}{\circ}}\mathbf{p}(i).$$

The 36 commutators between these operators are equivalent to the equations

$$(3) \quad I^{(z)} \underset{\lambda}{\overset{k}{\circ}} K^{(y)} - (-1)^{L} K^{(y)} \underset{\lambda}{\overset{k}{\circ}} I^{(z)} = 4i\hbar(-1)^{L}[(2x+1)(2y+1)]^{\frac{1}{2}}$$

$$\times \begin{Bmatrix} 1 & 1 & L \\ x & y & 1 \end{Bmatrix} J_{\lambda}^{(L)} + 2\hbar^{2} \delta_{L,0} . N . (2x+1)^{\frac{1}{2}}$$

where

$$J_{\lambda}^{(L)} = \sum_{i} \mathbf{r}(i) \underset{\lambda}{\overset{k}{\circ}} \mathbf{p}(i) \qquad \text{and} \qquad \begin{Bmatrix} 1 & 1 & L \\ x & y & 1 \end{Bmatrix} \qquad \text{is a Wigner 6-}j\text{ symbol}$$
$$\text{(Edmonds 1957).}$$

When $x = y = 2$, (3) implies 25 equations: $L = 0, 1, 2, 3, 4$ and $\lambda = -L$, $-L+1, \ldots, L$. The 6-j symbol is zero when $L = 3$ or 4. The commutator of $I_{\mu}^{(2)}$ and $K_{\tau}^{(2)}$ may be obtained from (3) by putting $x = y = 2$, $\lambda = \mu+\tau$, multiplying by $\langle 2\mu 2\tau \mid 2\ 2\ L\ \mu+\tau \rangle$, and summing over L:

$$(4) \quad I_{\mu}^{(2)} . K_{\tau}^{(2)} - K_{\tau}^{(2)} . I_{\mu}^{(2)} = (-1)^{\mu} . 2N\hbar^{2} . \delta_{\mu, -\tau} - 4i\hbar \sum_{\lambda} (-1)^{\lambda} \langle 1\mu - \lambda\ 1\ \lambda | 1\ 1\ 2\ \mu \rangle$$

$$\times \langle 1 - \lambda\ 1\ \tau + \lambda | 1\ 1\ 2\ \tau \rangle \sum_{j} r_{\mu-\lambda}(j) p_{\tau+\lambda}(j).$$

Equation (3) may be obtained, however, without considering components. $I^{(z)} \overset{k}{\circ} K^{(y)}$ can be related to $(-1)^{L} . K^{(y)} \overset{k}{\circ} I^{(z)}$ in three steps, described qualitatively by the symbolism:

$$\{r(i) \overset{z}{\circ} r(i)\} \overset{k}{\circ} \{p(j) \overset{y}{\circ} p(j)\} \to \sum_{st} \{r(i) \overset{s}{\circ} p(j)\} \overset{k}{\circ} \{r(i) \overset{t}{\circ} p(j)\}$$

$$\to \sum_{st} \{p(j) \overset{s}{\circ} r(i)\} \overset{k}{\circ} \{p(j) \overset{t}{\circ} r(i)\} \to \{p(j) \overset{y}{\circ} p(j)\} \overset{k}{\circ} \{r(i) \overset{z}{\circ} r(i)\}.$$

The second step may be accomplished by using (2). If $\mathbf{r}$ and $\mathbf{p}$ commuted, the other steps could be made by using the χ function (Hope 1952). The equation defining this transformation coefficient may be modified to give the following result: if $T^{(a)}$, $T^{(b)}$, $T^{(c)}$, and $T^{(d)}$ are tensors of rank a, b, c, d, respectively, and

$$T^{(b)} \overset{Y}{\circ} T^{(c)} - (-1)^{b+c-Y} T^{(c)} \overset{Y}{\circ} T^{(b)} = C^{(Y)},$$

then

$$(5) \quad \{T^{(a)} \overset{E}{\circ} T^{(b)}\} \overset{G}{\circ} \{T^{(c)} \overset{F}{\circ} T^{(d)}\}$$

$$= \sum_{XY} \chi \begin{pmatrix} a & b & E \\ c & d & F \\ X & Y & G \end{pmatrix} . \{T^{(a)} \overset{X}{\circ} T^{(c)}\} \overset{G}{\circ} \{T^{(b)} \overset{Y}{\circ} T^{(d)}\}$$

$$+ \sum_{XY} (-1)^{a+c+d+G-F-X} . [(2E+1)(2F+1)(2X+1)(2Y+1)]^{\frac{1}{2}}$$

$$\times \begin{Bmatrix} a & b & E \\ F & G & X \end{Bmatrix} \begin{Bmatrix} c & d & F \\ X & b & Y \end{Bmatrix} T^{(a)} \overset{G}{\circ} \{C^{(Y)} \overset{X}{\circ} T^{(d)}\}.$$

In the present application, $C^{(Y)}$ is given by (2).

The same procedure gives the commutators involving

$$J^{(z)} = \sum_i \mathbf{r}(i) \overset{k}{\circ} \mathbf{p}(i).$$

The results are:

(6) $\quad J^{(z)} \overset{k}{\circ} I^{(x)} - (-1)^{x+L} I^{(x)} \overset{k}{\circ} J^{(z)} = -2i\hbar[(2x+1)(2z+1)]^{\frac{1}{2}} \begin{Bmatrix} 1 & 1 & L \\ z & x & 1 \end{Bmatrix} \cdot I^{(L)},$

(7) $\quad J^{(z)} \overset{k}{\circ} K^{(y)} - (-1)^{y+L} K^{(y)} \overset{k}{\circ} J^{(z)}$

$$= (-1)^z \cdot 2i\hbar[(2y+1)(2z+1)]^{\frac{1}{2}} \begin{Bmatrix} 1 & 1 & L \\ z & y & 1 \end{Bmatrix} \cdot K^{(L)},$$

(8) $\quad J^{(w)} \overset{k}{\circ} J^{(z)} - (-1)^{w+z+L} J^{(z)} \overset{k}{\circ} J^{(w)}$

$$= i\hbar[(-1)^{w+z} - (-1)^L][(2w+1)(2z+1)]^{\frac{1}{2}} \begin{Bmatrix} 1 & 1 & L \\ w & z & 1 \end{Bmatrix} \cdot J^{(L)}.$$

In these equations, and in (3), x and y are assumed even.

If the vectors $\mathbf{r}(j)$ and $\mathbf{p}(k)$ are taken relative to the center-of-mass of the system, (2) becomes

$$\mathbf{r}(j) \overset{k}{\circ} \mathbf{p}(k) - (-1)^L \cdot \mathbf{p}(k) \overset{k}{\circ} \mathbf{r}(j) = i\hbar\sqrt{3} \cdot \delta_{L,0} \left(\delta_{j,k} - \frac{1}{N}\right),$$

and in (3) and (4) N is replaced by $N-1$. The other results are unchanged.

This work was done at the National Research Council, Ottawa, while I was a Postdoctorate Fellow in the Division of Pure Physics.

EDMONDS, A. R.   1957.   Angular momentum in quantum mechanics (Princeton Univ. Press, Princeton, N.J.), p. 92.
HOPE, J.   1952.   Ph.D. Thesis, University of London, England.
HOPE, J. and LONGDON, L. W.   1956.   Phys. Rev. **101**, 710.

d-WAVE CONTRIBUTION TO ELECTRON–HYDROGEN ATOM SCATTERING

R. P. McEACHRAN AND P. A. FRASER

The s- and p-wave phase shifts and the corresponding scattering cross sections for the elastic scattering of low-energy electrons by hydrogen atoms have been calculated theoretically by means of various approximate methods over the past 25 years. Most of the recent work in this field has been done using variational techniques (for example, Massey and Moiseiwitch 1951; Bransden *et al.* 1958; and Malik 1959). However, only in the last 2 years have

experimental measurements of the elastic scattering cross section been made over a wide range of energies of the incident electron. Such experiments were first carried out by Bederson et al. (1958) and then later by Brackmann et al. (1958). In the latter case there is satisfactory agreement between the theoretical and experimental results but in the former case Bederson et al. have measured cross sections greatly in excess of any of the theoretically predicted values. To help resolve the discrepancy it has been suggested (Bederson et al. 1958) that the d-wave phase shifts and cross sections be calculated.

Within the so-called exchange approximation (cf. Massey and Moiseiwitch 1951) for the elastic scattering of low-energy electrons by hydrogen atoms, the radial wave function for each partial wave is the solution of an integro-differential equation. By means of a Green's function this integrodifferential equation plus the appropriate scattering boundary conditions may be transformed into an equivalent integral equation (Morse and Feshbach 1953). A numerical method (Fraser 1958) was used to solve this integral equation on the Bendix G-15D digital computer. The s-, p-, and d-wave phase shifts and scattering cross sections were determined, within the exchange approximation, for the elastic scattering of electrons in the energy range 0 to 13.6 ev. The details of these calculations are given elsewhere (McEachran 1959). The results obtained for the s- and p-waves by this numerical method are in general accord with previous variational calculations for the exchange approximation and also with another numerical solution by Omidvar (1959); no results for the d-wave, obtained by a numerical method, have so far been published. However, Geltman (1959) has recently treated the problem by variational methods using a trial function that included excited states of the hydrogen atom, and has obtained results for the d-wave, as well as for the s- and p-waves.

The d-wave phase shifts, η_2^+ and η_2^-, for the space symmetric (singlet) and space antisymmetric (triplet) cases respectively are shown graphically in

TABLE I

Partial and total elastic scattering cross sections for the exchange approximation
(in units of πa_0^2)

Kinetic energy		s-Wave			p-Wave			d-Wave			Total.
ev	k^2	Q_0^+	Q_0^-	Q_0	Q_1^+	Q_1^-	Q_1	Q_2^+	Q_2^-	Q_2	Q
0.00	0.00	65.1	20.4	85.5							85.5
0.03	0.0025	58.7	20.1	78.8	0.000	0.000	0.00				78.8
0.13	0.01	45.2	19.4	64.6	0.000	0.003	0.00				64.6
0.54	0.04	22.4	17.0	39.5	0.004	0.048	0.05				39.5
1.22	0.09	11.1	14.1	25.2	0.014	0.213	0.23				25.4
2.18	0.16	5.74	11.4	17.1	0.032	0.540	0.57				17.7
3.40	0.25	3.05	9.23	12.3	0.052	0.953	1.00	0.0000	0.0010	0.001	13.3
4.90	0.36	1.65	7.54	9.19	0.067	1.290	1.36				10.6
6.66	0.49	0.92	6.02	6.94	0.071	1.440	1.51	0.0003	0.0080	0.008	8.46
7.65	0.5625	0.70	5.33	6.03	0.069	1.443	1.51				7.55
8.70	0.64	0.54	4.70	5.24	0.065	1.408	1.47				6.72
9.83	0.7225	0.42	4.15	4.57	0.060	1.347	1.41	0.0005	0.0154	0.016	6.00
11.0	0.81	0.34	3.67	4.02	0.051	1.269	1.27				5.32
13.6	1.00	0.24	2.89	3.14	0.035	1.094	1.09	0.0010	0.0400	0.041	4.27

Fig. 1 as a function of the energy of the incident electron. These phase shifts are quite small at low energies in comparison with the corresponding values for the s- and p-waves. As a consequence of this the d-wave scattering cross sections, $Q_{\frac{1}{2}}^{\pm}$, were relatively very small as may be seen in Table I. It was thus
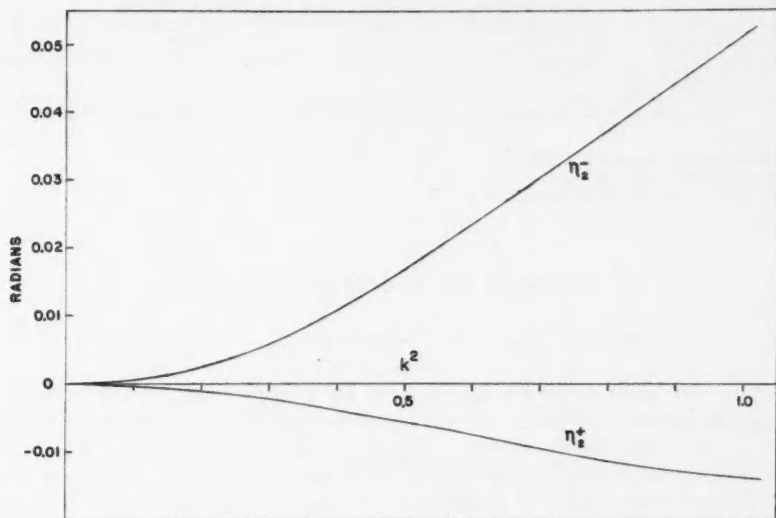

FIG. 1. The d-wave phase shifts as a function of the energy, k^2, of the incident electron in units of 13.6 ev.

found that, within the exchange approximation and up to electron energies of 13.6 ev, the inclusion of the d-wave partial scattering cross section affects the total elastic scattering cross section by at most 1% and therefore does not account for the difference between the theory and the experimental measurements of Bederson et al. (1958). It is almost certain that higher-order partial waves may be neglected at these low energies.

One of us (R.P.M.) gratefully acknowledges the support of the Ontario Research Foundation through a scholarship. This work has been supported in part by contracts with the Air Force Cambridge Research Centre and the Department of Defence Production of Canada, and since April 1959 by a research grant from the National Research Council of Canada. We wish to express our appreciation to Mrs. Joyce V. Walton for her assistance with the G-15D computer at Computing Devices of Canada in Toronto and also to Dr. M. A. Preston for making available to us the G-15D computer at McMaster University in Hamilton.

BEDERSON, B., HAMMER, J. M., and MALAMUD, H. 1958. College of Engineering, Research Division, N.Y.U., Technical Report No. 2, Electron Scattering Project, Contract No. ONR-285 (15).
BRACKMANN, R. T., FITE, W. L., and NEYNABER, R. H. 1958. Phys. Rev. 112, 1157.

BRANSDEN, B. H., DALGARNO, A., JOHN, T. L., and SEATON, M. J. 1958. Proc. Phys. Soc. 71, 877.
FRASER, P. A. 1958. Department of Physics, University of Western Ontario, London, Ontario, Scientific Report No. 4, Contract No. AF 19(604)-1718.
GELTMAN, S. 1959. 12th Annual Gaseous Electronics Conference, Washington, D.C., paper B-1.
MALIK, F. B. 1959. Z. Naturforschg. **14a** (2), 172.
MASSEY, H. S. W. and MOISEIWITCH, B. L. 1951. Proc. Roy. Soc. A, **205**, 483.
McEACHRAN, R. P. 1959. M.Sc. Thesis, Department of Physics, University of Western Ontario, London, Ontario.
MORSE, P. M. and FESHBACH, H. 1953. Methods of theoretical physics (McGraw-Hill Book Co., Inc., New York), p. 1072.
OMIDVAR, K. 1959. Institute of Mathematical Sciences, Division of Electromagnetic Research, N.Y.U., Research Report No. CX-37, Contract No. AF 19(604)-4555.

A NOTE ON THE REACTION $Zn^{64}(\gamma,n)Zn^{63}$

J. P. ROALSVIG,* R. N. H. HASLAM, AND J. L. BERGSTEINSSON

The activation curve for the reaction $Zn^{64}(\gamma,n)Zn^{63}$ has been determined from threshold to 23 Mev maximum photon energy. Zinc samples in the form of rectangular cylinders, $2.3 \times 2.3 \times 8.2$ (cm) with sheet thickness 0.5 mm, were irradiated in the center of the X-ray beam from the University of Saskatchewan 24-Mev betatron. The samples were placed with their cylindrical axes perpendicular to the beam, and with two of the sides parallel and two perpendicular to the beam direction. The irradiation times were about 3 minutes. The only competing reaction was $Zn^{67}(\gamma,p)Cu^{66}$, with a half-life of 5.1 minutes; the activity due to this reaction was found to be negligible 15 minutes after irradiation was stopped, and the samples were counted in the time interval from 20 to 40 minutes after irradiation.

The absolute yield value at 22 Mev was found relative to the reaction $Cu^{63}(\gamma,n)Cu^{62}$ in the usual way (Roalsvig and Haslam 1959; Roalsvig, Haslam, and McKenzie 1959). The value obtained was 1.49×10^8 n/mole 100 r. However, this value has to be corrected due to K-capture, which has been found to amount to 7% in the case of Zn^{64} (Huber et al. 1947). The corrected absolute yield will thus be 1.60×10^8 n/mole 100 r at 22 Mev. The activation curve normalized to this value is given in Fig. 1. The cross section was calculated by using the method of Penfold and Leiss (1958) and is given in Fig. 2. The characteristic values are given in Table I.

The reaction $Zn^{64}(\gamma,n)Zn^{63}$ has formerly been investigated by several authors; a summary of their results is given in Table I. The present yield value at 22 Mev is much lower than those obtained by Price and Kerst (1950) for the natural element, Katz et al. (1951) for the reaction $Zn^{64}(\gamma,n)Zn^{63}$ alone, and Montalbetti et al. (1953) also for the total neutron yield from the natural

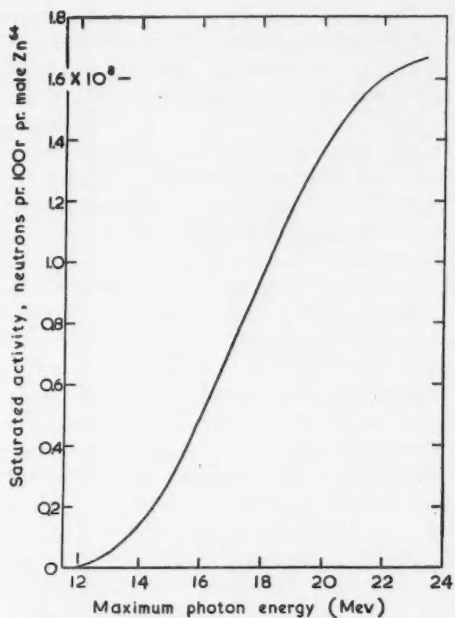*Present address: Physics Department, St. John's University, Jamaica 32, N.Y., U.S.A.

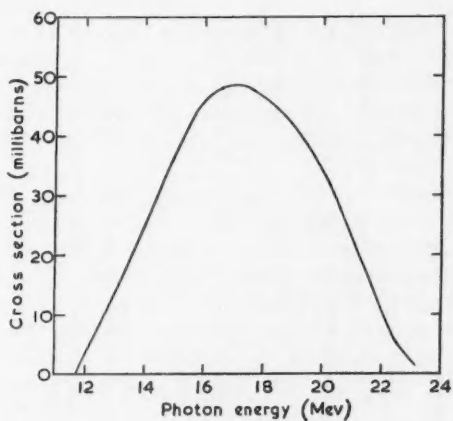FIG. 1.   Activation curve for the reaction $Zn^{64}(\gamma,n)Zn^{63}$ (corrected for K-capture).

FIG. 2.   Cross-section curve for the reaction $Zn^{64}(\gamma,n)Zn^{63}$.

TABLE I

References	Yield, n/mole 100 r	σ_{max}, mb	E_{max}, Mev	$\Gamma_{1/2}$, Mev	$\int_0^{E_1} \sigma_{(\gamma,n)} dE$, Mev-barn	(E_1, Mev)	Ratio $\{\sigma$ for $Cu^{63}(\gamma,n)\}/\{\sigma$ for $Zn^{64}(\gamma,n)\}$ at 17.6 Mev
Price and Kerst (1950)	2.35×10⁸ at 22 Mev†	120	18.5	7.1	0.83	(24)	
Katz et al. (1951)	2.82×10⁸ at 22 Mev	124	18.7	7.9	0.99	(24)	
Katz and Cameron (1951)*	(0.83 rel. to Cu⁶³ at 322 Mev)				(~.56)	(322)‡	
Strauch (1951)	(1.05 rel. to Cu⁶³ at 50 Mev)				0.77	(50)‡	
Marshall (1951)					(~.56)	(67)‡	
Sagane (1952)							
Montalbetti et al. (1953)	2.9×10⁸ at 22 Mev						
Bunbury (1954)							
Gavrilov and Lazareva (1956)	1.60×10⁴ at 22 Mev (.71 rel.	82	16.3	6.3	0.66	(27)	1.3
Present work	to Cu⁶³ at 22 Mev)	48	17.2	7.0	0.33	(23)	1.9

*Recalculation of values of Katz et al. (1951) using photon difference method.
†For natural element.
‡These values are calculated from a relative integrated cross section of 0.89 compared to the reaction $Cu^{63}(\gamma,n)$ Cu^{62}, assuming the cross section to be small above the giant dipole resonance.

element. However, since the other (γ,n) reactions in zinc are not well known, only the second one of these is directly comparable to the present value. Strauch (1951) and Marshall (1951) have measured the yield of the reaction $Zn^{64}(\gamma,n)Zn^{63}$ relative to that of the reaction $Cu^{63}(\gamma,n)Cu^{62}$ to be 0.83 at 322 Mev and 1.05 at 50 Mev respectively, as compared with 0.71 at 22 Mev of the present work.

Due to the lower yield value obtained in the present work, the calculated values for the maximum and the integrated cross section will also be much lower than those reported by Katz *et al.* (1951) and Katz and Cameron (1951). As seen from Table I, their values are higher than ours by a factor of 3. Recent results of Gavrilov and Lazareva (1956) are also higher than ours, by a factor of 2. Strauch (1951) measured the integrated cross section from threshold to 322 Mev relative to that of the reaction $Cu^{63}(\gamma,n)Cu^{62}$ to be 0.89. The integrated cross section for the giant dipole resonance for the latter reaction, as taken from Katz and Cameron (1951) and normalized to the new yield value at 22 Mev of Roalsvig, Haslam, and McKenzie (1959), is 0.63 Mev-barn. If we assume the cross sections to be very small above the giant dipole resonance, the integrated cross section of Strauch (1951) for the reaction $Zn^{64}(\gamma,n)Zn^{63}$ will be 0.56 Mev-barn. The same relative value as obtained by Strauch (1951) was also reported by Sagane (1952), integrating up to 67 Mev. Marshall (1951) reports a value 0.77 Mev-barn, integrating up to 50 Mev. Thus, the previously reported values for the integrated cross section are between 0.56 and 0.99 Mev-barn. These values are all much higher than the present result 0.33 Mev-barn.

Bunbury (1954) measured the ratio of the cross sections of $Cu^{63}(\gamma,n)Cu^{62}$ to $Zn^{64}(\gamma,n)Zn^{63}$ at 17.6 Mev to be 1.3. The present value for this ratio will be 1.9, indicating that Bunbury's cross section for $Zn^{64}(\gamma,n)Zn^{63}$ is somewhat higher than the present one.

As mentioned previously no comparison can be made with results obtained for the total neutron yield for the natural element. However, the yield and cross-section values reported in this work for the reaction $Zn^{64}(\gamma,n)Zn^{63}$ are lower than those of other investigators. For this reason the normalization against the reaction $Cu^{63}(\gamma,n)Cu^{62}$ was rechecked carefully several times with identical results.

In comparing our results with those previously obtained in this laboratory several points might be mentioned. The Penfold–Leiss method of calculation of cross sections used in this work yields values of peak and integrated cross sections some 40% lower than the photon difference method previously used. Also the absolute yield at 22 Mev of the reaction $Cu^{63}(\gamma,n)Cu^{62}$ is now thought to be about 20% lower than that used in 1951. Perhaps of equal importance is that our methods of correcting for self-absorption in the zinc and copper samples have been greatly improved.

BUNBURY, D. ST. P.   1954.   Proc. Phys. Soc. A, **67**, 1106.
GAVRILOV, B. I. and LAZAREVA, L. A.   1956.   Zhur. Eksptl. i Teoret. Fiz. **30** (5), 855.
HUBER, O., MEDICUS, H., PREISWERK, P., and SHEFFEN, R.   1947.   Helv. Phys. Acta, **20**, 495.

KATZ, L. and CAMERON, A. G. W.   1951.   Can. J. Phys. **29**, 518.
KATZ, L., JOHNS, H. E., BAKER, R. G., HASLAM, R. N. H. and DOUGLAS, R. A.   1951.   Phys.
      Rev. **82**, 271.
MARSHALL, L.   1951.   Phys. Rev. **83**, 345.
MONTALBETTI, R., KATZ, L., and GOLDEMBERG, J.   1953.   Phys. Rev. **91**, 659.
PENFOLD, A. S. and LEISS, J. E.   1958.   Analysis of photo cross sections (Physical Research
      Laboratory, University of Illinois, Champaign, Ill., U.S.A.).
PRICE, G. A. and KERST, D. W.   1950.   Phys. Rev. **77**, 806.
ROALSVIG, J. P. and HASLAM, R. N. H.   1959.   Can. J. Phys. **37**, 499.
ROALSVIG, J. P., HASLAM, R. N. H., and MCKENZIE, D. J.   1959.   Can. J. Phys. **37**, 607.
SAGANE, R.   1952.   Phys. Rev. **85**, 926.
STRAUCH, K.   1951.   Phys. Rev. **81**, 973.

RELATIVE INTENSITIES OF K–LL AUGER LINES IN $_{64}Gd^{156}$[*]

G. T. EWAN AND JANET S. MERRITT

The relative intensity measurements reported in this note were made
primarily for the purpose of comparison with the measurements reported in
an earlier paper on Sm^{152} (Ewan, Graham, and Grodzins 1960). This com-
parison was carried out because the relative intensities quoted for the K–LL
Auger lines in Sm^{152} were deduced on the assumption that there were no un-
reported conversion lines in this energy region. The possibility of mistaking a
weak conversion line for an Auger line is greatly reduced by the use of high
resolution. Further, where more than one nuclide is studied, it is very im-
probable that such weak conversion lines would occur at the same position
in the Auger spectrum in each case. Since the theoretical relative intensities
vary slowly with Z, the similarity in the measurements for $_{64}Gd^{156}$ and those
observed in $_{62}Sm^{152}$ makes it unlikely that either set of results is being seriously
affected by unreported conversion lines.

The K–LL Auger spectrum of Gd^{156} was observed in a study of the low-energy
conversion line spectrum of Eu^{156}. Sources of Eu^{156} were prepared by irradiating
enriched Sm^{154} (95%) in the NRX reactor for 1 month at a flux of 6×10^{13}
n/sq. cm sec. Eu^{156} is formed by the successive reactions $Sm^{154}(n,\gamma)Sm^{155} \xrightarrow{\beta^-}$
$Eu^{155}(n,\gamma)Eu^{156}$. High specific activity Eu^{156} was separated from the inactive
Sm by an ion exchange column method (Smith and Hoffman 1956).
Throughout the separation polythene ware was used to minimize picking
up inactive contaminants from container walls which would lower the specific
activity of the resulting source material. The separated europium chloride
was sublimed from a boat-shaped tantalum filament through a slot 0.040 in.
wide$\times$0.5 in. long onto a backing of Al foil 800 $\mu g/cm^2$ thick. The sublimed
source had an estimated thickness of ~ 20 $\mu g/cm^2$.

For these experiments the $\pi\sqrt{2}$ spectrometer (Ewan *et al.* 1959a) was set
at 0.1% resolution and the data recorded automatically as discussed in the

[*]Issued as A.E.C.L. No. 941.

TABLE I

Comparison of relative intensities of K-LL Auger lines in $_{64}$Gd^{156} and $_{62}$Sm^{152}

Transition	$L_1L_1(^1S_0)$	$L_1L_3(^1P_1)$	$L_2L_2(^1S_0)$	$L_1L_3(^3P_1)$	$L_1L_2(^3P_2)$	$L_2L_3(^1D_2)$	$L_2L_3(^3P_2)$
$_{64}$Gd^{156}	1.0 ± 0.07	1.40 ± 0.10	0.27 ± 0.07	1.11 ± 0.09	0.19 ± 0.09	3.08 ± 0.18	1.28 ± 0.09
$_{62}$Sm^{152}	1.0 ± 0.05	1.39 ± 0.06	0.26 ± 0.06	1.18 ± 0.06	0.29 ± 0.09	3.14 ± 0.13	1.39 ± 0.06
Theoretical $Z = 64$	1.0	1.30	0.18	1.86	0.24	4.42	2.00

Sm^{152} paper. The observed K–LL Auger spectrum is shown in Fig. 1. The high background is due to the presence of the β-ray continuum from Eu^{155} and Eu^{156}. The slope over the small energy region is due principally to the low-energy tails of the very intense K – 88.97-kev line in Eu^{156} and the strong K – 86.56-kev line in Eu^{155}.
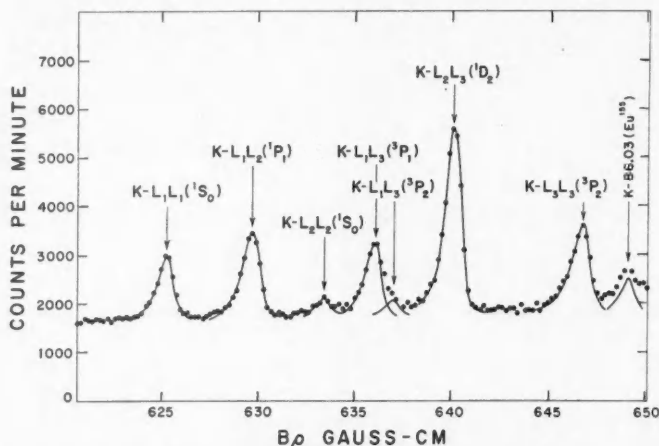
FIG. 1.   The K–LL Auger spectrum of Gd^{156} observed in a study of the β-decay of Eu^{156}.

The relative intensities of the lines were obtained by measuring the areas of the lines after subtraction of the contribution due to neighboring lines. The line counting rates were also plotted on a semilog scale after the β-ray continuum and background counting rates had been subtracted. The method of estimating the contributions of the tails from this type of plot is discussed more fully elsewhere (Ewan *et al.* 1959*b*). In estimating these contributions the line shape of the K – 88.96-kev line was used as a standard line shape in this energy region. It was found that the relative intensity measurements were sensitive to the exact line shape used. The shape assumed for the low-energy tail was varied in order to see what range of tail shapes were consistent with the data. This possible source of error has been included with the statistical counting errors, in the errors quoted for the intensities listed in Table I. The measurements were also corrected for the calculated (3%) variation in the counter window transmission from 33 to 36 kev.

The measured relative intensities are compared with the results for Sm^{152} in Table I. The good agreement between the two sets of results makes it unlikely that either is being seriously affected by unreported conversion lines. The theoretical relative intensities predicted by Asaad and Burhop (1958) for $Z = 64$ are also listed in Table I. The lack of agreement with the theoretical predictions is similar to that observed for Sm^{152} and confirms the conclusions discussed in the Sm^{152} paper (Ewan, Graham, and Grodzins 1960).

ASAAD, W. N. and BURHOP, E. H. S.   1958.   Proc. Phys. Soc. **71**, 369.
EWAN, G. T., GRAHAM, R. L., and GRODZINS, L.   1960.   Can. J. Phys. **38**, 163.
EWAN, G. T., GEIGER, J. S., GRAHAM, R. L., and MACKENZIE, D. R.   1959*a*.   Can. J. Phys. **37**, 174.
———— 1959*b*.   Phys. Rev. **116** (4).
SMITH, H. L. and HOFFMAN, D. C.   1956.   J. Inorg. & Nuclear Chem. **3, 243**.

LETTERS TO THE EDITOR

Under this heading brief reports of important discoveries in physics may be published. These reports should not exceed 600 words and, for any issue, should be submitted not later than six weeks previous to the first day of the month of issue. No proof will be sent to the authors.

The Unusual Cosmic Ray Events of July 17–18, 1959*

Unusual intensity changes in cosmic rays on July 17 and 18 have been noted by Carmichael and Steljes (1959) and by private communication with several other workers in this field. Differences in the intensity changes with different geographical positions and altitudes are apparent in the five Canadian stations where continuous intensity measurements have been undertaken and at Thule where there is close co-operation between the Canadian stations and that station operated by the Bartol Research Foundation.

The differences are unusual in that rapid increases in intensity which show decided differences at different localities have occurred after Forbush events. These intensity increases do not resemble the sudden increases that have occurred five times in cosmic ray history associated with solar flares. On the other hand it is quite possible that one or more of them may later be shown to be a flow of particles of solar origin, some of which have sufficient energy to affect sea level measurements at appropriate latitudes and longitudes.

The five Canadian stations and Thule form a net roughly triangular in shape covering geomagnetic latitudes from 57° to 88° and geographic west longitudes from 68.8° to 115.6°. It was decided to present the results in this note as soon as they were ready rather than wait for more detailed analyses of the many more stations that are exchanging data in the I.G.C. program.

The six stations involved have the following co-ordinates:

	Geographic		Geomagnetic lat.	Altitude, meters
	Lat.	Long.		
Thule	N. 76°33′	W. 68°50′	88.0°	260
Resolute	N. 74°41′	W. 94°54′	82.9°	17
Churchill	N. 58°45′	W. 94°05′	69.7°	39
Deep River	N. 46°06′	W. 77°30′	57.5°	145
Sulphur Mountain	N. 51°12′	W. 115°36′	58.2°	2283
Ottawa	N. 45°24′	W. 75°54′	56.8°	101

The equipment from which data are presented here consists of a standard neutron monitor of Canadian design (Fenton, Fenton, and Rose 1958) at Thule, Resolute, Churchill, Sulphur Mountain, and Ottawa; a somewhat larger standard neutron monitor at Deep River; and a standard cubical telescope at Resolute, Churchill, Sulphur Mountain, and Ottawa.

Figure 1 shows the intensity variation of the nucleon component at Sulphur Mountain and Resolute, the meson component at Sulphur Mountain and Churchill from July 11 to July 19 inclusive. A large Forbush decrease occurred on July 11 followed by a very slow recovery. This has not been an unusual occurrence during the current solar epoch. Before recovery to the pre-event level, a second similar event occurred on July 15 starting about 1000 hours G.M.T. This was followed (about 0000 hours on July 17) by an unusually rapid increase which appears superficially to be something quite different from the usual slow but irregular recovery from a rapid Forbush decrease. An examination of this increase marked A and B in Fig. 2 shows it had quite different characteristics at different stations. The increase at Sulphur Mountain was much greater in magnitude than at the other stations. When the shape of the intensity curve at the different stations is examined it is possible to describe the curve as two peaks in intensity one marked A at about 0600 hours and the second B at about 1600 hours on July 17. The two merge together, in the case of the Sulphur Mountain station, the intensity dropping very quickly when it was still high at the other stations. B might be interpreted as occurring earlier at this station making the over-all peak higher than elsewhere, or the high amplitude may be due to the high altitude of the station. The decrease after event B was no doubt a third Forbush decrease making the intensity at 0200 hours on July 18 the lowest that has occurred for some time, possibly the lowest during the present solar cycle.
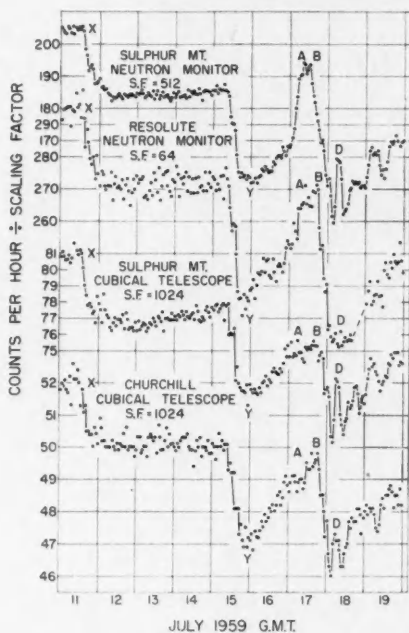
Fɪɢ. 1. Intensity level changes from July 11, 1959, to July 19, 1959, at Sulphur Mountain (neutron monitor and cubical telescope), Resolute (neutron monitor), and Churchill (cubical telescope). Hourly values are plotted. Time is G.M.T. The ordinate is counts per hour divided by the scaling factor (S.F.) which is shown for each curve. Data have been corrected for barometer changes.

The increase marked C (Fig. 3) started just at the minimum of this Forbush event and the intensity rose very rapidly for a few minutes only. Specific attention was drawn to this event by Carmichael and Steljes (1959). It can only be seen in Fig. 3 which shows 10-minute values and its significance might be questioned except at the Deep River and Sulphur Mountain stations where the counting rate was high enough to make it certain. The amplitude of this rapid increase was about 6% at these two stations. At the other stations there is some indication that it may also have occurred but the statistics are not good enough to be certain.

This particular event or increase "C" is the only unusual event in this group that resembles the sudden increases associated with solar flares. The increase is small compared with the last two (November 19, 1949, and February 23, 1956) and the decay time is rather short.

The fourth unusual event is that marked D in Figs. 2 and 3. The differences in this event at the different stations are very striking but are confirmed by agreement of nearby stations in such a way that there is no question about their validity. Figures 2 and 3 show that this event occurs with an amplitude of about 10% at Churchill and Sulphur Mountain. At Ottawa and Deep River it occurs 1 to 2 hours earlier and with much lower amplitude. At Resolute and Thule it is completely absent within the accuracy of the data.

The recovery after event D appears to be that normally occurring after a deep Forbush decrease.

A study of data from other stations is desirable before presenting definite conclusions about the nature of these events but a number of suggested approaches can be made from these data. It is difficult to say whether the increases A and B represent an increase in incoming particles or a collapse of the modulating system that decreases the intensity during a Forbush event. The A side of this increase may represent lower energy particles than the B side because it was more prominent at Sulphur Mountain while the meson component (Fig. 1) showed mainly at the time indicated by B at the four stations: Ottawa, Churchill, Resolute, and Sulphur Mountain. The event C resembles a solar flare increase but is only definite in the nucleon component where the counting rate is very high. There is no real evidence for it in the 10-minute meson counts at Ottawa, Sulphur Mountain, Churchill, or Resolute.
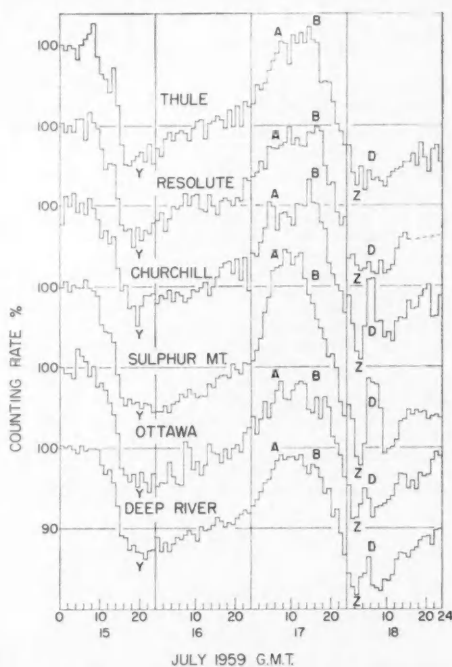
FIG. 2. Intensity levels changes from July 15 to 19, 1959, recorded with neutron monitors at Thule, Resolute, Churchill, Sulphur Mountain, Ottawa, and Deep River. The histogram represents hourly levels (G.M.T.) presented as a percentage of the mean level during the first 9 hours of July 15. Data have been corrected for barometric changes.

Event D suggests qualitatively a burst of particles having an asymptotic direction in or near the equatorial plane of the earth's dipole. Further analysis involving other stations is required to confirm this.

Table I shows the level of intensities at the important points discussed above as a percentage of the average during the first 9 hours of July 15.

TABLE I

Station	X	Y	A	B	C	Z	D
				% of first 9 hours of July 15			
				Nucleon component			
Thule	107.8	85	100	101	?	83	a
Resolute	108.4	87	97	99	?	82	a
Churchill	108.6	87	99	101	?	80	92
Sulphur Mountain	109.9	85	103	?	87	78	89
Ottawa	107.7	86	97	96	?	79	85
Deep River	108.6	87	98	97	86	81	86
				Meson component			
Resolute	103.5	93	98	98	a	91	a
Churchill	103.8	94	98	99	a	92	94
Sulphur Mountain	104.2	93	97	97	a	90	94
Ottawa	102.5	94	97	99	a	91	93

NOTE: The nucleon or the meson intensity level during the first 9 hours of July 15 is arbitrarily taken as the 100% level at each station. Column "X" represents the intensity during the first 14 hours of July 11, that is the intensity before this series of events. Column "Y" represents the minimum of the Forbush decrease on July 15 and column "Z" represents the lowest level between B and D or the lowest level after the Forbush event of July 17. A, B, C, and D are the levels of the peaks indicated by these letters on Figs. 1, 2, and 3. There is some uncertainty in selecting these intensity levels because of statistical fluctuations and some arbitrary smoothing has been used.
  ? Uncertain, because of inadequate statistics.
  a Strong evidence that this increase was not present.
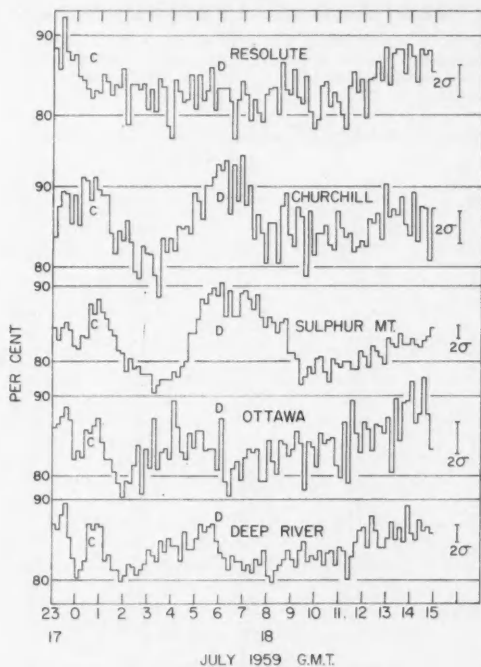
FIG. 3.   Intensity levels in 10-minute intervals from 2300 hours July 17 to 1500 hours G.M.T. July 18, 1959. The data are presented as a percentage of the average for the first 9 hours of July 15th. These data were taken from the original records without barometer correction but approximate barometer corrections have been made to bring the level of intensity to correspond with Fig. 2.

The authors would like to thank H. Carmichael and J. F. Steljes for permission to use the data from the Deep River Station.

CARMICHAEL, H. and STELJES, J. F.   1959.   Phys. Rev. Letters, 3, 392.
FENTON, A. G., FENTON, K. B., and ROSE, D. C.   1958.   Can. J. Phys. 36, 824.

B. G. WILSON*
D. C. ROSE†
M. A. POMERANTZ‡

*Sulphur Mountain Laboratory, National Research Council, Banff, Alberta.
†Division of Pure Physics, National Research Council, Ottawa, Canada.
‡Bartol Research Foundation, Swarthmore, Pennsylvania, U.S.A.

Frequency Measurement of Standard Frequency Transmissions[1],[2]

Measurements are made at Ottawa, Canada, using N.R.C. caesium-beam frequency resonator as reference standard (with an assumed frequency of 9 192 631 770 c.p.s.). Frequency deviations from nominal are quoted in parts per 10^{10}. A negative sign indicates that the frequency is below nominal.

Date, November 1959	MSF, 60 kc/s	GBR, 16 kc/s		KK2XEI, 60 kc/s
		7-hour average*	24-hour average	
1	−167	−164	−162	N.M.
2	N.M.	−152	N.M.	−69
3	N.M.	−159	N.M.	−69
4	−166	−160	−159	−73
5	−171	−159	−159	−70
6	N.M.	−154	−158	−70
7	−164	−160	−160	N.M.
8	N.M.	−164	−161	N.M.
9	−162	−162	−161	−70
10	−164	−158	−158	−71
11	−153	−158	−156	N.M.
12	−160	−154	−156	−69
13	−158	−153	−156	−68
14	−162	−160	−157	N.M.
15	−163	−160	−159	N.M.
16	−154	−159	−159	−72
17	−159	−156	−155	−69
18	−158	−160	N.M.	−73
19	−167	−157	−158	−69
20	−163	−160	−158	−71
21	−158	−156	−157	N.M.
22	N.M.	−162	−160	N.M.
23	−151	−155	−157	−65
24	−157	−158	−158	N.M.
25	−170	−156	−156	−69
26	−157	−153	−156	N.M.
27	N.M.	−160	−157	−69
28	N.M.	−154	N.M.	N.M.
29	N.M.	N.M.	N.M.	N.M.
30	−153	−164	N.M.	−74
Midmonthly mean	−161	−158	−158	−70
Midmonthly mean of WWV	−102			

NOTE: N.M. No measurement.
*Time of observations: 00.00 to 05.30 and 22.30 to 24.00 U.T.

The Cosmic Ray Increase of 17 July 1959

Some of the unusual intensity changes of cosmic rays observed during July 1959 are described in an accompanying note (Wilson, Rose, and Pomerantz 1959). Carmichael and Steljes (1959) suggested the possibility that the marked increase which began early on 17 July might represent a sea-level effect of cosmic rays from the sun, although they thought it more probable that the effect could be described as an unusual modulation of galactic cosmic radiation. We here present evidence from ionospheric-scatter signal intensity observations at about 38 Mc/sec that the sun indeed emitted particles of cosmic ray energy at this time.

In Fig. 1, the hourly median signal intensities observed for the communication links (a) between Iceland and England, and (b) between Labrador and Massachusetts are shown together with an estimate (in fine line) of normal signal intensity behavior. The interpretation of similar observations made during the great solar event of 23 February 1956 has already been discussed by one of us (Bailey 1959).

We first note in (b) the rise in signal intensity beginning at about 0000 U.T. on 17 July, while the Importance 3+ flare which began at 2115 U.T. on 16 July was still in progress, though it had passed its peak of activity. This increase appears to be a phenomenon of the type previously designated *early effect*.
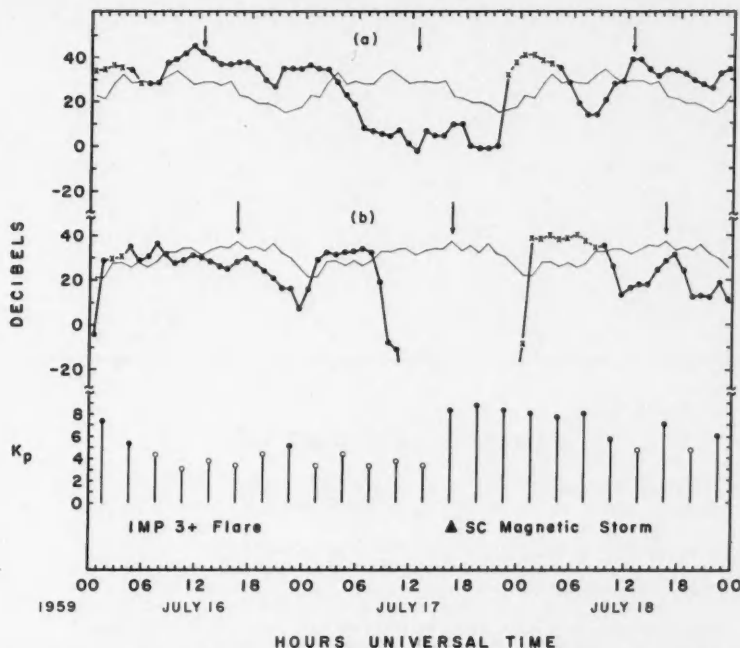
FIG. 1. Observed variation with time of intensity of signals propagated by ionospheric scattering with estimated normal variations indicated by the fine line. Vertical arrows indicate local apparent noon at path midpoint. X's indicate values obtained by interpolation during the presence of much stronger signals propagated by a different mode (perhaps E's). (a) Observations made in England of signals from Iceland at 37.15 Mc/sec. (b) Observations made in Labrador of signals from Massachusetts at 38.58 Mc/sec.

The large decreases in signal intensity which began at about 0300 U.T. in (a) and at about 0800 U.T. in (b) are sunrise effects characteristic of *late effect* absorption, indicative of the presence of a large excess of ionizing particles having rigidities above geomagnetic cutoff. It is in the D region of the ionosphere near the midpoints of these two communication links that absorption resulting from solar cosmic ray ionization is observed. These two midpoint regions correspond to a magnetic rigidity cutoff of about 10^9 volts.

Balloon-borne counters released shortly after the beginning of the flare indicated an enhanced intensity over College, Alaska (Brown and D'Arcy 1959). The total ionization at 10 g/cm^2 over Minneapolis, also above normal during the early hours of 17 July, increased greatly at about 1000 U.T. (Winckler 1959). Thus the arrival of a large flux of particles having rigidities well below normal cutoff occurred after the intensity of higher rigidity particles (above normal cutoff) had reached its maximum as indicated by neutron monitors. The occurrence at balloon altitudes of large fluxes of normally forbidden protons appears, in any case, to be associated with geomagnetic disturbance which normally begins many hours after the associated flare.

Although the shape of this event as observed at ground stations differs considerably from the five previous solar cosmic ray increases, the available evidence suggests the presence early on 17 July 1959 of flare-associated cosmic rays having rigidities above the geomagnetic cutoff.

BAILEY, D. K. 1959. Proc. IRE 47, 255.
BROWN, R. R. and D'ARCY, R. G. 1959. Phys. Rev. Letters, 3, 390.
CARMICHAEL, H. and STELJES, J. F. 1959. Phys. Rev. Letters, 3, 392.
WILSON, B. G., ROSE, D. C., and POMERANTZ, M. A. 1959. Can. J. Phys. 38, 328.
WINCKLER, J. R. 1959. Private communication.

DANA K. BAILEY*
MARTIN A. POMERANTZ†

*Present address: National Bureau of Standards, Boulder, Colorado.
†Bartol Research Foundation of the Franklin Institute, Swarthmore, Pennsylvania.

NOTES TO CONTRIBUTORS

Canadian Journal of Physics

MANUSCRIPTS

General.—Manuscripts, in English or French, should be typewritten, double spaced, on paper $8\frac{1}{2}\times11$ in. **The original and one copy are to be submitted.** Tables and captions for the figures should be placed at the end of the manuscript. Every sheet of the manuscript should be numbered. Style, arrangement, spelling, and abbreviations should conform to the usage of recent numbers of this journal. Greek letters or unusual signs should be written plainly or explained by marginal notes. Characters to be set in boldface type should be indicated by a wavy line below each character. Superscripts and subscripts must be legible and carefully placed. Manuscripts and illustrations should be carefully checked before they are submitted. Authors will be charged for unnecessary deviations from the usual format and for changes made in the proof that are considered excessive or unnecessary.

Abstract.—An abstract of not more than about 200 words, indicating the scope of the work and the principal findings, is required, except in Notes.

References.—References should be listed **alphabetically by authors' names**, unnumbered, and typed after the text. The form of the citations should be that used in current issues of this journal; in references to papers in periodicals, titles should not be given and only initial page numbers are required. The names of periodicals should be abbreviated in the form given in the most recent *List of Periodicals Abstracted by Chemical Abstracts*. All citations should be checked with the original articles and each one referred to in the text by the authors' names and the year.

Tables.—Tables should be numbered in roman numerals and each table referred to in the text. Titles should always be given but should be brief; column headings should be brief and descriptive matter in the tables confined to a minimum. Vertical rules should not be used. Numerous small tables should be avoided.

ILLUSTRATIONS

General.—All figures (including each figure of the plates) should be numbered consecutively from 1 up, in arabic numerals, and each figure referred to in the text. The author's name, title of the paper, and figure number should be written in the lower left corner of the sheets on which the illustrations appear. Captions should not be written on the illustrations.

Line drawings.—Drawings should be carefully made with India ink on white drawing paper, blue tracing linen, or co-ordinate paper ruled in blue only; any co-ordinate lines that are to appear in the reproduction should be ruled in black ink. Paper ruled in green, yellow, or red should not be used. All lines must be of sufficient thickness to reproduce well. Decimal points, periods, and stippled dots must be solid black circles large enough to be reduced if necessary. Letters and numerals should be neatly made, preferably with a stencil (**do NOT use typewriting**) and be of such size that the smallest lettering will be not less than 1 mm high when the figure is reduced to a suitable size. Many drawings are made too large; originals should not be more than 2 or 3 times the size of the desired reproduction. Whenever possible two or more drawings should be grouped to reduce the number of cuts required. In such groups of drawings, or in large drawings, full use of the space available should be made; the ratio of height to width should conform to that of a journal page ($4\frac{3}{4}\times7\frac{1}{2}$ in.), but allowance must be made for the captions. **The original drawings and one set of clear copies (e.g. small photographs) are to be submitted.**

Photographs.—Prints should be made on glossy paper, with strong contrasts. They should be trimmed so that essential features only are shown and mounted carefully, with rubber cement, on white cardboard, with no space between those arranged in groups. In mounting, full use of the space available should be made. **Photographs are to be submitted in duplicate;** if they are to be reproduced in groups one set should be mounted, the duplicate set unmounted.

REPRINTS

A total of 100 reprints of each paper, without covers, are supplied free. Additional reprints, with or without covers, may be purchased at the time of publication.

Charges for reprints are based on the number of printed pages, which may be calculated approximately by multiplying by 0.6 the number of manuscript pages (double-spaced typewritten sheets, $8\frac{1}{2}\times11$ in.) and including the space occupied by illustrations. Prices and instructions for ordering reprints are sent out with the galley proof.

Contents